Development of novel intra-articular injection formulations based on porous artificial cartilage

By

Xiaoyu Han

A thesis submitted to
the University of Birmingham
for the degree of
DOCTOR OF PHILOSOPHY

Nano-Formulation Engineering Research Group
School of Chemical Engineering
College of Engineering and Physical Sciences
University of Birmingham
September 2022

Abstract

Osteoarthritis (OA) patients suffer from joint pain during daily activities, which affects more than 40% of people older than 70 years old. The intra-articular injection (IAI) with drug delivery systems (DDSs) has been developed for OA treatment, which relieves pain feeling for patients but is difficult to stay in the articular space sustainedly. As different materials has been used as the drug carriers in the DDSs, considered to the nanometre-sized cartilage pores on the surface, the present thesis aims to focus on the nanoparticles and improve the nanoparticle-based solution lubrication via *in vitro* tribological measurement on an artificial cartilage system.

In this thesis, an artificial cartilage model was fabricated by porous polydimethylsiloxane (PDMS) coated with polyvinyl alcohol (PVA), which was applied as the substrate of the lubrication system in this thesis. The porosity of artificial cartilage varies from 54.6 ± 1.1% to 81.7 ± 0.7%, which is controlled by the sodium chloride fraction used in porous PDMS preparation. In combination with sodium chloride fraction and curing agent ratio, it is possible to control Young's modulus and coefficient of friction (CoF). By increasing the sodium chloride fraction or curing agent ratio of porous PDMS, it was found that the Young's modulus of porous PDMS decreases and the CoF of porous PDMS surface increases. With the coating of PVA, the porous PDMS surface was modified to hydrophilic as fresh cartilage, which increases the Young's modulus and decreases the CoF of the models. The structural, elastic, and tribological characteristics of the set of artificial scaffolds are aligned with values for the different OA stages (stages 0 - 3) of degeneration of the cartilage tissues, as defined by the International Cartilage Repair Society (ICRS).

Using the artificial cartilage models developed by PDMS coated with PVA, the nanoparticle solution parameters were found to impact the lubrication behaviour. The CoF of the nanoparticle solution was found to increase while the normal load increased, and the increase of nanoparticle size increases the CoF on the PDMS coated with PVA, which was increased from 0.042 ± 0.005 to 0.060 ± 0.025 when the size increased from 152.40 nm to 256.00 nm. A critical concentration of nanoparticles was found with the lowest CoF. While the nanoparticle concentration increases, the CoF of the nanoparticle solution decreases when the concentration is lower than the critical concentration and increases when higher.

Synthesised nanogels provided more different choices of nanoparticles to be compared in the present study. Compared to different types of nanogels, the nanogel prepared under the condition of the microfluidic chip with 2 bars pressure showed the lowest CoF. Moreover, the nanogel showed much higher efficiency than silica nanoparticles in reducing CoF of poroelastic surface, including artificial models and human osteoarthritis cartilage. At the concentration of 0.1 mg ml^{-1}, the CoF of nanogels (AEL 04) on human cartilage varies from 0.005 to 0.008, and the CoF of silica nanoparticles (Aerosil 150) is from 0.007 to 0.013. In addition, osteoarthritis articular cartilage mechanical properties were measured in this thesis with a wide range of Young's modulus and CoF; and the porous structure of cartilage were exhibited in AFM and SEM images.

Overall, this thesis replicated the articular cartilage with porous polymer materials, which fabricated a consistent artificial cartilage model with controllable mechanical properties. Moreover, the thesis studied the lubrication system of nanosized particles. The findings advance the understanding of nanofluid tribological behaviour on the artificial cartilage and confirm the better lubrication efficiency of nanogels and the best type of nanogel, which provides guidance for the IAI formulation improvement and the drug carrier choice in future work.

Acknowledgments

First of all, I would like to sincerely appreciate my supervisor Professor Zhengyu J. Zhang for his patient guidance during all these four years. And he supports me not only on academic research but also mental health and daily life, especially when I experienced the hard period during the pandemic and lockdown. I would like to thank my supervisor Professor Simon Jones for his support on bio-medical field, and the well-organised medical laboratory.

I gratefully acknowledge the Engineering and Physical Sciences Research Council (EPSRC) for providing funding to support me to finish the project and this thesis. I would also like to acknowledge the department of College of Engineering and Physical Sciences, the school of Chemical Engineering of the University of Birmingham for the favourable experiment laboratories.

I would like to thank all my group members for their guidance in the experiment and concern in the life during these four years.

I would like to express my acknowledge to Professor Scialla Stefano and Professor Emanuele Mauri for providing the nanogel preparation. I would like to thank Dr Dominika Nanus and Dr Susanne Wijesinghe for their help in cartilage collection. I would like to thank Dr Nicholas Davidson for providing the device of dynamic light scattering (DLS).

Lastly, I would like to thank my parents and all my family for their love, support and concern.

Contents

List of Figures

List of Tables

Acronyms

AFM Atomic force microscopy.

BMI Body mass index.

CA Curing agent.

CoF Coefficient of friction.

DDS Drug delivery system.

DLS Dynamic light scattering.

DMEM Dulbecco's modified eagle medium.

ECM Extracellular matrix.

FTIR Fourier-transform infrared spectroscopy.

HA Hyaluronic acid.

IAI Intra-articular injection.

ICRS International Cartilage Research Society.

LPEI Linear polyethyleneimine.

MEET Mixed emulsion/evaporation technique.

OA Osteoarthritis.

PBS Phosphate-buffered saline.

PCL Polycaprolactone.

PDMS Polydimethylsiloxane.

PEG Polyethylene glycol.

PGA Polylactic acid.

PLA Polylactic acid.

PLGA Poly(lactic-co-glycolic acid).

PVA Polyvinyl alcohol.

SCPL Solvent-casting particulate leaching.

SEM Scanning electron microscope.

Chapter One

Introduction

1.1 Motivation

Osteoarthritis (OA), the most typical form of arthritis, is considered as a multi-faceted disease including cartilage and synovium [1, 2]. Most patients who suffer from OA start from the age of 40 to 50, and over 40% of people older than 70 are suffering from the pain of osteoarthritis [3, 4]. In fact, the tendency shows that the number of young OA patients is increasing [3, 4]. Osteoarthritis impacts the movement of daily life, 80% of OA patients are suffered from joint movement limitation, and 25% of patients cannot act in most usual activities [5]. The morbidity and incidence of OA reported in 2017 were predicted at 3754.2 and 181.2 per hundred thousand people, which increased by 9.3% and 8.2% from the data in 1990 [6]. From the economic aspect, a model showed that a patient who suffered OA from 50 years old would reduce 62,383 pounds earning, and the government must pay 16,034 pounds for the benefits system [7]. The cost of OA in some developed countries was estimated, which are Spain ($1.2 billion, £2010 per patient per year), UK ($6.5 billion, £2010 per patient per year), and US ($12.7 billion, $2007 per patient per year) [8–10]. In summary, the high morbidity of OA disease caused a financial burden to the governments and patients.

As osteoarthritis is divided into six stages from healthy to the most severe, different treatment strategies are used accordingly. For early stages of OA, oral drugs are used to relieve the pain, and the late-stage patients can only replace the joints by surgery. Even though the immunity system attempts to repair the erosion by OA, the degeneration of cartilage in OA disease is persistent [11]. In recent years, viscosupplementation has been used for OA joint injection and decreases the pain feeling for patients. However, frequent injection and temporary improvement cannot solve the OA, then the injection formulation with the drug delivery system was introduced for targeted treatment. The drug carrier in the system also meets the difficulty of clearance by the human immunity system. Therefore, the behaviour of injection drug carriers is more focused on carrier targeting and drug release. In fact, nanolubricant provides the chance for the drug delivery carriers that afford the lubricant simultaneously, which relieves pain for patients.

With the progress of osteoarthritis, articular cartilage shows the degeneration in mechanical properties, and the surface of cartilage turns rougher with the fragment. In addition, the OA cartilage turns to soft, which can not provide enough support and lubrication for the joints, which causes the pain feeling to the patients. Besides the degeneration of osteoarthritis, cartilage is always along with the degeneration of mechanical properties. Although the injection of formulation has an evident effect on reducing the friction and releasing pain feeling from patients, the carriers with the drug will be cleared by lymphatic and blood vessels from hours to months [12]. Moreover, the drugs are unattainable to regenerate or reverse cartilage from OA, which can only slow down the progression and relieve the pain. Therefore, it is essential to maximise the efficiency of drug carriers in the drug delivery system. Considering the function of particle lubrication, it can potentially decrease friction by enhancing the lubricant effect of drug carrier particles. Therefore, the present project is focused on studying the behaviour of nanolubricant effect on osteoarthritis treatment from the aspect of lubrication.

1.2 Aim and objectives

The aim of this thesis is to develop novel intra-articular injection formulations based on suspensions of nanosized particulates, and demonstrate the benefits, in particular mechanical properties, on both artificial and human osteoarthritis cartilage under different conditions. There are four main objectives:

i) To fabricate the artificial cartilage system based on the polydimethylsiloxane (PDMS) matrix.

ii) To modify porous PDMS surface by specific chemistry.

iii) To study the lubrication behaviour of silica nanoparticles on soft material in different conditions.

iv) To study the lubrication efficiency of the specific types of nanoparticles.

To produce a uniform substrate system for lubrication analysis, the *in vitro* artificial system was considered to mimic different stages of OA articular cartilage. To achieve the objective of establishing artificial cartilage system, polymer material PDMS with Polyvinyl alcohol (PVA) coating film was used for constructing the three-dimensional scaffold. The sub-objectives of establishing artificial cartilage are below:

- Construct porous PDMS structures using sodium chloride (NaCl) crystals with gradients of curing agent (CA) ratio and sodium chloride fraction.
- Analyse the mechanical properties and tribological property with the change of variation, which are porosity, Young's modulus and coefficient of friction (CoF) .
- Apply the PVA film to the porous substrate surface, and confirm that the surface hydrophilicity has been modified to it as cartilage tissue.
- Identify the mechanical proprieties of PVA coated porous PDMS, and compare the change from pure PDMS.

Based on the artificial cartilage substrates, the silica nanoparticle and the nanogel particle are introduced for the lubrication test. To help solving the difficulty of injected drug short stay, the ultimate target of this project is to increase the lubrication of OA drug-loaded nanoparticles on the joint surface, which functions as lubricant. To achieve the second objective, the sub-objectives are shown as below:

- Measure the tribological coefficient of silica particles on the artificial cartilage models, altering the conditions of measurement, including velocities, load, concentrations, and the size of nanoparticles.
- Analyse the lubricity of nanogel and compare the CoF between different types of nanogel and different concentrations.
- Compare the lubricity between nanogel and silica nanoparticles on osteoarthritis cartilage.

1.3 Background

1.3.1 Cartilage and Osteoarthritis

Joint is a contact of skeletons with a complex structure, which consists of joint capsule, synovium component, tendon, ligament and menisci, and articular cartilage [13]. During the joint supports on the movement of daily activities, the joint structure is damaged by the injuries, which is associated with osteoarthritis.

Human cartilage is a multi-functional tissue supports movement by providing a smooth surface with a low CoF [14], which contains 80% of water [15]. The primary cartilage content in dry weight is collagen, in which has 90% - 95% of type II collagen [15]. Proteoglycan is the secondary content in cartilage dry weight, which constructs the crosslinking chains inside the tissue, where the aggrecan, decorin, biglycan and fibromodulin are mainly found [16]. The carboxyl and sulfate groups on cartilage provide highly water affinity by negatively charged, which results in the hydrophilic cartilage surface. The low replication capacity of anaerobic cells in chondrocytes limits the repairing potential for the OA cartilage [13]. The thickness of articular cartilage usually has 3 - 4 mm, which is recognised as the superficial zone (10 - 20%), the middle zone (40 - 60%) and the deep zone (30%). The lubricin and hyaluronic acid produced by chondrocytes and synovial cells provide lubricants for the articular surface [17].

Billions of people suffer from the osteoarthritis with pain and limitation of movement, and the osteoarthritis also causes a burden to government benefit system. Known as a long-term disease caused by "wear and tear", the cartilage, synovial membrane, periarticular tissues, and bones suffer from degeneration during the OA development. Moreover, chronic pain, inflammation, and stiffness occur in OA patients, and OA is the most common reason causing the disability amongst the old people [18]. It is challenging to avoid OA by well life habits, because ageing, obesity, sports, and heredity are all the pathogenic factors of OA disease [19–24].

Osteoarthritis is defined into six grades, from healthy (grade 0) to entirely damaged (grade 6), and the grade 1 to grade 4 are associated to the degeneration of articular cartilage. The thickness, morphology and mechanical properties are changed with the development of OA. For instance, the articular cartilage turns to softer and loses the capacity to reduce the CoF for joints. Once OA symptoms occur, low metabolic activity is the main reason causing the failure of articular cartilage regeneration. The non-pharmacologic and pharmacologic methods are introduced for OA treatment, from the oral medical treatment at the early stage to the surgeries at the late stage [25]. For the early OA stages, pain relief and anti-inflammatory drugs are used for emergencies, but the oral medicine is not able to regenerate the cartilage or even retard the process of degeneration. However, the review of osteoarthritis treatments shows that most treatments can slow down the degeneration and reduce the pain for the patients, even though the drugs such as sprifermin [26, 27] benefit joint structure and function improvement, there is still no long-term pharmacological treatment for halting or reversing OA progression [2]. Moreover, the mechanical status of joint figures out that regenerative or pharmacological treatment is difficult to recover the original biomechanical pathways from degenerated cartilage [2].

To increase the efficiency of OA treatment, viscosupplementation and drug delivery systems are raised in the OA treatment, which attempts to improve drug release efficiency. The injection of the drug delivery system (DDS) has been confirmed to benefit pain relief for patients and retain the degeneration of joints caused by OA disease. In fact, different molecules, sizes and types of hyaluronic acid (HA) and other drug carriers are introduced for the injection, but immunity system clearance of drugs and drug carriers result in the frequent injection clinically, which is the difficulty that injection therapy still meets in recovering cartilage from OA. Therefore, the present project is study to enhance the efficiency of the injected nanoparticle formulation by increasing of the lubrication effect.

1.3.2 Artificial cartilage

In the progression of osteoarthritis, most of lesions are limited on the surface of joint cartilage, and the loss of lubrication and support happen between the contact of cartilage. Moreover, a variety of cartilage mechanical properties has been widely reported from previous studies based on different specimens. In fact, the mechanical properties of cartilage differ from specimens in a wide range and distribution, which means single specimen properties are uncontrollable and unexpected. Therefore, it is necessary to develop a uniform *in vivo* system providing a platform for the cartilage lubricating test.

The cartilage tissue has few cells without vessels, nerves, or lymph, so the scaffold has been widely built for cartilage repair. Natural and artificial materials have been widely used for artificial cartilage replication. The hydrogel is structured by a three-dimensional polymer crosslinked network similar to the cartilage matrix, but the artificial cartilage built by hydrogel material has been reported to lack stiffness and strength [14]. Similarly, although natural material such as chitosan, gelatine, silk fibroin and hyaluronic acid was reported with good performance on cartilage repairing *in vivo*, the low load-bearing property requires a kind of stiffer material for *in vitro* studies. Most scaffolds are focused on the *in vivo* implant and regeneration of cartilage, however, this project is going to focus on the substrate that mimics the osteoarthritis cartilage for *in vitro* treatment.

PDMS has a long history in biomaterial replication applications. Due to the biocompatibility and biostability of PDMS, it is possible to use PDMS as an external substrate and applied in the implantation field [28]. In previous studies of PDMS preparation, different curing agent ratios changed the elastic modulus of PDMS, and the lower ratio used in preparation made the softer PDMS. In addition, the porous structure is the basic scaffold required for artificial cartilage replicating. The porous structure of cartilage has been widely reported, and artificial cartilage scaffolds have been prepared, referring to the porous characteristic. Although several porous structure preparation methods were used in the previous work, the three-dimensional printing and the solvent-casting particulate leaching (SCPL) technique were mainly used for the PDMS structure preparation. The SCPL method has been catalogued to several different techniques, such as emulsion templating technique and direct templating technique, and the pore-foaming agent used vary from distilled water to the sugar cubic. In this project, the crystals mixture and leaching method was used for porous structure preparation. The most essential advantage of SCPL are the procedure is easily handled and the process without chemical reaction. Considering the low cost and easy control of size and amount, sodium chloride was chosen as the filling for pore-foaming in this study.

1.3.3 Intra-articular injection formulation

OA is more complicated than physical damage on joints. Different treatment strategies have been applied for curing OA. The oral medicine strategy is commonly used in OA treatment, but side effects exist in oral treatment, including the risks of exposing the whole patient's system to the medicine. The intra-articular routine has been raised as the improvement of the therapeutical strategy, in which the local treatment has been used in OA therapy with the injection of cartilage OA area. For example, hydrocortisone has been attempted in a clinic by Hollander et al. [29, 30]. Furthermore, some low-availability medicine used in oral strategy can significantly affect the target treatment. On the other hand, rare complications have been caused by injection operations, only bacterial infection, bleeding, allergic, and nerve damage [31].

Therefore, viscosupplementation, which mainly consists of hyaluronic acid, was introduced in OA treatment that the injection of viscosupplementation benefits anti-inflammation, chondroprotection, analgesic and lubrication when injected into the joints. Based on the viscosupplementation, the injection formulation with drug was raised for targeting treatment. A wide choice of formulations and drug carriers, liposomes, nanoparticles, emulsions, cationic carriers and hydrogels has been reported and studied for injection formulation [32, 33]. Amongst the formulations, nanoparticle shows the excellent designable property, which provides the formulation potential as a nanolubricant in joints. Four kinds of effects play the leading role in the nanoparticle lubrication process, which are rolling effect, protective film effect, mending effect, and polishing effect. The rolling effect and protective film effect enhance the surface lubrication directly by rolling of nanoparticles and forming a film; the mending effect and polishing effect amend the surface, with the nanoparticles filling the surface, especially the grooves, and polishing the surface to reduce the roughness. The nanoparticles in the injection formulation impact the nanolubricant behaviour. The size, shape, and concentration influence the tribological properties. One of the study reported that the best nanoparticle size is 20 - 70 nm, while the spherical shape is the best nanoparticle morphology, and the best concentration of nanoparticle to reduce the CoF is between 0.2 - 1.0% [34].

1.4 Thesis overview

Chapter 2: This chapter reviews the literature about cartilage, osteoarthritis, artificial cartilage, injection formulation of osteoarthritis, and the relative theories and mechanisms used in the project.

Chapter 3: This chapter systematically introduces the theory of techniques used in this project. The sample preparation, solvent-casting particulate leaching technique, is introduced. And chapter 3 explains the working principle of the mature instrument, including atomic force microscopy, scanning electron microscope, X-ray microtomography, Fourier-transform infrared spectroscopy and dynamic light scattering. Also, the Forceboard, microtribometer and microindentation, which were partly self-designed, are introduced in Chapter 3.

Chapter 4: Based on the studies of curing agent ratio for crosslinking PDMS matrix and SCPL technique studies, a series of porous PDMS matrices were built as artificial cartilage substrates, the matrix showed an excellent tendency of Young's modulus and CoF. The model confirmed that the mechanical properties were controllable by NaCl and curing agent ratio added during preparation, the increasing of NaCl crystal ratio increased the porosity and CoF and decreased Young's modulus, and the reduction of curing agent ratio increased the CoF and decreased the Young's modulus. As the cartilage surface chemical property is hydrophobic while dehydrated and hydrophilic while hydrated, the PVA film coating was used to modify the porous PDMS surface to hydrophilic, and the surface contact angle of water decreased from hydrophobic to hydrophilic. As a result, the PDMS surface coated with PVA film has a stiffer surface than the pure porous PDMS matrix, and the CoF of PVA-coated PDMS decreased compared to pure porous PDMS.

Chapter 5: Based on the PVA-coated PDMS substrate, the Aerosil silica nanoparticles were tested on the Porous PDMS coated with PVA substrates, and different conditions were applied to the silica particles. The results of silica particle tests showed that the size, concentration and load applied affected the CoF results. The smaller size and a lower load showed a lower CoF, the rising concentration would decrease the CoF at first, and then the CoF increased when the concentration reached higher to a value. This chapter shows the lubrication behaviour of pure silica nanoparticles formulation and provides the influences of different conditions for the particle formulations.

Chapter 6: Some OA cartilage specimens at the late stage were obtained for this project. The surface morphology of cartilage captured the round shape pores on the surface and fibrous structure on the cut cross-section. A range of mechanical properties was obtained from human cartilage, and the values provided the actual properties of late-stage OA cartilage, which could provide the reference for the artificial cartilage models. The Aerosil silica nanoparticles and nanogels were applied to the lubrication behaviour tests. Four kinds of nanogel have been characterised by size and morphology, and the nanogel tribological characteristic was measured by AFM. Compared the nanogel with silica particles, nanogel provided significantly better lubrication, and the nanogels had a much lower CoF on both PVA-coated PDMS and cartilage samples.

Chapter 7: This chapter concludes the project results that the matrix of porous PDMS with PVA coating exhibited the controllable mechanical properties for mimicking the human osteoarthritis cartilage, and chapter 7 concludes the behaviour of nanogels on the porous polymer matrices and human cartilage, which reaches the aim of the present project. Moreover, this chapter presents my recommendation for future work.

Chapter Two

Literature review

2.1 Joint and cartilage

2.1.1 Joint structure

Synovial joint consists of the bands of connective tissue ligaments. Joint capsule, synovium component, tendon, ligament and menisci, as well as articular cartilage, are the essential parts of joints [13]. As the bearing load structure, human joints, especially knee and hip joints, can sustain a ten times body weight load [35].

Joint capsule is an essential part of the synovial joints (Figure 2.1). The joint capsule seals the joint as an isolated space, which provides a stable space by limiting the movement of joints [36]. The typical synovial joint capsule consists of dense fibrous tissue. In the joint cavity, the synovium produces the synovial fluid providing lubrication and nutrition to the articular cartilage [37]. Moreover, part of the capsule is thicker to provide the fixation points to the bone, and the capsule is attached firmly to the bone by fibrocartilaginous [13].

Synovium components are highly specialised mesenchymal cells and extracellular matrix

(ECM) [13]. The synovium content has two types of synoviocytes: type A of synoviocytes are produced from macrophages, which are responsible for the cleaning of fragment components in the cavity; type B of synoviocytes are fibroblast-derived cells, which leads to the hyaluronan and lubricin synthesis in the synovial fluid [13].

Tendon and ligament are also essential parts of joints. Dense and regular arranged connective tissues form the tendons, which are the main bridges that connect the muscle and bone and transfer the force from muscle to bone [37, 38]. Besides the primary function of transferring force, the tendon has been reported to be responsible for the stability of joints [13]. Alexander et al. [38] found that the biceps tendon reduced the translation in the humeral head, and another study [39] showed that the peroneus longus tendon helped the stability of the ankle joint. The ligament is defined as the dense bands that cross the joint and connect to the bone [40], and the collagenous fibres, one component of ligament, provide the function of the stability of normal range movement on the joint [38]. The ligament is occupied by the collagen matrix, which accounts for 70% to 80% of the dry weight, and the types of collagen is formed of approximately 90% type I and 10% type III [13].

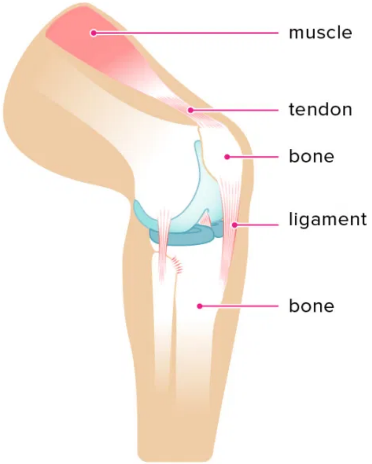

Figure 2.1: Schematic diagram of joint structure [41].

Meniscus used to be defined as an unnecessary component in the joint, which has been recently found to be effective in joint stability, load distribution, shock absorption, and lubrication [37]. When a pressure is applied on the meniscus, the synovial fluid will flow from the meniscus to the joint cavity space and contribute to the surface lubrication [42]. When the meniscus is moved out from surgery, the contact area decreases by 50% to 70%, which increases the contact stress and causes the degeneration of cartilage [42].

2.1.2 Cartilage

Articular cartilage is a soft tissue whose main component is water, accounting for 60 - 85% of the tissue. The fresh cartilage contains 15 - 22% of collagen, which includes types I, II, IV, V, VI, IX, and XI [16, 35]. Amongst the collagen of cartilage, 90 - 95% of which is type II [16, 35]. The dry cartilage weight contains 60% collagen, 25-35% proteoglycans and 15 - 20% non-collagenous and glycoproteins proteins [43]. The thickness of cartilage is usually 3 to 4 mm, as reported by Antons et al. [44] that the healthy articular cartilage thickness varying from 1484.00 ± 75.23 µm to 3624.40 ± 164.11 µm, and the average cell numbered are in the range from 32.70 ± 7.53 to 47.20 ± 10.51. The structure of articular cartilage above the bone is divided into three or four zones (Figure 2.2), which are superficial zone (10 - 20%), middle zone (40 - 60%) and deep zone (including calcified zone) (30%) [45, 46].

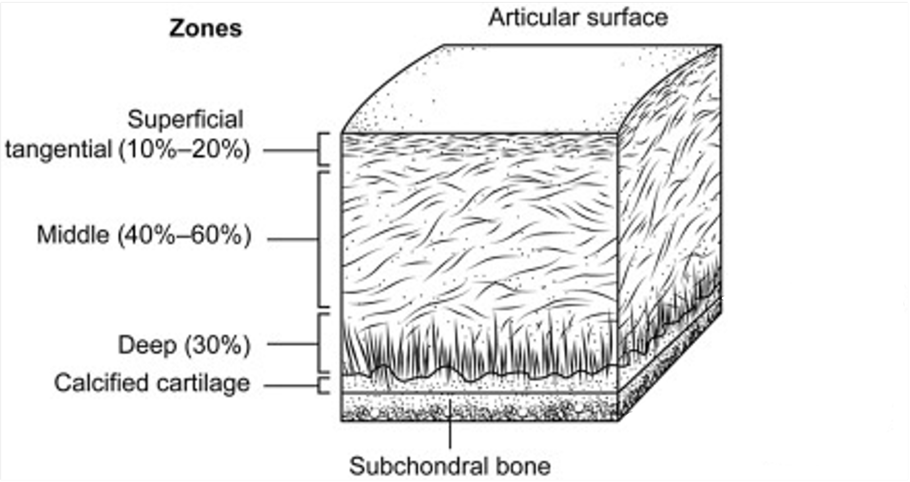

Figure 2.2: Schematic diagram of the articular cartilage layers [47].

The superficial zone is divided into two layers. The surface of cartilage is covered with a fibrils sheet with little polysaccharide, and the deeper layer is contributed by flattened ellipsoid-shaped chondrocytes, which helps the surface of cartilage parallel to the joint [43]. The content of the superficial zone has a high amount of collagen and a low amount of proteoglycan, moreover, water and fibronectin highly exist in this zone [43, 48]. Furthermore, the *in vitro* experiment reported that the superficial zone plays an essential role in the compressive behaviour [49]. The middle zone has the highest content of proteoglycans, and the fibres in the middle zone are bundled together. In addition, the direction of the fibres is perpendicular to the cartilage surface [50]. The deep zone has the lowest content of cells and water [45], which has the functions of protecting the joint to maintain the phenotype from mechanical loading, storing the growth factors and cytokines for chondrocytes, controlling the diffusion of kinds and concentrations of nutrients to chondrocytes, and acting like a signal transducer for the cells [43, 51, 52].

Articular cartilage is a viscoelastic tissue overlying on the bone, and the cartilage tissue is highly specialised in the joint [16]. It plays three crucial functions in the joint: i) providing a smooth surface with low frictional gliding, ii) absorbing the shock in the joints, and iii) minimising the peak pressures on the subchondral bone [51]. The mechanical properties of the healthy human articular have been reported in many studies. The coefficient of friction (CoF) of cartilage showed value difference via different measurements and specimens, but all the CoF values exhibited that the healthy cartilage has excellent lubrication behaviour with low CoF values. A review by Forster and Fisher [53] concluded the CoF of cartilage. In the hip function simulator machine under synovial fluid environment, the cartilage presented the coefficient from the lowest of 0.001 to the highest 0.042, and the friction measurement contacting cartilage with other material glass and metal showed the highest CoF value of 0.9 and the lowest CoF 0.014 [53]. The CoF values for the healthy knee and hip articular cartilage are 0.005 - 0.02 and 0.01 - 0.04 respectively [54]. The friction between cartilage and cartilage was measured as 0.36 [55].

The elastic modulus was reported to correlate to the depth of cartilage, the deep cartilage matrix is stiffer than the surface zone. The superficial zone layer was measured as 0.020 ± 0.003 MPa, and 6.44 ± 1.02 MPa at the calcified zone [44]. Besides the depth differences, it can be observed that the Young's modulus of cartilage in different joints area displays negligibly mechanical properties difference, and the regions on the joint has been divided into low weight bearing (LWB) and high weight bearing (HWB) [56]. Measured by nanoindentation, the mean elastic modulus of LWB region showed as 9.81 ± 8.88 MPa, which is higher than the HWB (4.46 ± 4.44 MPa), and the hardness calculated showed a similar comparison that LWB cartilage was 0.317 ± 0.397 MPa, while the HWB showed 0.317 ± 0.397 MPa [56]. Hence, the Young's modulus of cartilage has a wide range in different areas.

With the negatively charged groups found on the surface glycosaminoglycan (GAG) chains providing high affinity for water, the surface of cartilage shows hydrophilic [13]. The "smart surface" was found on the cartilage surface, that the wet surface of the cartilage is hydrophilic, and the dry surface of the cartilage is hydrophobic. [57, 58]. The loss of phospholipid overlay explains the change of surface chemical properties, and this influences the tribological characteristics of the cartilage [57–59]. The friction of cartilage was found to increase with the air-dried [57, 58]. Besides the phospholipid, the negative charge on the cartilage surface was reported to support the highly efficient natural joint lubrication [60].

2.2 Osteoarthritis

2.2.1 Overview

Osteoarthritis (OA) is the most typical form of arthritis which is frequently shown in old people [5, 11]. The data showed that 9.6% of men and 18% of women over 60, 80% of people over the 70 are suffered from OA [61]. Two types of OA were introduced as primary and secondary. The primary OA usually has undamaged ligaments and menisci, which is caused by the unknown degeneration and the repetitive loading on the thinned articular cartilage [62, 63]. The secondary OA is caused by injury, trauma or inflammatory factors [62]. A mass of research has reported different initiation and aggravating factors, such as age, injury, genetics, and obesity, which all could be related to the progression of OA [62]. However, no matter what factors were involved in the progression of OA from early stage to late stage, the eventual characteristic of OA is usually defined as abrasion of cartilage, and the end-stage OA always loses all cartilage with joint bone exposure [64, 65]. Therefore, OA patients will suffer from the disease all their life once the OA occurs. On the other hand, the large amount of OA patients and the chronicity of OA progression brought a burden to governments on health care systems [62].

2.2.2 Cartilage in osteoarthritis

Articular cartilage is a soft tissue that covers the surface of every joint bone. The scaffold and boundary of articular cartilage reduces the stresses and provides the support for joint loading, as well as a surface that bears the friction from activity actions [16]. During the development of OA, cartilage shows the degeneration and loss the mechanism to support activities. OA is considered as a long-term disease caused by "wear and tear", and low metabolic activity leads to the failure of articular cartilage to regenerate itself. The anaerobic cells are the main content on the chondrocytes, and the limited cells contact provides a low potential for cell replication, which contributes to the limitation of self-repair from OA injury [13]. OA disease is accompanied by the degeneration of scaffold and the variations in the mechanical properties, the pieces and particles stripped from worn joint cartilages float in the gap between the bones, which causes further degeneration and inflammation.

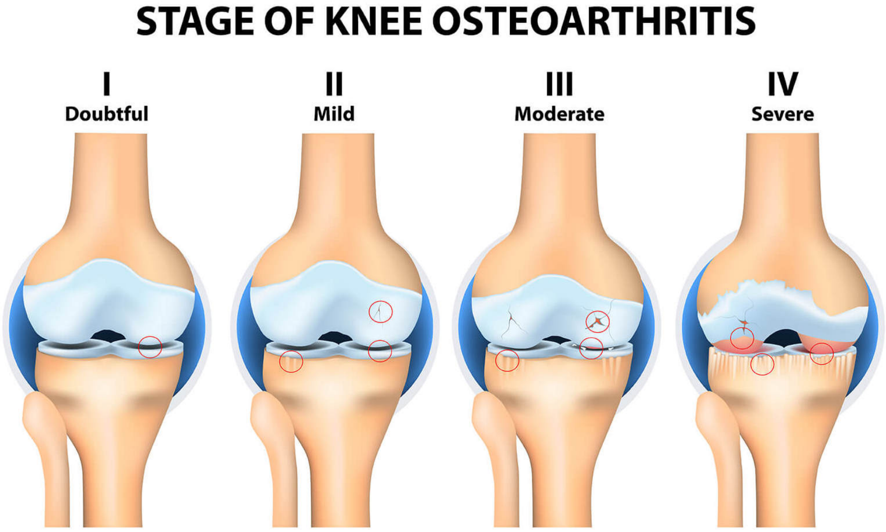

Figure 2.3: Schematic diagram of knee joint degeneration at different OA stages [66].

The International Cartilage Research Society (ICRS) divided OA into four grades from grade 1 to grade 4 (Figure 2.3), and the Osteoarthritis Research Society International

(OARSI) has introduced grade 5 and grade 6 into the OA assessment [67, 68]. Furthermore, grade 0 is used for the normal healthy cartilage, and the subchondral bone surface has deformation at grade 6. Only grade 1 to grade 4 involve the deformation of articular cartilage, and the articular cartilage is worn out in grades 5 and 6, which is used for describing the deformation of subchondral bone [67]. The definition of grade 0 to grade 4 are listed below [67]:

i) The healthy cartilage at grade 0 has an undamaged surface, and the matrix and cells are in typical architecture.

ii) Grade 1 articular cartilage also has an intact surface, but the matrix starts to show oedema and abrasion, and some cells also show the death cluster.

iii) The cartilage surface at grade 2 starts to discontinue, and the erosion shows up at the superficial surface zone. The cationic strain could reach one third depth of upper cartilage, and cells are kept dead cluster, and hypertrophy.

iv) Grade 3 cartilage fissures showed in the vertical direction and deep to the middle zone of cartilage, and the stain reaches 2/3 depth of the cartilage, cartilage domains adjacent to fissures.

v) OA joints at grade 4 lose the superficial and middle zone of the matrix of cartilage.

The cartilage attempts to generate and increase the content of proteoglycans and collagen, and tries to repair the degenerated tissue during the OA disease. However, the rate of repair is lower than it of cells and matrix death and break, which results in the degeneration of cartilage. During the OA development, the proteoglycan synthesis decreases in the matrix, which results in the load-bearing capacity decrease on OA joints [11]. At the bone correlated stages, the grade 5 articular still has an intact subchondral bone surface, but the surface is sclerotic bone. The grade 6 joint bone shows deformation and microfracture [67].

The mechanical properties of OA cartilage have been tested in many previous studies, and the surface roughness, Young's modulus and CoF are listed in the Table 2.1. As the essential mechanical properties of articular cartilage, the elastic modulus of articular cartilage was commonly reported to decrease with the degeneration of OA disease, and the CoF showed different tendencies in different studies.

ICRS grade	Young's modulus (MPa)			Coefficient of Friction (-)		Surface roughness (µm)	
Reference	Kleemann et al. [68]	Kumar et al. [69]	Ajdari et al. [69]	Lee et al. [70]	Ajdari et al. [69]	Lee et al. [70]	Ajdari et al. [69]
Grade 0	0.70 ± 0.10	-	∼ 0.54	0.119 ± 0.036	∼ 0.18 - 0.25	0.137 ± 0.250	∼ 0.7
Grade 1	0.50 ± 0.14	4.47 ± 1.23	∼ 0.36	0.151 ± 0.039	∼ 0.28 - 0.35	0.233 ± 0.550	∼ 1.7
Grade 2	0.37 ± 0.13	4.08 ± 0.64	∼ 0.28	0.158 ± 0.141	∼ 0.22 - 0.32	0.226 ± 0.550	∼ 2.2
Grade 3	0.28 ± 0.12	0.89 ± 0.37	∼ 0.16	0.409 ± 0.119	∼ 0.16 - 0.19	0.533 ± 0.200	∼ 3.2

Table 2.1: Mechanical and tribological properties of human cartilages suffering from OA from stage 0 to 3 as defined by the International Cartilage Repair Society.

2.2.3 Osteoarthritis treatment

Known as a long-term disease caused by “wear and tear”, cartilage, synovial membrane, periarticular tissues, and bones are all suffered from the degeneration. Chronic pain, inflammation, stiffness exist in OA patients, which are the main causes of the disability amongst the elderly [18]. Inflammation is introduced as the major factor causing OA [18, 22, 71–73]. It causes the symptoms of OA, including pain, tissue swelling and stiffness [74]. Besides the articular cartilage, the inflammation leads to thickening of the joint capsule. At the same time, the tendons, bursae and the ligament show the low-grade inflammation [11]. The remaining disease leads to the low-grade inflammation in the synovium, which causes patchy chronic synovitis and synovial hypertrophy [11]. The initial damage of cartilage causes the local inflammatory response, and the chronic wound was reported because of the repairing attempted by the body [75]. Furthermore, further cartilage loss, mechanical derangement, and overuse produce persistent injury, and this is recognised as the paradigm of inducing factors for chronic inflammation [76]. Compared to the normal fluids, OA tissues noted an increasing level of inflammatory protein contents [77, 78]. However, it is challenging to avoid OA through well life habits, ageing, obesity, sports, and heredity are all the pathogenic factors of OA disease [19–24]. Once OA symptoms occur, low metabolic activity leads to the failure of articular cartilage regeneration. In this case, total joint arthroplasty is the most popular treatment for the end stage [25]. For the early OA stages, pain relief and anti-inflammatory drugs are used for emergencies, but the present oral medicine is not able to regenerate the cartilage or even retard the process of degeneration.

Dozens of treatment strategies have been used in OA therapy. These strategies are divided into non-pharmacologic and pharmacologic methods [73]. About non-pharmacologic methods, appropriate exercise, diet and surgery can alleviate OA symptoms. A piece of research provided evidence that patients with scientific exercise programs got improved from OA symptoms. The results revealed that patients with restricting caloric intake and exercise had 24% physical improvement and 30.3% pain relief compared with those without diet and exercise [79]. For the patients at the end OA stages, surgery should be the only treatment. The surgical operations include joint lavage and debridement and total joint arthroplasty, which help incapacitated patients to recover the function of movement [80]. Assistive devices were also confirmed to be valuable in helping OA surgery patients' recovery. It was reported that 21 of 29 patients had less pain after joint replacement surgery with therapeutic knee taping in a study, and only 3/29 of the patients got pain relief without taping [81]. The most common elective surgery for knee OA is the arthroscopic knee surgery, even though the evidence shows this surgery method has a minimal benefit for all patients except for knee locking patients who need meniscectomy [82–85]. Although a significant placebo effect has been observed in the arthroscopic knee surgery, the substantial time costs and potential harms still remain controversial [86, 87]. Pharmacologic treatments include topical analgesics, acetaminophen and NSAIDs, hyaluronate injections, narcotic analgesics and Tramadol [73]. Topical analgesics are confirmed benefit to releasing the partial pain response. Topical capsaicin works after three to four weeks from being used and has more pain relief efficiency than placebo [88]. A study on acetaminophen involved 5986 patients and 23 studies about NSAIDs confirmed these two types of medicine has the benefit efforts on OA pain relief [89]. Hyaluronate injection prevents early OA stage patients from pain significant, but it should be operated per 3 to 5 weeks and costs much [73].

In pharmacologic treatment method, the intra-articular injection takes full advantage of drug availability, which avoids the disadvantages of loss during vessel transportation and systemic toxicity [90]. However, the constant moving and undergoing of synovial fluid requires the frequent injection of drugs, which increases the risks of infection, feeling uncomfortable, and frequent doctor visits [90]. Therefore, the drug delivery system (DDS) has been introduced as a potential therapy for OA disease [91]. Drug carriers was introduced in DDS, which is used for embedding drug and targeting delivery to the tissue, such as cartilage for the OA. Amongst drug carriers used, nanoparticle is one of the commonly used carrier, which is chosen for the present project. The nanoparticle is commonly defined as a spherical shape with a diameter between 10 to 1000 nm. The nanoparticle in the DDS provides the possibility of delivering non or poor dissoluble drug molecules, proteins and nucleic acids by cladding [91]. Some kinds of nanoparticles can pass through the barriers of cells and extracellular matrix (ECM), the charged tissue surface, such as chondrocytes, and specific biochemical moieties, such as the antibody, allowing the nanoparticle to be active in targeting the drug release position [92]. The prolonged resistant duration in the joint is the DDS efforts to date. To find the properties of nanoparticles behaviour *in vitro*, different kinds of nanoparticles were studied by animal model injection. One of the major findings is that larger molecular particles showed longer sustaining in the joint [92–94]. In the work by Mwangi et al. [94], besides the particle cleared speed, the enormous molecules (around 500 kDa) performed slower clearance in OA knees than it in healthy knees. And the carbon nanotube was found to improve the retention rate of nanoparticles [95]. Pradal and co-workers found that the injection of HA slowed down the escape of nanoparticles from joints [96]. The thermo-responsive nanospheres provided anti-inflammatory and chondroprotective effects at the same time, and the cold treatment enhance the duration of particles [97]. A significant results showed by Bajpayee et al. [98] that much more cationic particles remained in the joints than neutral particles, and the similar result showed in Morgen et al. study [99]. The broad studies of nanoparticle injection confirm the potential of drug delivery application and provide guidance for the nanoparticles used in this study.

Furthermore, from microscopic, genetic research has been widely used in retarding the development of OA disease. The mouse model is commonly used in studies by targeting editing specific genes in transgenic mice. It can show how these genes effected on OA tissue by different pathways. In these studies, TGF-β and the molecules downstream play an essential role in OA pathogenesis. Besides, inflammation factors such as IL-1, TNF-α, and nitric oxide might also be the disease eradication [72].

2.3 Artificial cartilage

2.3.1 Overview

Osteochondral grafting techniques have been developed much in the last decades, but due to the lack of proper integration between the implant and the autogenous cartilage tissue in the clinical repair process, the implant cannot form a whole with the damaged subchondral bone, which results in weak therapeutic effect [100]. In recent years, artificial cartilage scaffolds have been widely applied in cartilage defects repairing by orthopaedics, and its good performance has attracted much attention. Porous scaffold has been applied for artificial cartilage tissue engineering, the porous structure was usually constructed by natrual material, such as HA, silk fibroin , chitosan, and gelatin, and synthesised material such as PVA, polycaprolactone (PCL), polylactic acid (PLA), poly(glycolic acid) (PGA), and Polydimethylsiloxane (PDMS).

2.3.2 Cartilage tissue engineering

Cartilage tissue engineering aims to repair the degenerated articular cartilage covers on the joints, which was introduced in the early 1990s [101]. The *in vitro* constructed scaffold successfully substitutes the functional tissue, and the tissue engineering scaffold has the characteristics of biocompatibility and biodegradability, and the proper mechanical properties and matrices construct the suitable scaffold for cellular differentiation and/or maturation [102]. The essential materials for *in vivo* tissue engineering are cell, scaffold and growth factor, where the cell responds to tissue synthesis, and the scaffold supports the proper environment for tissue growth, and the growth factor assists and accelerates tissue regeneration [103].

In the tissue engineering scaffold, the polymer material has been mainly formed to hydrogels, sponges and fibrous meshes [104]. An excellent *in vivo* scaffold should control the degradation, promote the cell and ECM growth, allow the nutrients and wastes to pass through the scaffold, and provide mechanical integrity [104]. For the *in vivo* scaffold, the materials should be able to be degraded hydrolytically or enzymatically [105]. The mechanical property requirements for the *in vivo* can be applied to the external scaffold establishment.

Materials that replicate the cartilage can be sorted into natural and artificial (Table 2.2). Natural materials include gelatin, chitosan [106, 107], silk fibroin [108, 109], hyaluronic acid (HA) [110, 111] and some other proteins, the common challenges of natural scaffold are the source dependent variation and non-load-bearing. Most of the natural scaffolds are soft and delicate to tolerate the high load, and some materials such as collagen will be degenerated rapidly which results in unstable mechanical properties [112]. Therefore, it is difficult to use a natural matrix to replicate the joints *in vitro* as the substrates, even though some materials have good performance in cartilage repair *in vivo*. Most synthetic scaffolds use polymer scaffolds, such as PVA, PCL, PLA, PGA, and PDMS. Highly load-bearing is the most significant advantage of synthetic materials compared to natural materials. As an implant platform, PLA, PGA and poly(lactic-co-glycolic acid) (PLGA) could fully degenerate, but the degeneration products easily cause the inflammatory reaction between the joints to exacerbate the OA disease at some point [113–115]. On the other hand, PDMS has a long history of replicating tissue, especially in the implantation field, and biocompatibility and biostability provide a broad application for PDMS [28].

Material	Young's modulus	Characteristic	Reference
Gelatin	<10 kPa	-Biopolymer's biotoxicity -Biodegradability -Potential to induce cell migration	[116–118]
Chitosan	86.0 ± 16.5 kPa (dry) 4.5 ± 1.4 kPa (wet)	- Biocompatible - Biodegradability - Non-toxicity	[119–121]
Silk fibroin	10 ± 2 kPa (3% w/v) 50 ± 5 kPa (5% w/v)	-Biocompatibility -Biodegradability	[122, 123]
Hyaluronic Acid	8.84 ± 0.11 kPa	-Tissue healing, expansion of cell proliferation and migration -Angiogenesis -Inflammatory response control	[124, 125]
PDMS (10:1 w/w)	2.13 ± 0.15 MPa	-Adsorption of proteins -Non-toxic -Biocompatible -Biocompatibility can be improved by modification of hyaluronic acid	[126–128]
PLA	520 – 560 kPa 0.28 ± 0.04 GPa (spiral scaffold)	-By-products of hydrolysis are toxic to implanted cells -Biodegradable	[118, 129–131]
PCL	∼7 MPa	-Bioresorbability -High mechanical strength -Low swelling ratio -Biocompatible	[132–134]

Table 2.2: Young's modulus and characteristics of artificial cartilages constructed by different materials.

2.3.3 PDMS and PVA

PDMS is known as a polymer of organosilicon with the elastic property as rubber, and has been used widely in biological and biomedical applications over the past few decades. The characteristics of biocompatibility and low cost make it possible to use PDMS in this tissue replication study [135]. By changing the mixing ratio of silicone elastomer and curing agent before incubation, it can modify different mechanical properties of PDMS, such as Young's modulus. The study by Gupta et al. [136] established different ratios of PDMS between the silicon with the crosslinking agent. With the weight ratios of 10:1, 15:1, 20:1, 25:1 and 30:1, the elastic modulus decreased from 1.50 MPa at 10:1 to the 0.50 MPa at 25:1, similar to Wang's work where the elastic modulus decreased from 3.59 ± 0.11 MPa at 5:1 to 0.56 ± 0.021 MPa at 33:1 [137]. The heating temperature and heating time have been reported to influence the mechanical properties of PDMS. The increase in the incubating temperature decreased Young's modulus of PDMS, and a linear correlation between temperature against modulus showed from 25 °C to 200 °C [138, 139]. The ultimate tensile stress did not change too much with the increasing heating duration [139]. Therefore, the characteristic of different crosslinking agent ratios provides the idea to make a gradient of PDMS to replicate mechanical properties as the degenerated OA cartilage. Besides the replicating of mechanical properties of OA cartilage, in the present work, polyvinyl alcohols (PVA) was used for improving the surface chemical property of PDMS matrices.

Polyvinyl alcohols (PVA) is a hydrophilic polymer with hydroxyl end groups, which is insoluble in aliphatic and aromatic hydrocarbons, esters, ketones, and oils, and soluble in water [140]. The hydrolysis step in PVA preparation can be controlled to affect the final grade of PVA polymer, and additional thermal cycles can change the PVA solubility, crystallinity, and chemical properties [141, 142]. As a high-molecular polymer, the molecular weight of PVA has a wide range from 30,000 to 200,000. In the early 1930s, PVA has been used for wide fields, including industrial, commercial, medical and food applications [143]. With the characteristics of water solubility, biocompatibility, adhesive property, low toxicity, and biodegradability, PVA has been widely involved in the biological field. These favourable properties allow PVA to be recognised as a suitable candidate in tissue engineering. For instance, PVA-based hydrogel applications have been applied to skin tissue, bone tissue, cartilage tissue, cancer cells, vascular tissue, and other tissues [141].

The PVA film coating has been applied on different substrates for surface modification. From the work by Trantidou et al. [144], PDMS surface was treated by O_2 flow and PVA solution at 110 °C for 15 minutes, then the surface chemical property of PDMS has been reported to be modified from hydrophobic to hydrophilic. Then the PDMS surface contact angles decreased from over 100 ° to 21.0 ± 3.2 °. With the similar method, porous PDMS was also successfully coated with PVA film by Zhou et al. [145], the air plasma treated porous PDMS was cycled immersed in PVA solution and dried, which is an easy handled method that only requires a few techniques and steps for the PVA coating.

2.3.4 Porous PDMS structure

One of the critical basic parameters of tissue engineering is the porous structure [146, 147]. From previous cartilage tissue engineering, all scaffolds established the porous matrix as the framework, no matter nature or polymer materials [147–151]. In addition, the cartilage scaffold porosity reported to be similar to the bone layers [147]. With porous structure, the poroelasticity of cartilage plays the essential role in load-bearing by fluid pressurization and viscous drag of flow [152], which has been proved to provide the viscoelasticity of cartilage [153].

Porous PDMS has been introduced in various applications, including biomedical field, flexible conductors, sensors, oil/water separation appliances, and microfluidics [154]. In the project of Liang et al., the sponge PDMS with Ag and Cu coating constructed a stable flexible conjunction to light up the LED light [155]. In the work of Duan and co-workers [156], they fabricated porous PDMS with conductive carbon nanotubes coating as a network, and the structure conductivity showed 15 times higher than the aligned structure. A piece of research [157] filled porous PDMS with single-layer carbon nanotubes, which has the potential of applications in variable resistors, pressure sensors and ice-repelling electrodes. Another study [138] used multi-walled of carbon nanotubes which could achieve robots wireless control. The porous PDMS also showed the ability of oil absorption. With the hydrophobic surface, PDMS could possess for oil/water separation and storage for the oil. For instance, Choi et al. [158] constructed porous PDMS with selective absorption for the oil. In the biomedical field, porous PDMS polymer can refill the DDS by syringe injection because of the enormous interconnected internal spaces in the porous PDMS structure [154].

Porous PDMS scaffold has been widely applied in cartilage tissue engineering, and several methods have been introduced for 3D PDMS structure preparation. The emulsion templating technique is reported with the droplet injection system by Thurgood et al. [159], where the droplets were injected by a microfluidic structure, and the inner sponge space was connected by the uniform round pores. The direct templating technique used sugar cubic model was used with unincubated PDMS under the vacuum pressure, the PDMS was modelled by capillary infiltration into the sugar template, and the porous structure was approached by the leaching of sugar [160]. Three-dimensional printed porous PDMS showed excellent load-bearing capacity and strain-reversible. The three-dimensional printed structure was neatly and controllable by the program, which has potential for tissue regeneration applications [161]. The salt crystals mixture and leaching method was widely used in porous PDMS preparation [162, 163]. Furthermore, phase separation technique, gas foaming technique, freeze drying method, and several other methods were introduced for porous structure preparation [154, 164]. Compared with the methods used for porous structure preparation, the salt filling and leaching method has the advantages of low cost and easy operation. The salt choice can control the porous scaffold. The porosity of the structure increases by using the smaller size of crystals, and the compressive modulus of the scaffold increases with the larger size of crystals [163, 164]. In the study of porous Polyurethane (PU) made by salt leaching, while the salt size increased from 212 nm to 531 nm increased the compression modulus from 12 kPa to 27 kPa, and the porosity of porous PU decreased from 92% to around 87% [165]. Another work by Zhang et al. [163] showed that when the size of salt crystal increased from 181 µm to 459 µm, the porosity decreased from 85.5% to 79.9%. In addition, the adding of crystal weight ratio increases the porosity and decreases the modulus of the porous scaffold [163, 164].

2.4 Intra cartilage injection formulation

2.4.1 Overview

Intra-articular injection (IAI) formulation is now considered as a short-term treatment for OA pain relief. For instance, the IA hyaluronic acid was reported efficiency to relieve the OA knee joint up to 24 weeks [166]. Hence, drug delivery system is introduced for long-term treatment [167]. With the beneficial of the drug carriers, drug can be delivered to the targeted position of joint now. Furthermore, because of the efficiency of the nanolubrication that nanoparticles are able to reduce the friction in the previous work, the present study aim to improve the of drug carriers efficiency by enhancing the drug carriers lubrication.

2.4.2 Injection formulation

The injection formulation for OA joints can be classified as nanoparticles, liposomes, emulsions, cationic carriers and hydrogels. Large sized carriers in DDSs meet the challenges of *in vivo* instability, low bioavailability, systemic side effects, low solubility, and slow absorption [32, 33]. Nanosized particles have the advantage of controlled specific targeting [32, 168], which reduces toxicity and improves efficiency. Liposomes are composed of the phospholipid bilayer to a spherical shape [169], hence, the inside layer can be designed for hydrophilic drugs and the space between the layers can be designed for encapsulate lipophilic drugs. The liposomes have the advantages of being biocompatible, biodegradable, flexible and specific targeting to reduced the systemic side effect [169–172]. Emulsion-based formulations are used for different applications, including topical and transdermal [173]. Moreover, the oil phase, aqueous phase, surfactant, and cosurfactant are the main contents of the emulsion formulation [174]. The emulsion keeps the solubilised form of drugs and is highly dissolvable to both lipophilic and hydrophilic compounds [175]. The nanoemulsion and microemulsion were found to be more stable than traditional emulsion. The enormous emulsion (≥ 1 µm) has the disadvantage of easier sedimentation caused by high gravity, but smaller sized emulsion droplet provides charge on the surface that can stabilise the emulsion to against sedimentation by Brownian motion [176]. Therefore, the smaller sized emulsion of formulation provides stabilisation of the joint injection. Because the cartilage surface is composed of the negatively charged glycosaminoglycan (GAG) group within a complex collagen network, the positively charged agent has a higher bonding force on the cartilage surface, which provides a longer retention time inside the tissue [177, 178]. In this case, the cartilage surface performs as a drug reservoir rather than a drug barrier by binding on the cartilage surface by the charged carriers [177].

2.4.3 Viscosupplementation

Viscosupplementation consists of the exogenous HA injection into joints, which aims to recover the mechanical properties of the synovial fluid. The HA is reported with the benefits of anti-inflammation, chondroprotection, analgesic and decreasing friction [57]. The classification of viscosupplementation is in the GAG group [179]. High molecular weight (HMW) HA plays the functions as lubricant and shock absorber in the joints, which is benefited by the high viscosity [180]. The native HA molecule weight in the articular fluid is 4 - 10 million Da, whose concentration is around 0.35 gram per 100 ml [181]. Because HA has a short stay duration in joints, viscosupplementation can not benefit joints as the substitution of synovial fluid in a long-term effect [182]. The clinical results showed that viscosupplementation's effects are also attributed to the restoration of joint rheology, anti-inflammatory, anti-nociceptive, synthesis of normalised endogenous HA, and chondroprotection [183]. The HA supplement by viscosupplementation also reduces the pain-triggering molecules and inflammatory matrix metalloproteinases (MMP) [184, 185]. HA in different molecular weights has been prepared for viscosupplementation. Low molecular weight (LMW) is prepared as 0.5 - 1.5 million Da, which is recognised as the maximum concentration that facilitates interaction with target synovial cells and reduces inflammation [186, 187]. Moreover, HMW HA is prepared as 6 - 7 million Da and developed similarly to the native HA. Therefore, HMW HA has higher efficiency than LMW HA in joints pain relief [181].

As the viscosupplementation formulation retains the more significant amount of fluid in the joint cavity space, it provides a better anti-inflammatory activity and decreases the prostaglandin E2 and bradykinin concentration [188–190]. The previous research showed the high efficiency of viscosupplementation treatment on the ankle [185]. The injection of HA to the OA hip joints showed an improvement in pain relief after three to six months without significant side effects after the injection [191]. For the stage 4 OA patients who need total knee arthroplasty, the HA injection was reported that it could delay the necessary total knee arthroplasty after 3.8 years [185]. Even though viscosupplementation is regarded as a safe treatment for OA, there are 1 - 3% of patients show typical side effects after the injection. The erythema, stiffness, soreness, and swelling will sustain one to two days with mild symptoms. Some uncommon severe side effects, such as allergic reaction, bursitis, and infection, should be noticed [192]. The operation in clinical viscosupplementation injection to the joints, especially to the knee, is usually processed directly in the office, when 2 ml of HA is injected to the joints capsule space. The injection to the local soft tissue as corticosteroid would cause uncomfortable [185].

2.4.4 Nanolubricant

From previous work, nanoparticles added nanofluid showed the property of friction reduction [34]. The mechanical principles of nanoparticle reducing friction could be catalogued into four types: rolling effect, protective film effect, mending effect, and polishing effect (Figure 2.4). The rolling effect and protective film effect enhance the lubricant directly. The spherical nanoparticles roll on the surface to replace the direct sliding of two fixed surfaces. The protective film effect of nanoparticles forms a nanoscaled film on the surface to reduce wear and friction. The mending effect and polish effect are helping on the lubrication by enhancing the surface. The mending mechanism shows the mass nanoparticles would fill into the grooves on the surface and compensate for the loss of the surface. The polishing effect will make stiff nanoparticles act as the abrasive to rub the surface, which decreases the CoF by reducing the surface roughness [34].

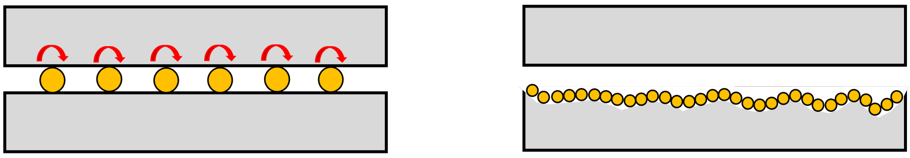

Rolling effect   Protective film effect

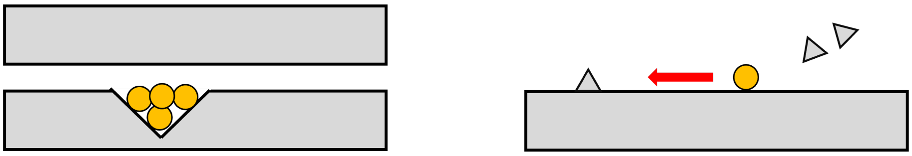

Mending effect   Polishing effect

Figure 2.4: Schematic diagram of nanoparticle lubrication mechanisms between the frictional surfaces [193].

The valuable kinds of nanoparticles were studied, such as metal, metal borate, metal sulphide, metal carbonate, metal oxide, silicon dioxide, and carbon compound [194]. The size of particles has been attempted from 2 nm to 120 nm [34]. The additive of nanoparticles exhibits anti-wear and anti-friction properties during the nanolubrication [34]. The characteristics of nanoparticles show the enhancement of lubrication, such as shape, size and concentration [34]. For instance, palm oil methyl ester (POME) was widely added in lubricants as an ester functional group additive [195]. Different concentrations of POME were added in 3%, 5%, 7% and 10% in the study by Maleque et al. [196]. The study showed that over 5% of POME improved the tribological properties and decreased the CoF even under the higher load (up to 64 kg). The primary challenge of lubricant preparation is to stabilise the particle suspension in the lubricant, because the long period of usage of unstable suspended lubricant would form the sediments and agglomerates [197]. According to the work by Anilkumar et al. [198], a kind of nanoparticles (megaHPGs) contented lubricant acted as particulates in joints, and the particles are soft, in weight of millions molecular, and exist as single particles. In addition, the lubricant in the study has the advantage of high water solubility, low intrinsic viscosity, and compactness [198]. And the lubricant showed ability to decrease CoF between rigid and elastic materials [198]. Another lubricant introduced by Lawson et al. [199] showed a 50% value decrease of bovine synovial fluid by adding biocompatible nanoparticles.

Biodegradable nanoparticle-based nanolubricant has attracted the attention of study in the past years. The additive can enhance the properties of lubricants, but some of the additives from vegetable oil impact the environment and human health. The nanoparticle size, shape and concentration all impact the lubricant mechanical properties, especially tribological properties. The best size of particles was reported from 20 nm to 70 nm, and the spherical nanoparticles in concentration of 0.2 - 1.0 wt.% is the best condition for the nanoparticles based nanolubricant [34, 200, 201]. For instance, the good performance of nanoadditives contented CuO, TiO_2, or SiO_2 enhanced the nanolubricant tribological behaviour [34, 200, 202]. The chemical modification to the nanoparticles improved the tribological properties of lubricant, and the hybrid nanoparticles showed better performance than single kind particle-based lubricant [203].

2.5 Contact mechanics

Hertzian model is the simplest model in AFM-based analysis for the indentation, which assumes the tip as a hemispherical shape and disregards the adhesive forces [204]. In the present project, the spherically colloidal probe was applied, which is comfort to the Hertz model. In addition, the Hertzian model could be used on the microindentation measurement, which used the tiny tip to indent the sample in the experiment.

The work of Hertz et al. is known as the beginning of classical contact mechanics [205]. Two spheres should contact at a point from theoretical, and the pressure should be infinite to both sides. But in reality, the elastic deformation creates a small contact area which limits the considerable stress [206]. Therefore, Hertzian contact problems should obey several assumptions [206]:

i) The elastic limit should be over the strains, and the strains are small.

ii) The surface of the sample is continuous, and the contact area should be much smaller than the contacting bodies.

iii) Each sample should be able to be considered as an elastic half-space.

iv) The surface does not exist friction. Besides, the contact models violated the assumptions are usually called as non-Hertzian [206].

About the Hertzian contact, elastic bodies contact areas and indentation depths theory was summarised by Zhu [206]. As shown in Figure 2.5, different contact surfaces indentation mechanisms are calculated by different equations, the related situations and equations are concluded below [206]:

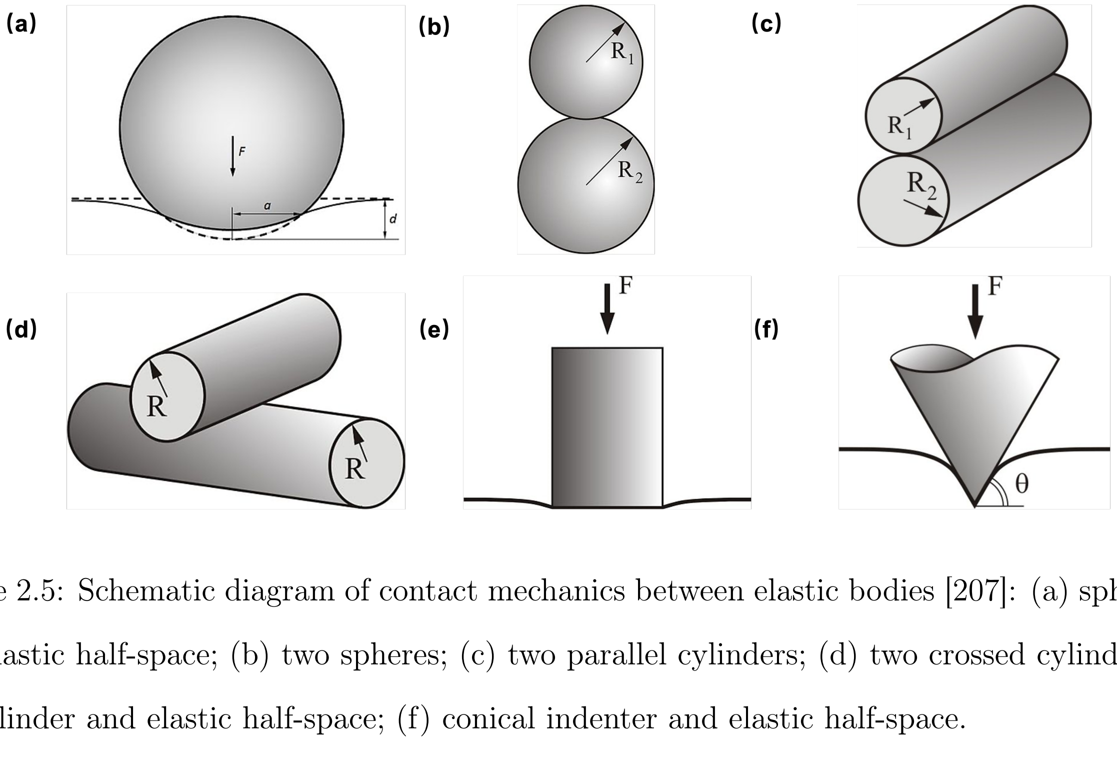

Figure 2.5: Schematic diagram of contact mechanics between elastic bodies [207]: (a) sphere and elastic half-space; (b) two spheres; (c) two parallel cylinders; (d) two crossed cylinders; (e) cylinder and elastic half-space; (f) conical indenter and elastic half-space.

1) Contact between a sphere and an elastic half-space (Figure 2.5(a)):

$$\frac{1}{E} = \frac{1}{2} * (\frac{(1 - v_1^2)}{E_1} + \frac{(1 - v_2^2)}{E_2}) \tag{2.1}$$

$$d = (\frac{2 * F^2}{E^2 * R})^{1/3} \tag{2.2}$$

where the E_1, E_2 are elastic moduli and v_1, v_2 are the Poisson's ratio of each contact material respectively. The R is the radius of sphere. F and d are the load force applied and deformation depth, and all the same in the following equations in this chapter.

2) Contact of two spheres(Figure 2.5(b)):

$$\frac{1}{E} = (\frac{1 - {v_1}^2}{E_1} + \frac{1 - {v_2}^2}{E_2}) \tag{2.3}$$

$$\frac{1}{R} = (\frac{1}{R_1} + \frac{1}{R_2}) \tag{2.4}$$

$$d = (\frac{9 * F^2}{16 * E^2 * R})^{1/3} \tag{2.5}$$

The maximum contact pressure P_{max} is:

$$P_{max} = \frac{3F}{2\pi * a^2} \tag{2.6}$$

where the E_1, E_2 are elastic moduli and v_1, v_2 are the Poisson's ratio of each contact material respectively. R_1, R_2 are the radius of two spheres, and the contact area radius ‘a’ is calculated by the following equation:

$$a = \frac{3F * R^{1/2}}{4 * E} \tag{2.7}$$

3) Contact between two parallel cylinders (Figure 2.5(c)):

$$d = (\frac{4F * (\frac{1-v_1{}^2}{E_1} + \frac{1-v_2{}^2}{E_2})}{\pi * L(\frac{1}{R_1} + \frac{1}{R_2})})^{1/2} \tag{2.8}$$

The maximum contact pressure P_{max} is:

$$P_{max} = \frac{2F}{\pi * d * L} \tag{2.9}$$

E_1, E_2 are elastic moduli of two contact bodies, R_1 and R_2 are the radii of two cylinders section, L is the length of contact.

4) Contact between two crossed cylinders (Figure 2.5(d)):

This could be transformed to the sphere with R radius and an elastic plan.

5) Contact between a rigid cylinder and an elastic half-space (Figure 2.5(e)):

$$F = 2R * E * d \tag{2.10}$$

R is the radius of cylinder contact surface, and E is the modulus of elastic half-space material.

6) Contact between a rigid conical indenter and an elastic half-space (Figure 2.5(f)):

$$F = \frac{2E}{\pi(1-v^2)} * \frac{d^2}{\tan(\theta)} \tag{2.11}$$

where θ is the angle between the surface and conical indenter; E and v are the elastic modulus and Poisson's ratio of elastic half-space material.

In the present work, equations 1), 5), and 6) were used in AFM and mircoindentation measurement, which are the elastic half-space contact with sphere, cylinder and conical indenters. Moreover, the equations were applied for the modulus and adhesion calculation.

Chapter Three

Methodology

3.1 Solvent-casting particulate leaching technique

Of the several methods in preparing porous 3D structures, solvent-casting particulate leaching (SCPL) method is demonstrated in a number of previous work, with a facial and practical method that controls the pore size, porosity and internal connectivity [164, 165, 208, 209]. It has been demonstrated that SCPL methods can establish a 3D structure with a wide range of mechanical properties by controlling the amount and size of pore-foaming agents. For instance, while the size of the pores was larger than 200 µm, and the porosity of the porous scaffold was higher than 90% [210, 211]. Furthermore, elastic modulus, interconnectivity, and coefficient of friction (CoF) of porous scaffold prepared by SCPL method can be controlled by the pore-foaming agent as well. Because of the advantage of controllable mechanical properties, the SCPL method is commonly used in the biomaterial field, such as cartilage and bone tissue engineering [164, 212].

The basic principle of the SCPL technique is mixing scaffold materials, by mixing size-controlled solid particulates with the polymer materials homogeneously, and removing the particulates in an appropriate solvent after the polymer scaffold is cured, it is possible to fabricate porous matrix (Figure 3.1). Finally, the sample is formed up with the pores, which show as the shape and size of pore-forming agent. Based on the different properties of solvents and pore-foaming agents, previous studies designed several kinds of methods to establish porous scaffolds.

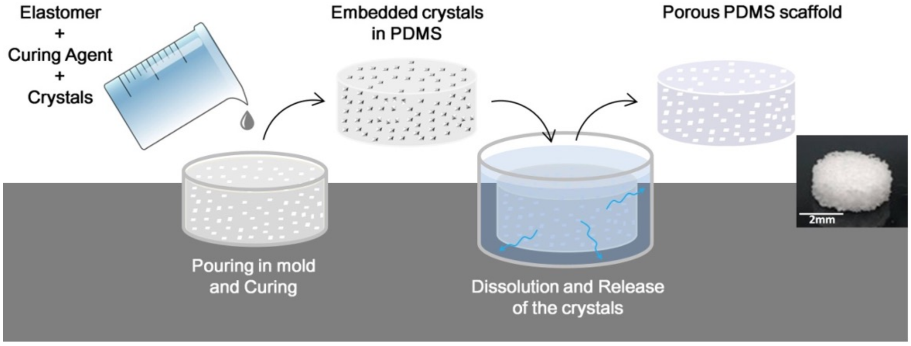

Figure 3.1: Schematic diagram of the protocol of preparation of the porous polydimethylsiloxane (PDMS) matrices and photograph of one sample of the foam-like PDMS obtained at the end of the process.

In the present work, the size around 200 µm sodium chloride crystals were filled into the mixture of silicone and curing agents solution, and the salt crystals were dissolved by water after the PDMS was incubated to the solid. With the low fraction of sodium chloride, the crystals were found sunk into the bottom of the container during the heating step. Moreover, the low fraction showed undissolved salt crystals left inside the PDMS matrix, which is full surrounded by PDMS, and the high salt fraction showed the even sample that the crystal full filled in the PDMS matrix.

3.2 Atomic force microscopy

3.2.1 Introduction

Atomic force microscopy (AFM) was invented by Binning, Quate and Gerber in 1986 [213]. AFM is able to measure most kinds of surfaces, such as glass, polymers, composites or even biomaterials [214]. The AFM can measure the sample images by analysing the constant probe-sample interaction, and measure the force through the function of their mutual separation. Hence, AFM has been applied in different subjects, including chemistry, biology and engineering. AFM is one kind of scanning probe microscope that can measure nanometre-scale samples by a 1 nm to 20 nm diameter sharp tip [214–216]. Besides the morphology scanning as microscopy, AFM can measure mechanical properties on a nanoscale, such as friction, stiffness and adhesion force. Basically, AFM can measure the force interactions between the cantilever and sample. According to the variety of interactions, sorts of scanning probe microscopes (SPM) were created, such as magnetic force microscope (MFM), dipping force microscope (DFM), and friction force microscope (FFM) [217]. Contact mode and dynamic mode are operational modes based on the different contact measuring methods. The limitation of the AFM scanning scale is about 150 × 150 micrometres [214], and the lateral resolution and vertical resolution are limited to under 1.0 nm and 0.1 nm, respectively [214].

The cantilever is used for approaching the sample surface. Silicon, silicon dioxide and silicon nitride are used for making cantilevers [218, 219]. Different shapes and flexible are invented for different samples and conditions. For instance, triangle and beam shapes are invented for cantilevers, and the tip for the approach is designed as the sphere, pyramid, arrow and so on. With different types of cantilevers, AFM can detect the surface using different forces such as van der Waals, mechanical contact, chemical bonding, capillary, electrostatic, and magnetic forces. For specific sample requirements, AFM could use for measuring under vacuum, ambient phase and liquid phase but not requiring complex preparation.

3.2.2 Operational principle

The cantilever probes are flexible, which helps the cantilever displace along with the atom force between the tip and sample. To detect the cantilever tip and sample by an atom-forced distance, the cantilevers should be located close to 0.1 - 100 nm during the measurement. In addition, there are attractive forces, van der Waals interaction, electrostatic force, and chemical force can give a reaction between the cantilever tip and sample [220].

Figure 3.2 shows the essential components of AFM, which are a light source which emits the laser, a nanosized cantilever probe, and a photodetector divided into four quadrants. The laser reflection of the cantilever enables it to reflect on the piezoelectric actuator. The tip approaches the sample by the connect piezo in Z-direction movement, and the piezo moves to the selected values of X and Y when the tip touches the sample surface. The cantilever tip bends to follow the shape of the sample surface. The vertical movement and lateral or torsional bending drive the reflection of the laser, which will be detected on the quartered photodetector. Four areas are divided on the photodetector (Figure 3.2) to determine the movement and bending of cantilever tip. The vertical position of cantilever tip is determined by the signal difference between I + II and III + IV, and the torsional bending of cantilever is detected by the difference between I + III and II + IV.

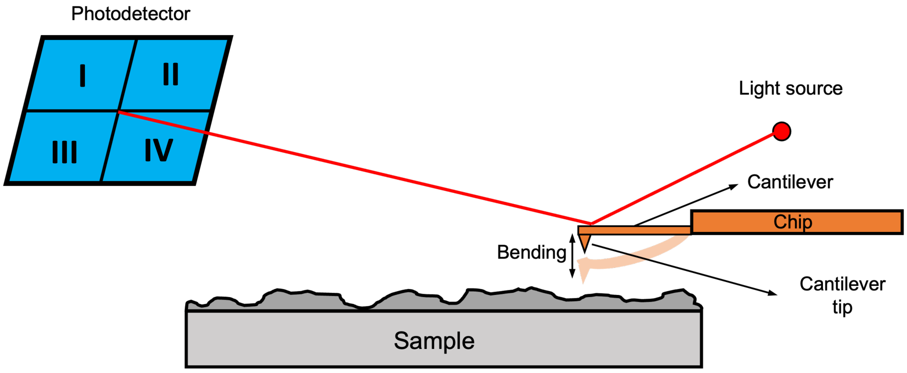

Figure 3.2: Schematic diagram of the operation principle of an AFM.

However, various operating modes are invented in the AFM technique, which depends on the sample, environment, and purpose required of the experiment. For different modes, AFM cantilever behaves in different as Figure 3.3 shows [221]. The contact mode is the mode that cantilever probes direct contact with the surface permanently. The images are brought by the repulsive short-range force between the probe and the sample. Two modes can be operated in contact mode: i) constant force mode; ii) constant height mode. In the constant force mode, a force (setpoint in the software) should be set as the expectation value to be controlled as the force between the probe and surface. The force is approached by systemically checking and adjusting the Z piezo. During the scanning of the constant height mode, the Z piezo position is fixed, and the photodetector signal collected results in the image of sample. Compared with these two contact modes, the constant force mode can be used to scan on a much rougher surface than the constant height mode, and the constant height mode produces images on a flatter surface faster than the constant force mode.

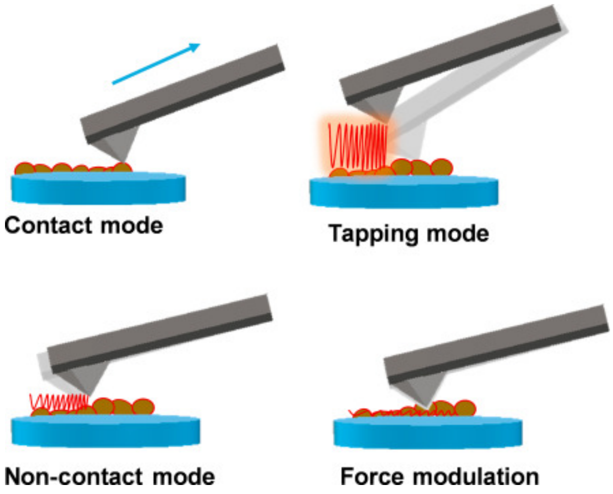

Figure 3.3: Schematic diagram of different technique modes involved in AFM operation [221].

Tapping mode belongs to the dynamic mode, and the probe is in contact with the surface at a constant frequency. Before the probe engagement, the desired setpoint should be set for the scanning amplitude of oscillation. The amplitude of oscillation changes when the probe contacts with the surface, and the Z piezo mechanism adjusts to maintain oscillation amplitude.

Besides tapping mode, some other classifications of dynamic modes are used depending on the manufacturer with an appropriate AFM. Non-contact is called “close-contact mode”, which works in the force regime and obtains high-resolution images with small interaction forces. When the amplitude is set to a considerable value (up to about 100 nm), the intermittent contact mode can be applied for cantilevers under large amplitude and high forces. Another imaging mode measures every pixel by force versus distance curves and moves the cantilever laterally when the tip and surface are not in contact. This mode is called “jumping mode”, “quantitative imaging mode (QITM)”, or “peak force mode”, which depends on manufacturers [222].

As the voltage signal can respectively detect the vertical bending and horizontal torsion from (I + II) - (III + IV) and (I + III) - (II + IV), the signal could be translated from electrical signals to mechanical signals as force. The the normal deflections of cantilever can be converted proportional to the normal load, and the friction force could be shown by the torsional deflection of cantilever after removing the normal force [223].

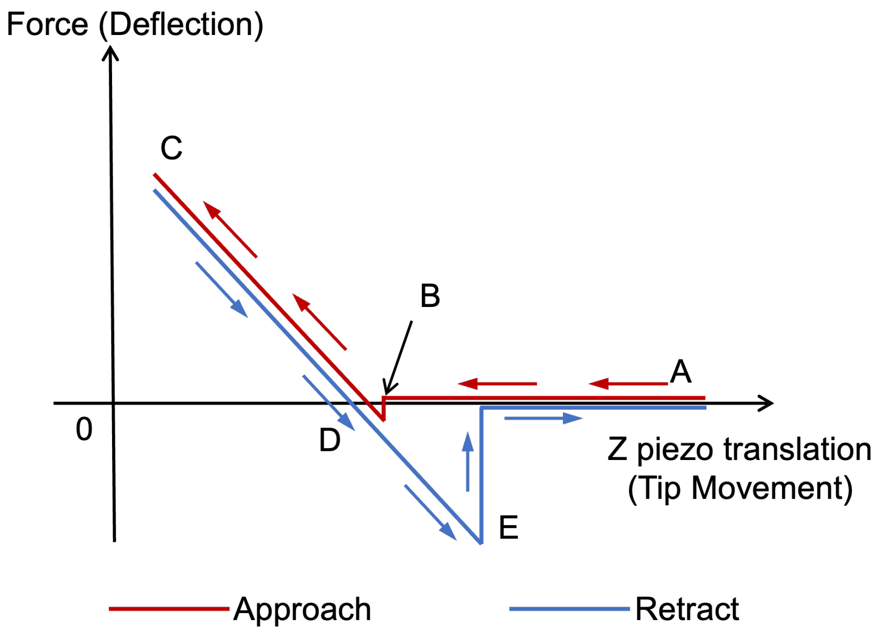

Figure 3.4: Schematic diagram of a force curve exhibiting the Z piezo translation versus cantilever deflection.

The force between the probe and the surface can be measured by the sensitive detection of AFM. As Figure 3.4 shows, at point A, there is no force because of the far distance of the probe to the surface. The attractive force showed at point B while the probe is close to the surface, and then it jumps to the contact force from the attractive force, which presents the force of indentation to point C. During the withdrawal period, the contact deflection decreases as the path of engagement. Because of the strong adhesive force between the surface and cantilever tip, the cantilever adhesive contacts the surface until point E rather than directly escaping from the surface at point D.

3.2.3 AFM application in the project

Dimension 3100 AFM and multimode 3-HR AFM were used for surface image and force measurement in the present project. The images were obtained by 0.08 N m^{-1} and 0.32 N m^{-1} contact cantilevers with sharp tips, and the force measurement used cantilevers with the colloidal tip. Because the PDMS matrix and cartilage are high density crosslinked, to exhibit the matrix mechanical proprieties entirely, a 4 µm radius spherical borosilicate probe was stuck on the 40 N m^{-1} spring constant tipless cantilever. Compared with the classic contact mode cantilever, the 40 N m^{-1} cantilever with a borosilicate tip can against the adhesive of PDMS and cartilage surface. A similar probe was reported in the previous study for cartilage force measurement as well [224]. In addition, the tribological measurement was captured by multimode 3-HR AFM, which has the advantage on liquid-phase measurement with only dozens of microlitres liquid.

3.3 Scanning electron microscope

3.3.1 Introduction

Scanning electron microscope (SEM) technique can effectively analyse the organic and inorganic materials from nanometre to micrometre. The maximum magnification that SEM could reach varies from 300,000 × to 1,000,000 × in some modern models [225]. The energy-dispersive X-ray spectroscopy is usually built in SEM to provide qualitative and semi-quantitative results, and the energy-dispersive X-ray spectroscopy provides the ability to analyse the composition of elements in the sample.

There are three types of SEM, conventional SEM (CSEM), environmental SEM (ESEM) and low vacuum SEM (LVSEM). In CSEM, the electron beam interacts with the sample under the high vacuum of 10 to 6 torr, and the low energy secondary electrons (SEs) will be ejected from the surface of sample. The high vacuum circumstance causes dehydration and cracking of some samples, such as concrete. The ESEM allows the electron beam and specimen to interact at elevated pressures (0.2 to 20 torr), and the varied pressure can decrease the hydration of the sample because the water minimum liquid maintenance is 4.6 torr. LVSEM is similar to the ESEM that LVSEM eliminates the requirement of coating and surface charging. In addition, the pressure of LVSEM is from 0.2 to 2 torr [225].

3.3.2 Facility principle

In Figure 3.5, the diagram shows the internal structure and parts that compose the SEM. The primary electrons are released from the machine, which provide energy to the specimen surface to activate atomic electrons on the surface. The surface of the specimen releases the SEs and other signals that SEM could collect, and the images are usually formed from the analysis of SEs from each point. Therefore, the SEM requires the vacuum circumstance to avoid eliminating the requirement of coating and traction of electrons with the gas molecules [226].

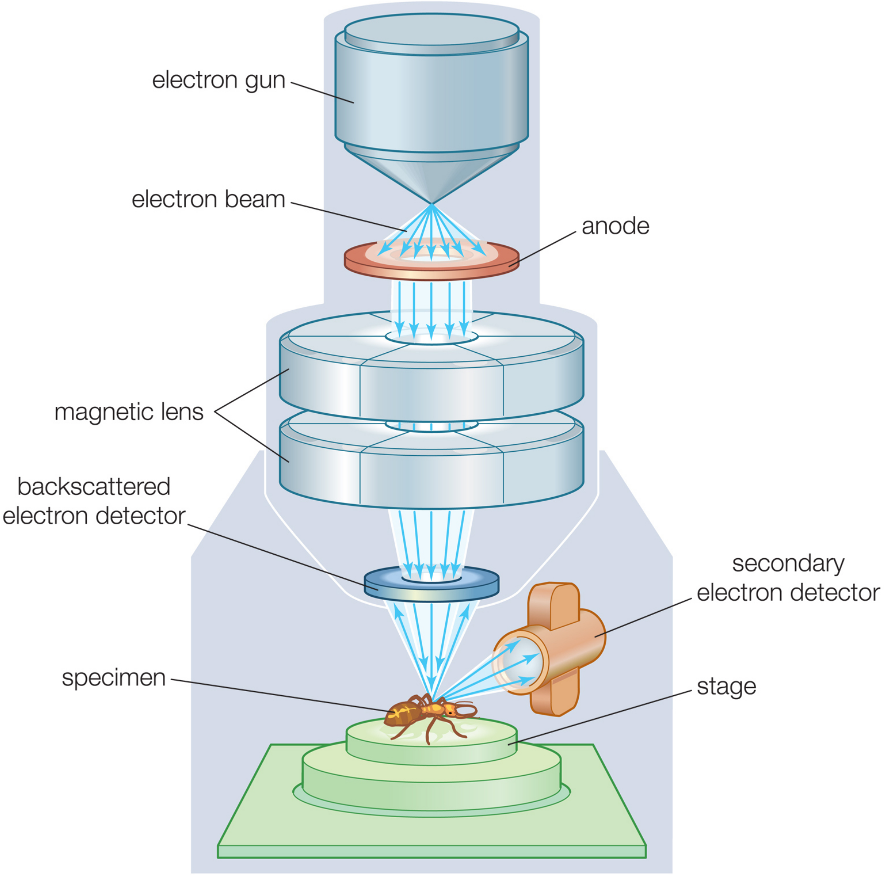

Figure 3.5: Schematic diagram of the imaging principle of a SEM.

Figure 3.5 shows that the primary electrons are produced from an electron gun that accelerates particles by heating or high energy (1 - 40 keV). The electron particles are restrained to a beam by magnetic field lenses in a vacuumed column, and the primary electron beam will interact with the sample surface area. The accelerated electrons will scatter after the first contact with the surface. The scattering of electrons is dependent on the concentration and atom types on the sample and the energy of the beam. A higher sequence of the atom and higher concentration will decrease the scattering of electrons, and the increased beam acceleration will increase the scattering process. The high voltage applied to acceleration will push the electrons farther into the sample. The incoming electronic specimen will interact with a variety of signals, such as SEs, backscattered electrons (BSEs), visible light (cathodoluminescence – CL), and photons (X-rays used for elemental analysis). The images are usually formed based on SEs, which are the most important in building morphology and topography of samples. The BSEs are usually used for exhibiting the contrasts for a multiphase sample composition. The element analysis is according to different types of atoms with their specific X-ray reflection wavelength. The non-destructive of characteristic allows the element analysis can be repeated in SEM.

The sample of SEM should be fixed on a stage, and carbon or metal tape is usually used for fixing the sample on the stage. The sample to be analysed should be electrically conductive, which can avoid the surface overcharging. The sample without electrically conductivity should be sputter covered by a layer of carbon or metal, such as gold and platinum, which allows the surface to reflect the electrons.

3.3.3 SEM application in the project

Model TM3030 and 7000F JEOL SEM were used for the measurement in the present work. The SEM was applied to obtain sample (surface) morphology and used for verifying the micro or nanoscale accessories in the experiment, such as cantilever tips. PDMS, silica nanoparticle, and nanogel were generally operated with metal sputter coating and scanned under different magnifications. Before usage, the cartilage samples were stored in liquid environment. To avoid the vapour damage of the SEM, cartilage samples were all dehydrated at 70 °C in an oven before the metal coating. However, the model TM3030 cannot obtain details of the surface when the magnification is over 10000 ×, so TM3030 was used for capturing PDMS and accessories in the research. 7000F JEOL was applied for the nanoparticles, nanogel and cartilage morphology for capturing more details of samples, and the maximum magnification is up to 30000 ×.

3.4 X-ray microtomography

3.4.1 Introduction

X-ray microtomography, also called micro-CT, can establish the 3D structure of the material at a micrometre scale, including nontransparent materials [227, 228]. The internal details of scaffolds can be shown by images with better than 1 µm resolution. The micro-CT technique is non-destructive for many materials, and it is allowed to be operated to scan samples under different conditions [229]. Even though the sample allowed for micro-CT is typically minimal, X-ray microtomography can be used for scanning various types of materials [230–233].

3.4.2 Facility principle

The principle of X-ray microtomography is X-ray absorption physics, which constructs the three-dimensional structure by tomographic reconstructing two-dimensional projection images mathematically [229]. As shown in Figure 3.6, the structure of electron-dense or electron-poor sample can be observed by the contrast against the background [234]. The tomography combines the images from the different orientations of the sample. When the angular steps between each radiography are small enough, the software can construct the appropriate 3D model by calculating attenuation coefficient value of every position [235]. There are three essential steps of X-ray microtomography: i) image acquisition, ii) back projection and 2D slice reconstruction, and iii) 3D reconstruction. The raw tomographic data is obtained by computerised tomography, and it will be output as the signal output or sinograms from different angles. These images from different angles and directions can be reconstructed to a 3D model by the software [229].

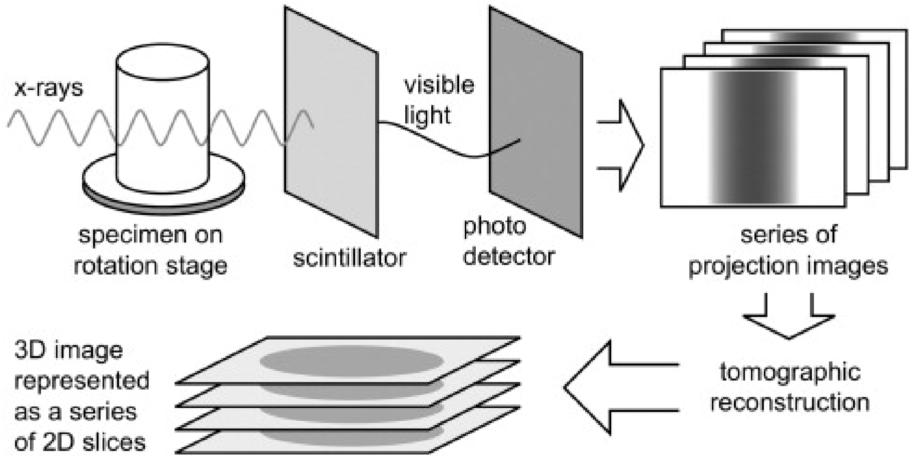

Figure 3.6: Schematic diagram of the imaging principle of a micro-CT.

3.4.3 Experimental application

The X-ray microtomography was used for exhibiting and analysing the three-dimensional structure of the porous PDMS in this study. Every section layer of PDMS was shown by the analysis software, and the pore structure and the internal crossed structure could be clearly observed. In addition, X-ray microtomography built three-dimensional models for porous PDMS, so that the 3D models could be operated to check the internal structure from any angle and layer. With the benefit of the micro-CT software, the porosity and interconnectivity were automatically calculated according to the section layers.

3.5 Fourier-transform infrared spectroscopy

Fourier-transform infrared spectroscopy (FTIR) was used to establish the chemical nature of the samples, particularly the modified surface. The fundamental vibrations of functional groups correlate to the infrared absorption bands, and the different infrared absorption bands are used for group identification. Infrared detection usually cannot identify the symmetric vibration, especially the centre symmetry molecule. This characteristic allows the FTIR to detect all asymmetric vibrations from the molecule, especially the amino acids and water, which are difficult to be detected from other techniques [236].

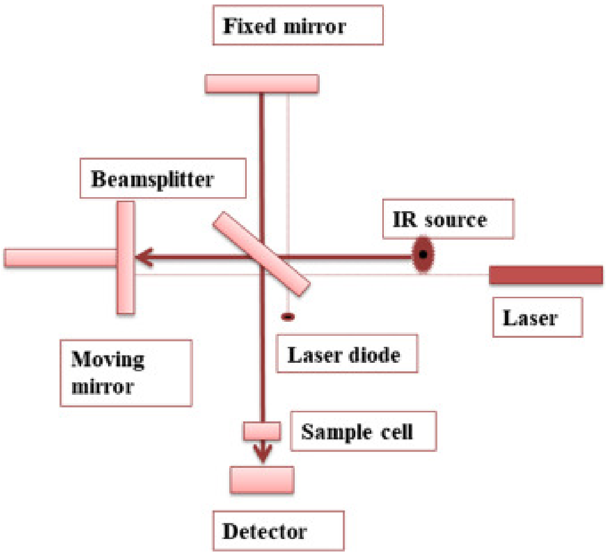

Figure 3.7: Schematic diagram of the principle of a FTIR [237].

The technique of the FTIR principle is based on the transitions between quantised vibrational energy states (Figure 3.7). When the photon transfers from a lower energy state to a higher energy state, infrared spectroscopy (IR) radiation will show up and can be absorbed by FTIR. The molecular bonds occur in vibration when the photon is transferred to a high energy state. The wavenumber and frequency have an extensive varying range. Different molecular bonds have specific wavenumbers/frequencies that show IR absorption peaks, similar to the fingerprint of functional groups. As shown in Figure 3.7, a typical FTIR should be built with a source, sample cell, detector, amplifier, A/D converter, and computer. The radiation passes through the interferometer to the detector, and the wavelength of radiation passed through the sample usually ranges from 10000 to 100 cm^{-1}. Then the radiation absorbed is transferred to vibrational or rotational energy and detected by the detector. The signal on the detector will be transferred to a digital signal by an A/D converter according to the Fourier Transform, and the result of the spectrum will be shown in the range of 4000 to 400 cm^{-1} [237]. The peak height is usually dependent on the amount of chemical bonding. The more the energy state transformed, the higher the peak shows. When interaction occurs between the bond, especially hydrogen bonding interaction, the peak will show broader than usual. The present study applied FTIR to verify the PVA coating on PDMS. The specific functional group between PDMS and PVA is -OH, which benefited PVA-coated samples to show a strong and broad peak between 3550 - 3200 cm^{-1}.

3.6 Dynamic light scattering

Dynamic light scattering (DLS) is the technique used for carrying out colloidal nanoparticles size from solution. According to the scattered light of the laser passes through the colloidal solution, differences in particles' Brownian motion contribute to the DLS analysis. The larger particles have slower motion than smaller particles, and the slower motion scatters much light from large particles. The DLS technique also provides the aggregation of nanoparticles through the set-up X-ray diffraction. The different varieties of aggregation will be shown with density in the plotted result [237]. In the present work, the silica nanoparticle size was detected by DLS, and the size distribution as normal distribution because of the aggregation. As the DLS type used in this study cannot define the smallest size, the size shown in the results corresponded to the peak values.

3.7 Other Technique

3.7.1 Tribology

Forceboard and microtribometer are the equipment for friction coefficient measurement. The basic principle is that the machines can record the horizontal direction force applied on the detector. The detector of Forceboard is on the state plate, and the detector of microtribometer is connected to the arm for the load applied. The CoF was automatically given by Forceboard, and Forceboard records the force applied vertically and the CoF. The CoF value measured by microtribometer is calculated manually based on the load weight applied, friction values recorded and Newton's Second Law. In all tribological measurement, a 3 mm diametre borosilicate ball was used as the counterpart.

For the measurement of the PDMS matrix, a self-build model was applied for Forceboard and microtribometer. First of all, a pure PDMS model was solidified in a petri dish, which should be about 2 mm thicker than the sample. Then, the centre of the PDMS was cut out by a cork-borer, which was also used for porous PDMS preparation, then the hole in the PDMS model is suitable for the samples. The porous PDMS samples were pushed into the hole of the PDMS model, and the liquid used for the experiment was filled in the hole of the PDMS model. In Forceboard measurement, the PDMS model was moved out from the petri dish because the detector of Forceboard is at the bottom of the model, and the PDMS model adhered on the Forceboard sample stage. For cartilage measurement, the bottom of cartilage was stuck on a petri dish by super glue, and then the cartilage was immersed under the fluid level.

3.7.2 Surface energy

The definition of contact angle is the angle of liquid at the three-phase boundary, the angles are exactly at the intersection of gas, liquid and solid, and the three-phase could be gas, liquid and liquid at some conditions [238]. When the droplet spreads on the substrate surface, the liquid performed as good wettability on this surface, which shows the contact angle lower than 50 °. On the other hand, the surface shows hydrophobic when the droplet remains the shape and the contact angle is higher than 90 °. The droplet of water used 4 µl for each contact angle test in this study. The contact angle images were captured by Contact Angle Goniometer (Ossila, UK), and the angle measurement was analysed by the software ImageJ.

3.7.3 Microindentation

Microindentation setup used in this project is built with FH 5 force gauge (Sauter, Germany) and LTS Long Travel Stage (Thorlabs, Inc., UK). A cone tip and a flat tip were chosen to be screwed on the microindentation for different samples. The flat tip is a 1.5 mm diameter round shape, and the cone tip has a 60° prong. The MATLAB code controls the microindentation engagement and withdrawal, before the experiment operation, the speed and maximum force detected are the essential parameters that should be input into the code. The microindentation can record the moving distance and force applied on the tip, the engagement of indentation tip following the configured speed until the maximum force. The engagement will stop once the force value approaches the configured maximum value and then withdraw at the same speed to the original position. The figure will be plotted as moving distance against force, and the engagement and withdrawal are plotted in two lines. According to the principle of contact mechanics described in Chapter 2.5, the modulus of samples can be analysed based on the engagement lines.

Chapter Four

Fabrication of three dimensional porous artificial cartilage based on PDMS

4.1 Introduction

During daily activity, the joint motion causes compressive, shear and tensile stresses on cartilage, which is up to 20 MPa, and the cartilage can tolerate 10 - 40% compressive strains. The excellent mechanical performance is benefited from the porous structure of cartilage. In previous studies, cartilage exhibited flow-dependent poroelasticity [239, 240], which plays an essential role in load-bearing, as well as fluid transport and lubrication [241, 242]. In addition, the lubrication of cartilage was reported with low friction coefficients, which is from 0.0005 to 0.04 with synovial fluid lubricating [239].

Osteoarthritis (OA) articular cartilage is degenerated from healthy cartilage tissue [239]. The international cartilage repair society (ICRS) defines degenerated OA cartilage into four stages, the healthy articular cartilage is introduced as stage 0, and the cartilage is complete worn at stage 4 [243, 244]. In addition, it has been reported that the physical mechanical properties of OA cartilage were found to change along with the degeneration of tissue, such as stiffness, surface roughness and friction coefficient [68, 70, 245]. And the physical mechanical properties are correlated to the progression of OA degeneration [68, 70, 245]. With the development of OA, the structure of cartilage deteriorates integrally, which compromises their ability to sustain the mechanical compression experienced by joints and results in increased friction that accelerates the degeneration process [246]. As a result, cartilage's surface morphology, porosity, and mechanical properties span a broad range [68, 70, 247, 248]. The mechanical properties of different stages OA cartilage was reported in previous work, the values were listed in Table 2.1. In the table, the Young's modulus of cartilage decreases as the OA progresses, and the surface roughens along with the exacerbation of the OA disease.

According to the porous characteristic of cartilage and the broad range of cartilage mechanical properties, the three-dimensional porous scaffold was commonly used for establishing artificial cartilage. Natural and synthesised polymer materials have been reported to build specific structures as artificial cartilage, such as silk protein hydrogels [249], HA [124, 125], PCL [132–134], PLA [118, 129–131] and PLGA [113]. The modulus values and characteristics of porous scaffold constructed by these materials has been shown in the Table 2.2. In fact, the mechanical properties of those porous scaffolds are not satisfactory enough to replicate the mechanics of articular cartilage. For natural materials, such as chitosan [249], collagen [250] and hyaluronic acid [251], were emphasised replicating the biocompatibility, but limited on the strength of cartilage [252], which have less shear and compressive moduli than cartilage tissue, even degenerated OA cartilage [68, 251]. Similarly, polyethylene glycol (PEG) based scaffold was reported with low Young's moduli around 40 kPa [253]. For synthetic materials, improved mechanical properties have been presented, such as PCL scaffold was reported Young's modulus as 6.85 ± 1.83 MPa, but the synthesised materials were less suitable for use at a bio-interface [252, 254].

Polydimethylsiloxane (PDMS) is well-known as a non-crystalline polymer, it has been used in tissue engineering because of its excellent mechanical properties and biocompatibility [255–257]. PDMS has excellent stability properties in aqueous media for replicating cartilage friction tests in different solutions, and the general PDMS has similar compressive modulus as cartilage [68, 69, 258]. Similar to the degeneration of OA cartilage mechanical properties, adjusting crosslinking ratio in PDMS has been confirmed to control the elasticity of the matrix [259–262]. PDMS had been used in studies to make porous scaffolds. For instance, Zhang et al. [163] used SCPL method to prepare porous PDMS with the varying number of salts (from 0.10 g ml^{-1} to 0.30 g ml^{-1}), size of salts (∼181 µm to ∼459 µm), and fusion water per cent (0 wt.% to 7 wt.%), the results showed in a wide range of porosity from ∼72% to ∼86%, and the range of compressive modulus was from 1.0 to 5.2 MPa. Similar results were also reported in other porous scaffolds prepared SCPL method [249, 263–265], therefore, porosity has been controlled by the method of SCPL, which varied the porosity of the scaffold with changing pore-foaming agents. In addition, Khosla and co-workers [161, 258] have studied the friction of porous PDMS in water under the pressure of a glass probe, which provides the idea for porous PDMS lubrication measurement.

The limitation of PDMS potential application is hydrophobic surface [266], where the cartilage surface is hydrophilic [57, 58]. Therefore, several methods have been exploited to modify the PDMS surface into hydrophilic [144, 267–269]. Most methods were reported to start with oxygen plasma treatment, which can active the surface groups on PDMS [270, 271]. Exposure to oxygen plasma turns the formation of PDMS surface into an inorganic silica-like surface layer [272, 273], and the oxidised chains are scissored to hydroxyl groups on the PDMS surface [144]. The hydroxyl groups provide more potions for PDMS surface treatment, especially polymers growth. One of the demonstrates of treated PDMS is further operated with the atom transfer radical polymerization (ATRP) method and grown by the synthesised polymer brushes on PDMS surface, which costs numerous chemicals and requires complicate operations [274–276]. Besides ATRP method, PVA film is widely applied on

PDMS surface treatment by film coating, which requires less operations and cost than the polymer-brushes grafting [144, 266].

Poly-vinyl alcohol (PVA) is a synthetic linear polymer with the advantages of low environmental impact, reliable water solubility and biodegradability, which allowed PVA commonly used on bioplastic, food products and packaging systems [277–280]. Furthermore, PVA presents hydrophilic because of the hydroxyl groups, and the PVA film coating has been confirmed with the hydrophilic surface chemical property as well [144, 266, 281]. In a work of PVA hydrogel for cartilage tissue replacement [282], PVA was prepared as cryogels, and the scaffold showed that PVA cryogels could approach the similar osmotic, physical and frictional properties to the native cartilage. Overall, PVA has excellent potential for cartilage replicating application and can be prepared simple and low cost.

An excellent shape memory of porous PDMS is demonstrated [163, 283], which confirms that PDMS, coupled with SCPL method, can offer a great opportunity to fabricate a series of porous structure, replicating articular cartilage of different OA stages by adjusting porosity and mechanical properties. As a systematic study, considering not only the porosity and stiffness of a porous PDMS, but also the tribological properties, is required to mimic cartilage of various stages of OA [283, 284].

In the present work, the system developed a suite of the proposal for preparing porous PDMS. Controlling the fraction of pore-foaming agent and crosslinking in PDMS could approach a wide range of mechanical properties, such as surface morphology, porosity, stiffness and friction, which achieved the substrate analogous to cartilage in different stages. Based on the scaffold of porous PDMS, the PDMS matrices were modified by PVA for consisting the surface chemical property to. Even though the modulus and CoF properties were enhanced and decreased from the porous PDMS matrix, the tendency of porous structure mechanical properties was still in accord with the porous PDMS.

4.2 Materials and methods

4.2.1 Materials

Sylgard 184 silicone, sodium chloride, and polyvinyl alcohol (Mw = 89,000 - 98,000, 99% hydrolysed) were purchased from Sigma-Aldrich (Dorset, UK). Phosphate-buffered saline (PBS) tablets were purchased from Fisher Scientific (Loughborough, UK).

4.2.2 Preparation of porous PDMS scaffold

PDMS matrix was prepared by mixing Sylgard 184 silicone with the curing agent (CA) came together. The sodium chloride crystals were added to the mixture and mixed well. Then the mixture was put in the vacuum oven with 300 MPa negative pressure for 2 hours to remove the bubbles produced in stirring, followed by 75 °C heating for 2 hours. After the incubating, the PDMS resulted in solidification mixed with sodium chloride crystals. However, the samples were prepared less than 4mm thick, and then the samples were cut into a 12 mm diameter circular shape by a cork-borer [285, 286]. After that, the samples were immersed in de-ionised water for 24 hours, and the sodium chloride crystals were dissolved and leached out from the pieces. PDMS and CA weight proportions were prepared with five different ratios, which were used: 5:1, 10:1, 15:1, 20:1, and 25:1 (w/w) to adjust the degree of crosslinking, whilst the weight ratios of NaCl crystal and PDMS were kept according to the following ratio to change the porosity of the prepared porous matrix: 1:1, 2:1, 4:1, 6:1, and 8:1, which are expressed as 50%, 67%, 80%, 87%, and 89% respectively. According to the PDMS ratios and NaCl ratios, the porous scaffolds were presented as ‘X - Y’, which X is the ratio of PDMS with CA and Y is the percentage of sodium chloride.

After locating the modulus needed from the porous PDMS matrix by controlling the porosity of the structure. Referred to Young's modulus of different stages of OA cartilage from previous research, the artificial cartilage scaffold was chosen to replicate different OA cartilage stages. Four NaCl fractions were chosen for the four stages of OA cartilage, which were 3.5:1, 5:1, 6.3:1 and 7.5:1. Therefore, porous PDMS was prepared to 10:1 - 78%, 10:1 - 83%, 10:1 - 86% and 10:1 - 88% as substrate. These four series of porous PDMS substrates were immersed in 10% hydrochloric acid (HCl) solution for 24 hours and washed by distilled water for three times. The HCl treated substrates were immersed in 2 wt.% PVA solution for 10 minutes and then dried under 60 °C, the PVA solution infiltration and dry steps were cycled for three times. Lastly, the samples were incubated in a vacuum oven at 110 °C for 1 hour.

4.2.3 Microstructure characterisation

Porous PDMS scaffold properties were scanned by X-ray microtomography by Bruker (Skyscan 1172, Coventry, UK), and the power was set as 70 kV voltage and 80 µA current. The camera pixels set for structure section images were 14.88 µm. The software 'CTvol' was used to analyse porosities and interconnectivity. For all chosen sections, the region of interest was set based on a round section with a 5.5 mm radius. To calculate the porosity ϕ the Equation 4.1 was used:

$$\phi(\%) = \frac{(V_{total} - V_{PDMS})}{V_{total}} \times 100\% \tag{4.1}$$

where V_{PDMS} is the volume of solid material, while V_{total} is the total volume of the region of interest that is a cylinder of 0.3 mm thick with 5.5 mm of cross-section radius. Porous PDMS surfaces were generated by a tabletop SEM (TM3030, HITACHI, UK) at a voltage of 15 kV and a magnification 400 ×.

4.2.4 Surface morphology

The planar PDMS coated with PVA was used for film morphology test, the samples were tested by AFM (Dimension 3100, Veeco, Cambridge, UK) and SEM (7000F, JEOL, UK). The PNP-TR-Au (Nanoworld, UK) cantilever used for scanning PVA film, the 0.08 N m^{-1} was chosen. SEM parameters were at the voltage of 10 kV and 2000 × magnification.

4.2.5 Surface chemical groups

Fourier transform infrared spectroscopy (Nicolet 380, Thermo Fisher Scientific, UK) detected the porous PVA coating on PDMS, the wavelength measured from 500 - 4000 cm^{-1}. Planar PDMS, planar PDMS coated with PVA, 10:1 - 78%, 10:1 - 83%, 10:1 - 86% porous PDMS coated with PVA and 10:1 - 78% porous PDMS were used for surface chemical groups measurement.

4.2.6 Surface energy measurement

Planar samples were used for the surface energy measurement. 4 µl droplets were dropped on PDMS, hydrochloric acid treated PDMS and PVA-coated PDMS. The contact angles were captured by the machine Contact Angle Goniometer (Ossila, UK), and the angles were analysed and calculated by ImageJ.

4.2.7 Nanomechanical properties

Atomic force microscope with a Nanoscope Controller (Dimension 3100, Veeco, Cambridge, UK) helped to obtain the force curves from porous PDMS. The 40 N m^{-1} spring constant tipless cantilever was used for indentation, and a borosilicate colloidal probe (Apex Probes Ltd, UK) was glued on the tipless cantilever. The radius of colloidal probe was 4 µm, and the force applied on the samples was 1 µN. The Hertzian behaviour and spherical probes used on the cantilever tips make it suitable to fit and calculate Young's modulus of the elastic samples with the Hertz model [287, 288]. The Young's modulus was given by the average of 100 force curves and calculated automatically by using Python nanoscope analysis code, and the code used the following Equation 4.2.

$$F = \frac{\frac{4}{3}E}{1 - v^2}\sqrt{R}\delta^{\frac{3}{2}} \tag{4.2}$$

where the E is Young's modulus, F is the force applied on the samples, v is the Poisson's ratio of PDMS, which is 0.5 as reported [138], R is the radius of colloidal probe, and the δ is the indentation depth, which was obtained from the Nanoscope package automatically.

The Young's modulus of porous PDMS coated with PVA was obtained in nanoscale and microscale indentation. The nanoscale indentation on PVA-coated PDMS used AFM, which is same as porous PDMS. A self-built microindentation with a 1.5 mm diameter planar tip was applied indentation on porous PDMS coated with PVA, and the maximum load set up for the indentation was 1 N.

4.2.8 Tribological measurement

A customer-built model [289] was used on the microtribometer (Longshore Systems Engineering, UK) for tribological measurement. The test was carried out in distilled water. A 3 mm diameter borosilicate ball applied 30 grams load on the porous PDMS. For each sample, the glass ball slid 7 mm in length with 0.5 mm s^{-1} velocity, and it repeated five cycles. The static friction was discarded in the coefficient of friction (CoF) calculation. The contact pressure during the tribometer measurement was 0.208 MPa. The PVA-coated PDMS tribological property was tested by Forceboard single system (Industrial Dynamics, Sweden) and tribometer. In Forceboard measurement, put the load of 0.5 ± 0.2 N on sliding, and the tribometer applied 30 g on the load. The contact pressure during the Forceboard measurement was 0.354 ± 0.142 MPa. Both Forceboard and tribometer used a 3 mm diameter borosilicate ball as the contact surface, the sliding velocity 0.5 mm s^{-1}, and the sliding length of 7 mm was applied to both facilities.

4.3 Results

4.3.1 Porous PDMS

4.3.1.1 Morphology and 3D structure

Porosity was introduced to a series of PDMS mixtures of varied elastomer: CA ratios using NaCl crystals. Upon mixing, the fraction of the NaCl crystals, alongside the rheological properties of the PDMS mixture, determine the distribution of the NaCl crystals in the matrix, which will become the voids in the final porous matrix. It can be observed that the more NaCl included in the mixture, the greater porosity of the matrix. In previous studies, the pore sizes were found to be dependent on the size of the crystals [163, 283]. Therefore, in the present study, the diameter of the crystals was kept constant at approximately 200 µm. The viscosity of the PDMS was found to change as a function of the cross-linking agents [259] - the weight ratio of elastomer was kept less than 25:1 since the PDMS-crystals mixtures could not reach a steady porous solid state. It is estimated that each individual NaCl crystal would experience a similar magnitude of the gravitational force of 0.170 µN, buoyance force 0.081 µN, and viscous force that is dependent on the viscosity of the surrounding medium, around 0.720 µN. Sedimentation of NaCl crystals to the bottom half of the mixture was observed for mixtures where a low fraction (50 and 67 wt.%) of NaCl was used, which was driven by the overall force experienced at individual crystal levels. This resulted in a less homogeneous distribution of pores across the PDMS matrix after being cured in the vacuum oven for two hours. Therefore, all the scanning and test are based on the bottom 3 µm thickness piece of every sample.

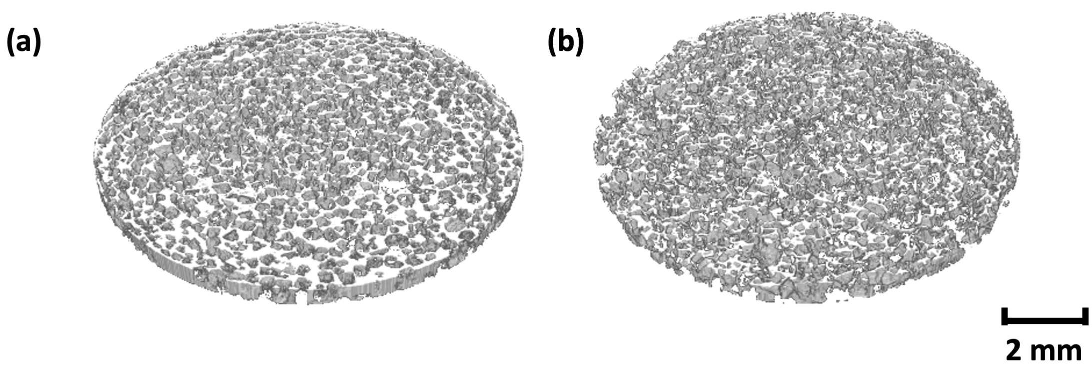

Figure 4.1: Three-dimensional structure of porous PDMS ((a) 5:1 - 67%; (b) 5:1 - 89%) constructed by X-ray tomography. The white part is the PDMS content and the grey part is the pores.

The three-dimensional scanning by X-ray microtomography shows similar morphology as surface morphology scanning, which internal structure is pore structure, and the porous scaffold is constructed by thin crosslinked PDMS fibrils. The lower filling of sodium chloride structure can be observed in large PDMS bulks connected, and the structure of 5:1 - 89% are most connected as fibril rather than massive PDMS.

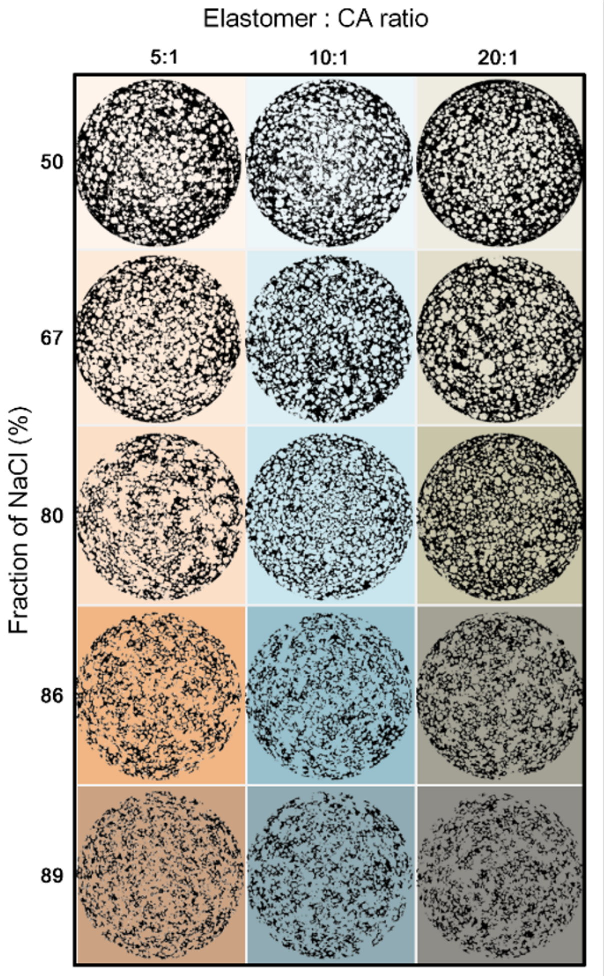

Figure 4.2: Section layers scanned by micro-CT of porous PDMS matrices prepared in three elastomer: CA ratios with additional salt in five different concentrations.

Three-dimensional structural information, including shape, size, geometry, and interconnectivity of pores, of all porous PDMS samples was established from the bottom side of the matrices using X-ray tomography. Figure 4.2 lists all sections of different elastomer: curing agent ratios and NaCl ratios, the sections of each sample are looks with similar appearance, so the Figure 4.2 only picked one from each sample. From Figure 4.2, it can be observed that the connectivity of PDMS is thinner when the sodium chloride ratio increased, which was the same as what was observed from the three-dimensional structure.

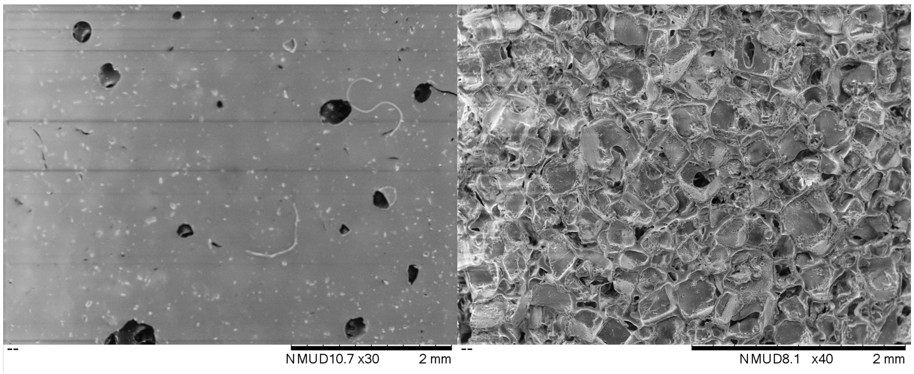

Figure 4.3: Surface SEM images of porous PDMS surface (Left: 5:1 - 67%; right: 5:1 - 89%).

In Figure 4.3, SEM surface scanning compares 5:1 - 67% and 5:1 - 89% of porous PDMS, which has a significant difference in the surface morphology. For instance, when the NaCl ratio is 67%, the surface is shown as planar with pores, which is from the contact of the bottom of petri dishes during the preparation, and the holes were the sinking of sodium chloride crystals. On the other hand, with the NaCl: PDMS ratio came to 89%, the sinking of sodium chloride crystals was full filled the bottom of PDMS, which caused the surface of 5:1 - 89% all showed the shape of sodium chloride. Even though the interior has fibrous structure for both low and high NaCl fraction PDMS, it could be only observed that the edge of where crystal leached out contributed fibrous structure on the surface in high NaCl fraction PDMS, but not the low fraction porous PDMS.

Based on the X-ray microtomography model analysis, Figure 4.4(a) shows the porosity which was calculated by the Equation 4.1. For each set of PDMS samples, the porosity keeps constant with the changing of PDMS and CA ratio, and porosity is found to increase with the increase of NaCl fraction. On the contrary, Figure 4.4(b) shows that the connectivity decreases with the increase of NaCl fraction. The overall range of porosity covers from 55%

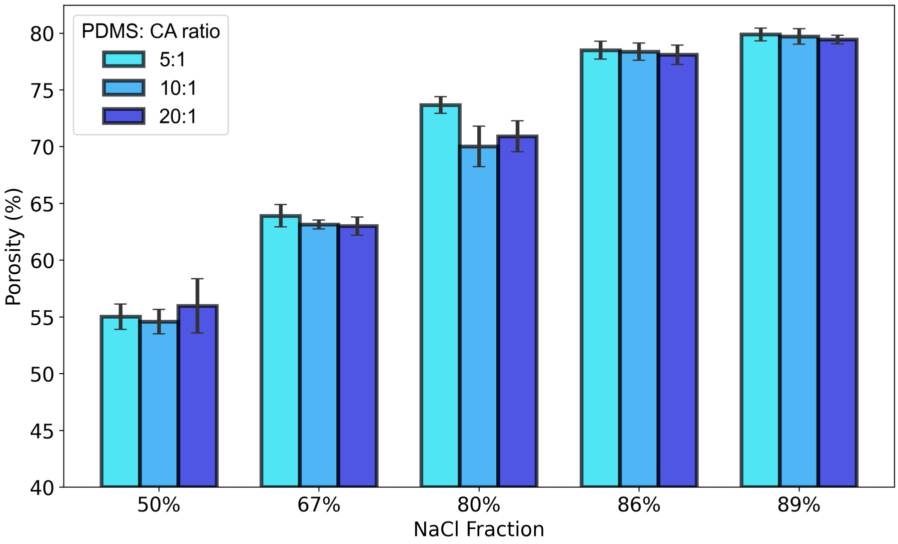

(a)

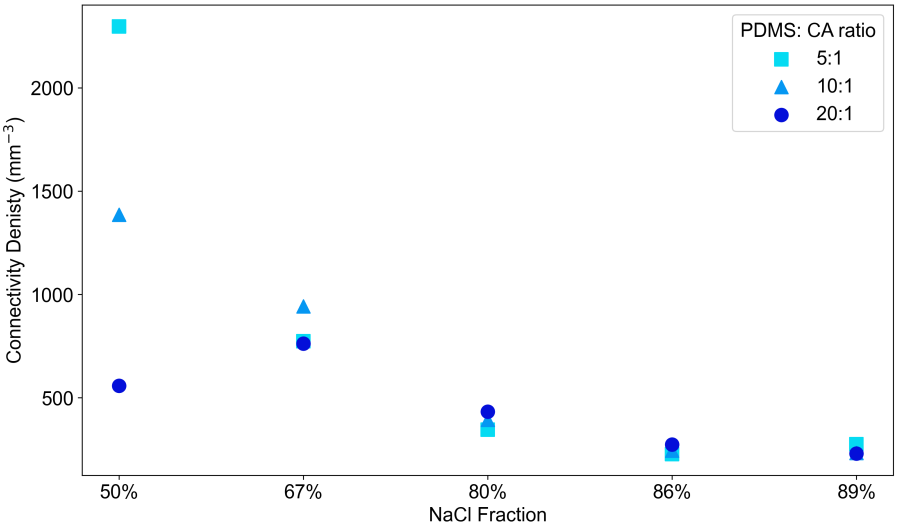

(b)

Figure 4.4: (a) Porosity and (b) connectivity density of porous PDMS matrix as a function of the concentration of NaCl in the same 3 porous matrices where the elastomer is mixed with curing agent in ratios 5:1, 10:1 and 20:1.

to 80% and inter-connectivity covers from 230.0 mm^{-3} to 2297.5 mm^{-3}, and the magnitude by which porosity changed showed barely any dependence on the ratio between PDMS and CA. It confirms that sodium chloride crystals are the primary element for the structure of porosity.

Although porosity of cartilage is not included as a criterion for OA diagnosis because no trend is drawn between porosity and OA stages, a diversity of porosity values has been reported in the literature for cartilage affected by OA [68, 243, 248]. The porous PDMS matrix developed can represent a broad range of porosity, from 63% to 81%. It is possible to further increase the porosity by using NaCl crystals of reduced size with greater concentrations, which was accomplished in several previous works where maximum porosity was up to 90% [163, 257]. In addition, the porous platform could facilitate the additional flux of polymeric and cellular substances [290], which is an essential factor for the ultimate application of using artificial cartilage samples for *in vitro* tests.

4.3.1.2 Young's modulus

From previous PDMS elastomer studies, it is well established that increasing of concentration of crosslinking agents would establish a stiffer PDMS elastomer [291, 292]. Combined with SCPL methods, it approached to control the mechanical properties of porous PDMS matrix. The Young's modulus of porous PDMS was quantitatively measured by colloidal AFM probes by the nanoindentation method. Figure 4.5(b) shows the values of Young's modulus by NaCl fraction and crosslinking agent ratios. Between the five series of PDMS samples, it was found that increasing the concentration of CA can significantly improve the Young's modulus of PDMS, which is consistent with the literature. A similar effect can also be accomplished by increasing the fraction of NaCl crystals used.

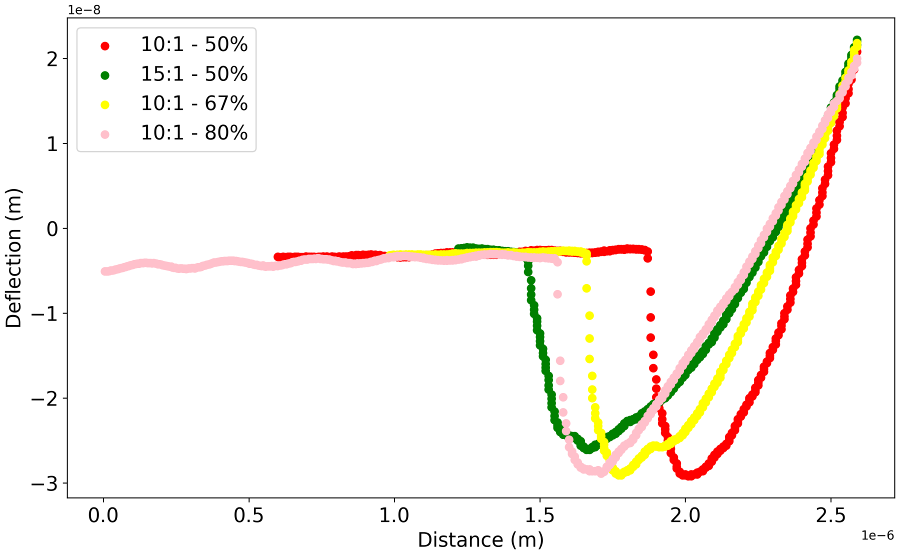

(a)

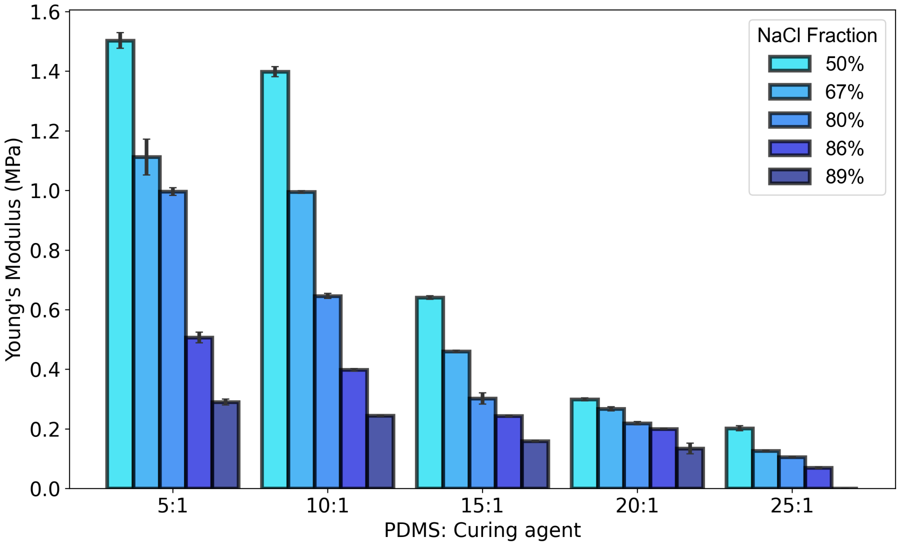

(b)

Figure 4.5: (a)Force curves of some of porous PDMS samples in AFM force measurement. (b)Young's modulus as a function of the concentration of NaCl in five porous matrices where the elastomer is mixed with curing agent in ratios 5:1, 10:1, 15:1, 20:1 and 25:1.

Figure 4.5(a) shows some force curves of porous PDMS. Figure 4.5(b) shows a significant tendency that the Young's modulus of porous PDMS decreases whilst the decreasing of curing agent. Compared to the same concentration of curing agent ratio of PDMS, it can be seen that the increase of NaCl fraction decreases Young's modulus. The most significant Young's modulus value in this set is 1.5 MPa, which is measured from sample 5:1 - 50% with the highest CA concentration and most little NaCl fraction; and the lowest Young's modulus value from 25:1 - 87%, which has the lowest CA concentration and the highest NaCl fraction in the series. These two extreme values and the tendency shown in the Figure 4.5(b) confirm the hypothesis based on previous studies [259–262, 293] that both porosity and Young's modulus were expected to be adjusted by the changing of CA and NaCl ratio in the preparation. Therefore, these two parameters could have a synergistic effect to further expand the range of coverage, which is broadly aligned with the values reported previously using PDMS and other polymer-based materials [135, 254]. A result does not be claimed in the Figure 4.5(b) is 25:1 - 89%, because a smooth indentation curve was difficult to be captured by AFM. In fact, PDMS has been reported that the adhesive force is correlate to the curing agent ratio. The less curing agent ratio in PDMS made the matrix much sticky [294, 295], which is consistent in this work. At the same time, the increase of NaCl fraction increases surface roughness. Even though it was reported that rougher surface decreases elastic solid surface adhesion [296], the present work showed that the rougher surface enhances the adhesion force. This could probably because that the indentation behaviour expanded the rough PDMS surface to a smooth contact surface with sphere probe, which resulted to a larger contact area [297, 298]. In addition, the deformation was found in the AFM measurement that the modulus values kept decreasing from the first indentation to the final indentation. It can be explained by the crosslinking structure being stretched at an unobservable scale, which manifests as Young's modulus decreasing each test.

Porous materials with controllable mechanical characteristics are highly desirable as artificial cartilage: natural materials tested previously were too soft (low modulus) to sustain any applied load [31, 252], which is unsuitable for replicating human cartilage. The porous

PDMS matrix fabricated in the present study covered a similar range of Young's modulus compared to cartilage [299–301], which offered exceptional mechanical properties. More importantly, changing the crosslinking density and porosity can be used as an effective platform to generate a series of artificial cartilage, replicating the deteriorated mechanical integrity observed in the degenerated natural cartilage as the OA progresses [68, 70, 247, 248, 302].

4.3.1.3 Tribological properties

For the purpose of mimicking OA cartilage, a custom build microtribometer has been used for testing porous PDMS tribological properties. Figure 4.6(a) shows an example of porous PDMS frictional raw data, which are samples 5:1 - 50% and 20:1 - 50%. Figure 4.6(b) shows the porous PDMS CoF at different concentration of curing agent and fraction of NaCl crystal. The lowest friction coefficient of the series was obtained from 5:1 - 50%, with value of 0.033 ± 0.002; the CoF measured from 25:1 - 87% has the highest value of the series 0.133 ± 0.010.

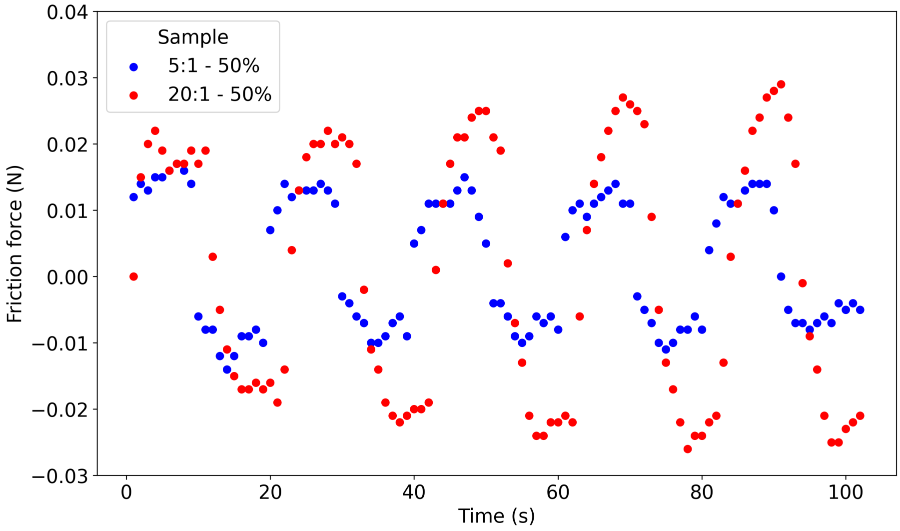

(a)

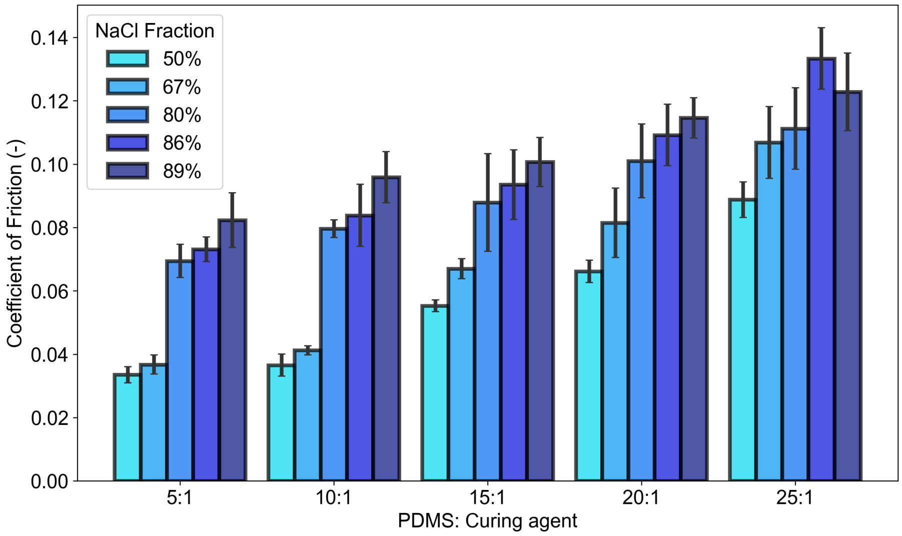

(b)

Figure 4.6: (a) A frictional raw data example of model 5:1 - 50% and 20:1 - 50%. (b) CoF as a function of the concentration of NaCl in five porous matrices where the elastomer is mixed with curing agent in ratios 5:1, 10:1, 15:1, 20:1 and 25:1.

The concentration of curing agent and filling dependence is similar to the behaviour of Young's modulus, which could be confirmed by the well-established contact mechanics [303, 304]. As the SEM images show in Figure 4.3, the surface morphology of sample 5:1 -

89% has significant cubic holes due to the dissolved salt crystals. Oppositely, sample 5:1 - 67% is found with smooth surface with a few pores. Obviously, the contact surface area is determined by the physical geometry of two objects.

The porous structure of cartilage and the hydrogel structures are described with the poroelasticity model before, which considers the physicochemical interactions at the contact interface, the deformation under compression, and the contribution of the interstitial fluid upon the applied pressure [305–308].

The surface of OA cartilage suffered from the impact of the degeneration is unavoidable and undeniable. The CoF and the surface roughness increase in a positive correlation. Cartilage from late-stage patients has a surface rougher than patients suffering from early-stage OA. The range of CoF is wide, which could be affected by the measuring duration, loading configuration and solution measured. Here the suite of porous PDMS proved to be able to reproduce the tendency of the change of surface properties with OA by using the two influential factors: CA and NaCl concentration. Increasing the fraction of sodium chloride and reducing the ratio of the curing agent could effectively replicate the degeneration of the surface's cartilage tissues.

Previous studies [308] shown that the tribological characteristics of porous matrix is related to the equilibrium friction coefficient μ_{eq}, and the time-dependent fluid load fraction F_f with the Equation 4.3 below

$$\mu = \mu_{eq}(1 - F_f) \tag{4.3}$$

which suggests that a high fluid load fraction could effectively help to further reduce the overall CoF, and vice versa. Péclet number, P_e, was used to evaluate the time τ required to drain the liquid out of the contact region versus the actual contact time that is a/V, whereby a is the contact radius and V is the sliding velocity [309]. An analytical model developed by Moore and Burris [308] suggests that a large P_e is essential for effective interstitial lubrication that underpins the exceptional tribological properties of articular cartilage. The P_e can be defined as

$$P_e = \frac{V \cdot a}{E_{eq} \cdot k} \tag{4.4}$$

where E_{eq} is the equilibrium compression modulus and k is permeability, respectively.

Furthermore, the fluid load fraction of the frictional force can be calculated upon the calculated P_e

$$F_f = \frac{P_e}{P_e + 1} = \frac{V \cdot a}{V \cdot a + E_{eq} \cdot k} \tag{4.5}$$

In the present work, both sliding velocity (V) and contact pressure, consequently radius of the contact area (a), were kept constant. A reduction in either compression modulus (E_{eq}) or permeability (k) would result in an increase of the Péclet number and the fluid load fraction, and subsequently a decreased CoF. However, when the present work attempted to fit permeability against equilibrium friction coefficient, the permeability did not show the reduction tendency as expected. The fitted equilibrium friction coefficient μ_{eq} is much lower than the matrices friction coefficients obtained from experiment, which is contrary to the physical mechanism that μ_{eq} should higher than CoF. Even though the fitting force the μ_{eq} is higher than μ, the permeability could not reach to a well tendency. Hence, it is essential to obtain the μ_{eq} of porous PDMS for the mathematical fitting in future work.

Furthermore, the permeability of a porous PDMS is able to be measured [310], which is one of the important parameter of porous models. The permeability shows the fluid flow rate through the medium, which is related to establish the extent of pore percolation and tribological property in aqueous environment. Refer to the Equation 4.4 and 4.5, it is essential to measure the permeability of porous PDMS in future work, which can help to establish a mathematic model for artificial cartilage system tribological property.

4.3.2 Porous PDMS coated with PVA

4.3.2.1 Surface morphology and thickness

As the PDMS surface chemical property is hydrophobic and the aqueous cartilage surface is hydrophilic, the PVA was introduced in this project for coating on the porous PDMS matrix. PVA film coating on PDMS has been confirmed to modify the surface chemical properties in previous studies [144, 266, 281]. Therefore, AFM and SEM are used for capturing the surface of planar PDMS coated with PVA. Figure 4.7 exhibits the images of SEM and AFM, both images show the wrinkle on the surface. The distance of wavelength L = 4.81 ± 0.70 µm. Compared to the porous PDMS substrate, the PVA shrinking film provides a rougher pattern on the surface rather than the smooth surface form from solidified PDMS and the NaCl crystals.

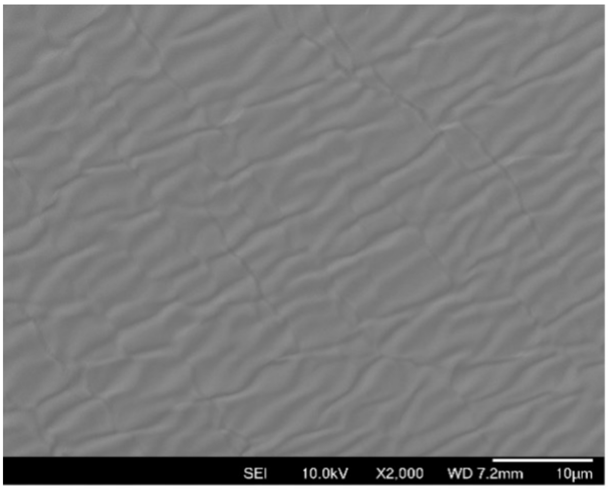

(a)

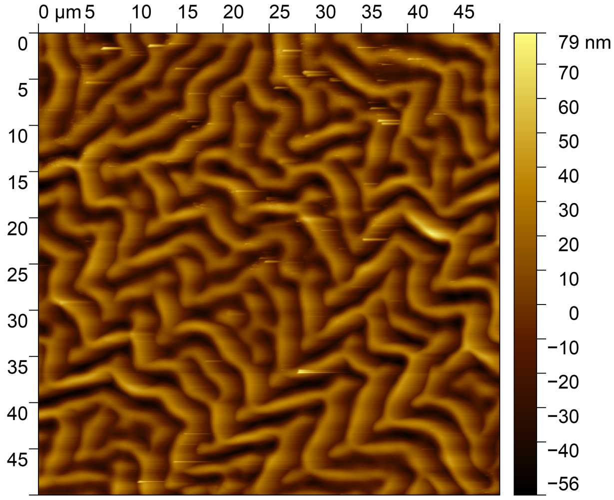

(b)

Figure 4.7: Surface images of planar PDMS coated with PVA captured by (a) SEM and (b) AFM (ambient).

The wave pattern of PVA film was caused by the high temperature (110 °C) heating in the preparation, because the pure PDMS curing at the same temperature did not show any wave pattern in the present work as a benchmark. A similar pattern was reported when the PDMS was coated by Au/Ti film. As shown in Figure 4.8, both ordered and disordered wave patterns were found by Whiteside et al. [311, 312] that the film bucked when the PDMS was heated to 110 °C and cooled, and the shrinking was explained due to the expanded of PDMS and then the film coating contracted with the PDMS surface in different rate [311–313]. In fact, when the deposition temperature is much higher than the experiment applied, the mismatch of film expansion and substrate expansion will make residual thermal stresses inevitably arises [314].

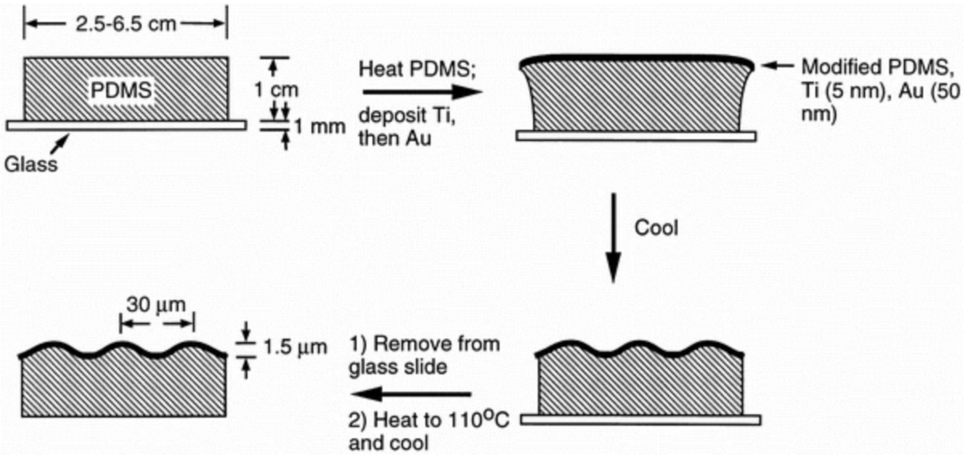

(a)

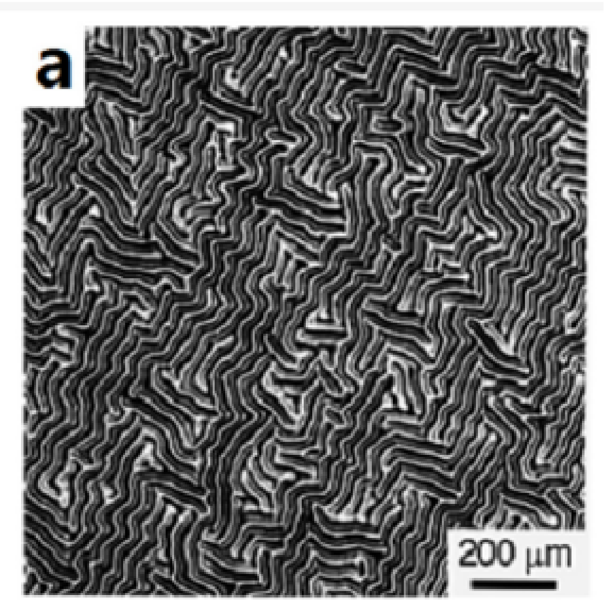

(b)

Figure 4.8: Schematic diagram of (a) the preparation of PDMS coated by Au/Ti, and (b) one of the surface film pattern exhibition [311].

When the PDMS surface is exceptionally smooth and the temperature is lower than the deposition temperature, the wave pattern will be ordered, and the equation below can be used to estimate the film thickness [311].

$$\sigma_0 = \frac{E_m(a_p - a_m)(T_D - T)}{1 - v_m} \tag{4.6}$$

$$\sigma_{crit} \approx 0.52(\frac{E_m}{1 - v_m^2})^{\frac{1}{3}}(\frac{E_p}{1 - v_p^2})^{\frac{2}{3}} \tag{4.7}$$

$$L \approx 4.36t(\frac{E_m(1 - v_p^2)}{(E_p(1 - v_m^2)})^{\frac{1}{3}} \approx 4.31t(\frac{E_m}{E_p})^{\frac{1}{3}} \approx 27.90t \tag{4.8}$$

E_m	E_p	a_m	a_p	v_m	v_p
707.9 MPa [315]	6.9 MPa	70 µm m^{-1} °C^{-1} [316]	310 µm m^{-1} °C^{-1} [317]	0.45 [318]	0.48 [311]

Table 4.1: Parameters required in Equation 4.6

The equi-biaxial compressive stress σ_0 (MPa) of film was given by Equation 4.6 [319], where T is the temperature used for film heating, and T_D (°C) is the deposition temperature of PVA. E_m (MPa) and E_p (MPa) are the Young's moduli of PVA and PDMS, and a_p and a_m (°C^{-1}) are the PDMS and PVA film coefficients of the thermal expansion, v_m and v_p are the Poisson's ratios of PVA and PDMS. The equi-biaxial compressive film stress arises because the thermal expansion coefficients of PDMS and (PVA) film has a considerable mismatch, which is more than four times [311]. When the temperature is cooled down, the equi-biaxial compressive stress will increase and the film started shrunk at the critical value which is the critical compressive stress σ_{crit} (MPa) (Equation 4.7) [320]. The wavelength L (µm) and the thickness of the film t (µm) are calculated based on the correlation between the sinusoidal wave pattern and thickness in Equation 4.8 [320]. According to values required in this study (Table 4.1), it can be calculated that the critical compressive stress σ_{crit} is 11.28 MPa. According to the wavelength was measured that L = 4.81 ± 0.70 µm, the PVA film thickness t in this study can be calculated to 0.17 µm.

The interferometer captured a similar pattern as Figure 4.9 shows, the order and disorder wave patterns can be observed on the surface of planar PDMS coated with PVA. The surface roughness of planar PDMS coated with PVA was calculated as $S_q = 0.32 \pm 0.02$ µm.

Figure 4.9: Interferometer image of the surface of planar PDMS coated with PVA in ambient.

4.3.2.2 Modified surface properties

To validate the PVA coating on the PDMS, planar and porous PDMS and PVA-coated PDMS surface were characterised by FTIR. The wavenumber was detected from 500 cm^{-1} to 4000 cm^{-1}. Figure 4.10(a) and (b) show the infrared spectrum curves of the samples. All the samples had the characterised peaks of Si-CH$_3$ bonding at 789 cm^{-1} and 1259 cm^{-1} and Si-O-Si bonding at 1020 cm^{-1}, which are the typical peaks of PDMS. Compared the chemical structure diagram between PDMS and PVA, oxhydryl (-OH) is the specific end group in PVA. According to the previous studies, the infrared spectrum curve of PVA shows a broad peak at 3200 cm^{-1}, which is the adsorption of hydrogen bond groups [321, 322]. Therefore, the peak at 3200 cm^{-1} can be used for validating the PVA coating on the PDMS.

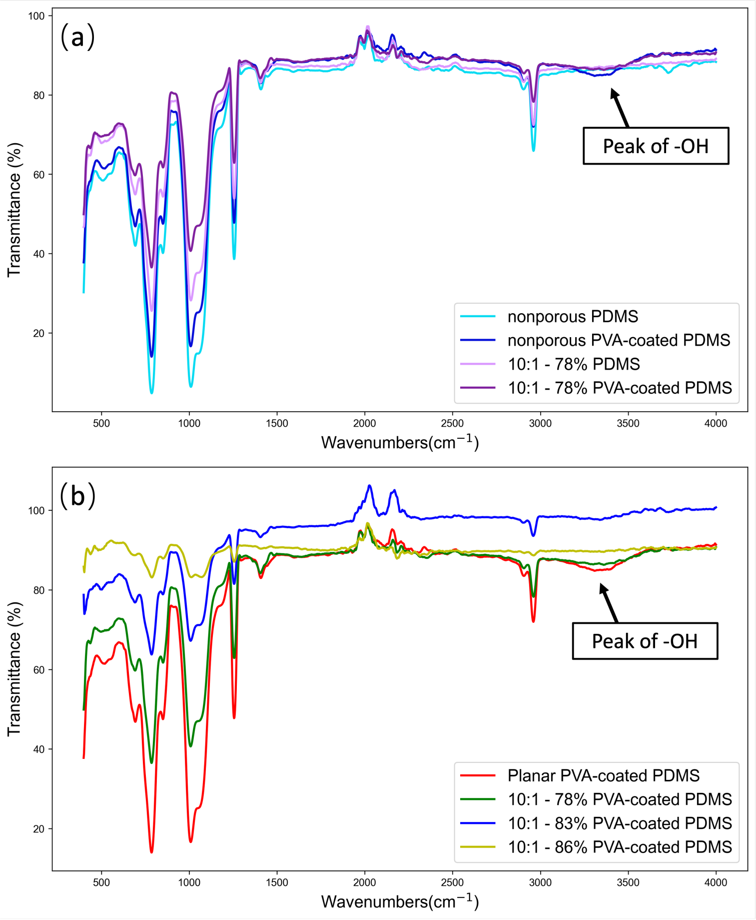

Figure 4.10: (a) FTIR optical of PDMS and PVA-coated PDMS matrices. (b) FTIR optical of porous PDMS coated with PVA in different porosity.

Compared to the PVA-coated PDMS and pure PDMS, a weak and broad peak can be observed in Figure 4.10(a) at around 3200 cm^{-1} on PVA-coated samples, and it shows planar lines at 3200 cm^{-1} on pure porous PDMS samples. With the increase of sodium chloride filling which grows the porosity of scaffold, the Figure 4.10(b) indicates the change of peaks between planar and different types of porous PDMS coated with PVA. The peak at 3200 cm^{-1} weakens when the sodium chloride fraction of PVA-coated PDMS increases, especially the sample 10:1 - 86%, which does not show a peak but a straight line around 3200 cm^{-1}. The similar appearance was observed in a FTIR work by Shi et al. [323] that the higher concentration of silica added as the pore-foaming agent, the lower height peaks showed for the samples.

Figure 4.11 shows the surface energy comparison between the PDMS, PVA-coated PDMS and HCl-treated PDMS, which were tested on the planar samples. As shown in Figure 4.11, the PVA-coated PDMS shows a lower contact angle to the 10% hyaluronic acid treated PDMS. Compared to the pure PDMS, the contact angle after HCl treated is decreased from 115.0 ± 1.0 ° to 69.9 ± 1.0 °, and the contact angle of PVA-coated PDMS is 59.6 ± 2.8 °. Reported from previous PVA coating work [266], the surface contact angles are similar to the present work, which is 71.5 °. Therefore, the surface chemical property of porous PDMS has been changed from hydrophobic to hydrophilic by PVA coating, which is same as the typical surface hydrophilicity of cartilage [57, 58].

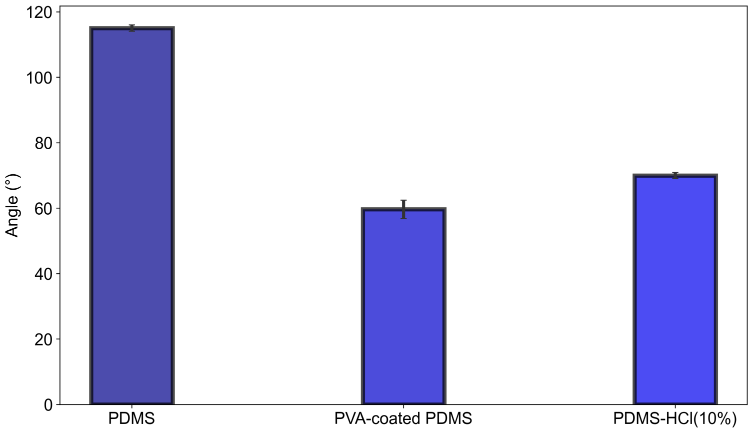

Figure 4.11: Contact angles of distilled water on PDMS, PDMS coated by PVA, and HCl treated PDMS.

4.3.2.3 Young's modulus

The modulus of porous PDMS coated with PVA was measured by AFM and microindentation. The AFM measurement procedure was same as the porous PDMS, and the microindentation was measured by a 1.5 mm diameter planar tip, the maximum force applied was 1.0 N. As shown in Figure 4.12, the AFM results show that the Young's modulus of PVA-coated PDMS matrices are from 5.04 ± 1.48 MPa to 1.84 ± 0.58 MPa, and the microindentation measured the modulus of matrices are from 0.28 ± 0.01 MPa to 0.03 ± 0.003 MPa. Both tests showed that PVA-coated PDMS has the same tendency as porous PDMS, it can be observed that the increase of NaCl fraction in matrices decreases the modulus of PVA-coated PDMS.

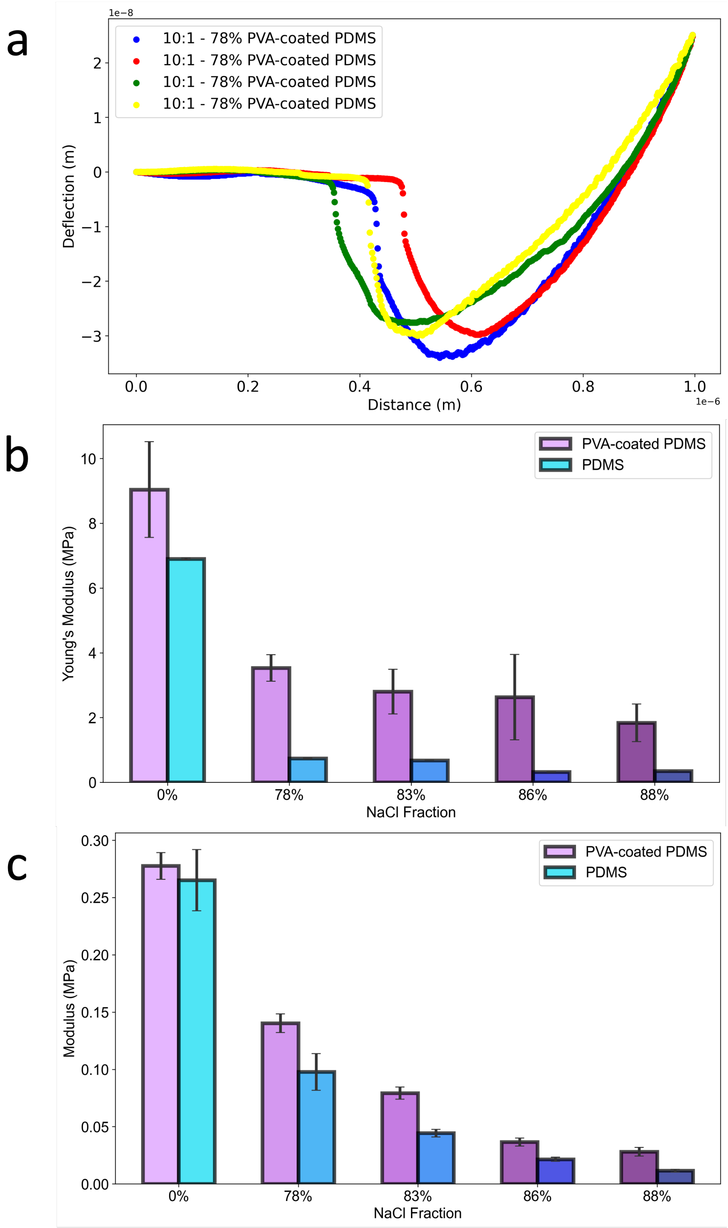

Figure 4.12: Modulus as a function of the concentration of NaCl in matrices, and the comparison between PDMS and PVA-coated PDMS. (a) AFM force curves of porous PDMS coated with PVA. (b) Young's modulus measured by AFM; (c) modulus measured by microindentation.

The coating of PVA film provides enhancement on the PDMS surface. The modulus of

PVA is much higher than the PDMS. The PVA Young's modulus was reported as 707.9 MPa [315], and the classic PDMS, with the curing agent ratio of 10:1, was reported as 2.61 MPa [137]. From Figure 4.12, it can be observed that the modulus of PVA-coated PDMS has a significant increase from the pure porous PDMS structure in both AFM and microindentation results. Compared to the modulus value results from two facilities, there is a giant difference between the same samples, and this was caused by the measurement method differences. In the AFM measurement, the radius probe was 4 µm with the indentation depth of 1 - 3 µm, while the microindentation measurement used a 6 mm radius flat tip, with the indentation depth higher than 1 mm. As the thickness of the scaffold was 3 - 4 mm and the surface diameter was 12 mm, the contact area and indentation depth in the AFM measurement were not sufficient to represent the whole porous structure modulus. Furthermore, with the 0.044 µm PVA film, the AFM indentation was much more applied on the PVA film rather than the scaffold. Therefore, the altering of PVA coating PDMS with porous PDMS modulus in AFM measurement was larger than the microindentation.

4.3.2.4 Tribological properties

Tribological experiment of PVA coated porous PDMS was tested by Forceboard and microtribometer, both facilities measurement were took place in ambient and water. As shown in Figure 4.13, most of CoF results show a tendency with the change of NaCl fraction. In both microtribometer and Forceboard aqueous tests, the 10:1 - 78% has the lowest CoF values, which are 0.010 ± 0.0002 and 0.924 ± 0.137, respectively. The largest CoF is in the ambient test of sample 10:1 - 88%, which has the CoF as 0.270 ± 0.004 and 1.570 ± 0.726 in microtribometer and Forceboard test respectively.

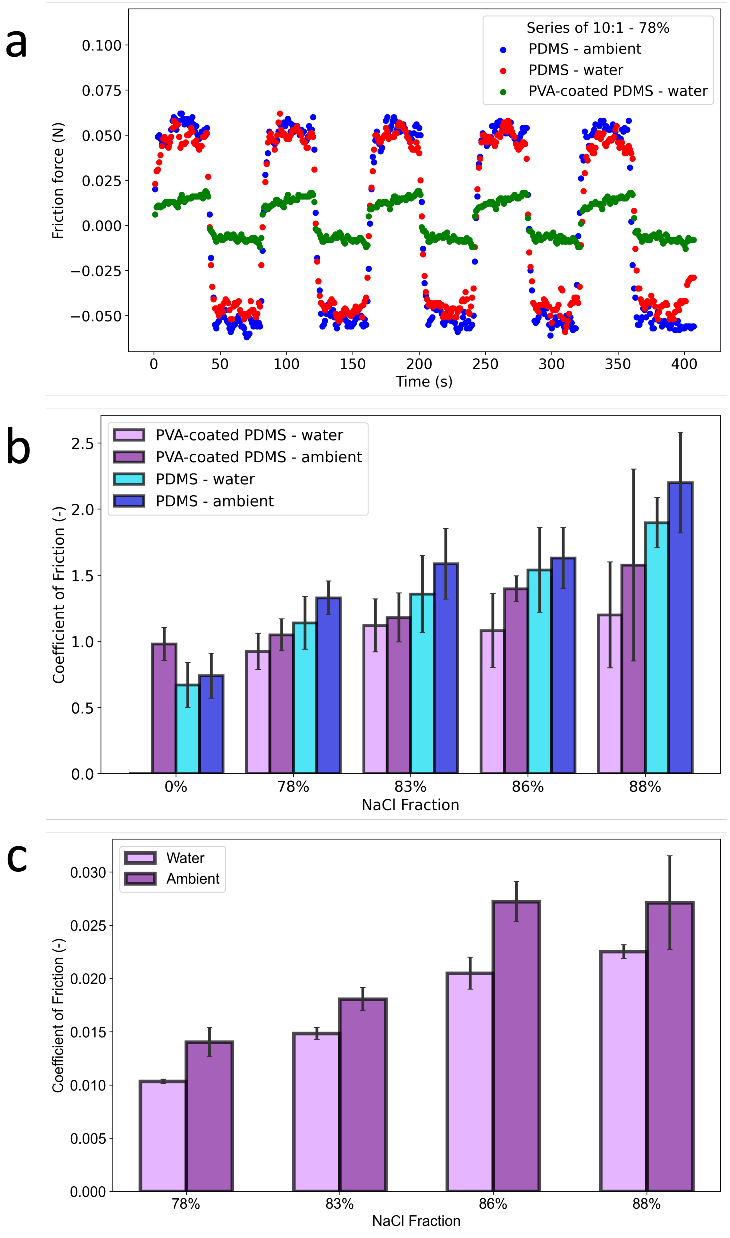

Figure 4.13: CoF as a function of the concentration of NaCl in PDMS and PVA-coated PDMS, which was measured under the ambient and water. (a) Tribometer measurement raw data of 10:1 - 67% porous PDMS (ambient and water) and 10:1 - 67% PDMS coated with PVA (water); (b) CoF measured by Forceboard; (c) CoF measured by microtribometer.

Figure 4.13(a) shows some of raw data of tribometer measurement of porous PDMS and porous PDMS coated with PVA, which are 10:1 - 67% porous PDMS measured in ambient and water, and 10:1 - 67% PDMS coated with PVA measured in water. In Figure 4.13(a), it could be obvious observed the difference of friction force between porous PDMS and porous PDMS coated with PVA. Figure 4.13(b) displays the CoF of PVA-coated PDMS and the porous PDMS measured by Forceboard, which illustrates the CoF of porous PDMS is significantly higher before PVA film coated. The wettability of PVA film coated samples have been changed from porous PDMS, which was reported to increase the surface adhesion force [324–326]. Compared to the water and ambient tests, all aqueous CoF values are lower than ambient, which is commonly reported that water is affected as the lubricant [327, 328]. It can be observed that the planar PDMS coated with PVA in ambient is higher than the planar PDMS, which is opposite to the other series of tests. This can be explained by the wave pattern on the planar PDMS coated with PVA as Figure 4.7 shows, the pattern on the matrix surface increases the surface roughness, and the surface roughness values was confirmed positive correlated to the CoF values of the surface [329–332]. As shown in Figure 4.13(c), the microtribometer results show the same tendency as Forceboard results that the CoF tested in water are lower than the ambient CoF values [311, 319]. The CoF of 10:1 - 78% PVA coated matrix is lower than 10:1 - 50% porous PDMS shown in Figure 4.6, 10:1 - 86% PVA coated matrix is lower than 10:1 - 80% porous PDMS shown in Figure 4.6, which confirms that the PVA coating efficiently decreases the CoF of porous matrices.

4.4 Discussion

4.4.1 Porous PDMS

The thickness of porous PDMS has been controlled and limited to under 4 mm, which followed the introduction of the SCPL method to easy leaching out the salt particles [165].

From this work, the sodium chloride fraction under the 67% was still found particles left in the matrices (Figure 4.14), which is undoubtedly surrounded by the PDMS elastomer. Hence, the fraction of salt crystals should be controlled to higher than 67% in the further work to leach out the particles entirely.

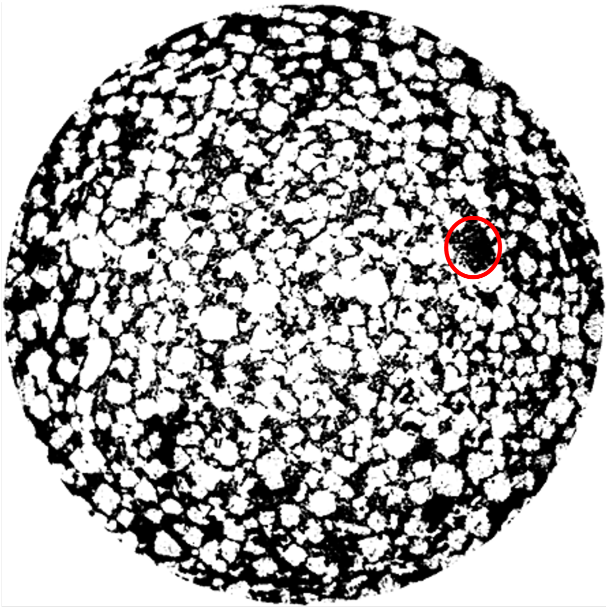

Figure 4.14: A section of 10:1 - 50% porous PDMS with an undissolved sodium chloride crystal.

To replicate the OA cartilage, the fibril structure of interior PDMS is similar to the articular cartilage. As the surface of healthy articular cartilage has no fibrous structure explored, the low NaCl ratio matrix has an analogous surface to mimic the early stage of OA cartilage, and the high NaCl ratio matrix surface, which explored the fibrous structure, could be acquired to mimic the late-stage OA cartilage with surface degenerated.

As the SCPL preparation does not involve chemical reaction, the correlation between the porosity and NaCl fraction should be calculated by the followed equation:

$$\begin{aligned}\phi(\%) &= \frac{V_{total} - V_{PDMS}}{V_{total}} \times 100\% = \frac{V_{NaCl}}{V_{NaCl} + V_{PDMS}} \times 100\% \\ &= \frac{\frac{m_{NaCl}}{\rho_{NaCl}}}{\frac{m_{NaCl}}{\rho_{NaCl}} + \frac{m_{PDMS}}{\rho_{PDMS}}} \times 100\% = \frac{\frac{m_{NaCl}}{\rho_{NaCl}}}{\frac{m_{NaCl}}{\rho_{NaCl}} + \frac{(\frac{1-a}{a})m_{NaCl}}{\rho_{PDMS}}} \times 100\% \\ &= \frac{0.965a}{2.16 - 1.195a} \times 100\%\end{aligned} \tag{4.9}$$

where the m_{NaCl} and m_{PDMS} are the weight of sodium chloride and PDMS, ρ_{NaCl} and ρ_{PDMS} are the density of sodium chloride and PDMS. And a is the fraction of NaCl in the matrix, which was calculated by the average of 5:1, 10:1 and 20:1 scaffolds. By substituting the fraction of NaCl and porosity measured from micro-CT, Figure 4.15(a) shows that the porosity results did not fit with the Equation 4.9. This is because the measurement of porosity chose the 0.3 mm in the bottom for the superficial zone porosity, which had direct contact with the tribological measurement. From Figure 4.15(a), it could be noticed the higher NaCl filled, the better porosity fitted to the equation, and the 89% samples can be observed that crystals had fully filled the matrix and no sinking of NaCl. Therefore, it could assume that the porosity measured in this study is for the surface and impacted by the sedimentation, the lower fraction of NaCl in the matrix has a larger error than the principal calculation. Therefore, a parameter C is introduced for neutralising the influence of particle sinking, based on the principle of porosity calculation, a similar fitting is assumed as the following equation:

$$\phi(\%) = (\frac{0.965a}{2.16 - 1.195a} + C * (1 - a)) \times 100\% \tag{4.10}$$

By fitting to the porosity measured from porous PDMS, the parameter C was fitted as 0.480 ± 0.043. As shown in Figure 4.15(b), the porosity of porous PDMS in this work is better agreed to the Equation 4.10. Therefore, the equation 4.10 can be used for the further porous PDMS porosity prediction.

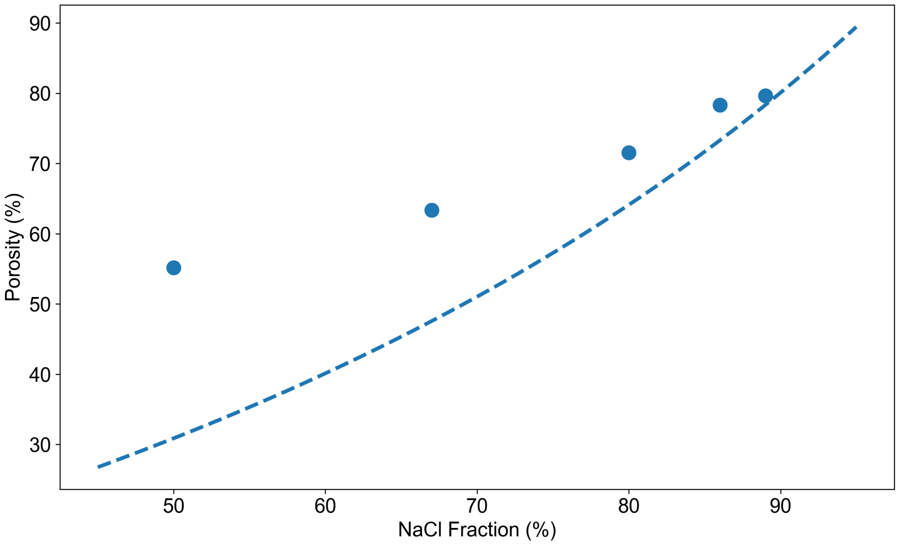

(a)

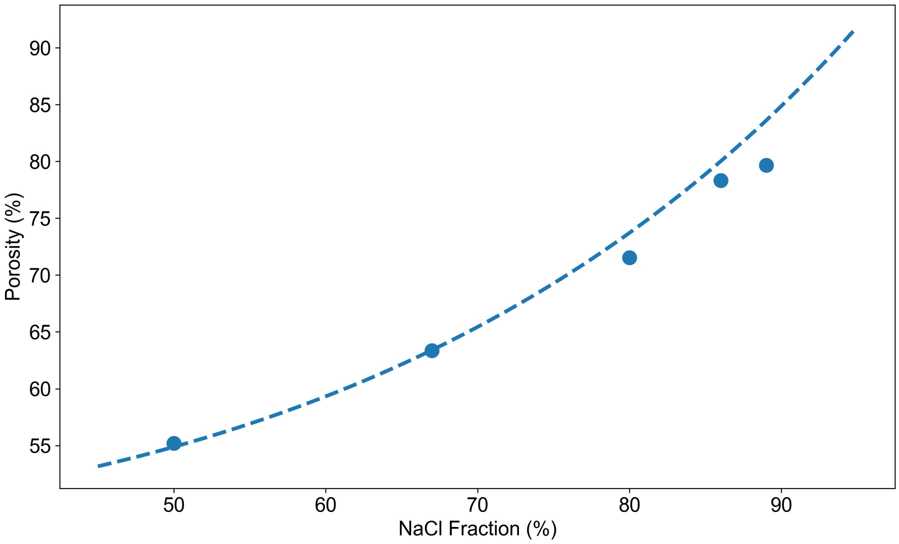

(b)

Figure 4.15: Fitting curves of equations according to the porosity of the porous PDMS as a function of NaCl fraction used in preparation. (a) Fitting curve fitted by Equation 4.9; (b) fitting curve fitted by Equation 4.10.

It has been described the correlation of Young's moduli with porosity in an equation

[333–335]:

$$E = cE_0(1 - \phi)^n \tag{4.11}$$

where E is the Young's modulus of samples, E_0 is the Young's modulus of the materials without pore, and ϕ is porosity, which was used to fit the experimental results of the present work. The c and n were reported that $0.1 \leq c \leq 4$ and $n \approx 2$ [333]. As the porosity is not correlated with the curing agent ratio of PDMS, the porosity values used for the fitting are averaged the results of 5:1, 10:1 and 20:1 (Table 4.2).

NaCl fraction (%)	Porosity (%)
50	55.19 ± 0.007
67	63.34 ± 0.005
80	71.53 ± 0.019
87	78.31 ± 0.002
89	79.66 ± 0.002

Table 4.2: Average porosity of different NaCl fractions calculated from the porosity results of X-ray tomography.

Based on the equation 4.11, when c = 1 and the n = 2, the equation is well fitted to the results in present study, and the fitted E_0 values are listed in Table 4.3. As Figure 4.16 appears, the model equation between Young's modulus and porosity well described the behaviour of different ratios of curing agent of PDMS.

PDMS: CA	E_0 (MPa)
5:1	8.24 ± 0.85
10:1	7.13 ± 0.23
15:1	3.39 ± 0.22
20:1	1.87 ± 0.36
25:1	1.03 ± 0.90

Table 4.3: Non-porous PDMS Young's modulus of different CA ratios fitted by Equation 4.11.

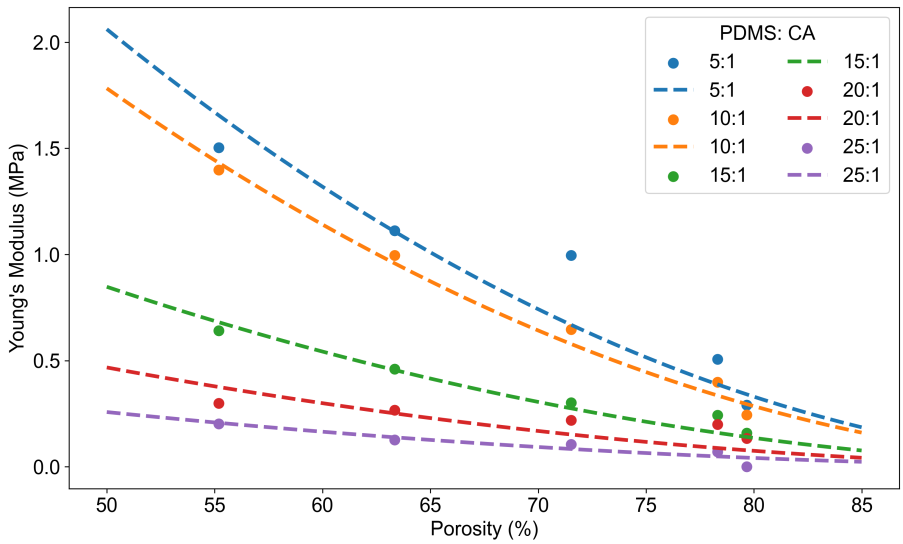

Figure 4.16: Young's moduli and coefficients of friction of the porous PDMS matrix as a function of porosity (scattered) and their best fits (dashed lines).

In previous studies, the Young's modulus of poroelastic models was reported as strain rate correlated [336, 337]. In the present work, the comparison was focused on the modulus difference between different preparation parameters rather than the change of same model. Therefore, this study used the unified measurement condition for all samples have kept reliable of comparison results.

According to the surface properties of OA cartilage in previous studies, the frictional coefficients increase correspondingly with the increase of surface roughness [70, 338]. The increase of porosity by adding NaCl has been shown to the link of surface roughness in SEM images in Figure 4.3. As the relationship between CoF and porosity shown in Figure 4.6, the increase of CoF corresponded with the increase in porosity. It has been concluded as an equation from the previous study that CoF has an inverse correlation between contact areas [339], which means the increasing of pores on the surface increases the CoF on PDMS, this is the same as the tendency shown as the study results in this work.

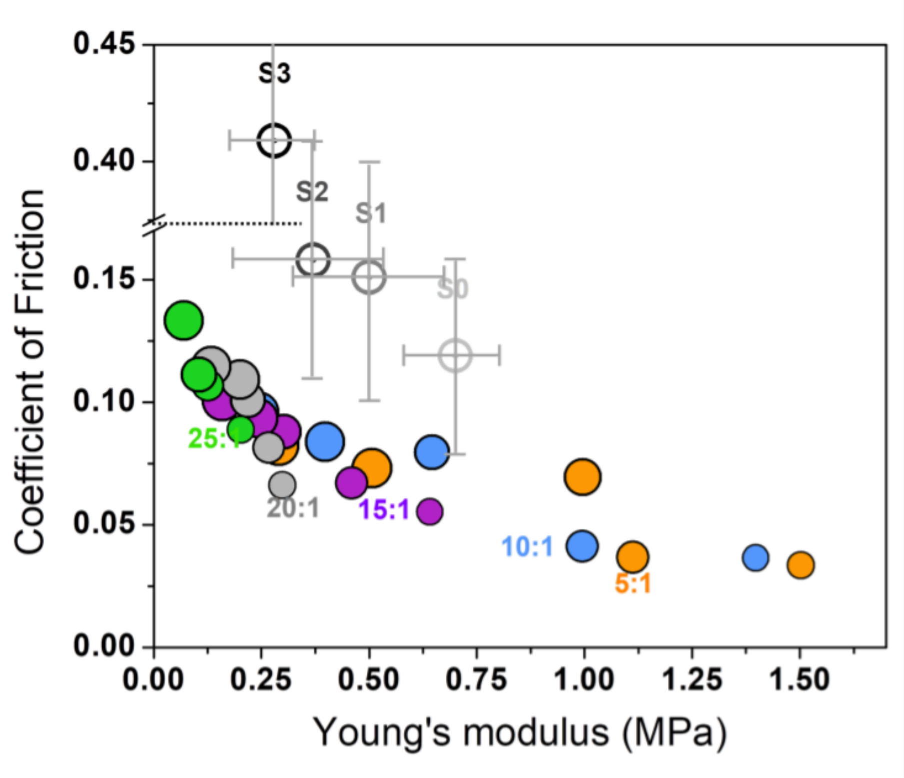

Figure 4.17: Cartography of the suite of porous PDMS (filled circles) prepared with different Young's modulus and CoF compared with the stages (S) of OA (open circles). The range size of the filled circles is linked to the range of porosity from 55% to 80%, the smaller diameter the lower the porosity. The groups of colours represent the 5 different elastomer to CA ratios.

As the clinical observation on OA patients' cartilage, the deteriorated progress of OA disease usually along with the increasing of the CoF on friction sliding, and degenerated to the softer tissue [70, 340], which is performed in measurement as lower Young's modulus. The mechanical properties variation tendency of OA progression is the same as the increase of porosity for porous PDMS in this study. The Young's modulus and CoF different stage of OA cartilage has been plotted with the porous PDMS measured from the present work in Figure 4.17. The standard deviations are smaller for the porous PDMS than for human OA cartilage and allow a diversity of the properties of the structures within the same stage of

OA, such as porosity.

The mechanical properties of different ICRS grades cartilage had been reported in massive of previous studies, which has been shown in the Table 2.1 and the absolute values in these studies showed a wide range. According to the review literature about bio-tissue mechanical measurement, the results showed two significant appearances that the values was influenced by the specimens individual differences, and as well as the measurement methods impacted the final results [287, 341, 342]. Therefore, for mimicking the different stages of OA cartilage, the similar test methods results were chosen for this work. The Young's modulus and CoF for cartilages of different OA stages and the porous PDMS samples prepared in the present work are presented in Figure 4.17, as grey open circles and coloured circles respectively. The standard deviations are smaller for the porous PDMS than for human OA cartilage and allow a diversity of the properties of the structures within the same stage of OA, such as porosity. The suite of PDMS provides a good range of Young's modulus and porosity to replicate the different stages of human OA and their diverse mechanical and structural properties, despite that further improvement can be made to increase the CoF that are for now lower than those presented by the real cartilages affected by OA [68, 70, 343]. This could be achieved by increasing the roughness of the surface and introducing a positive gradient of CA concentration from the bulk to the top surface. The reported values of Young's modulus for cartilage are approximately 0.60 - 0.80 MPa, 0.50 ± 0.14 MPa, 0.37 ± 0.13 MPa, and 0.28 ± 0.12 MPa for stages 0 to stage 3, respectively [68], which is well within the range explored in the present work.

As the artificial cartilage scaffold with the purpose of replicating different stages of OA cartilage, similar modulus porous PDMS was prepared according to the Equation 4.11. With the standard PDMS curing agent ratio 10:1, the fractions of NaCl were calculated as 3.5:1, 5:1, 6.3:1 and 7.5:1, which were expressed as 10:1 - 78%, 10:1 - 83%, 10:1 - 86% and 10:1 - 88%. Considered the 'smart' surface that cartilage was hydrophobic in air-dried, the porous PDMS scaffold could be used for the ambient cartilage research substrate [57, 58]. On the other hand, the cartilage hydrophilic surface property in the aqueous environment was different from the PDMS surface, therefore, the surface modification scheme was proposed with PVA film coated.

4.4.2 Porous PDMS coated with PVA

In Forceboard measurement, the wave pattern on the surface changed the surface roughness, and increased the CoF of the planar PDMS coated with PVA because of the correlation between the surface roughness and coefficient and friction [329–332]. Nevertheless, the CoF tests of planar PVA-coated PDMS samples under the water were too low to be measured, compared to the pure planar PDMS, it could be confirmed the wave pattern was removed by water. In fact, a test was used for validating it is easy to remove the wave pattern from PVA-coated PDMS in the aqueous environment. The planar PVA-coated PDMS was immersed in the water for 5 minutes and then scanned the surface morphology by AFM, and the results showed the surface was smooth flat. Therefore, the aqueous measurement can ignore the influence of the wave pattern. On the other hand, the roughness of the wave pattern of PVA coating film was much less than the high roughness of the porous structure.

Different temperature prepared PVA film were measured with contact angles in previous study, and it was reported that the contact angle was depended on the baking temperature [344], and the PVA film contact angles increased from 48 ± 1 ° when the baking temperature was 20 °C to the 66 ± 2 ° when the baking temperature was 180 °C. Even though the PVA film contact angle in this work was consistent with the range from the literature reported, the PVA contact angle was reported as 58 ± 2 ° at 135 °C, which is lower than the 59.6 ± 2.8° at 110 °C, therefore, some other factor affected the surface chemical property to the PVA film. The surface roughness has been confirmed correlated to the contact angle [325], Wenzel et al. [326] and Cassie et al. [324] had concluded the equations for the affected from the rougher surface. The conclusions claimed that the rougher surface would increase the surface contact angle, which explains the higher contact angle value in this work.

The Young's modulus against porosity equation has excellently fitted the porous PDMS. Therefore, the present work is attempting to fit a equation to PVA coated matrices. The porous PDMS used for comparison in this study was not excellently fitted by the Equation 4.11, but close enough, and the error is highly likely caused by the systematic error from sample preparation and measurement. According to the Equation 4.10, the porosity of the series of samples was calculated. When the fractions of NaCl were 78%, 83%, 86% and 88%, the porosity of the superficial scaffolds are 71.86%, 76.74%, 80.01% and 82.37%, respectively. Then, the fitting to the Equation is plotted in the Figure 4.18(a). Obviously, it can be observed that the fitting with Equation 4.11 does not work on the PVA-coated PDMS, which is predictable because the matrix was not a homogeneous material. By using a parameter E_0' to replace the E_0 in the Equation 4.11, a well fitting curve is shown in Figure 4.18(b) when the E_0' was calculated to 50.45 ± 4.37 MPa. On the other hand, the E_0' is the equivalent Young's modulus of the non-porous PVA-coated PDMS matrix in this study.

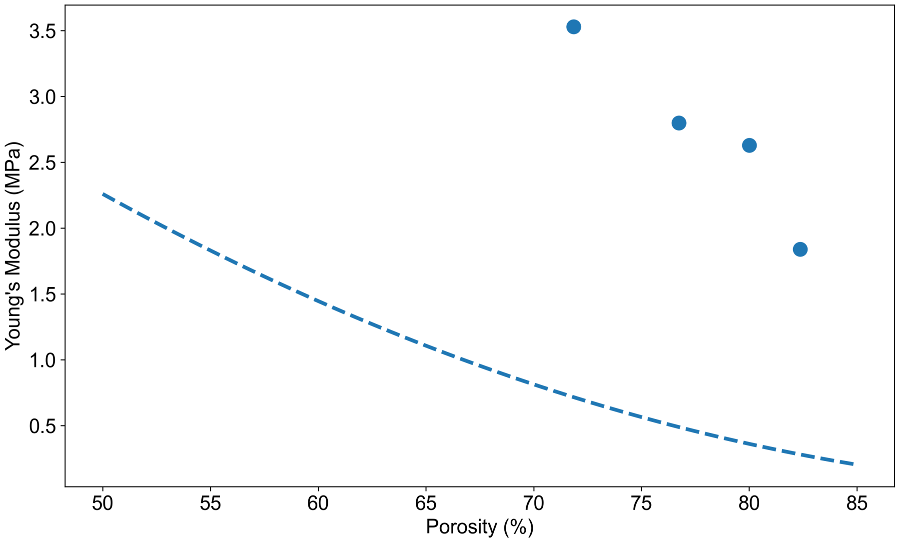

(a)

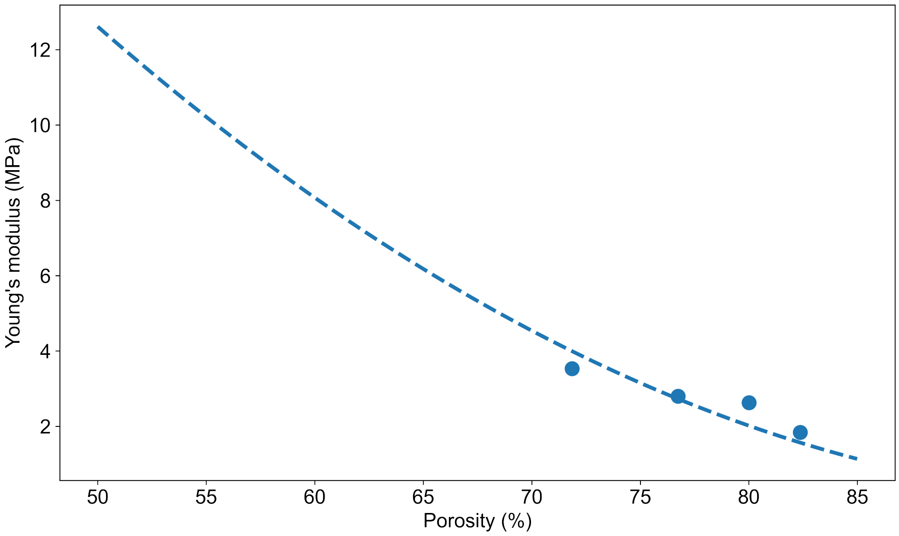

(b)

Figure 4.18: Young's modulus fitting attempts according to Equation 4.11 against porous PVA-coated PDMS matrices. (a) Fitting curve fitted when $E_0 = 9.04$ MPa; (b) fitting curve fitted when $E_0' = 50.45$ MPa.

4.5 Summary

In the present work, the porous PDMS structure has a suitable mechanical property to be considered as artificial OA cartilage, and it has the possibility of the platform for the *in vitro* tests for OA treatment.

From the results, porous PDMS had two controllable variations in the preparation: concentrations of crosslinking and pore-foaming agent. The PDMS matrix reached porosity from 54.6 ± 1.1% to 81.7 ± 0.7% upon increasing NaCl concentration. With the equation fitted for porosity, it was controllable to prepare the expected porosity by adjusting the fraction of NaCl. The Young's modulus varying decreased from 1.50 ± 0.03 MPa to 0.07 ± 0.003 MPa upon increasing the elastomer to curing agent ratio and sodium chloride fraction. Inversely, the CoF of the porous PDMS matrix comes with an increase from 0.033 ± 0.002 to 0.133 ± 0.001. By comparing with OA cartilage mechanical properties, the high concentration of crosslinker and the low concentration of NaCl would be the suitable choices for mimicking the early stage of OA cartilage.

To modify the porous PDMS surface from hydrophobic to hydrophilic, the porous PDMS was successfully coated with the PVA film. The film thickness was calculated as 0.044 µm. The film showed wave patterns on surface of PVA-coated PDMS, and this has an impact on the ambient friction test, but not the aqueous. The surface of PDMS has been modified to hydrophilic by PVA coating, which could better mimic cartilage tissue in the liquid environment. Similar to the porous PDMS, the sodium chloride fraction could control the CoF, and the modulus of PVA-coated PDMS. In this study, the PVA-coated PDMS Young's modulus was proved stiffer than the porous PDMS, resulting from 3.53 ± 0.41 MPa to 1.84 ± 0.58 MPa. And the CoF was measured from 0.010 ± 0.0002 to 0.022 ± 0.0006 by microtribometer test, and the Forceboard results show that the CoF of the porous

PVA-coated PDMS was lower than the porous PDMS in both ambient and aqueous tests.

Chapter Five

Lubrication efficiency of silica nanoparticles based IAI formulation on artificial cartilage

5.1 Introduction

The porous scaffold of cartilage provides poroelasticity property to the tissue, which plays a role in load-bearing, lubrication and fluid transport [345]. Previous studies confirmed that the synovial fluid behaves as the vehicle for transporting the lubricant molecules, such as hyaluronic acid and lubricin [346, 347]. The viscosupplementation which is consists of hyaluronic acid benefits to anti-inflammation, chondroprotection, analgesic and decreasing lubrication. But, without the drug delivery system (DDS), the small molecules such as analgesics, glucocorticoids, and hyaluronic acid were easy to be metabolised by synovial fluid and extracellular matrix barrier [348]. For example, the half-life of methotrexate is 0.59 - 2.9 hours, ibuprofen is 1.9 hours, and diclofenac is 5.2 hours [12]. Therefore, for osteoarthritis (OA) targeting treatment, drug delivery systems with drug carriers are applied in the research [12].

Biodegradable polymer or bilayered lipid are usually used as the materials of nanoparticles. As cartilage has porous scaffold and the pore size on the cartilage surface was reported as nanometre-scaled, nanoparticles are proposed for the drug delivery system, which has a appropriate size to pass through the surface of cartilage and benefit the pharmacokinetics of therapeutic agents [348]. Recently, nanoparticles were developed to enhance lubrication in the joint, such as silica nanoparticles and liposomes [349–351]. Compared with traditional lubricants, the nanoparticle based lubricant has unique advantages on aqueous lubrication, and the rolling mechanism of colloidal nanoparticles on surface sliding reduces the friction [349, 352, 353].

According to the principle of nanoparticle lubrication, the nanofluid lubricants affect the friction by four different effects: rolling effect, protective film effect, mending effect and polishing effect [34, 354]. The rolling effect and protective film effect decrease the coefficient of friction (CoF) directly from the particle's mechanical behaviour. The mending effect and polishing effect enhance the lubrication by modifying the substrate surface morphology [34]. In the rolling effect, the spherical nanoparticles are considered as load-bearing balls between the gap of the surface. The rolling of spherical particles contributes to the sliding friction by mixing sliding friction and rolling friction. Moreover, the bearing of nanoparticles should be able to keep the shape and rigidity during friction, which requires low loading and shearing surface [355]. The protective film effect usually constructs the protecting film on the surface by the reaction of treated material additive [354] or tribosintered [202]; The film could protect the wear of particles in lubricant [356] and reduce the expansion of surface cracks [354]; The mending effect introduces the compensation of surface loss by the nanoparticles. The nanoparticles fill the grooves and uneven area on the interacting surface to decrease friction [357]. Moreover, the polishing effect was proven that the particles could fill out the valleys on the surface, which is also referred to as “artificial smoothing”, decreasing the surface friction by decreasing the surface roughness [355].

According to the study by Peng et al. [353], SiO_2 nanoparticles provided the lowest CoF when the concentration between 0.1% to 1.0%. Another study [358] showed that the silicon dioxide particles dispersed in coconut oil kept decreasing the CoF until the concentration of SiO_2 increased to 1.25%. The hard nanoparticles plowed between the surface at the beginning of test, then more spherical nanoparticles rolled into the contact area acted nanosized ball bearing that reduced friction coefficient. Besides the concentration of nanoparticles influences the tribological properties, some other parameters of nanoparticles show the impact to lubrication system, which includes the nanoparticle size, the shape of nanoparticles, the nanostructure of particles, and the nanoparticle surface functionalisation [359]. A model of nanoparticle contact with a rough surface was built in Ghaednia's work [360]. The results claimed that the higher concentration of nanoparticles, the smaller particles and the smooth surface could decrease the CoF. The literature also reported the challenge of wear on the surface caused by particles [360]. The nanoparticle-based DDS shows a positive effect on lubrication [361, 362] by decreasing the CoF, which is beneficial for the OA treatment. In past studies [361, 362], nanoparticle lubrication tests were focused on the hard surface, which is different from elastic surface as cartilage. Therefore, a porous elastic artificial cartilage applied in the present project is benefit to understand the lubrication behaviour on poroelastic material.

A summary of nanofluid behaviour was concluded by Sharma et al. [363] that nanoparticle-based fluids deformation are depends on the concentration of nanoparticle. Most nanofluid performs Newtonian behaviour at low nanoparticle concentration that stress and strain rate shows a linear correlation, and high concentrated nanofluid performs non-Newtonian behaviour. Moreover, at the same concentration, the nanofluid shows Newtonian behaviour at low shear rate, which exhibits non-Newtonian behaviour at high shear rate. Therefore, the present study have to validate if the rheology of nanoparticle solution rheological property changed when the concentration and sliding rate changed in the measurement.

This chapter studied the basic lubrication behaviour of silica particles on polydimethylsiloxane (PDMS) based substrates. According to the nanofluid properties reported that influence the lubrication, the present work studied the influences of particle size, the normal load applied, the sliding velocity, and the particle concentration. By excluding the impact of viscosity influence, the parameters of nanoparticle changed in the study showed the influence of the CoF on porous matrix.

5.2 Materials and methods

5.2.1 Silica nanoparticle suspension

Fumed silica nanoparticles were purchased from Lawrence Industries, Ltd., UK. Three kinds of silica nanoparticle Aerosil 90, Aerosil 150 and Aerosil 380 were chosen for this project. Phosphate buffered saline (PBS) tablets were ordered from Fisher Scientific (Loughborough, UK). Planar and 10:1 - 83% porous PDMS coated with PVA were used as tribological measurement substrate. Silica nanoparticle Aerosil 150 particles was dissolved to 8 concentrations by PBS solution, which were 0.01%, 0.1%, 0.5%, 1.0%, 1.5%, 2.5%, 3.0% and 5.0%. In the meanwhile, silica nanoparticle Aerosil 90 and 380 were prepared to 1.0% by PBS buffer.

5.2.2 Particle characteristics

Particle appearance was measured by SEM (7000F, JEOL, UK). The powder of Aerosil silica nanoparticles were poured evenly on carbon dioxide tape, and the SEM images were captured at 10 kV voltage and 1000 × magnification. The size of Aerosil particles was measured by DLS (Zetasizer, Malvern Panalytical, UK). Three types of Aerosil particles were dissolved in deionised water to 100 ppm, the solution was sonicated for 15 minutes at room temperature, then 10 ml of each type of Aerosil silica nanoparticle were extracted to DLS tests. The particle size was calculated by DLS software automatically according to the distribution curves.

5.2.3 Tribological measurement

The sample of 10:1 - 83% porous PDMS coated with PVA was used for all microtribometer measurement. In self-built tribometer measurement, 3 mm diameter glass ball was used, and the sliding length was 8 mm for all tests [289]. The experiment conditions of tribometer and nanofluid system were varied, the test conditions are shown in Table 5.1.

Test	Load	Velocity	Concentration of nanoparticle
1	30 g and 50 g	0.5 mm s^{-1}	1% of Aerosil 150
2	30 g	0.1 mm s^{-1}, 0.5 mm s^{-1}, 1 mm s^{-1}, 2 mm s^{-1}, 10 mm s^{-1} and 20 mm s^{-1}	1% of Aerosil 150
3	30 g	0.5 mm s^{-1}	0.01%, 0.1%, 0.5%, 1.0%, 2.5% and 5.0% of Aerosil 150
4	30 g	0.5 mm s^{-1}	1% of Aerosil 90, Aerosil 150 and Aerosil 380

Table 5.1: Experimental conditions of each set of tribological measurement.

In AFM tribological measurement, 4 µm borosilicate sphere probe were applied on cantilever. The concentrations of 0.1%, 0.5%, 1.0%, 1.5% and 3.0% of silica nanoparticle (Aerosil 150) solution were in use on the AFM friction measurement, and 10 µl of each solution were added between cantilever and substrate. The AFM tribological measurement increased load from 0 nN to 2000 nN - 2500 nN in each test. The concentration 0.0%, 0.5%, and 1.0% sliding distance was 3 µm, and concentration 1.5% and 3.0% sliding distance was 1 µm.

5.2.4 Rheology

The nanoparticles of Aerosil 150 were diluted to 0.01%, 0.1%, 0.5%, 1.0%, 2.5% and 5.0% in PBS buffer. For each test, 0.4 ml of solution was extracted to the HR-1 Discovery Hybrid Rheometer (TA instrument, UK), and the shear rate was sped up from 200 s^{-1} to 1500 s^{-1}.

5.3 Results and discussion

5.3.1 Morphology of silica particles

Aerosil silica nanoparticles were spread on the tape before the SEM test, environmental SEM was applied for silica particles morphology capturing. Figure 5.1 shows the morphology of nanoparticles of Aerosil 90, 150 and 380.

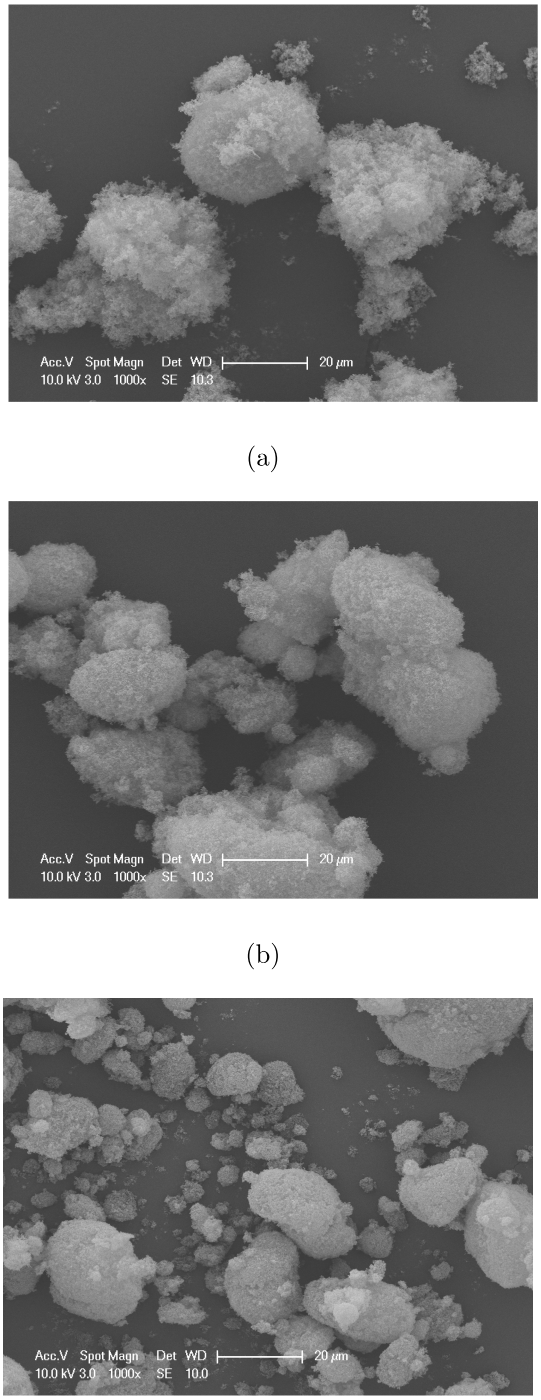

(a)

(b)

(c)

Figure 5.1: SEM images of three types of silica nanoparticles. (a) Aerosil 90; (b) Aerosil 150; (c) Aerosil 380.

As shown in Figure 5.1, the agglomerating behaviour is observed between the particles, which is due to the adhesion of particles and the weak forces between each particle [364]. Hence, it is unable to distinguish any single nanoparticle in SEM images and compare the size of nanoparticles. Therefore, the DLS was used for measuring the size of silica nanoparticles. Figure 5.2 shows the results of the nanoparticle size of Aerosil 90, 150 and 380, which were resulted as 256.00 ± 4.82 nm, 215.06 ± 2.12 nm and 152.00 ± 1.86 nm, respectively. However, according to literature results [365–367], the average silica nanoparticle sizes were much smaller than the size results shown in Figure 5.2, the average sizes of Aerosil 90, 150 and 380 were reported as 20 nm, 14 nm and 7 nm (Table 5.2). Even though the results showed the significant difference, the sizes of three types of particles were in the same order that Aerosil 90 was more considerable than Aerosil 150 than Aerosil 380.

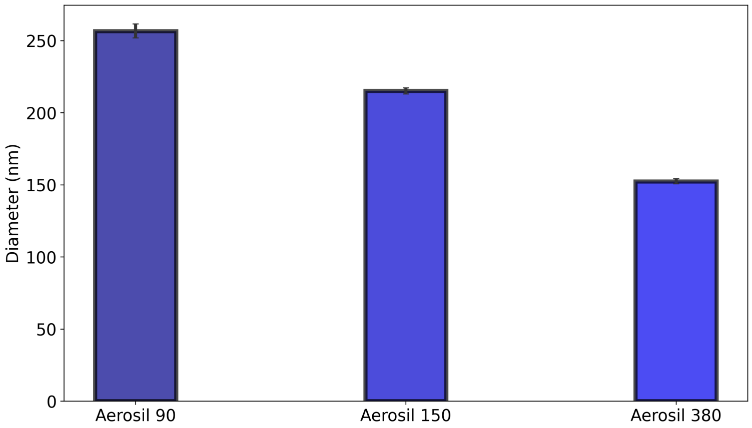

Figure 5.2: Three types of nanoparticle size measured by DLS.

Particle type	Aerosil 90	Aerosil 150	Aerosil 380
Size	20 nm [366, 367]	14 nm [367]	7 nm [365]

Table 5.2: Three types of nanoparticle size reported in literature.

The difference between DLS result and literature could be caused by the aggregation of nanoparticles. The nanoparticles showed dynamic aggregation behaviour, and it has been observed with dynamic formed and broke apart [368]. The van der Waals force, the electrostatic interactions and the capillarity due to liquid bridging play essential roles in the particles aggregation [368, 369]. According to the interfacial force boundary layer theory [370, 371], the colloidal nanoparticles were affected by the random Brownian diffusion and interaction energy at the same time. For the much smaller scale, the random kinetic energy leads to the behaviour of aggregation [369].

5.3.2 Tribological property

For studying nanoparticle microscaled tribological behaviour, silica nanoparticles of Aerosil 150 were prepared as 1.0%, 2.5% and 5.0% for the initial measurement. The comparison of CoF values was tested with a 3 mm diameter spherical glass ball on porous PDMS and PDMS coated with PVA (10:1 - 83%), which results are shown in Figure 5.3.

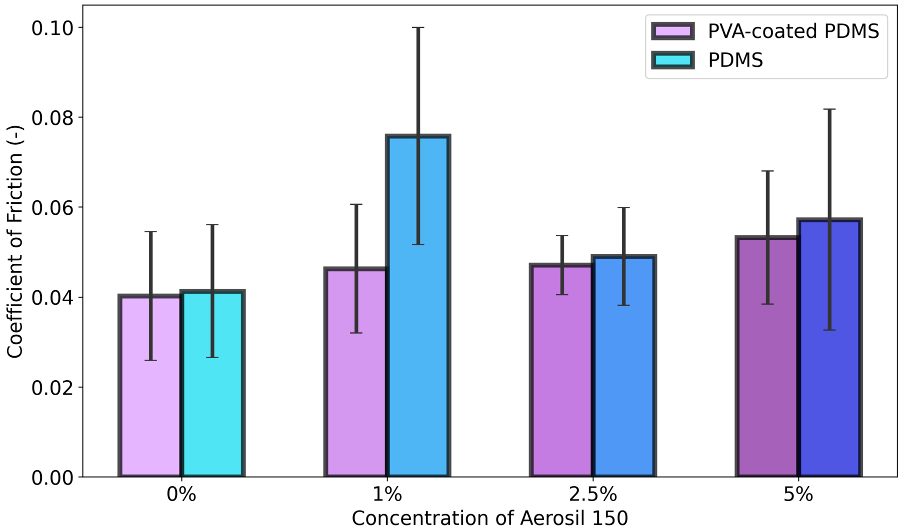

Figure 5.3: CoF as a function of the concentration of nanoparticles (1.0%, 2.5%, and 5.0% of Aerosil 150) on porous PDMS and PVA-coated PDMS.

Figure 5.3 shows that pure PDMS matrices have higher CoF than PVA-coated PDMS, which shows the same tribological behaviour as previous work in Chapter 4. Compared with the CoF of different concentrations in the same series, Figure 5.3 shows that when the concentration of nanoparticles is equal to and higher than 1.0%, the CoF of both porous PDMS and PVA-coated PDMS were higher than the CoF without particles added. However, this is contrary to what was observed in most of the previous studies that the nanofluids should provide a decreasing behaviour for lubrication [359, 372]. In this case, the present work introduced 0.01%, 0.1%, 0.5% as supplement, the result is shown in Figure 5.4.

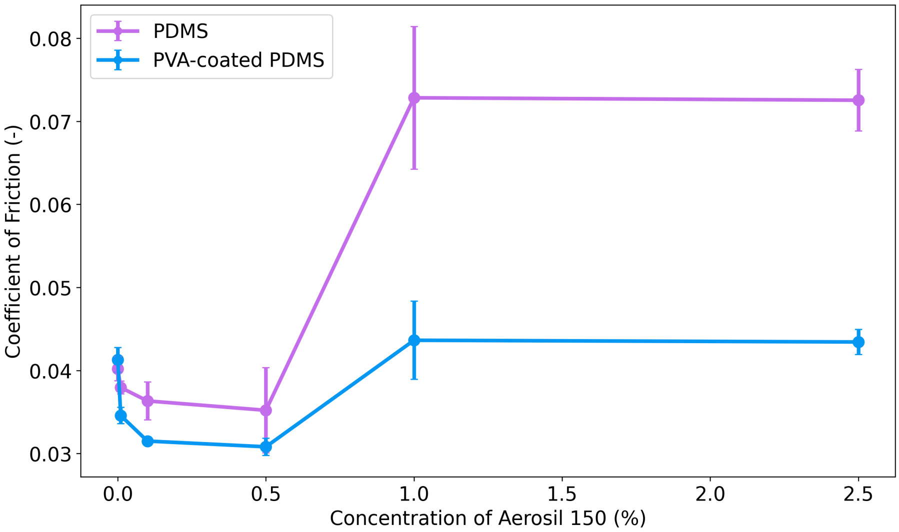

Figure 5.4: CoF as a function of the concentration of nanoparticles (0.01%, 0.1%, 0.5%, 1%, and 2.5% of Aerosil 150) on porous PDMS and PVA-coated PDMS.

The supplement of a low nanoparticle concentration solution was measured at the same substrates and conditions. The Figure 5.4 shows that both porous PDMS and PVA friction coefficient significantly decreased while the nanoparticles were added to the solution, even at 0.01% of concentration. Then the decrease of CoF is not significant as the first-time nanoparticles were added. The CoF decrease rate slowed down from 0.1% to 0.5%. In both porous PDMS and PVA-coated PDMS measurements, the CoF increased after the concentration came to higher than 0.5%.

In addition, five concentrations between 0.1 mg ml^{-1} to 3.0 mg ml^{-1} were measured by AFM in nanoscale (Figure 5.5). The measurement took place on the planar PDMS coated with PVA, which can eliminate the influence of roughness and porous surface of substrates. Similarly, with the increase of nanoparticle concentrations, the CoF shows a decreasing tendency at the primary adding, and then the CoF values increase after the concentration reaches 1.0%.

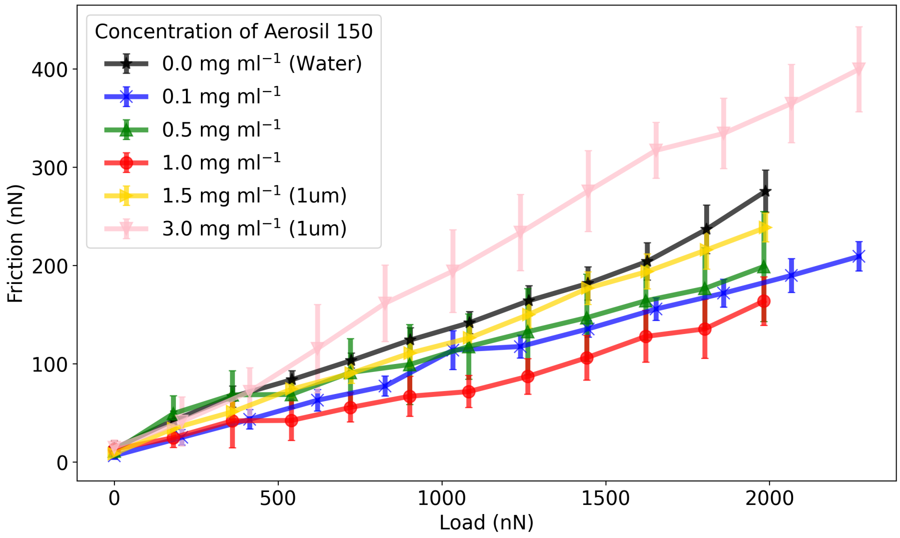

(a)

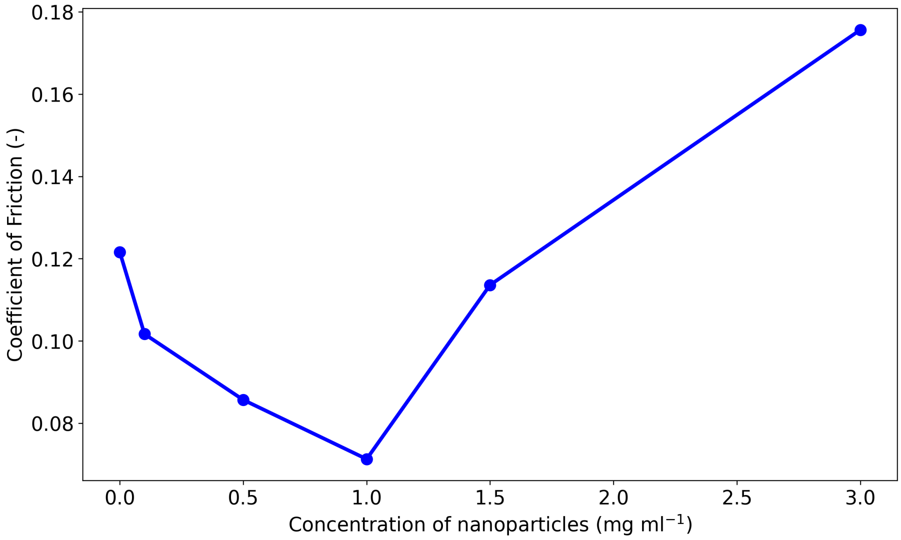

(b)

Figure 5.5: (a) Raw data of AFM friction force measurement on planar PDMS coated with PVA, the maximum load applied is 2500 nN. (b) CoF values calculated from the raw data.

Usually, in the models of particle lubrication from previous work, nanoparticles are described that the increase of nanoparticle concentration can decrease the CoF. In the present study, the contribution of nanoparticles to lubrication shows under a specific concentration, and the concentration higher than the specific value could be observed with negative effect on lubrication. In fact, a study showed the same tendency of particle concentration against friction coefficient as the present work [373]. Therefore, although the critical concentration points were different because of the different types of solvent and substrate used, the CoF tendency of colloidal nanoparticles lubrication can be confirmed as decrease at first and following with increase.

Based on the four effects of CoF, the rising concentration engaged the more particles attached to the surface and provided the rolling movement, which could benefit the sliding [372, 374]. However, when the concentration came to the limitation concentration, the surface would fully occupy the space area of the surface, after the collapse full filled by nanoparticles, the stack of particles would pile over the surface, even where it used to be smooth, the excess of particles on the surface created the rougher surface after the collapse filled, which explained the rising of CoF with further adding of nanoparticles. Although the microtribometer substrate was porous PDMS and AFM used planar PDMS, both CoF results showed a critical concentration with the lowest CoF, which means the full occupation of nanoparticle on the surface could occur on both planar and porous scaffold. Considered that the OA cartilage has a porous surface and porous scaffold, therefore, the concentration of nanoparticles for the OA injection should not only consider the quantity demanded by the drug delivery systems. In addition, it is worth testing the best concentration that best contributes to the cartilage lubrication, which could decrease the CoF and relieve the pain from OA patients' joints.

To study the size effect of the particle solution lubrication, 1.0% of three kinds of nanoparticles were applied in the measurement. The results and the CoF against size are shown in Figure 5.6.

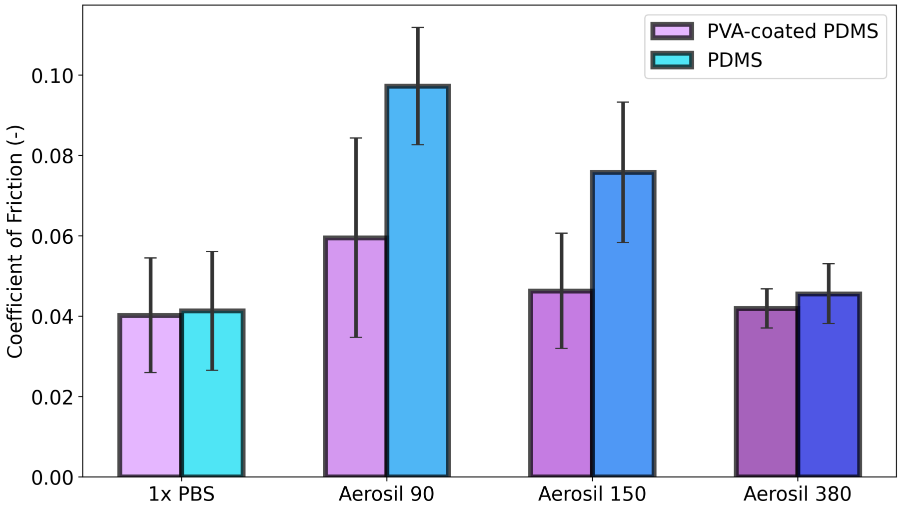

(a)

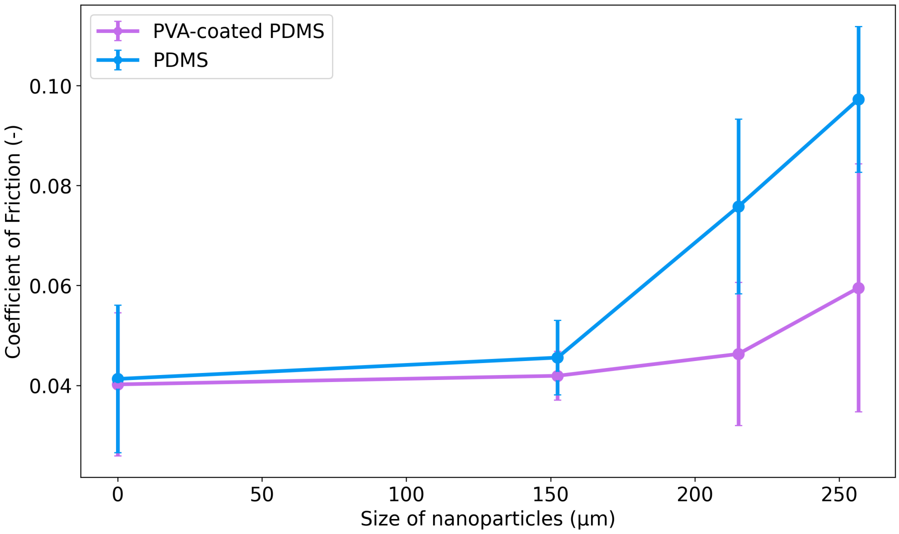

(b)

Figure 5.6: (a) CoF as a function of the types of silica nanoparticle in porous PDMS and porous PVA-coated PDMS. (b) The silica nanoparticle size against the CoF on porous PDMS and porous PDMS coated with PVA.

By adding 1.0% of nanoparticles of Aerosil 90, 150 and 380, the CoF was higher than the pure PBS as solvent. The porous PDMS shows higher CoF than PVA-coated PDMS, which was consistent with what was observed in the previous results. In the meanwhile, the CoF shows the correlation with particle size, which is shown in Figure 5.6 that the larger sized nanoparticle shows higher CoF. According to a model of particles, lubrication was the same as what was reported in the previous study [360]. When the nanoparticles were not fully covered the contact surface at the same concentration, numbers of smaller nanoparticles distributed between the contact area are more than larger nanoparticles. At the same time, the volume per cent increases, and more particles could be suspended in the lubrication system, which played a better rolling effect with smaller actual contact areas [360]. Moreover, smaller particles have a better mending effect on filling in the fissure and grooves on the rough surface. Therefore, the smaller particle size should be able to decrease the CoF of the lubrication.

The load applied is vital for cartilage, which supports the body in the joints. The 30 g load applied in the present work was increased to 50 g and repeated on the 10:1 - 83% porous PDMS coated with PVA. The results are shown in Figure 5.7. It is significant that the higher normal load applied on the PDMS matrices results in higher CoF.

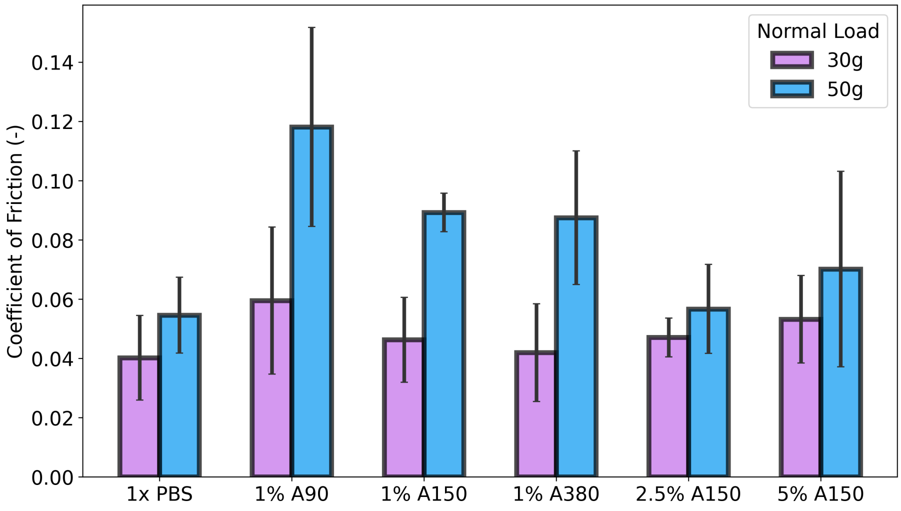

Figure 5.7: CoF as a function of the load applied on porous PDMS and porous PVA-coated PDMS, different types and concentrations of silica nanoparticle of Aerosil 150 were applied in the tests.

The reduced Young's modulus E_{total} is calculated by the equation below:

$$\frac{1}{E_{total}} = \frac{3}{4}\left(\frac{1-{v_1}^2}{E_1} + \frac{1-{v_2}^2}{E_2}\right) \tag{5.1}$$

where the v_1 and v_2 were the Poisson's ratio of the glass ball and PDMS, and E_1 and E_2 were the Young's modulus of the glass ball and PDMS. From the fundamental borosilicate parameters and PDMS parameters, the Poisson's ratio of glass is 0.2 [375], the Poisson's ratio of PDMS is 0.5 [138], E_1 and E_2 were reported as 64 GPa [375] and 2.8 MPa. Hence, the reduced Young's modulus in the present work was 4.98 MPa.

Contact area radius r and contact area A could be expressed as

$$r = \sqrt[3]{\frac{RF}{E_{total}}} \tag{5.2}$$

$$A = \pi * r^2 \tag{5.3}$$

where the R was the radius of the glass ball applied on the porous PDMS, which was 1.5 mm. The F is the normal load applied on the sample, as the load applied was 30 g and 50 g, and the normal load was 0.294 N and 0.490 N. Therefore, the approximate contact pressure P should be

$$P = \frac{F}{A} \tag{5.4}$$

Figure 5.8(a) shows that the correlation between the contact area and the normal load based on the present work. The increase of normal load will increase the contact area between the tip and sample. For example, the 10:1 - 77% porous PDMS contact area increases from 6.24×10^{-7} m^2 to 8.78×10^{-7} m^2 when the load raised from 30 g to 50 g, and the contact pressure of 50 g increased from 0.47 MPa at 30 g to 0.56 MPa. By increasing the load applied on the samples, the contact pressure increases in the present work even though the contact area increased. The contact pressure is increased 19.1% when the weight increased from 30 g to 50 g. In fact, a similar situation has been reported that the higher load increased the CoF on an uncoated and a hydrogel coated PDMS surface [376].

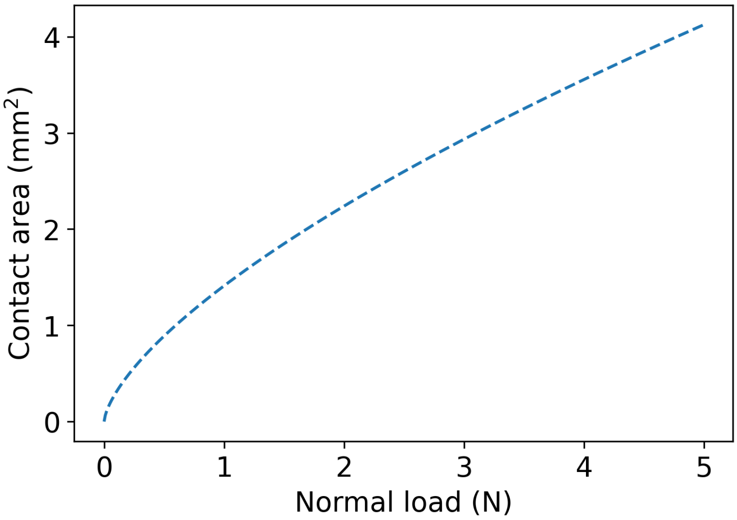

(a)

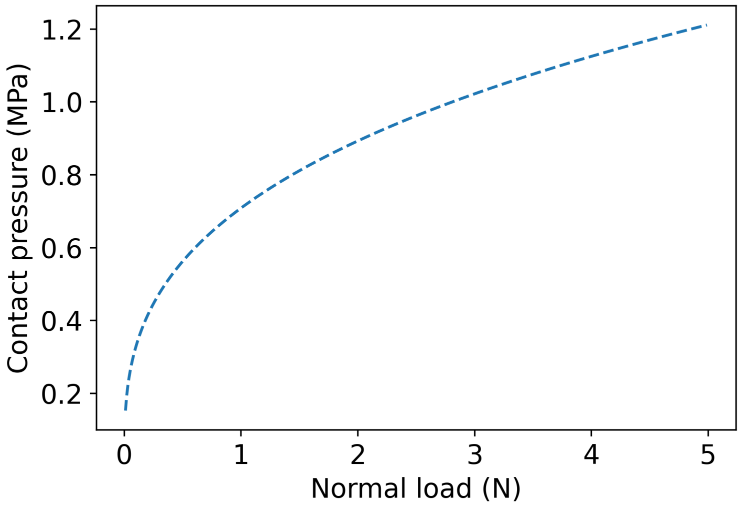

(b)

Figure 5.8: The models of (a) contact area and (b) contact pressure on the surface against the normal load applied on the 10:1 - 83% porous PDMS matrix according to the microtribometer measurement in the present work.

According to the equations above, a correlation diagram can be drawn for the 10:1 - 83% porous PDMS used in the present work, as Figure 5.8(b) shows. It could be seen in the present model that with the increase of the normal load on the spherical glass, the higher contact pressure would apply on the substrate. Based on the basic lubrication knowledge, the higher contact pressure would cause a higher CoF at low sliding speed. Moreover, at a high velocity, the lubrication mode could be turned from the hydrodynamic mode to the boundary mode, which could increase the lubrication of the samples [377].

Figure 5.9 shows the CoF as a function of the sliding velocity. PBS buffer, silica nanoparticles of Aerosil 90, Aerosil 150, and Aerosil 380 were used in the tests. The velocities applied in the tests were 0.1 mm s^{-1}, 0.5 mm s^{-1}, 1.0 mm s^{-1}, 2.0 mm s^{-1}, 10.0 mm s^{-1} and 20.0 mm s^{-1}. As shown in Figure 5.9, the increase of sliding velocity decreases the CoF rapidly. The sliding speed against CoF was reported the negative correlation on different substrate, included rigidity material such as steel [378] and aluminium [379], polymer materials such as poly(methyl methacrylate) (PMMA) and low-density polyethylene (LDPE) [377]. According to the lubrication behaviour described by the Stribeck curve, the increased speed turned the friction from boundary lubrication to mix lubrication to the hydrodynamic lubrication. The friction will be shifted from direct contact to the hydrodynamic pressure. During the hydrodynamic state, a layer of the film will be created to separate the surface contact, which performed as decreased the CoF [380, 381].

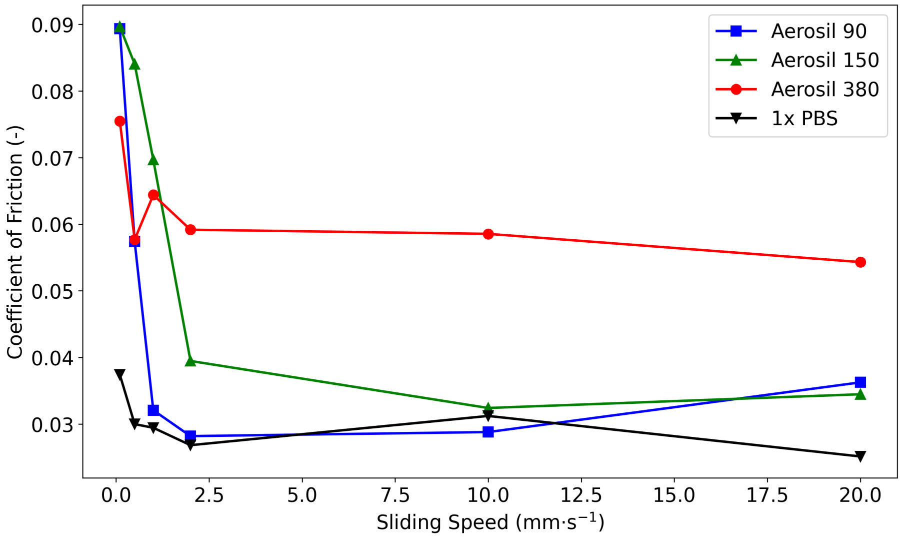

Figure 5.9: CoF as a function of the sliding speed on porous PDMS and porous PVA-coated PDMS, which includes PBS buffer, 1.0% of Aerosil 90, 1.0% of Aerosil 150, and 1.0% of Aerosil 380.

According to previous studies of nanofluid lubricants, two properties of nanoparticle-based lubricants influenced the CoF on the substrate, which are viscosity and surface physical effects.

The Stribeck curve x-axis is the Hersey number which is described as ηN/P, where the η is the fluid viscosity, N is the fluid entrainment speed, and P is the normal load applied on the per unit length of contact. In addition, the viscosity of fluid was reported correlated with the velocity and the concentration of fluid, therefore, to convince the influence of the velocity and normal load influence of coefficient, the viscosity should be excluded from the lubrication system.

In this case, a supplement work of rheology of solutions was measured by increasing the shear rate from 200 s^{-1} to 1500 s^{-1}, six concentrations of nanoparticle of Aerosil 150 were used in rheology measurement.

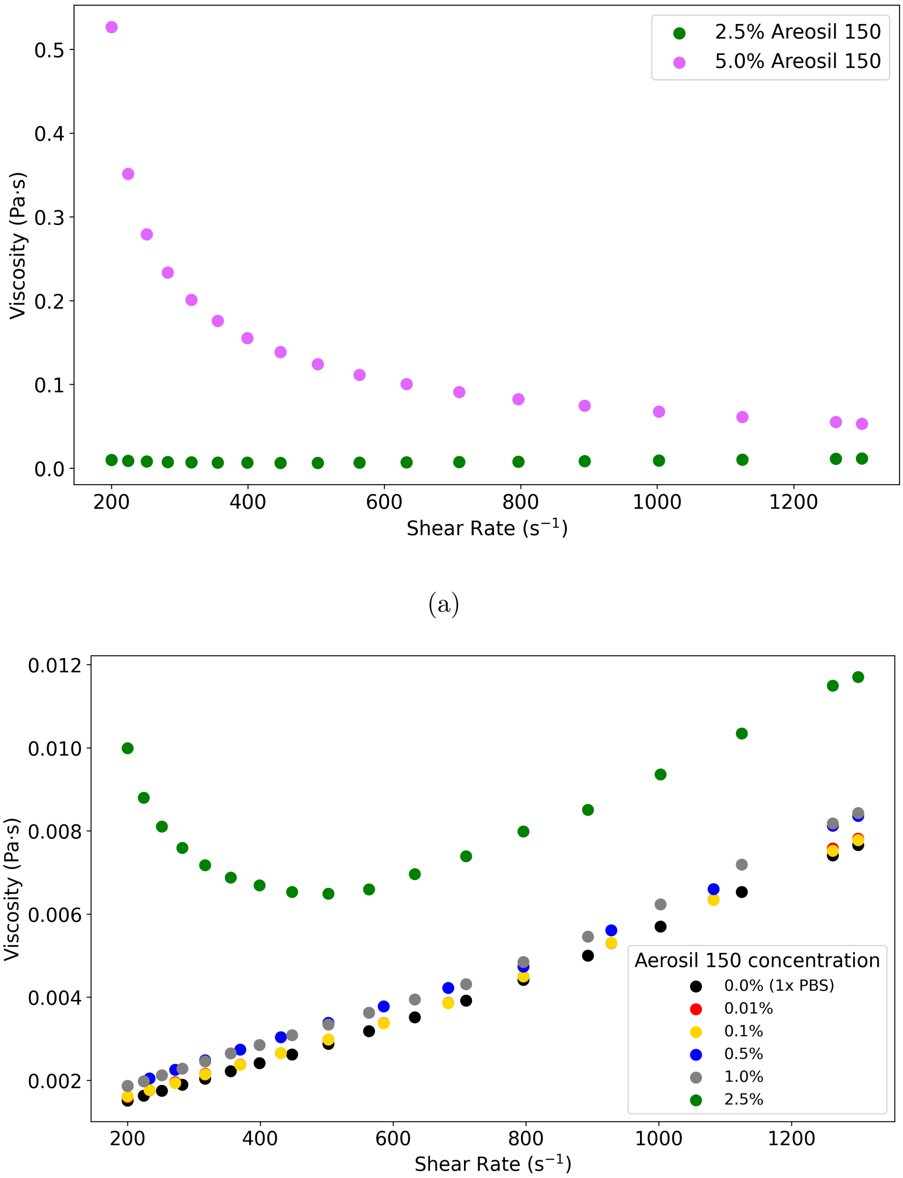

(a)

(b)

Figure 5.10: Rheology curves of silica nanoparticle (Aerosil 150) at different concentrations. (a) Rheology curves of 2.5% and 5.0% of Aerosil 150; (b) Rheology curves of PBS buffer, 0.01%, 0.1%, 0.5%, 0.01%, 1.0%, and 2.5% of Aerosil 150.

Figure 5.10 shows the rheological curves of silica nanoparticle of Aerosil 150. At 200 s^{-1}, the PBS curve shows the lowest viscosity at 1.51 cP, and the concentration of 5.0%

shows the highest viscosity, which is 53.05 cP. At 1500 s^{-1}, the highest viscosity is at the curve of concentration of 5.0% as 526.62 cP. The change of viscosity values is too low to influence the nanoparticle tribological behaviour. From a previous study, the viscosity of less than 50 cP would be concluded as low viscosity solution [382]. In addition, when the normal load applied was 30g in the present work and assume the shear rate at 1500 s^{-1}, the biggest Hersey number is 1.68×10^{-4} at 5%, where the lowest Hersey number is 4.8 $\times 10^{-6}$ at PBS buffer. The order of magnitudes of Hersey number is too low to influence the lubrication behaviour. Therefore, the viscosity of fluid used in the present project could be ignored as low viscosity solution, and the conclusions of the influence of concentration, normal load, and velocity of silica nanoparticle lubricant could be convinced based on the variation changed in the tests.

The study by Zheng et al. [383] showed the HA-based nanospheres grafted with 2-methacryloyloxyethyl phosphocholine (MPC), the friction of nanoparticles was tested on the silicon wafer. Compared with distilled water, HA and HA-MPC nanoparticles, the CoF decreased from 0.10 (water) to 0.03 (HA-MPC). The study of concentration of solution showed the increase of nanoparticle ratio of solution decreased the CoF [383]. The CoF increased while the sliding frequency increased from 1 Hz to 4 Hz, which was explained by the shear-thinning of the HA backbone in nanoparticles. The increase of load showed the much stabilised CoF values with 10 minutes duration. Another study by Rudge et al. [384] showed the CoF on PDMS by lubricated with microparticles, the work studied in the ambient environment, which presented the influence of particles of lubrication directly. The study changed the sliding velocity, particle size, normal load applied, and surface coverage in the lubrication system. According to the study by Rudge et al., there were four conclusions as the results. i) The increase of normal load on the particles increased CoF, ii) the increase of surface coverage of nanoparticles decreased CoF, iii) the increase of sliding speed showed the increase of CoF, and iv) the increase of particle size increased the contact radius and resulted in the decrease of friction. These conclusions are consistent with the results in the present work.

Based on the previous studies, it could be convinced that in the particle lubricating system, the increase of particle size could increase the contact radius and area on the substrate, which decreased the CoF of the system. And the increase of load increased the CoF, which increased the contact pressure calculated and presented by Figure 5.7 and Figure 5.8. Even though most of studies showed that the increase of sliding speed increased the CoF in their lubrication system, the Stribeck curve could explain that the lubrication system in Zheng et al. [383] was the hydrodynamic lubrication that the sliding speed had a positive correlation with the CoF.

The increase of particle coverage shows the decrease of CoF to the lubrication, which exhibits the surface influence of surface contact effects with particle rolling. With the increase of particle coverage on the surface, a friction model with dry particles correlated CoF with the coverage film and substrate surface. The equation showed as below [385]:

$$u = X * u_{film} + (1 - X) * u_{surface} \tag{5.5}$$

where the X is the percentage of surface covered with particles, u_{film} and $u_{surface}$ CoF of substrate without particle covered. Moreover, the rolling and film effects has been described that the particles film decrease the CoF from the original surface, the increase of particle on the surface could explain the decrease of surface CoF. The pore size of the porous PDMS substrate in the present work was about 200 µm in diameter, and the diameter of aggregated nanoparticles could only approach hundreds of nanometres. As the solution was sonicated before the tribological test, the sufficient liquid used in the tests should evenly disperse the nanoparticles inside the pores and on the surface. Therefore, the surface coverage of nanoparticles could affect the lubrication system with the rolling and film protective effects on the surface of porous PDMS.

5.4 Summary

The silica nanoparticles were measured on the porous PDMS and PVA-coated PDMS. After excluding the influence of viscosity of the nanofluid, the conclusion could be summarised based on the results of the CoF measured. The CoF on the porous structure has been confirmed to be influenced by the particle size, concentration of nanoparticles, sliding speed, and the load applied on the substrate. The concentration was observed with the optimum concentration, which provided the lowest CoF. In the present study, the silica nanoparticles of Aerosil 150 showed the best concentration at 0.5% at the microscaled lubrication system and 1.0% at the nanoscaled. With the size of nanoparticles decreased from 256.00 ± 4.82 nm to 152.00 ± 1.86 nm, the CoF of PVA-coated porous PDMS substrate decreased from 0.59 ± 0.02 to 0.41 ± 0.005, which showed the smaller particle size has lower CoF than larger particles. By increasing the normal load from 0.294 N to 0.490 N, the higher load applied on the surface increased the contact pressure and increased the CoF. By increasing the sliding velocity from 0.1 mm s^{-1} to 20.0 mm s^{-1}, the increase of sliding velocity decreased the CoF of the substrate. The silica particle system provided the method to discover the best conditions for the different intra-articular injection formulations for the OA drug delivery treatment, which would provide good lubrication with the drug-loaded delivery systems.

Chapter Six

Development of nanogel based lubricant function as IAI formulation on OA cartilage

6.1 Introduction

Intra-articular injection (IAI) is one of the method used clinically to relieve the pain of osteoarthritis (OA) joints, which is developed from intra-articular steroid injections [386]. As the intra-articular space between the healthy cartilage is filled by the synovial membrane and synovial fluid [387, 388], intra-articular injection of high-dose viscosupplements was developed from IAI as a physical intervention [386]. Besides viscosupplements, the glucocorticoids, non-steroidal anti-inflammatory drugs, and selective COX-2 enzyme inhibitors [389] are also the popular drugs for OA injection. However, the exposed drugs show the disadvantages of short retention and adverse reactions [389]. To increase drug retention capacity and reduce adverse reactions, the drug delivery system (DDS) was developed with slow release effect [389–391], which solved the problem of rapid clearance with suspension and binding of drug carriers [390, 392]. According to the previous DDSs studies, drugs residence time in the joint is determined by the size: the macromolecules carriers (>10 kDa) usually escaped through lymphatic vessels within months, and the fastest carriers (<10 kDa) could be cleaned in hours by blood vessels [393]. Furthermore, the release of drug amount was usually limited by the particles, and it was less than required for the OA treatment. Therefore, multiple injections were required in the DDSs therapy. The drug carrier performance in DDS is affected by lots of factors, such as size, shape, surface charge, hydrophobicity, roughness, and rigidity of drug carriers [394]. Therefore, different types and methodology were applied for the development of DDS drug carriers. For instance, hydrogel, microparticles and nanoparticles functionalised with polymer brushes grafted were used for the delivery system [395], and the surface of carriers was attempted to be coated with different groups, such as -NH_2, -COOH and -SH [394].

Amongst the carrier used in DDS, nanoparticle is one of the most common used DDS for IAI, which has the advantage of safety, easy modification, and the function of sustained-release [390]. On the other hand, biodegradable materials have been applied for injection studies, because of the better drug released applications than traditional medicine. For example, hydrogel particle (or nanogel) is a type of crosslinked polymer which was widely used for *in vivo* injection [12, 396]. The nanogel is formed by three-dimensional architecture, and the network of nanogel provides excellent capacity for holding a large amount of water [397]. In the drug-loaded systems, the effective water content of nanogel provides similar water contents with biological tissue approximate 70% or higher, hence the hydrogel particles have decent biocompatible property for *in vivo* applications [398]. Furthermore, nanogel scaffolds can afford drugs up to 50% of its weight, which is much higher than other nanoparticles [399]. Compared with other delivery carriers, nanogel presents the advantages of respond for the external stimuli, including swelling, permeability, viscoelasticity, and hydrophobicity [400]. Due to the specific physicochemical structure, nanogel can be designed with other specific characteristics. By controlling the crosslinking pore size, density and degradation kinetics, nanogel can be a controllable material for the drug delivery system [401]. For instance, i) the deformability enhances the binding and retention capacity of nanogel in tissue, ii) the nanogel crosslinked structure has potential to prolong the circulation time by enhancing the stability, iii) highly hydrophilic interior network of hydrogel has potential to protect hydrophilic compounds with bio-macromolecule drug or small-molecule, and iv) modular drug loading and release profile can significant improve efficiency of drug loading, which reduces the drug toxicity and side effects at the same time [400].

Based on the traditional chemical and physical synthesis pathways to synthesised nanogel, a recent work by Emanuele et al. [402] used the method of microfluidics in synthesis, which is able to accurately control the nanogel during at the microscale by mixing and physical processes. In addition, the microfluidic synthesis technology can customise the nanosystem in surface properties, payload delivery, release profile, polydispersity, and size [403]. The most prolonged drug release profile has been delayed to approximate to 300 hours, which was usually reported as lower than 100 hours. With the open-source tool development and machine learning technique, the nanogel can be designed under a microfluidic platform without expertise and resources [402]. Moreover, including the advantages of nanogel and microfluidics technique, the nanogels has the potential for encapsulation of proteins cells, or antibodies with size-controlled. In this way, the hyaluronic acid (HA) based nanogel synthesised by microfluid technique was introduced in the present work.

Besides the wide range of mechanical properties of OA cartilage, the pore size of healthy and OA cartilage was reported. For adult healthy cartilage tissue, the average pore size within the extracellular matrix (ECM) is around 6.0 nm [16, 404–406], and another study about unhealthy cartilage pore size resulted in 10.71 ± 6.45 nm [407]. In addition, the early-stage OA cartilage has been reported with increased porosity [408–410]. In a piece of research by Wen et al. [411], the fibrous structure was shown in all regions of cartilage, and

AFM captured individual collagen fibrils from articular cartilage [411]. Hence, it is validated that healthy cartilage was content with tight fibrils and OA cartilage composed of loosely collagen fibrils. The fibrous structure was also captured in the studies by Ghosh et al. [247] and Hughes et al. [412], in which AFM images showed the fibrils on the surface.

As the study in chapter 5 showed that the silica nanoparticle solutions improved the lubrication behaviour of porous structures, more variety of nanogel nanoparticles were introduced in the present work to develop the tribological influence factors by different types of nanoparticles. This chapter studied on how different types of nanogels affect the lubrication behaviour, and the study compared the friction effects on the polymer substrate and human cartilage tissue. Moreover, human OA articular cartilage was collected in this project, this chapter exhibited the morphology of cartilage surface and measured the mechanical and tribological properties of cartilage tissue.

6.2 Materials and methods

6.2.1 Materials

Human OA cartilage samples were collected from patients undergoing joint replacement surgery at the Royal Orthopaedic Hospital Birmingham (NRES 16/SS-0172), and processed at the Institute of Inflammation and Ageing (Queen Elisabeth hospital, Birmingham, UK). Dulbecco's Modified Eagle Medium (DMEM) was purchased from Sigma-Aldrich (Dorset, UK). Four types of nanogel samples were provided by the Emanuele Mauria's research group. Phosphate-buffered saline (PBS) tablets were purchased from Fisher Scientific (Loughborough, UK). Hyaluronic acid was purchased from Bloomage Freda Biopharm CO., LTD.

6.2.2 Preparation of nanogel solution

The preparation method of nanogel used in the present work is shown in Figure 6.1, which is particularly explained in a previous work [413]. The nanogel was synthesised based on HA and linear polyethyleneimine (LPEI) . The coupling agents N-(3-dimethylaminopropyl)-N'-ethylcarbodiimide hydrochloride (EDC) and nhydroxysuccinimide (NHS) were added into the HA solutions, and the LPEI solution was diluted in HCl. The dichloromethane (DCM) was added to the activated HA solution to be sonicated. Then, the LPEI solution was added into the system followed with sonication and emulsion. The nanogel sample was collected by freeze-dried after the evaporation of organic solvent, which was sponge-like solid. Based on the synthesis condition differences, the nanogels were named from AEL 01 to AEL 04, and the differences of nanogel preparation conditions were listed in the Table 6.1. The sponge-like nanogel solid was diluted to 3.0 mg ml^{-1} by distilled water and stored at 4 °C for preparation.

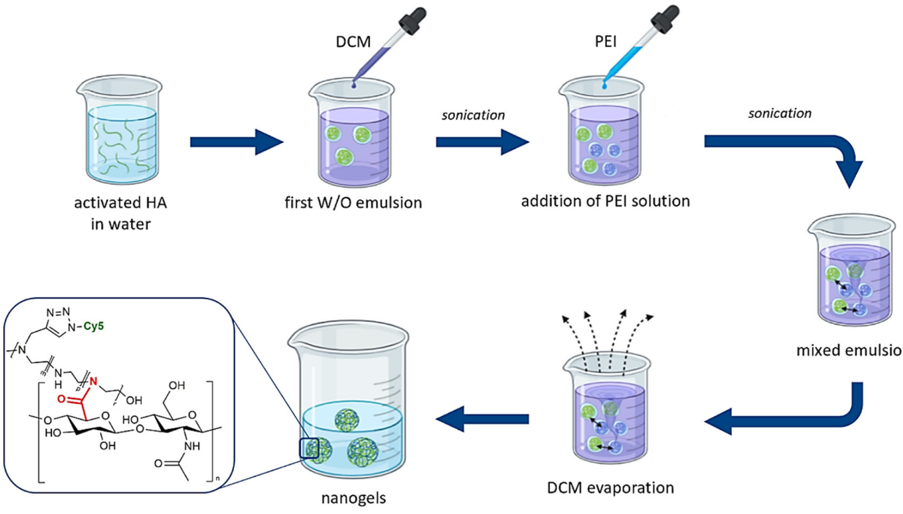

Figure 6.1: Schematic diagram of synthesis procedure of nanogels through the mixed emulsion/evaporation technique (MEET) [413].

Name	Type of nanogels (synthesise conditions)
AEL 01	Nanoprecipitation
AEL 02	Chip at 0 bar (NGs in microfluidic chip without pressure)
AEL 03	Chip at 2 bars (NGs in microfluidic chip with pressure)
AEL 04	Mixed emulsion MEET (mixed emulsion/evaporation technique) without further purification

Table 6.1: Synthesis condition differences of four types of nanogel.

6.2.3 Preparation of human OA cartilage

All cartilage samples were collected from the hip bone, the cartilage was cut from the bone by scalpels, and the cartilage pieces were stored in DMEM (Sigma-Aldrich, Dorset, UK) at 4 °C. The cartilage pieces were washed by immersed in PBS buffer before usage. The information details of cartilage sample donators are listed in the Table 6.2 below:

Sample Code	Gender	Age	BMI
MFX 412	F	66	34.57
MFX 416	F	73	31.60
MFX 417	M	71	24.51
MFX 418	F	60	23.30
MFX 420	F	76	21.14
MFX 421	M	69	34.14
MFX 422	F	73	30.04
MFX 423	M	81	33.95
MFX 430	F	76	23.15
MFX 437	F	72	24.92
MFX 438	F	75	19.78
MFX 439	M	63	33.99
MFX 440	M	68	32.53
MFX-RHH 048	M	62	30.50

Table 6.2: Donor description including gender, age, and body mass index (BMI) of the patients.

6.2.4 Cartilage morphology

Cartilage sample pieces were heated in the oven at 70 °C for 24 hours for dehydration after being washed with PBS buffer. A small flat area would be cut from dried cartilage. The cartilage measurement used the Dimension 3100 AFM with a Nanoscope III controller (Veeco Instruments Inc., Cambridge, UK), and the field-emission SEM (XL 30 ESEM-FEG, FEI, Oregon, USA). For the SEM measurement, cartilage pieces were stuck on a carbon dioxide tape and coated with sputter platinum before SEM scanning. The images were captured at 10.0 kV voltages and 500 × to 10000 × magnitude. The pore size calculation was based on the 3000x magnitude images, and the fibril calculation was based on 10000 × magnitude images. In AFM measurement, 0.32 N m^{-1} contact mode cantilever was used for images captured, and the scan size was from 5 × 5 µm to 10 × 10 µm.

6.2.5 Cartilage modulus

The Young's modulus of cartilage was measured by the indentation under the customer-build microindentation. The cartilage immersed in the PBS buffer in the microindenter sample cells, a 60 ° cone tip applied force from 0 to 0.5 N on the cartilage at the speed of 0.1 mm s^{-1}. Each patients' cartilage used three pieces in the measurement. The calculation of Young's modulus was followed by the Equation 2.11.

6.2.6 Nanogel morphology

The nanogel solution was diluted to the concentration required before experiment, then the solution was sonicated for 10 minutes at 25 °C.

Nanogel morphology was carried out using the same AFM and SEM facilities as cartilage samples. In AFM measurement, 2 µl of each type of nanogel solution was dropped on the Thermo polysine slides (Thermo Fisher Scientific, Waltham, MA). After the solution was air-dried on the slides, 0.08 N m^{-1} contact mode cantilever was used to record the morphology of nanogels, the scanned size was varied from 5 × 5 µm to 30 × 30 µm. In SEM measurement, 2 µl nanogel solution were dropped on the mica and air-dried at room temperature. The mica with dried nanogel was coated with sputter platinum before SEM scanning. The SEM was scanned under the SE (secondary electrons) detection mode at 10.0 kV voltage and magnitude was varied from 3000 × to 25000 ×. The software Gwyddion was used for AFM image analysis, and the software ImageJ was used for SEM particle size measurement.

6.2.7 Tribological measurement of PVA-coated PDMS

The planar polydimethylsiloxane (PDMS) coated with PVA friction was measured on the Multimode Nanoscope III AFM (Veeco, CA), nanogel solution was diluted to 3.0 mg ml^{-1} and 1.5 mg ml^{-1} in distilled water. 10 µl of nanogel solution was dropped on a 10 × 10 mm PVA-coated PDMS as substrate, the measurement started after the AFM signal was stable. 40 N m^{-1} cantilever glued with a 4 µm radius colloidal probe and applied the force from 0 nN to 2000 - 2500 nN on the PDMS coated with PVA, the highest force applied varied depends on the cantilever calibration discrepancy. The sliding length was 1 µm to 3 µm depending on the stability of voltage values, and the sliding velocity was 0.5 mm s^{-1}. PBS and HA (preparation corresponded concentration) were measured in the same condition as the benchmark.

6.2.8 Tribological measurement of cartilage

Cartilage tribology was measured by the microtribometer [289] and Multimode AFM, three pieces of cartilage of the same code were used for the measurement. In microtribometer measurement, the cartilage pieces were glued on plastic petri dishes and immersed in PBS buffer. 30 g load was applied with a 3 mm diameter glass ball on the cartilage. The glass ball slid 10 mm length at the speed of 0.5 mm s^{-1}. The AFM tribological measurement used 40 N m^{-1} cantilever with a 4 µm radius borosilicate tip. PBS buffer, 0.1 mg ml^{-1} AEL 04 and 0.1 mg ml^{-1} Aerosil 150 were used as lubricant in the AFM measurement. All parameters applied were same as nanogel AFM tribological measurement.

6.3 Results and discussion

6.3.1 OA cartilage surface morphology

Human OA cartilage was collected from the joint replacement surgery and processed by the Institute of Inflammation and Ageing. The collected cartilage was stored in the DMEM at 4 °C. For AFM measurement, the cartilage was dried after being washed by PBS. Contact mode cantilever (0.32 N m^{-1}) was applied on surface morphology measurement. The height image and 3D morphology image are shown in Figure 6.2.

In Figure 6.2(a), different layers can be observed on the cartilage surface, the left part of image shows a long line with shadow, which could be told as the broken of one piece of cartilage layer, similar layers edge structure can be observed on the top-middle of the image as well. Although the pore structure was widely reported exist in cartilage, the present AFM work did not capture any pore morphology on the surface. Lots of fragment pieces were observed in AFM images, such as the bottom of Figure 6.2(a) and mid-right of Figure 6.2(b), the fragments are distributed or gathered on the surface. Considered to the compositions of cartilage, the pieces can be considered as the broken cartilage and polysaccharide substance. According to the AFM images captured in the previous studies [247, 414], the porous structure was difficult to be observed in AFM images. The surface of cartilage usually showed as rough and irregular surface but unbroken, in which layers structure were challenging to be exhibited on the surface either. It was highly like the fragments suspended in the aqueous by the moving of the cantilever. Therefore, the dried cartilage AFM images sacrificed the aggrecan fibril details on the surface but showed more details about the fragments' morphology [415]. In Figure 6.2(c), the 3D image shows that the cartilage surface was out of flatness, the planar surface can not be captured from any part of planar surface. Quantitatively, the root mean square height S_q of cartilage surface is 0.157 ± 0.032 µm, which illustrates that the surface roughness of cartilage is rougher than a smooth and planar surface. The roughen surface of OA cartilage was widely reported, such as a similar AFM study by Lee et al. [70] captured with a larger scale showed the stage 3 of OA articular cartilage R_q is 0.533 ± 0.200 µm.

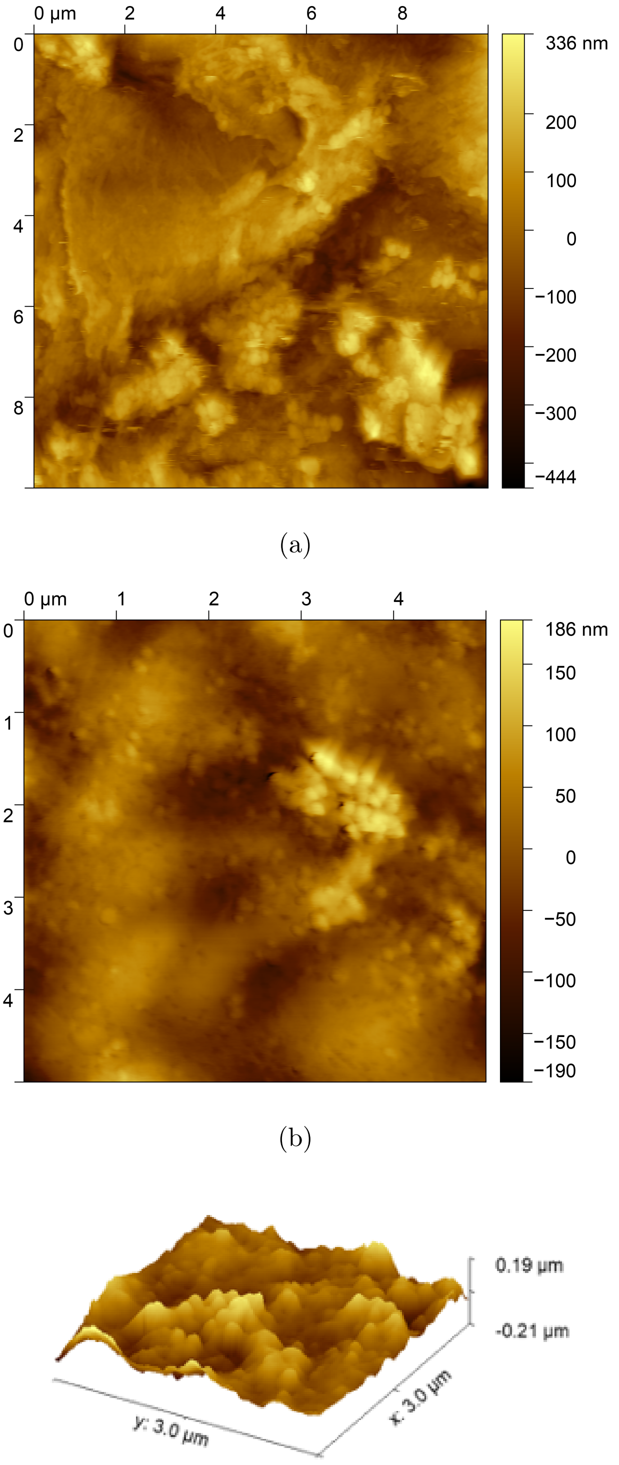

(a)

(b)

(c)

Figure 6.2: AFM images of human OA cartilage captured in ambient. a) Surface of sample MFX 412; b) Surface of sample MFX 416; c) 3D image of sample MFX 416.

Before SEM tests, the cartilage specimens were fully dehydrated and coated by platinum. Environmental SEM was used for capturing cartilage surface, and the result images are shown in Figure 6.3. It is well established that cartilage is constructed by the crosslinked collagen, which forms to the highly porous structure [248, 416, 417]. In Figure 6.3(a), the pore structure can be observed clearly on the cartilage surface. The pores are in a wide range of sizes and distributed evenly on the surface rather than gathering in any specific area of cartilage. In the study by Simon et al. [418], the unworn and worn cartilage was measured under the SEM and ESEM, the healthy cartilage surface showed smooth and planar morphology, and a few numbers of small pores and small particles could be observed on the surface, which was the evidence of sub-surface chondrocyte collapse was the fixation results could be seen. In worn cartilage images, more pores were shown on the surface than healthy cartilage, and the pore size was larger than the healthy cartilage surface [418]. Although the pores were observable in SEM images, the structure of the pore could not be observed in AFM images, which is same as what has been captured in the present work.

Figure 6.3(b) captured the edge of cartilage specimen, which is the cut section of cartilage. The fibrous structure can be easily captured in most of section part in the present SEM study, which exhibited and proved the crosslinking structure of cartilage. Furthermore, the surface of cartilage show cracks due to the high voltage electron beams as Figure 6.3(c). The cracking process displayed the structure of the fibrils with breaking continuously, and the pore structure could be observed formed by the fibrils under the valley. This can also prove that the pore structure is not only existed on the surface of the cartilage tissue, but also the whole structure. One of the typical phenomena of cartilage degeneration in OA progression has been reported [419]. Some images show that the cartilage surface has fragment pieces attached. The surface became rougher and broke into pieces, and the shape of the surface was shown as scales, which was observed as Figure 6.2 and Figure 6.3 shown. In a previous study, similar fragment pieces were found on early OA cartilage SEM as well, such as the study by Desrochers et al. [420], the fragments could be observed evenly distributed on the cartilage surface, and pore structure could be observed as well.

The fibrous structures could be significantly observed in Figure 6.3(b), especially the cut section showing the stretched-out fibrils. The cut-off section shows the cartilage layers of the scaffold, which was observed in mouse cartilage and was described as sheet-like [412]. The randomly orientated collagen fibrils established the territorial matrix, and the interterritorial matrix has a parallel with the layers of the territorial matrix. Even though the fibril has orientated direction, it was challenging to find an overall direction as orientation [412].

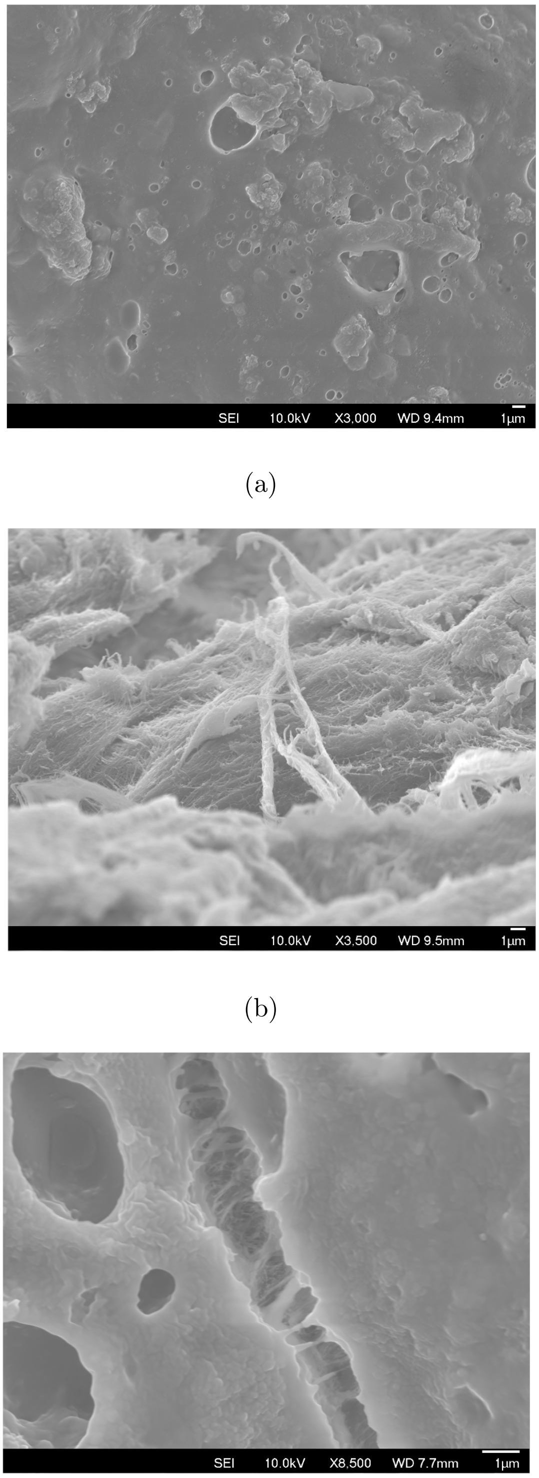

(a)

(b)

(c)

Figure 6.3: SEM images of human OA cartilage. (a) Surface of sample MFX 416; (b) cut-edge of sample MFX 440; (c) crack torn exhibited on the cartilage surface during the SEM images test on MFX 418.

In SEM images, two different characteristics of pores were observed on the cartilage surface, which is shown in Figure 6.4. The tiny pores usually display a circular shape (Figure 6.4(a)), and the surface around the tiny pores usually looks flat and relatively smooth. The large pores usually show an irregular shape (Figure 6.4(b)), and it is challenging to observe the planar surface surrounding the large pores, the irregular pores were usually one closely next. In fact, these two types of pore existed in the same sample in different areas, such as MFX 438 and MFX 440.

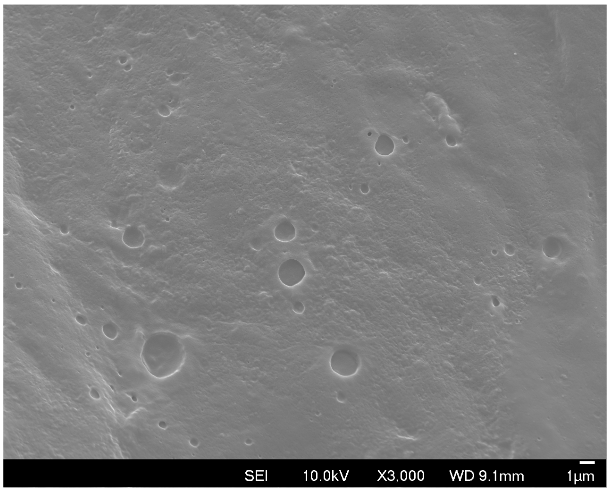

(a)

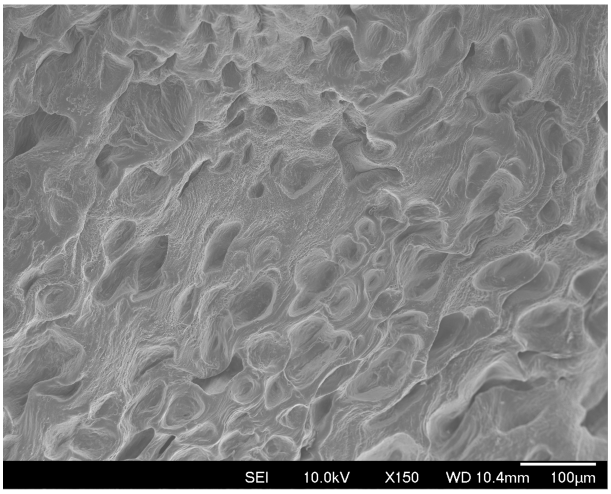

(b)

Figure 6.4: Two types of pores morphology observed on human cartilage in SEM images: (a) the small pores on the surface of MFX 438, (b) the large pores on the surface of MFX 438.

The sizes for two different pores are displayed in Figure 6.5(a) and (b). The small pore sizes are from 0.267 ± 0.138 µm to 1.691 ± 0.866 µm, and the mean average size of the small pore is 0.947 ± 0.556 µm; the large pore size are from 2.510 ± 0.849 µm to 83.986 ± 32.493 µm, and the mean average size of the large pore is 25.208 µm. The wide difference between the pore size values illustrates that these are two different kinds of tissue construct. Compared to the cartilage SEM images in previous studies, the pore size was usually reported from several to dozens of nanometres. The morphology exhibited in other research is similar to tiny pores on the cartilage surface. On the healthy cartilage, the sub-surface chondrocyte collapse of the thin amorphous surface layer causes the healthy cartilage to show a similar shape [418]. Therefore, the smaller pores could be suggested as the pore construct of cartilage tissue. As the range of pores was from hundreds of nanometres to around 1.5 µm, the nanoparticle whose size is smaller than one micrometre is better to be introduced for the drug delivery to the cartilage interior. Even though the scales and cracks were observed on the early OA cartilage surface, the morphology of pores was in regular shape and not as shown in Figure 6.4(b). There are two ideas of the large pore formation. Because the cartilage was fully dried before the SEM test for the vacuum environment, the wrinkle could be observably after the dehydration, The large pore might be the vein of wrinkles and assumed as the pores. Another possibility is that pores of this size can only be observed at the end-stage cartilage, which was the sample collected in the present work. Moreover, Figure 6.5(c) shows the cartilage fibril width, which is in a small range. The thinnest was MFX 430 at 0.065 ± 0.025 µm, and the most expansive fibril was MFX-RHH 048 at 0.107 ± 0.022 µm [411]. Fibril structure might have the potential for further cartilage study, which is beyond the scope of the expectation of the current project.

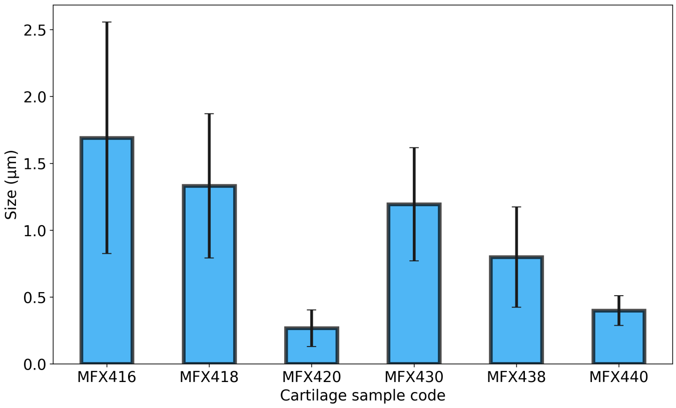

(a)

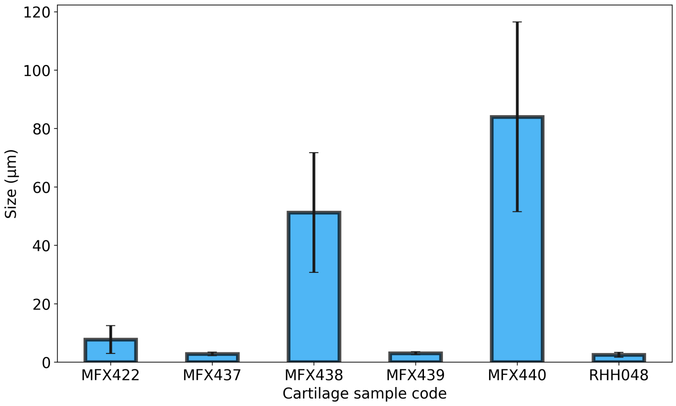

(b)

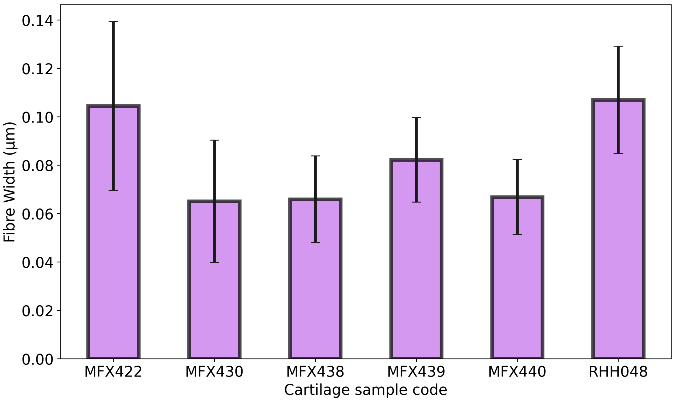

(c)

Figure 6.5: OA cartilage pores size and fibril width measured from SEM images. (a) Size of small pore on cartilage surface; (b) size of large pore on cartilage surface; (c) Width of fibril of cartilage.

6.3.2 Mechanical properties of OA cartilage

To measure the Young's modulus of human OA cartilage, the cartilage specimen was indented by a 60 ° cone tip under the microindentation. The calculation of cartilage Young's modulus was referred to the Equation 2.11. The cartilage was immersed in the PBS buffer during the test. Figure 6.6(a) shows the Young's modulus of cartilage, which is distributed in a wide range. The lowest modulus value is 0.019 ± 0.001 MPa measured from MFX 416, and the highest modulus 0.124 ± 0.009 MPa was measured from MFX 417. Compared to the results in Chapter 4, the modulus of PVA-coated PDMS obtained on the microscale was from 0.028 ± 0.004 MPa to 0.140 ± 0.008 MPa, although the cartilage obtained in the present study was from the late-stage patients, the planar PVA-coated PDMS provided the modulus of 0.278 ± 0.012 MPa, which has the room to increase the modulus of porous PDMS coated with PVA to mimic the early-stage OA cartilage. Hence, the model established in this project has an available range of stiffness for replicating OA cartilage.

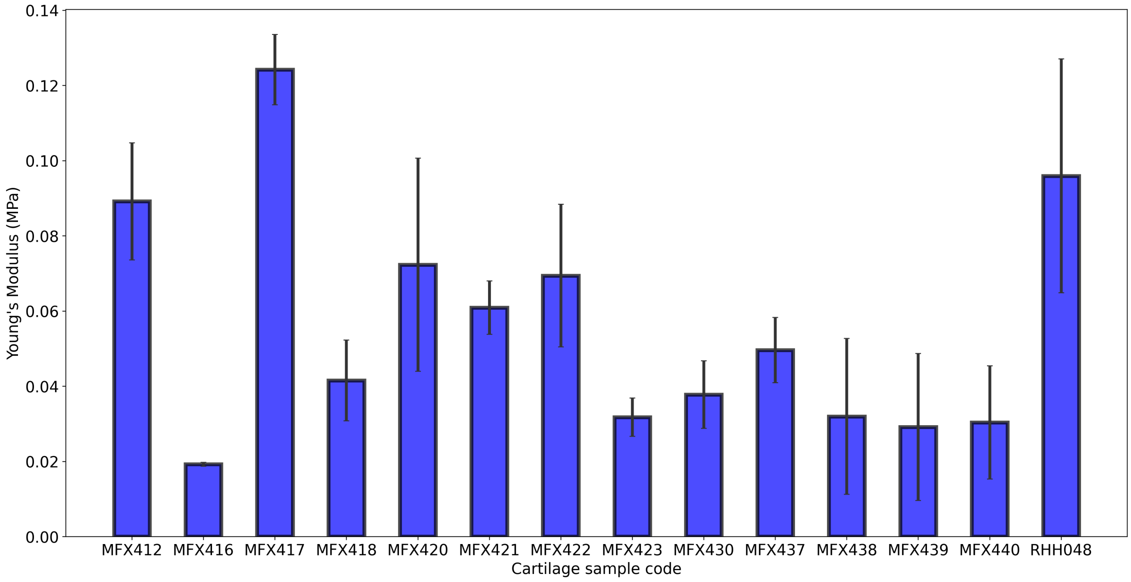

(a)

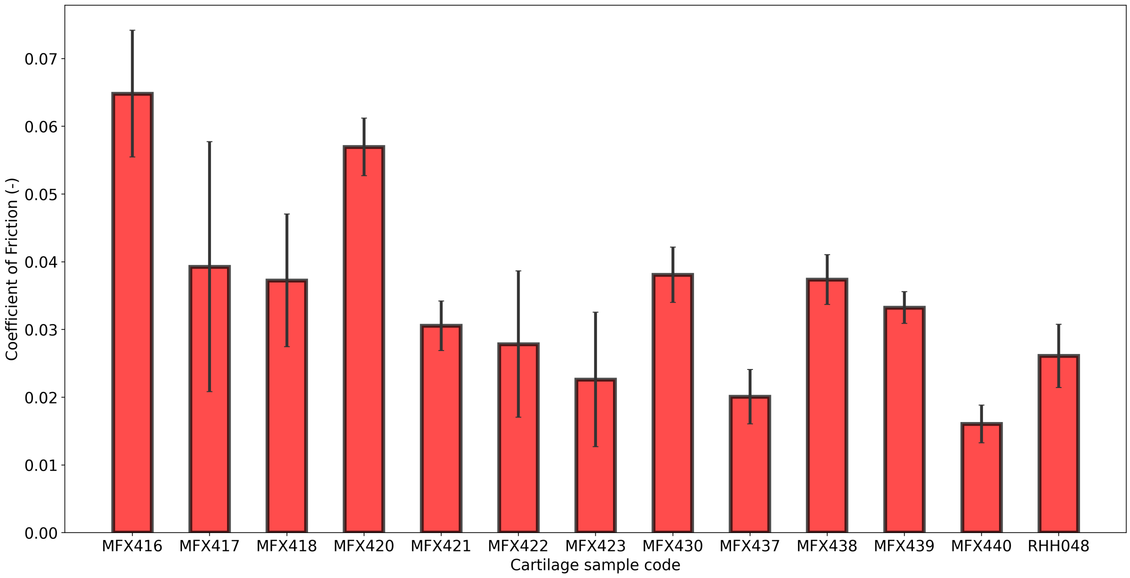

(b)

Figure 6.6: (a) Young's modulus and (b) CoF values of each code of human cartilage sample.

The friction measurement of OA cartilage was obtained by a microtribometer with a 3 mm diameter spherical glass ball, and the cartilage was immersed in PBS during the test. Similar to the modulus results, cartilage samples presented a wide range of CoF. The highest

CoF 0.065 ± 0.009 was measured from MFX 416, and 0.016 ± 0.003 is the lowest CoF value measured from MFX 440. The value of cartilage CoF is lower than what was reported (Table 2.1) [69, 70], which should be caused by the different contact area and materials. The porous PDMS coated with PVA was measured at aqueous by microtribometer under the same conditions in Chapter 4, and the CoF value was from 0.010 ± 0.001 to 0.023 ± 0.001. As the porous PDMS was established to replicate the early-stage OA cartilage, which has lower CoF than the late-stage cartilage in the present work, the tribological property of artificial cartilage in the present study can be consistent with the artificial matrices made in the present work.

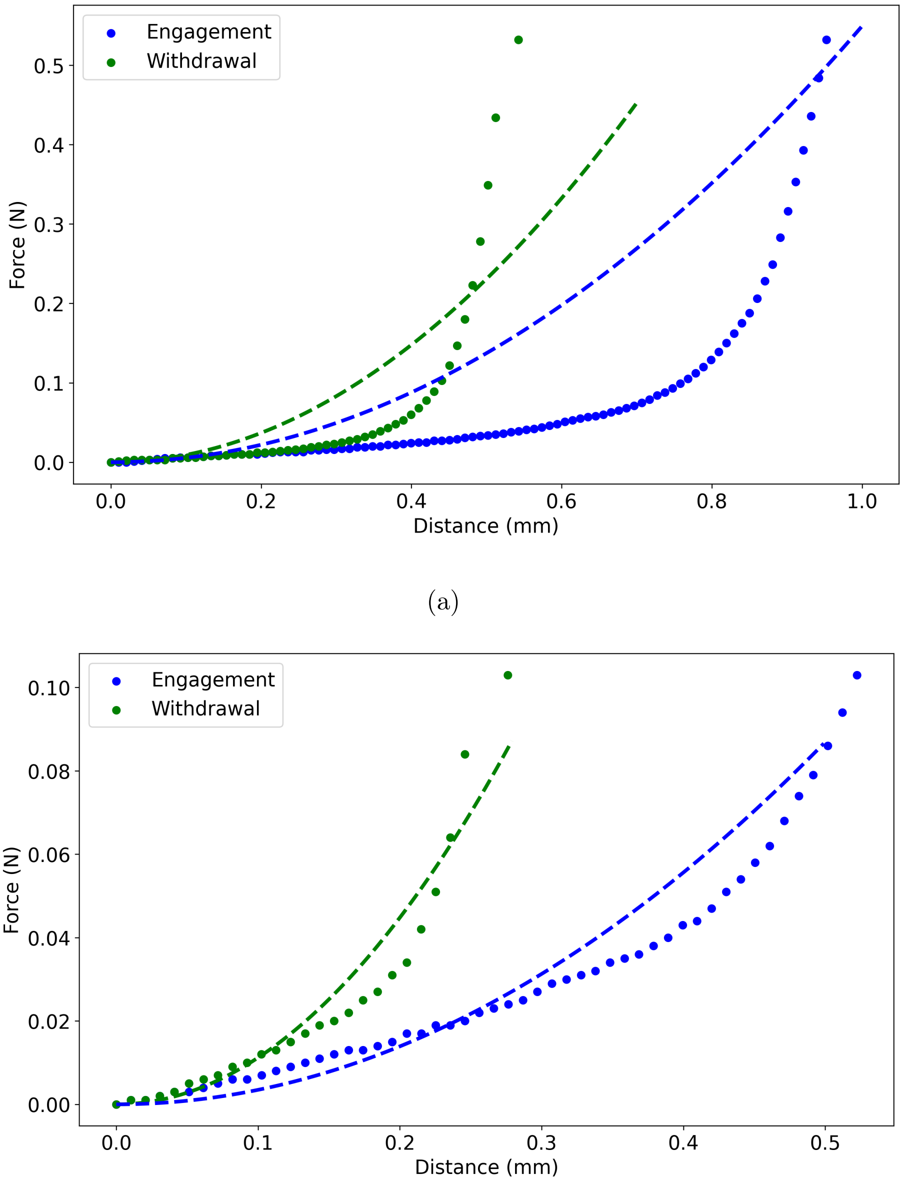

(a)

(b)

Figure 6.7: Raw data of micromanipulator indentation on cartilage MFX 412: (a) maximum force at 0.5 N; (b) maximum force at 0.1 N.

In the cartilage microindentation tests, the approach and withdrawal curves showed differences. For instance, Figure 6.7 shows two raw data of MFX 412 when the maximum forces were 0.5 N (Figure 6.7(a)) and 0.1 N (Figure 6.7(b)), the fitting curves was fitted from

Equation 2.11. In Figure 6.7(a), the Young's modulus measured from withdrawal was higher than the engagement curve, which means that cartilage tissue lost the poroelastic scaffold and resilience property after the indentation. The collagen and protein in cartilage had already run off during the OA disease *in vivo*, and the crosslinked fibrils could not support the springback for the tissue structure. However, even if the maximum load decreased to 0.1 N, the loss of poroelastic can still be observed obviously in Figure 6.7(b), the modulus was increased from 0.131 ± 0.003 MPa to 0.422 ± 0.02 MPa. The viscoelasticity of early OA cartilage was detected by AFM in the study by Desrochers et al. [224], the 40 N m^{-1} glass probe applied 1, 2 and 5 µN load indentation with high frequency, and the instantaneous moduli were decreased generally with the progress of indentation. In a study by Desrochers et al., the cartilage modulus decreased from 0.9 MPa to 0.7 MPa and confirmed that the OA cartilage increased viscous behaviour [224]. The pressure of the tribological test might compress the structure and polish the surface by sliding on the loosened cartilage, which smooths the surface and shows a lower CoF than the actual value.

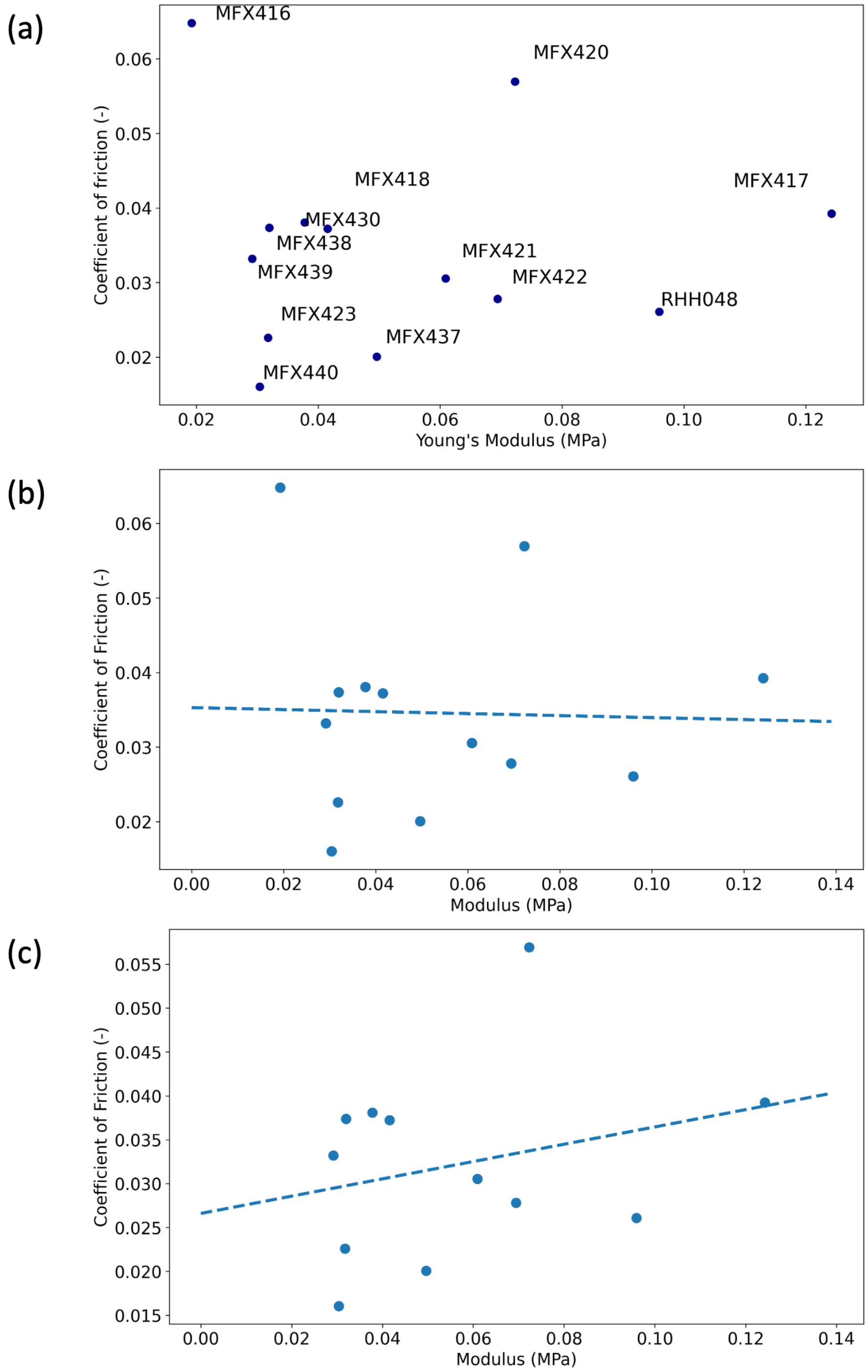

Figure 6.8: (a) Cartilage modulus against the CoF, each point shows one type of cartilage sample. (b) Linear fitting curve correlates the modulus and CoF of cartilage in the present study. (c) Linear fitting curve correlates the modulus and CoF of cartilage in the present study without MFX 416.

Combined with Young's modulus and CoF, the mechanical properties of cartilage collected in this work have been defined in the range as Figure 6.8(a) shows. The Young's moduli of end-stage cartilage are from 0.019 ± 0.0023 MPa (MFX 416) to 0.124 ± 0.024 MPa (MFX 417), and the CoF values are from 0.016 ± 0.002 (MFX 440) to 0.065 ± 0.001 (MFX 416). Human OA cartilage Young's modulus was reported in lots of studies, the late-stage OA cartilage Young's modulus was reported in the range of 0.16 to 0.89 MPa [68, 69, 421], and the coefficient of friction (CoF) was consistent as reported OA cartilage CoF from 0.160 to 0.409 [69, 70]. Figure 6.8(b) shows the correlation between the Young's modulus against CoF, which does not present any linear relation. The positive linear relation can be observed when MFX416 is removed, which consists with the previous studies. As in previous studies, it is difficult to show the OA cartilage mechanical property correlation tendency because the individual specimen result is unexpected. Therefore, more specimens are required in future work to study the correlation between modulus and CoF. A theory introduced by Bowden and Tabor [422] shows that the surface increased the adhesive force with the increase of contact area. And a study on PDMS [423] showed that the frictional property of viscoelastic model has a strong dependence on elastic modulus, and viscoelastic dissipation and adhesive dissipation are the primary mechanisms of friction difference. Therefore it is essential to study the influence of adhesive frictional force in the future work.

According to the previous studies, it was well-known that the degeneration of cartilage during OA process correlated to the patients' gender, age, and obesity [12, 424–426]. Therefore, the study pretends to link the mechanical properties measured with the patients' details, and the results are presented in Table 6.3, Figure 6.9 and Table 6.4.

	Coefficient of friction	Young's modulus (MPa)
Male	0.029 ± 0.014	0.068 ± 0.042
Female	0.046 ± 0.019	0.051 ± 0.024

Table 6.3: Young's modulus and CoF of human cartilage of different genders.

As reported, females are easier to suffer from OA and show worse situations. The results in this project confirmed this point as Table 6.3 shows, the mean average CoF of the male is 0.029 ± 0.014 and mean average Young's modulus was 0.068 ± 0.042 MPa, and the female mean average CoF is 0.046 ± 0.019 and mean average Young's modulus is 0.051 ± 0.024 MPa. As the OA cartilage degeneration would cause lower Young's modulus and higher CoF, the lower Young's modulus and higher CoF value of female cartilage show that female patients have worse OA symptom than male patients.

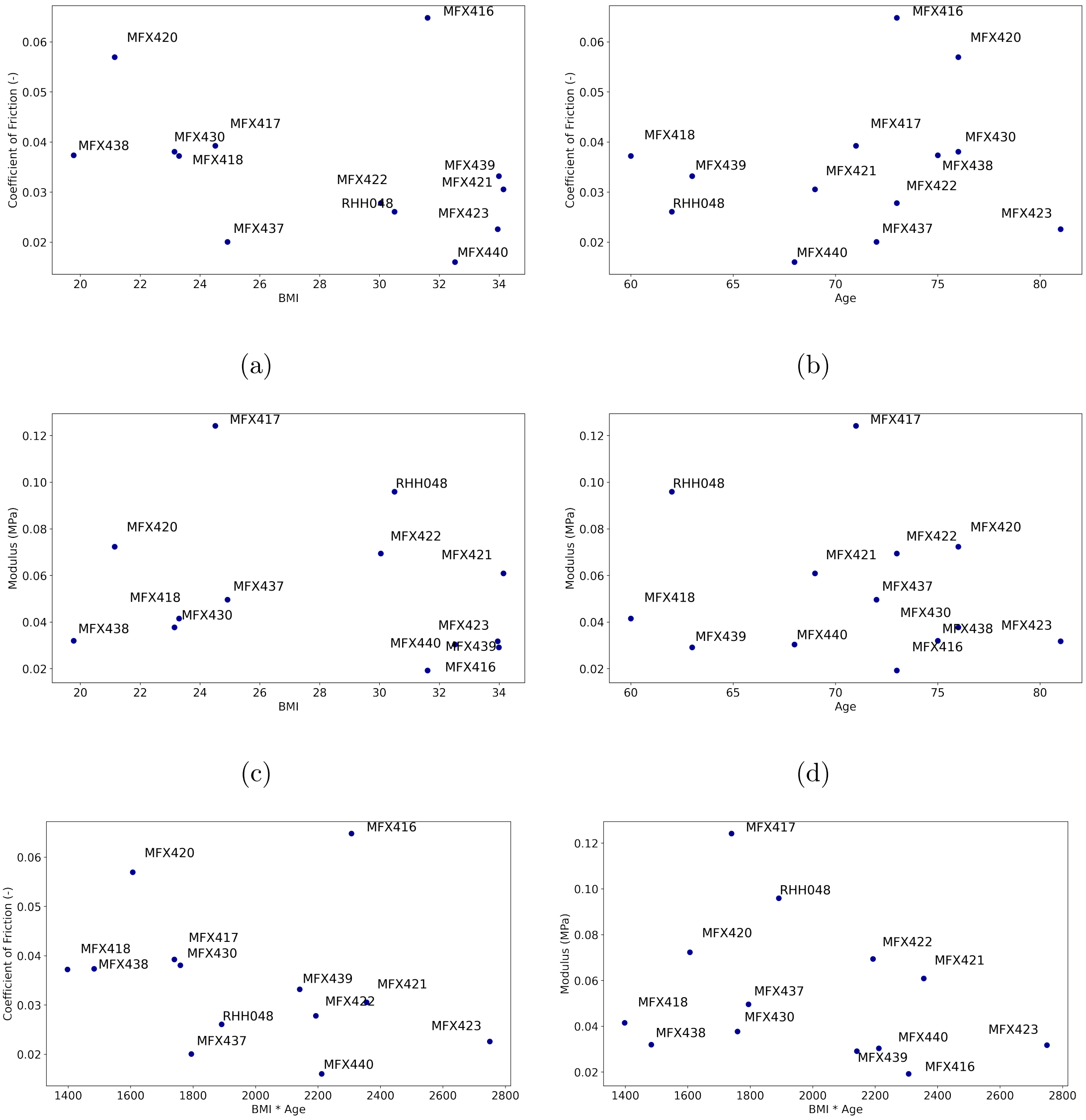

(a) (b)

(c) (d)

(e) (f)

Figure 6.9: Attempts of correlation between BMI or age to the mechanical properties of OA cartilage. a) BMI – CoF; b) Age – CoF; c) BMI – Modulus; d) Age – Modulus; e) BMI*Age – CoF; f) BMI*Age – Modulus.

Moreover, the older and overweight patients showed severer cartilage degeneration. According to the information provided, the present work attempted to correlate by plotting all data results, as shown in Figure 6.9(a) - (d). However, it is impossible to make a significant analysis of Figure 6.9(a) to (d). Therefore, no matter obesity or age did not show any significant tendency with the increase in age or obesity based on the data collected in this work. Even though the influence combined weight and age by multiplying the age by BMI values, the tendency still did not show up with the CoF or Young's modulus (Figure 6.9 (e) and (f)).

Therefore, the present work sorted out the age as over and under 70 years old, and BMI as normal weight (BMI < 30) and overweight (BMI > 30). As Table 6.4 shows, the cartilage from over 70 years old patients shows worse mechanical properties, which has a higher mean average CoF and lower mean average Young's modulus [12]. Regarding the obesity influences, Young's modulus showed that the overweight patients' cartilage have a lower mean average modulus than normal-weight patients' cartilage, which convinced that obesity gave rise to degenerated cartilage. The CoF shows that the normal-weight specimens had higher values, which is opposite to expectation. Therefore, the hypothesis is that the overload of the joint applied more pressure on the cartilage, and the high compression on the degenerated OA cartilage tissue "polish" the surface, which finally exhibited a smoother surface than specimens from normal-weight patients.

	Coefficient of friction (-)	Young's modulus (MPa)
Overweight	0.033 ± 0.020	0.053 ± 0.030
Normal weight	0.038 ± 0.019	0.060 ± 0.035
Over 70 years old	0.041 ± 0.024	0.055 ± 0.034
Under 70 years old	0.029 ± 0.001	0.059 ± 0.030

Table 6.4: Young's modulus and CoF of human cartilage of four groups, which are overweight, normal weight, over 70 years old, and under 70 years old.

6.3.3 Nanogel morphology

To show the shape and characteristics of nanogels, the sponge-like nanogel was dissolved by distilled water. Then the solution was dropped on the Thermo polysine slides and air-dried before the measurement. The morphology scanning of AFM used 0.08 N m^{-1} contact mode cantilever, and SEM measurement was pictured under the SE detection mode.

Figure 6.10 displays the morphology of nanogel particles, which are distributed on the glass slides, and the large light spots on images show the morphology of nanogels. Besides spherical particles of most nanogels, some rod-like and ellipse shape nanogels can also be observed. Compared the size between the four types of nanogel, significant size differences can be observed, especially between AEL 01 and AEL 04. Actually, not only between the different types of nanogels, the size differences could also be observed among the nanogels which belonged to the same type. Such as Figure 6.10(a) shows, a much more significant particle and two tinier light spots. Besides the significant points observed, more minor inconspicuous light spots could be observed on the image background, which is highly like the stain of unreacted residual from preparation. Because the samples were difficult to filter, the stain could be LPEI, PEI-Cy5, and the incomplete synthetic HA gels [413, 427]. The synthesis process showed that the nanogel polymers were combined crosslinked polymer chains, and the chains were combined by the reactive groups bonding or the electrostatic interactions. Although the process could not guarantee that all polymer chains participated in the reaction, once some of the gels were only combined by a few chains, they could be shown as small pieces in the sample.

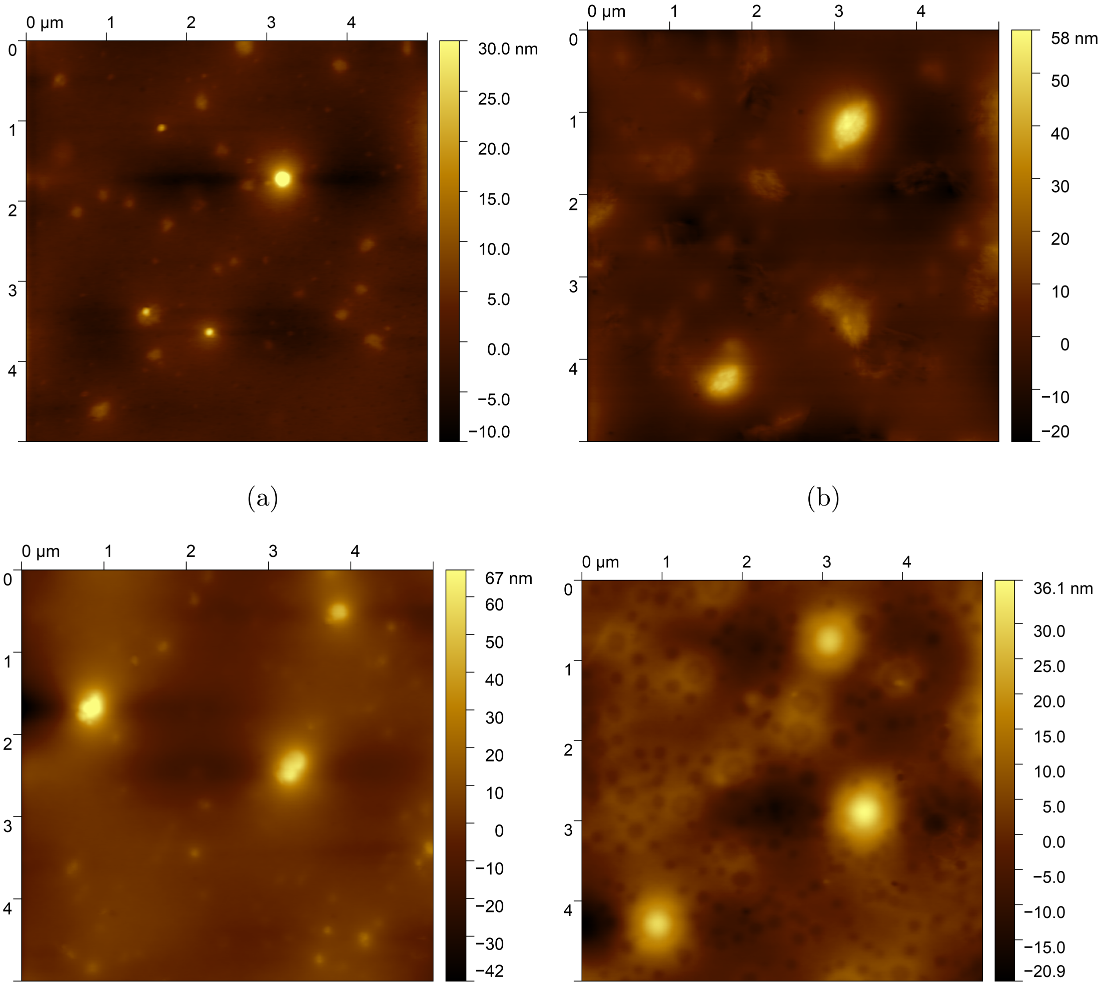

(a)

(b)

(c)

(d)

Figure 6.10: AFM images of four types of nanogel measured in ambient: (a) AEL 01; (b) AEL 02; (c) AEL 03; (d) AEL 04.

Figure 6.11 shows the AFM phase images of nanogel particles, which presents the edge of particles better than height images. As shown in Figure 6.11(a), the nanogel was shown with the clear round edge of one nanogel particle, which is easy to be measured the size of particles. In Figure 6.11(b), the overlap of nanogel can be easily observed, two or three nanogel particles were not successfully isolated from each other, which also caused difficulty for the size measurement.

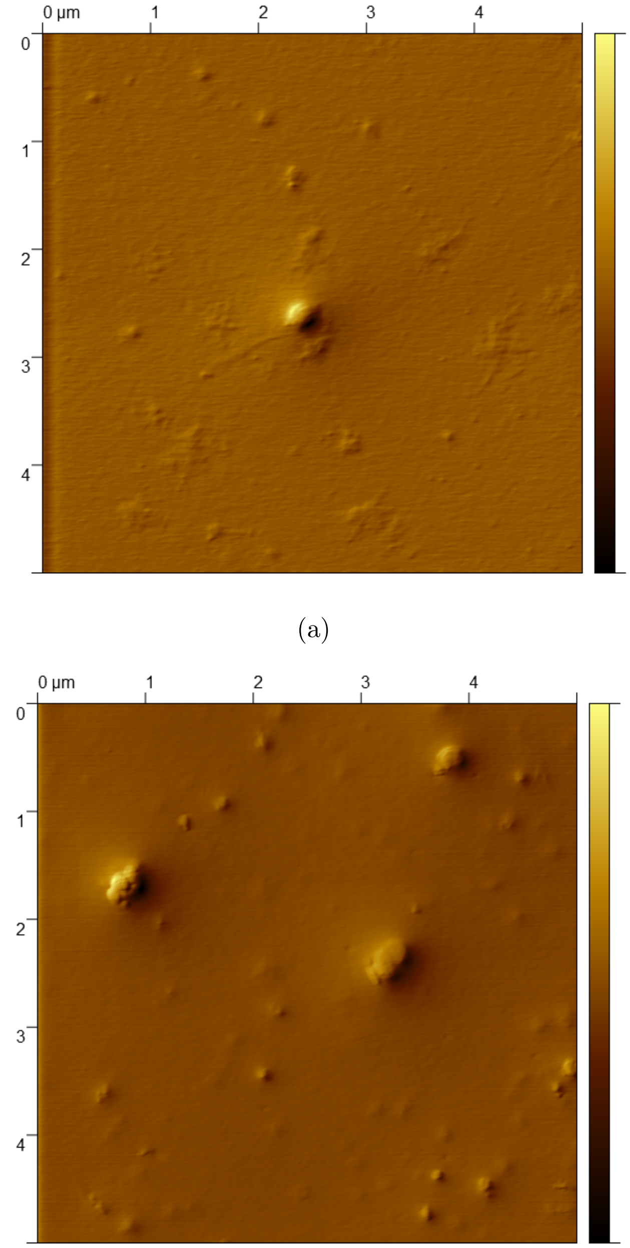

(a)

(b)

Figure 6.11: AFM phase images of (a) AEL 01 and (b) AEL 03.

Figure 6.12 shows the nanogel SEM images, which presents the much clear geometry of nanogel. Except AEL 01, nanogel AEL 02, 03, and 04 show the regular circular shape in SEM images. In Figure 6.12(a), the AEL 01 nanogel particles show the irregular shape, because the AFM images (Figure 6.10(a)) showed that the hydrated nanogel were in the circular shape, it is highly possible that the high vacuum procedure of SEM test preparation shrunk the surface and shape of AEL 01. In addition, dozens of the AEL 01 and AEL 03 particles show the aggregation behaviour in SEM images, which was not clear observed in AFM images, and several of nanogel particles also show the aggregation behaviour in AEL 04.

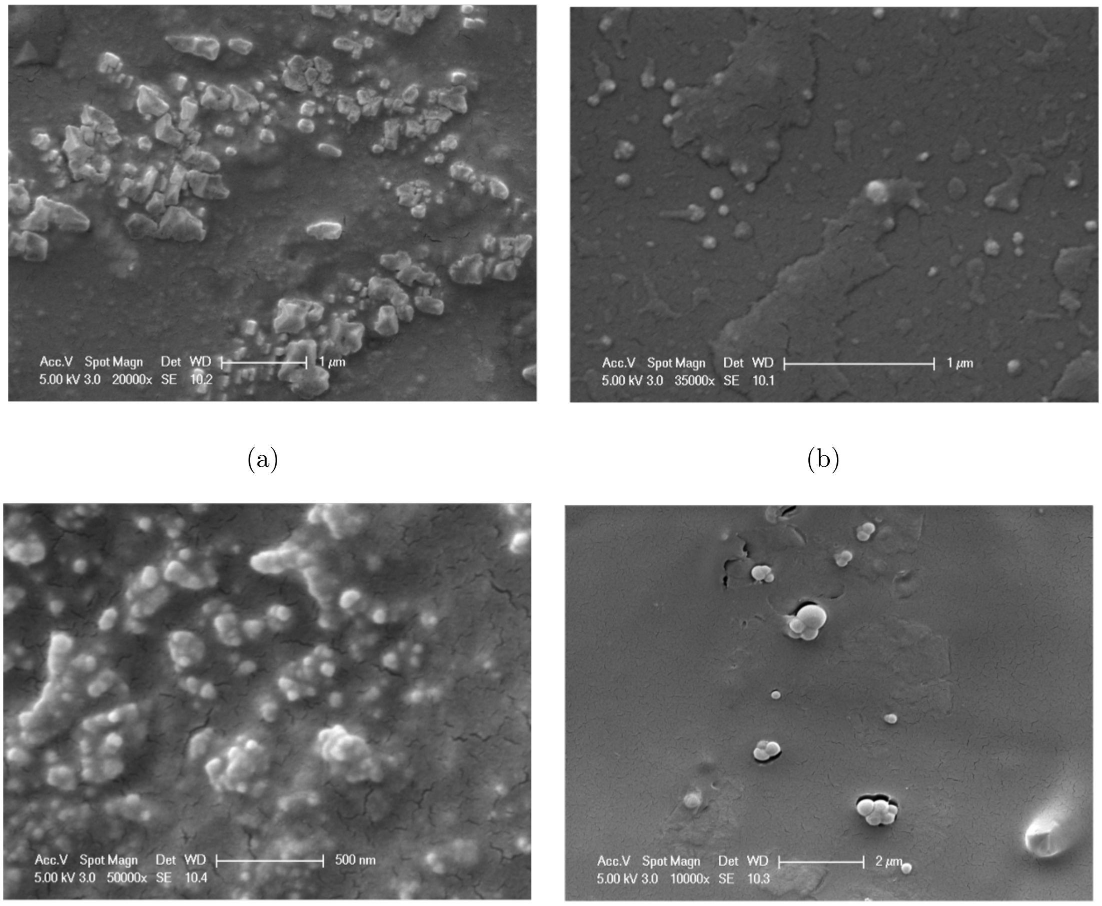

(a) (b)

(c) (d)

Figure 6.12: SEM images of four types of nanogel: (a) AEL 01; (b) AEL 02; (c) AEL 03; (d) AEL 04.

The nanogel sizes were measured by software Gwyddion and ImageJ for AFM and SEM images, respectively, and the results are listed in Table 6.5. In addition, the DLS data measured by Emanuele et al. [428] is also listed in Table 6.5 for comparison. In the present work, SEM and AFM were operated under vacuum and ambient circumstances. Hence the nanogel would be more dehydrated than the stretch structure in aqueous circumstances. Moreover, the SEM facility applied vacuum pressure in the measurement, which could exacerbate the dehydration of nanogel particles. The size of particles measured according to the SEM and AFM images (Table 6.5) show that the sizes measured from SEM images are smaller than the size measured from AFM images. It could be compared that four types of nanogels showed various water losses from normal pressure to the vacuum, possibly caused by the internal crosslinking structure differences.

Average size (nm)	AFM	SEM	DLS (measured by Emanuele et al.[428])
AEL 01	191.2	168.3	224.0
AEL 02	494.5	360.5	188.0
AEL 03	438.8	149.1	92.4
AEL 04	752.0	736.7	228.6

Table 6.5: Nanogel particle size measured according to AFM and SEM images, and the nanogel size measured by DLS by Emanuele et al. [428].

Even though the nanogel solution had been sonicated before being dropped on the substrate, the SEM images clearly show the particle of nanogels were aggregated after the air-dried, hundreds of particles aggregated in AEL 01 and AEL 03 images, and a few numbers of particles combined in AEL 04. The typical Marangoni effect could occur on the colloidal particles: the crosslinked polymer chains would spread according to the surface gradient, and the mass of particles would be driven by the Marangoni effect, which would finally cause the aggregation of nanoparticles during the deposition procedure of sample preparation [413, 428]. Furthermore, the aggregation phenomenon has been observed in AFM tests as well. Although nanogels were usually difficult to be uniformly distributed on the glass sides, the distribution of nanogels would usually be detected in some concentrated areas rather than uniformly distributed. The same concentrated behaviour was observed in the SEM measurement as Figure 6.12 exhibits.

The AFM measurement shows that AEL 01 had the smallest size at 191.2 ± 28.4 nm, and AEL 03 shows the smallest in SEM image measurement at 149.1 ± 8.3 nm. Both images consistently show that AEL 04 has the most significant size with 752.0 ± 21.0 in AFM images and 736.6 ± 23.1 in SEM images. Moreover, the DLS measurement by Emanuele et al. [428] showed the size of these four nanogels in the aqueous (Table 6.5). Therefore, the size obtained from DLS showed a much lower value than AFM and SEM, which is abnormal because the hydration would cause the particle size to be more significant.

Because the AFM, SEM and DLS results show in the same order of magnitude, two possibilities could explain the abnormal results. As the Marangoni effect was described and the combination was observed in SEM measurement, although the AFM and SEM could be observed in the single particle, it could not exclude that some particles combined and shaped similar to a single particle. In addition, the size calculated based on AFM and SEM images only chose 15 samples for each measurement, which was not representative for the massive number of nanogels. Moreover, as the lubrication was measured under the aqueous environment, the size comparison for further analysis should be better using the DLS results, which rank the size as AEL 04 >AEL 01 >AEL 02 >AEL 03.

6.3.4 Lubricant comparison

To compare nanogel and silica nanoparticles, the friction measurement was tested by AFM at nanoscale, which was limited by the amount of nanogel solution volume. The 4 µm radius colloidal probe with 40 N m^{-1} cantilever was applied for the load applying. 10 µl of nanogel solution was added as the lubricant between the cantilever tip and substrate, which was planar PDMS coated with PVA for all tests. In addition, PBS buffer and equivalent concentration HA solution were used as benchmark [413]. Figure 6.13 exhibits the raw data of the nanogel lubrication, Figure 6.13(a) presents raw data of 3.0 mg ml^{-1} nanogel solutions and Figure 6.13(b) presents concentration at 1.5 mg ml^{-1}. With increased tendency, the slope of increased lines can be considered as the CoF of the PVA-coated PDMS lubricated by nanogel solutions, and the CoF comparison is shown in Figure 6.13(c).

Figure 6.13 shows that the CoF of HA is lower than pure water lubrication. Compared to the nanogels, it is evident that the nanogel plays a better lubricant on the PVA-coated PDMS than HA solution, which was consistent with the therapy studies of hydrogel for OA joints [429]. In principle, HA solution decreased the CoF by increasing the fluid viscosity [430]. Based on the thick viscosity of hydrogel fluid, the nanogel particles affect the lubrication system by rolling and protective effects, which explains the further decrease of CoF than pure HA lubricant.

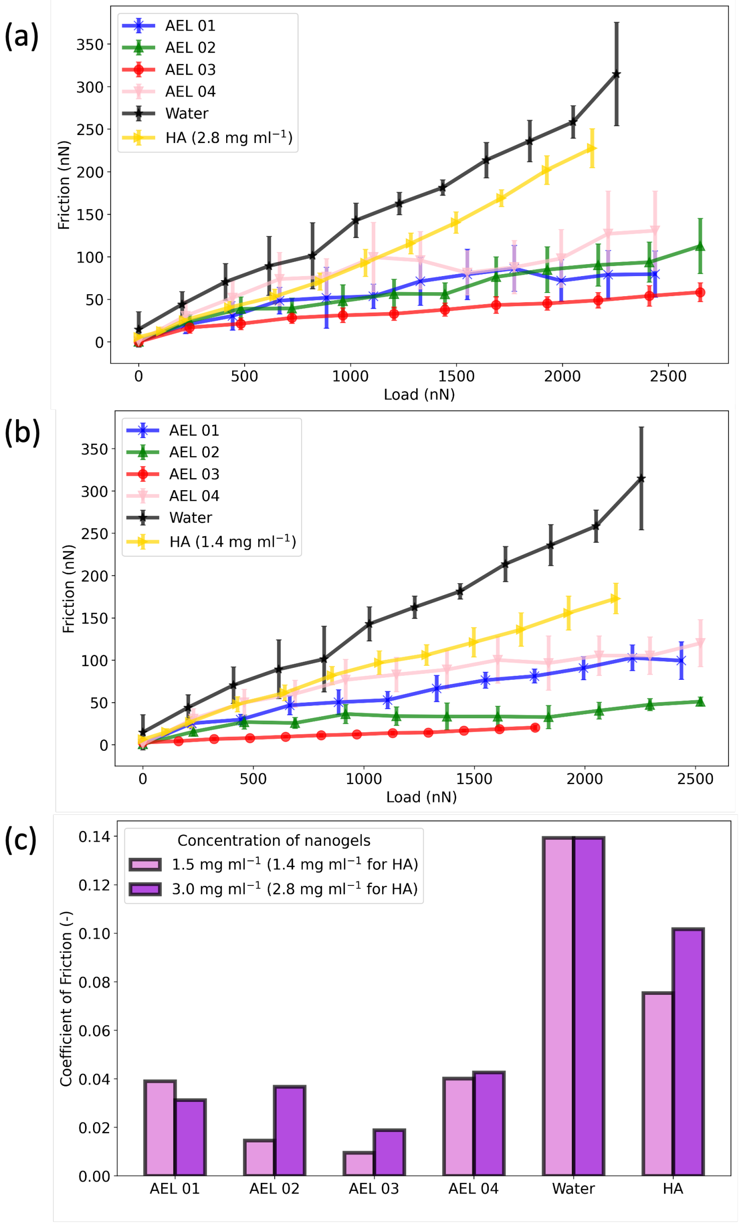

Figure 6.13: AFM tribological measurement results of nanogels on planar PDMS coated with PVA, the maximum load applied is 2800 nN. (a) Raw data of friction as a function of the normal load with the lubricants of water, HA (2.8 mg ml^{-1}), and four types of nanogels (3.0 mg ml^{-1}); (b) Raw data of friction as a function of the normal load with the lubricants of water, HA (1.4 mg ml^{-1}) and four types of nanogels (1.5 mg ml^{-1}); (c) CoF of water, HA and four types of nanogels.

Using AFM to measure the CoF for the four types of nanogels clearly shows the lubricant capacity of these particles. In both 1.5 mg ml^{-1} and 3.0 mg ml^{-1} measurement, the AEL 03 shows the best lubrication with the lowest CoF, which is 0.010 at 1.5 mg ml^{-1} and 0.019 at 3.0 mg ml^{-1}. Moreover, AEL 04 shows the highest CoF at both concentrations, which is 0.040 at 1.5 mg ml^{-1} and 0.043 at 3.0 mg ml^{-1}.

Figure 6.14 shows the correlation between the CoF of nanogel against the size of nanogel particles (based on DLS results). According to the silica nanoparticles measurement in Chapter 5, the nanoparticle CoF would increase with nanoparticle size. In Figure 6.14, it can be observed that the tendency of nanogel against particle size was similar to silica nanoparticles, but the tendency was not ideally consistent with the expectation. Different from silica particles, nanogel was made in different conditions in this study. Besides the influence of size, the modulus, contact pressure and end groups could also be impacted by the lubrication system. In the discussion of nanogel and nanoparticles, the deformation of nanogels would improve lubrication. As the AEL 02 - 04 were increased, the CoF from 1.5 mg ml^{-1} to 3.0 mg ml^{-1}, one of the predictions was that the deposition of nanogels had covered the surface and began to pile up with the deformation. In this way, the AEL 01 with a larger size should have the same conditions as piled particles.

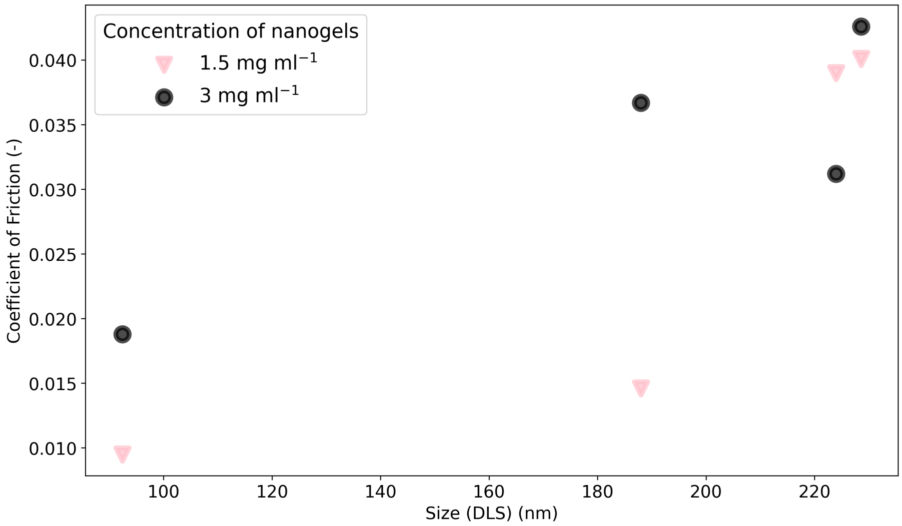

Figure 6.14: Nanogel size (measured by DLS) against CoF of 1.5 mg ml^{-1} and 3.0 mg ml^{-1} nanogel on planar PDMS coated with PVA.

Figure 6.15 shows the lubrication comparison of silica nanoparticles and nanogels solutions. The test conditions and parameters were same as the study for nanogel comparison. Figure 6.15(a) and (b) exhibit the raw data at 3.0 mg ml^{-1} and 1.5 mg ml^{-1}, respectively. Figure 6.15(c) shows the comparison of CoF at two concentrations. Compared to nanogel with silica particles, it was significant that the silica particle had much higher friction coefficient values than nanogel. For example, at the concentration of 1.5 mg ml^{-1}, silica nanoparticle Aerosil 150 decreased CoF from 0.140 to 0.114 while AEL 04 decreased CoF value from 0.140 to 0.040 at the same conditions. However, AEL 04 showed the highest CoF among the nanogel lubricant, and the lowest CoF decreased to 0.010 by AEL 03, which means nanogels could provide much better lubrication than silica nanoparticles on soft material. Moreover, the nanoparticles of Aerosil 150 increased the CoF at 3.0 mg ml^{-1}. From the lubricant studies on silica particles in Chapter 5, the shear thinning nanoparticle fluids showed the CoF decreased at the beginning of adding, and then the CoF increased after concentration came to higher than critical concentration. According to the silica nanoparticles (Aerosil

150) concentration research by AFM in Chapter 5, the best concentration of nanoparticle of Aerosil 150 as lubricant was detected at 1.0 mg ml^{-1}, and the lowest CoF showed on the planar PDMS coated with PVA was 0.071, which is still higher than the CoF of AEL 04 at 1.5 mg ml^{-1}. Furthermore, the CoF of nanogel at the concentration lower than 1.0 mg ml^{-1} was difficult to be authentically recorded, because the voltage values were too low to show, which means the nanogel could decrease the CoF to a much lower value. In conclusion, the nanogel provides much better lubrication than silica particles on soft materials. Compared the CoF between 1.5 mg ml^{-1} and 3.0 mg ml^{-1}, the AEL 01 and AEL 02 show the opposite level at two concentrations. As Chapter 5 confirmed, the CoF decreased and then increased with the rising of concentration, and a limitation of concentration existed to provide the lowest lubrication. The situation could explain that the AEL 01 concentration for the lowest CoF was higher than 3.0 mg ml^{-1}.

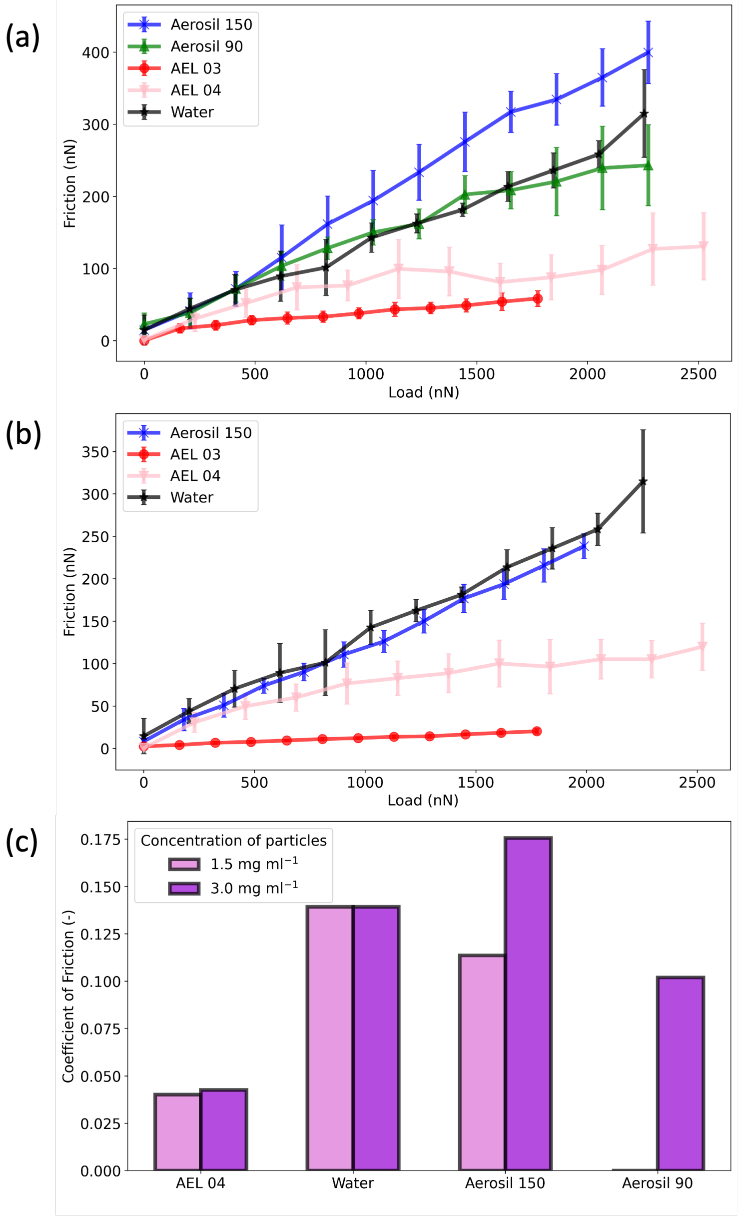

Figure 6.15: AFM tribological measurement results of nanogels and silica nanoparticles on planar PDMS coated with PVA, the maximum load applied is 2600 nN. (a) Raw data of friction as a function of the normal load with the lubricants of water, silica nanoparticles (Aerosil 90 and Aerosil 150), and nanogels (AEL 03 and AEL 04) at 3.0 mg ml^{-1}; (b) Raw data of friction as a function of the normal load with the lubricants of water, silica nanoparticles (Aerosil 150), and nanogels (AEL 03 and AEL 04) at 1.5 mg ml^{-1}; (c) CoF of water, silica nanoparticles (Aerosil 90 and Aerosil 150) and nanogels (AEL 03 and AEL 04).

From the previous AFM friction tests on cartilage, the microscale boundary lubrication without interstitial fluid pressurization would not be affected by the biphasic lubrication mechanisms [431, 432]. Therefore, the cartilage nanoscaled friction measurement was applied on the multimode AFM. silica nanoparticle Aerosil 150 and nanogel AEL 04 were chosen for the lubrication behaviour comparison, and PBS buffer was used as control. The nanogel AEL 04 and silica nanoparticle Aerosil 150 were diluted to 0.1 mg ml^{-1} for the tests. Three cartilage samples had been successfully recorded the CoF for two particles. Figure 6.16(a), (b), and(c) show the raw data of PBS, silica particles, and nanogels on cartilage from three different patients, and Figure 6.16(d) compares the CoF values of each raw data. Compared to the PBS buffer, all three tests showed that nanogel and silica particles decreased CoF for cartilage surface, and nanogel has better tribological behaviour than silica nanoparticles as the lubricant. PBS buffer lubricated on the cartilage surface shows the CoF from 0.018 to 0.036, which is in the CoF results range of the microtribometer. After adding particles as the lubricant, the CoF of AEL 04 on cartilage is from 0.06 to 0.09, and the CoF of silica nanoparticles Aerosil 150 on cartilage is from 0.08 to 0.16. The CoF for different samples has a significant value difference. For instance, the CoF value of PBS on MFX 430 is two times of MFX 437, and the CoF values of nanogel AEL 04 on MFX 430 and 434 are higher than the CoF value of nanoparticles of Aerosil 150 on MFX 437. Although the cartilage samples were collected and prepared by the same methods, the individual sample difference is incalculable, and it is more important to compare the values on the same sample.

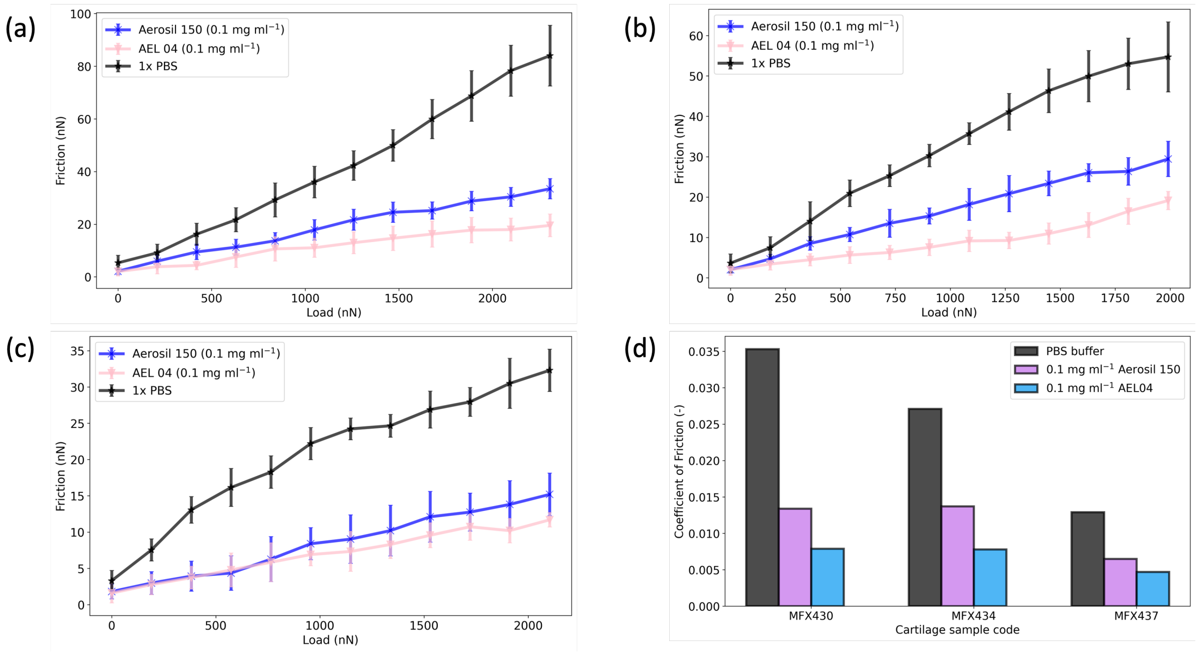

Figure 6.16: AFM tribological measurement results of nanogels (AEL 04) and silica nanoparticles (Aerosil 150) on human OA cartilage samples, the maximum load applied is 2300 nN. (a) Friction raw data of MFX 430; (b) friction raw data of sample of MFX 434; (c) friction raw data of sample of MFX 437; (d) CoF of silica nanoparticles (Aerosil 150) and nanogels (AEL 04) on the samples of MFX 430, MFX 434, and MFX 437.

With higher concentrations of nanogels and nanoparticles, it was challenging to be recorded the signals from the multimode AFM. The CoF values presented on the cartilage in AFM tests could be observed to be extremely low. The highest value obtained in the AEL 04 test on cartilage was 0.009, which was lower than the best lubricant AEL 03 CoF value on PVA-coated PDMS surface, which was 0.010, which verifies that even the late-stage OA cartilage still provides a well-performed surface on tribology. In addition, the nanogel used in the present work was reported as slightly negative charged [428]. On the negatively charged cartilage surface, the attachment of nanogel particles should be worse than the neutral particles but still showed excellent performance for the cartilage surface lubricating. Therefore, the nanogel has the potential to be more lubricated with a positive charge on the particle surface.

Particle type	Young's modulus
Silica nanoparticle	5.5 - 88.7 GPa [433, 434]
polymer grafted nanoparticle	0.14 - 6.9 GPa [434]
Nanogel	3 kPa - 13 MPa [435–438]

Table 6.6: Young's modulus of different types of nanoparticles.

According to Figure 6.15(c) and 6.16(d), it is significant that the nanogels provided much better tribological properties in the lubricant system than silica nanoparticles on PVA-coated PDMS and cartilage tissue that nanogels decreased more CoF. The hydrogel crosslinked with polymer chains would usually be considered an elastic material. Hence, the compression on the nanogel polymer network in hydrogel would be considered with elastic behaviour. The modulus would decrease with less combination of polymer chains. The less elastic modulus nanogel would be softer, and the same compression on softer nanogel could have more deformation than stiffer particles, and then the contact areas would be more extensive. According to the classical physics equations, increasing the contact area will decrease the contact pressure, which would benefit the lubrication system and decrease the CoF. As the silica nanoparticles are usually considered as rigid material [439, 440], which has stiffer mechanical properties than nanogel (Table 6.6), even though the size of AEL 04 was more considerable than Aerosil 150, the increase of contact area improves the lubrication system of nanogel solutions. Similarly, the polymer grafted particle has modulus from 0.14 MPa to 6.90 MPa, which is stiffer than nanogel and hardly deformed under pressure. Therefore, besides the suitable size of nanogel, the excellent deformability during the friction decreased much more than other stiff nanoparticles, which has a high potential as a carrier for the drug delivery system.

6.4 Summary

In the present study, the cartilage surface morphology and mechanical properties were measured, and the work compared the nanogels with silica nanoparticles on polymer and biotissue substrates. The cartilage surface morphology was captured by SEM and AFM. The porous and multilayer structure were observed in SEM images. Furthermore, the fibrous structure was observed at the edge of cut-off sections. The pore size of OA cartilage was from 0.267 ± 0.137 to 1.691 ± 0.866 µm, and the width of fibril was from 0.065 ± 0.025 to 0.437 ± 0.143 µm. The mechanical properties of cartilage were obtained, which provided the mechanical values range of late-stage OA cartilage. The CoF of cartilage varied from 0.016 ± 0.003 to 0.065 ± 0.009, and the Young's modulus was in the range of 0.019 ± 0.001 MPa to 0.124 ± 0.009 MPa.

The nanogels have been proven as a better lubricant for cartilage than silica nanoparticles. Four types of nanogel made under different conditions have been studied for the function of lubricating on planar PDMS coated by PVA. Compared to the lubrication on the PVA-coated PDMS, the HA-based nanogels showed better lubrication than pure HA, which benefited from the effects of spherical particles. The rolling effect provides rolling friction with nanogel particles. Compared with the four types of nanogels, AEL04 showed the highest CoF on the substrate, and AEL 03 showed the lowest CoF. The CoF of AEL 04 was 0.040 at 1.5 mg ml^{-1} and 0.043 at 3.0 mg ml^{-1}, and the values of AEL 03 was 0.010 at 1.5 mg ml^{-1} and 0.019 at 3.0 mg ml^{-1}. Similar to silica nanoparticles, the reduction of nanogel size decreased the CoF. Even though the silica nanoparticle and nanogel were both at the nanoscale, the lower modulus of nanogel provides a larger contact area and less contact pressure during the lubrication, which benefits the reduction of the CoF of the tribological system. Therefore, compared to the nanogel and silica particles' lubrication efficiency on PVA-coated PDMS and the cartilage, it could be confirmed that the nanogels provided better lubrication than silica particles on both polymer substrate and biotissue. Moreover, the negatively charged nanogel used in the present work should be able to be improved to a positive charge to enhance the binding with the cartilage surface, which is negatively charged.

Chapter Seven

Conclusion and future work

7.1 Conclusion

The present thesis establishes a series of the porous polymeric matrix that can mimic articular cartilage degenerated in different stages of osteoarthritis (OA) with improved consistent mechanical properties. Based on the porous polymer scaffold, the present work studied the parameters that influence the lubrication of nanoparticle-based fluids. The results show that the tribological behaviour of nanoparticles is affected by particle size, normal load applied, sliding velocity and particle concentration. Furthermore, four types of hydrogel-based nanogel are introduced in this thesis to study the lubricant behaviour and to compare to the silica nanoparticles. The nanogel shows better lubrication efficiency than silica nanoparticles on elastic materials, including polydimethylsiloxane (PDMS) based artificial cartilage and human OA cartilage. In the OA articular cartilage from patients, the present study exhibits the surface morphology of cartilage and measured the range of human OA cartilage mechanical properties of Young's modulus and coefficient of friction (CoF).

7.1.1 Artificial cartilage

An *in vitro* artificial system is prepared by porous PDMS with polyvinyl alcohol (PVA) coating to mimic OA cartilage in different stages. The artificial scaffold has controllable mechanical properties, which are controlled by the curing agent ratio and sodium chloride fraction in porous PDMS.

With the reduction of curing agent ratio, the porous PDMS shows decreased Young's modulus and increased CoF. By increasing sodium chloride fraction of porous PDMS scaffold, the scaffold comes with decreased Young's modulus from 1.50 ± 0.03 MPa to 0.07 ± 0.003 MPa and increased CoF from 0.033 ± 0.002 to 0.133 ± 0.001. Moreover, the porosity of porous PDMS scaffold increases with the increase of NaCl fraction as well, which varies from 54.6 ± 1.1% to 81.7 ± 0.7%. The sinking of sodium chloride are observed when the low fraction of NaCl. Therefore, the porosity can not be calculated by the physical properties of PDMS and NaCl. For predicting the porosity of the bottom layers of the scaffold, a mathematic model is used for calculating the porosity, based on the bottom porosity results obtained from the present work. Similarly, another mathematic model shows the relationship between Young's modulus and porosity.

To replicate the articular cartilage surface chemical property, the surface of PDMS is modified to hydrophilic with a thin film coating by PVA. A wave pattern is captured on the surface of planar PDMS coated with PVA, which is explained by the expanding and different speeds of contracting. Moreover, the PVA film thickness is calculated according to the correlation between film thickness and wavelength, which is results in 0.17 µm. At the same time, the PVA layer changes the physical properties of the porous PDMS. As the PVA has a higher modulus than PDMS, the porous scaffold with PVA coating shows stiffer property than pure porous PDMS. The Young's modulus of porous PDMS coated with PVA varies from 3.53 ± 0.41 MPa to 1.84 ± 0.58 MPa. In addition, the hydroxyl groups on PVA combined with the water-based solution by hydrogen bonds, resulting in the porous PDMS coated with PVA having the lower friction coefficient than porous PDMS matrices, which resulting from 0.010 ± 0.0002 to 0.022 ± 0.0006.

7.1.2 Silica nanoparticles-based lubricant

Silica nanoparticle-based nanofluids were applied to the tribological measurement on the porous polymer scaffolds in the present study. Without the impact of the viscosity of nanofluid, different conditions of silica nanoparticle-based fluid show the influence on the lubrication systems, which includes nanoparticle size, concentration of nanoparticles, normal load applied and sliding velocity.

The increase in nanoparticle size shows the increase of the CoF. The CoF increases from 0.042 ± 0.005 to 0.060 ± 0.025 on PVA-coated PDMS when the size increased from 152.40 nm to 256.00 nm. While the normal load applied on the porous matrix increases from 30 g to 50 g, the CoF of all the lubricants increases. With the sliding velocity increase, the CoF of the lubrication system rapidly decreases during low velocity and then slightly increases at the concentration of 5%, which could be explained by the Stribeck curve. There is a critical concentration of nanoparticle-based lubricant. The CoF of the lubrication system reduces when the concentration of nanofluid increases lower than the critical concentration, and then the CoF increases with the increase of particle concentration. This trend has been confirmed in both nano and microscaled measurements, that Aerosil 150 shows the lowest CoF 0.035 ± 0.005 at 0.5% in microtribometer measurement and 0.071 at 1.0 mg ml^{-1} in AFM measurement. The critical concentration can be explained by the fact that nanoparticles are fully piled on the surface when the concentration is over the critical value, and the piled nanoparticles increase the CoF by increasing the surface roughness.

The parameters of silica particles play essential parts in lubrication on the porous polymer matrices. The application could help further study drug delivery systems on the porous OA cartilage tissue, and the results are beneficial to adjusting the parameter of nanoparticles to decrease the lubrication at the same time as drug release.

7.1.3 Human cartilage

AFM and SEM showed the surface morphology of human cartilage. The SEM images show the pore structure on the surface, in which tiny pores shows circular and regular edges with diameters varies from 0.267 ± 0.138 µm to 1.691 ± 0.866 µm. AFM and SEM images of the cartilage surface show small fragments distribution, which is highly possible broken during the degeneration of OA. The fibrous structure can be significantly observed on the cut-off section of cartilage SEM images. Moreover, the cartilage shows the multi-layers structure on the section with the fibres stretched out from the edge of each layer. Moreover, the cartilage surface was torn into cracks in SEM measurement, which shows the internal fibrils broken rapidly.

The mechanical and frictional properties of human OA cartilage are measured in the present work. The Young's modulus and the CoF of human cartilage are results from 0.019 ± 0.001 MPa to 0.124 ± 0.009 MPa and from 0.016 ± 0.003 to 0.065 ± 0.009, respectively. During the mechanical property measurements, the curves of cartilage indentation tests show that the withdrawal of indentation results in a lower modulus than engagement, which is explained by the loss of structural strength after the pressure. By classifying the results according to the patients' information, the comparison of Young's modulus and CoF shows that females older than 70 and overweight patients' cartilage show worse mechanical properties in lower Young's modulus and higher CoF. The overweight cartilage showed a lower coefficient, which might be because of the higher load "polished" cartilage surface.

7.1.4 Nanogel lubricant

Four types of nanogel synthesised by hydrogel were introduced in the present work. The nanogels show circular shapes in AFM images, most of which show irregular morphology in SEM images because of the dehydration. Furthermore, the aggregation can be observed in both AFM and SEM images, and the size of nanogels measured based on the images are compared with DLS results, which show that the DLS results are more convincing as the natural nanogel size.

Compared to the CoF of nanogels on the planar PDMS coated with PVA, the particles prepared by microfluid chip at 2 bars (AEL 03) shows the best tribological behaviour with CoF of 0.010 at 1.5 mg ml^{-1} and 0.019 at 3.0 mg ml^{-1} on planar PDMS coated with PVA. On the other hand, the nanogel synthesised by mixed emulsion/evaporation technique (AEL 04) shows the worse performance as a lubricant, which CoF on planar PVA-coated PDMS 0.040 at 1.5 mg ml^{-1} and 0.043 at 3.0 mg ml^{-1}. The results of CoF between nanogels can be correlated to the size of the nanogel that the smaller particles show a lower CoF. Although AEL 04 shows the highest CoF amongst nanogels, compared to AEL04 and silica nanoparticles in planar PVA-coated PDMS measurement, nanogels show much lower CoF than silica nanoparticles. In the tribological measurement on cartilage, silica nanoparticles decreased the CoF than PBS buffer, which confirms that the nanoparticles are effective in the cartilage surface lubrication system. At the same time, nanogel shows a much significant lower CoF than silica nanoparticles, the nanogel presented better effectiveness in decreasing the friction on the cartilage surface. The CoF of nanogels (AEL04) on human cartilage varies from 0.005 to 0.008 and the CoF of silica nanoparticles (Aerosil 150) is from 0.007 to 0.013. The softer nanogels show more deformation than the silica nanoparticles, which might be the reason that nanogels decrease the CoF by increasing the contact area under the same conditions.

7.2 Future work

This thesis established a porous artificial system to mimic OA cartilage in different stages, and developed the efficiency of lubrication system based on silica nanoparticles and nanogels. However, some considerable steps could be taken in future work to establish better artificial structure and to enhance the lubrication efficiency of nanoparticles.

The present work attempted to measure the porosity of cartilage via X-ray tomography, the less density is a challenging to show the cartilage porosity clearly. Some previous results reported the cartilage or OA cartilage porosity, but the range was too wide to be convinced as the OA cartilage structure. Therefore, the future work needs to focus on the OA porosity, which was helpful for the artificial cartilage to precisely mimic the cartilage's porosity in different stages. The cartilage mechanical properties against the OA influence factors contact could not be concluded by the scatter plots but by the classified tables, which meant that more cartilage should be measured, to show the significant correlation between the mechanical properties and OA disease influence factors. As the pore size of cartilage was measured as nanosized, the pore-foaming agent of sodium chloride can be considered to be replaced by any nanosized soluble agent, which can better mimic OA cartilage physically.

It was difficult to locate the tip of the cantilever to the position of the particles, therefore, the modulus result was failed to be obtained based on the methodology in the present study. Without the modulus results of nanogel particles, it is unable to correlate the CoF with the stiffness of nanogel and build a mathematic model. Hence, it is essential in the future work to obtain the stiffness mechanical property to benefit the further choice and improvement on the nanogel particles.

Lastly, most of the present work develops the lubrication system based on the studies of mechanical properties. However, the cartilage surface is reported with negatively charged glycosaminoglycan (GAG) groups within a complex collagen network, which is not replicated by the present artificial system. Therefore, it could be improved in future work to coat the negatively charged chemicals on the scaffold to mimic GAG groups. Based on the negatively charged surface, differently charged nanogels can be applied to study the charge influence of nanoparticles on the porous artificial cartilage.

Appendix One

Appendix

A.1 AFM code template

```
pip install nanoforce

pip install numpy

pip install plotly

pip install scipy

pip install easygui

from nanoforce import AFM

expt = AFM()

expt.run()

expt_1.nanoscope_params()

expt_1.set_def_sens(100)
```

```
expt_2.set_spr_const(0.32)

expt_1.nanoscope_read()

expt_1.plot_raw(1)

expt_1.baseline()

expt_1.baseline(start_pos = 0.5, end_pos = 0.7)

expt_1.contact()

expt_1.plot_adjusted(10)

expt_3.plot_curves()

expt_1.delete_curve()

expt_1.calc_adhesion(plot_hist = True)

expt_1.calc_modulus(poisson_ratio = 0.4, indenter_radius = 20 * 10e-9)

expt_2.calc_modulus(plot_hist = True)

expt_1.plot_adhesion_modulus()

expt_1.save_data(’filename’)
```

A.2 Donators information

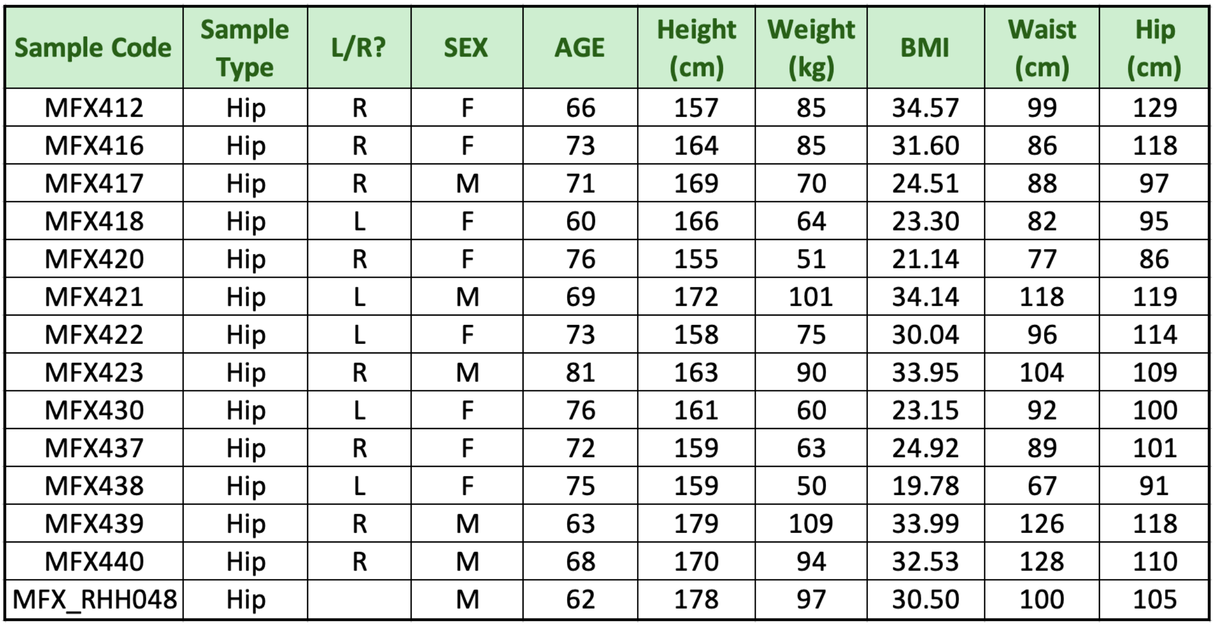

Sample Code	Sample Type	L/R?	SEX	AGE	Height (cm)	Weight (kg)	BMI	Waist (cm)	Hip (cm)
MFX412	Hip	R	F	66	157	85	34.57	99	129
MFX416	Hip	R	F	73	164	85	31.60	86	118
MFX417	Hip	R	M	71	169	70	24.51	88	97
MFX418	Hip	L	F	60	166	64	23.30	82	95
MFX420	Hip	R	F	76	155	51	21.14	77	86
MFX421	Hip	L	M	69	172	101	34.14	118	119
MFX422	Hip	L	F	73	158	75	30.04	96	114
MFX423	Hip	R	M	81	163	90	33.95	104	109
MFX430	Hip	L	F	76	161	60	23.15	92	100
MFX437	Hip	R	F	72	159	63	24.92	89	101
MFX438	Hip	L	F	75	159	50	19.78	67	91
MFX439	Hip	R	M	63	179	109	33.99	126	118
MFX440	Hip	R	M	68	170	94	32.53	128	110
MFX_RHH048	Hip		M	62	178	97	30.50	100	105

Figure A.1: Donor information of osteoarthritis patients.

A.3 Cartilage AFM images

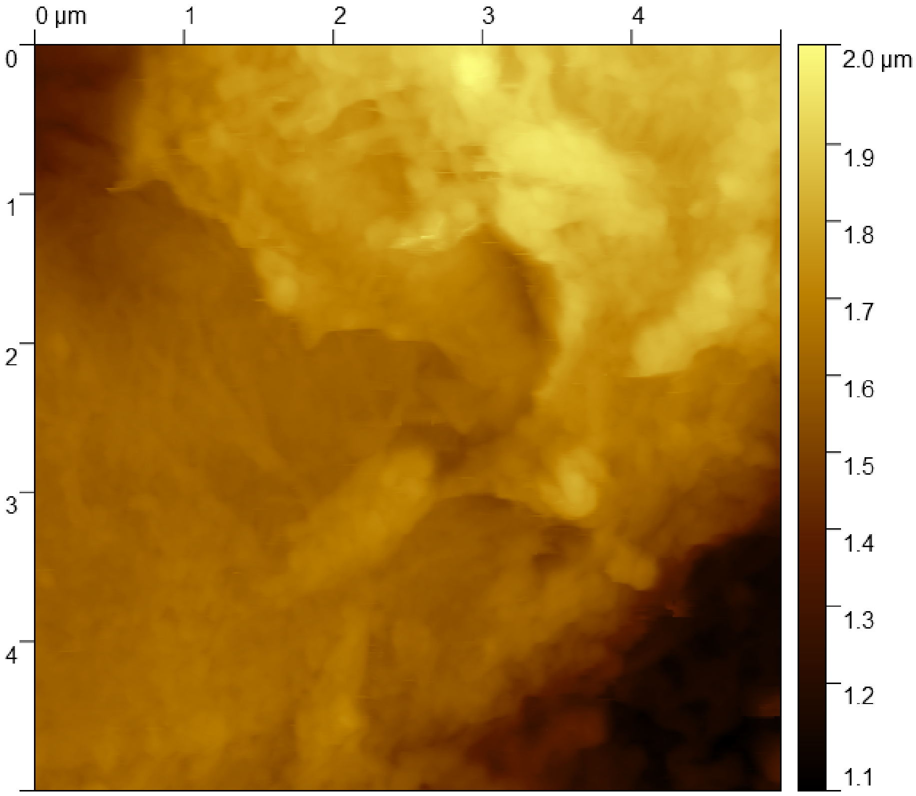

Figure A.2: AFM images of cartilage MFX 412.

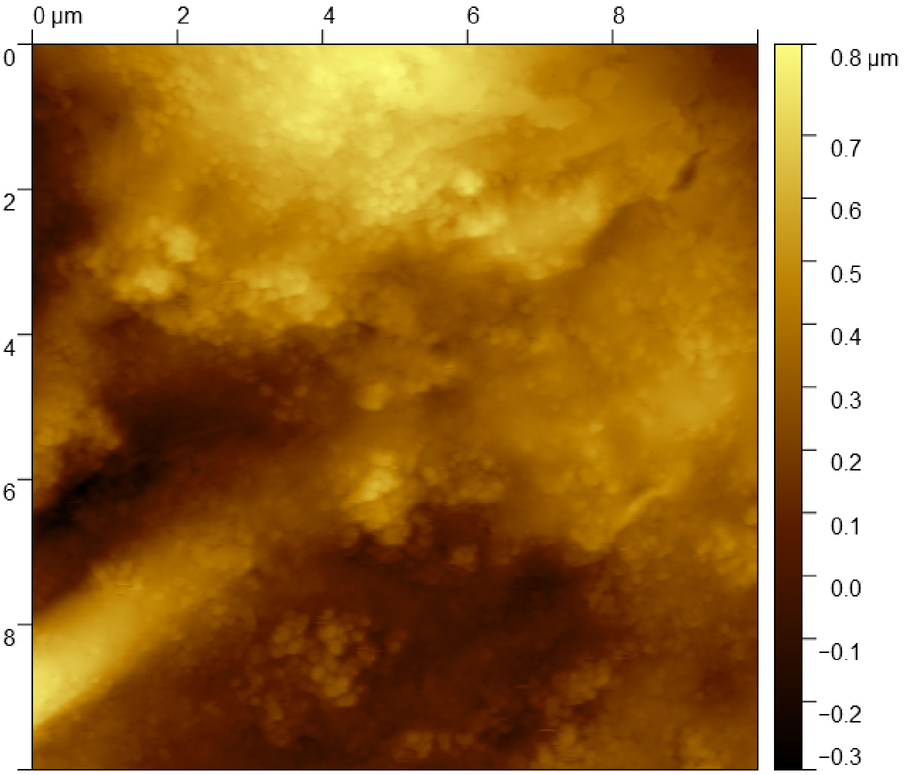

Figure A.3: AFM images of cartilage MFX 416.

A.4 Cartilage SEM images

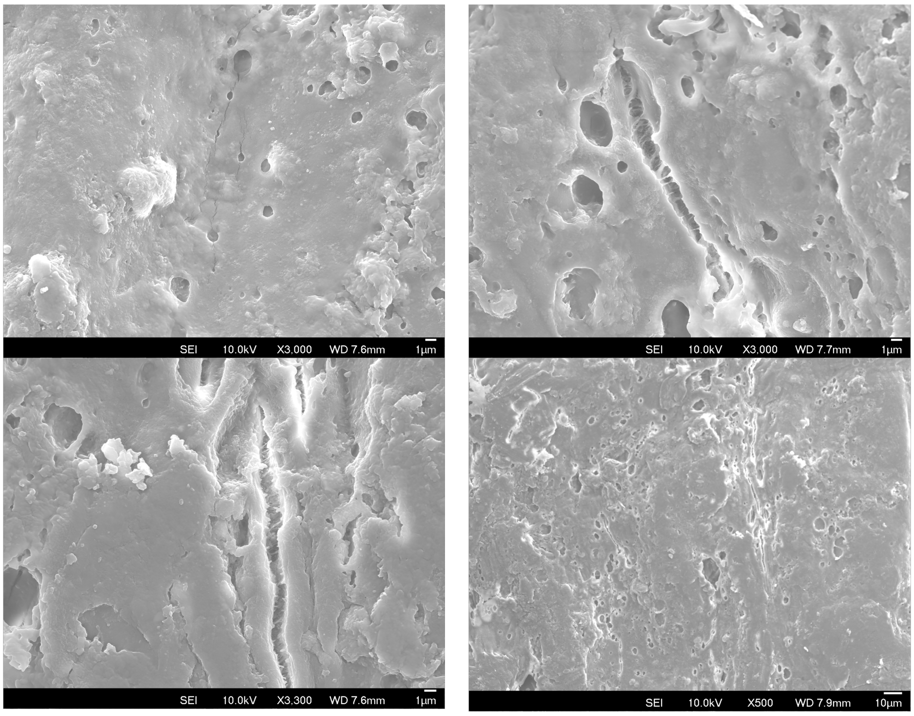

Figure A.4: SEM images of cartilage MFX 418.

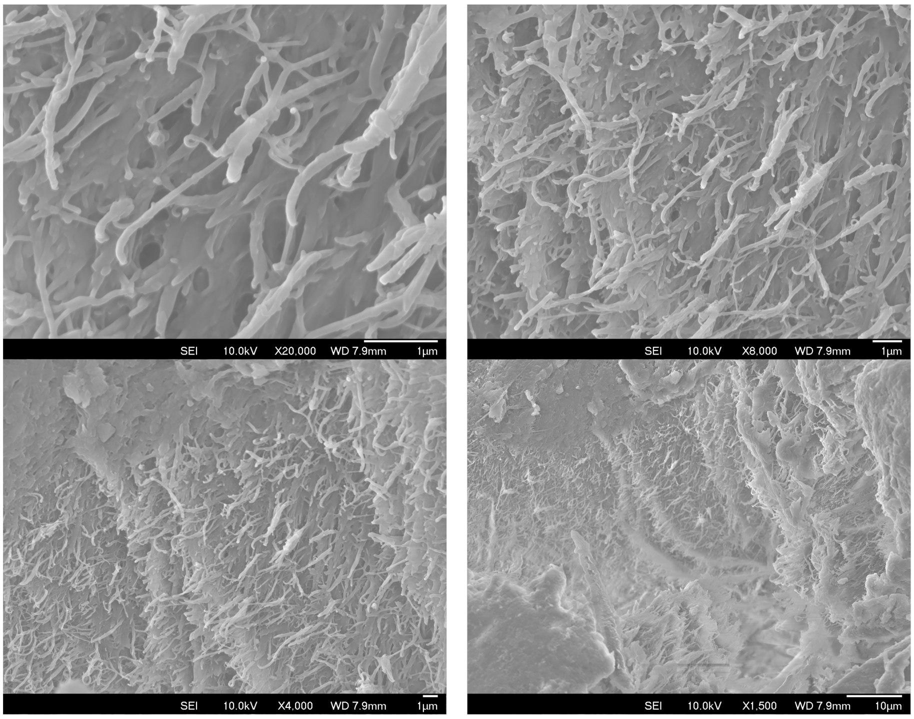

Figure A.5: SEM images of cartilage MFX 422.

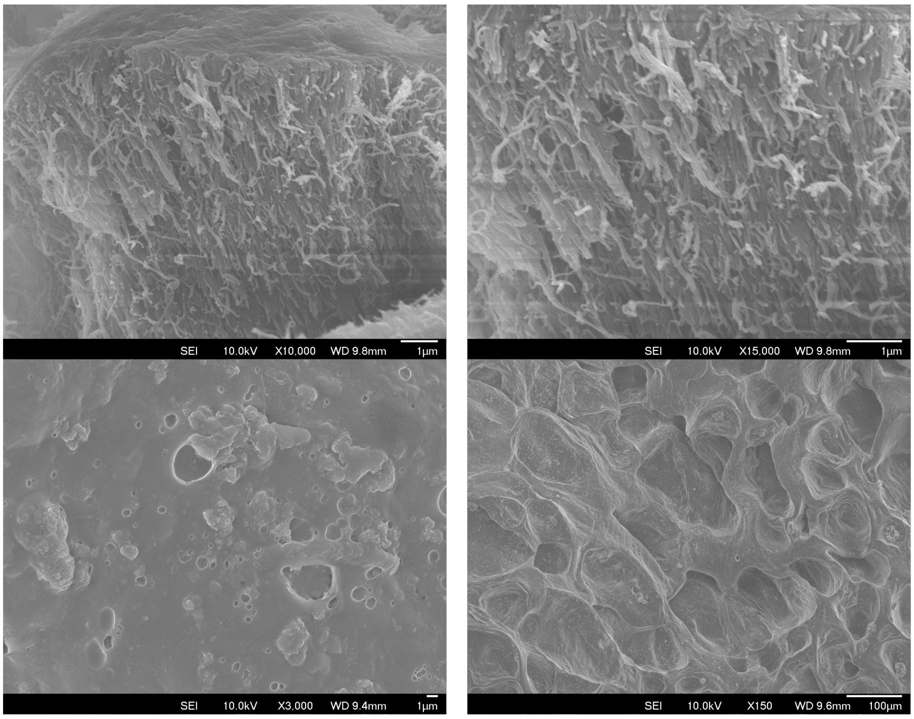

Figure A.6: SEM images of cartilage MFX 440.

References

[1] URL: https://www.arthritis.org/health-wellness/about-arthritis/understanding-arthritis/what-is-arthritis (visited on 08/22/2022).

[2] S. Grässel and D. Muschter. "Recent advances in the treatment of osteoarthritis". In: *F1000Research* 9 (2020).

[3] J. Graham, T. Novosat, H. Sun, B. Piper, J. Boscarino, M. Kern, V. Duboski, E. Wright, P. Schepman, R. Robinson, et al. "Osteoarthritis in a large integrated health system population: 18-Year retrospective review". In: 72 (2020).

[4] O. J. Morgan, H. J. Hillstrom, S. J. Ellis, Y. M. Golightly, R. Russell, M. T. Hannan, J. Deland III, and R. Hillstrom. "Osteoarthritis in England: incidence trends from National Health Service hospital episode statistics". In: *ACR Open Rheumatology* 1.8 (2019), pp. 493–498.

[5] P. M. Brooks. "Impact of osteoarthritis on individuals and society: how much disability? Social consequences and health economic implications". In: *Current Opinion in Rheumatology* 14.5 (2002), pp. 573–577.

[6] S. Safiri, A. A. Kolahi, E. Smith, C. Hill, D. Bettampadi, M. A. Mansournia, D. Hoy, A. Ashrafi-Asgarabad, M. Sepidarkish, A. Almasi-Hashiani, G. Collins, J. Kaufman, M. Qorbani, M. Moradi-Lakeh, A. D. Woolf, F. Guillemin, L. March, and M. Cross. "Global, regional and national burden of osteoarthritis 1990-2017: a systematic analy-

sis of the Global Burden of Disease Study 2017". In: *Annals of the Rheumatic Diseases* 79.6 (2020), pp. 819–828.

[7] R. Martins, N. Kotsopoulos, M. K. Kließ, C. Beck, L. Abraham, S. Large, P. Schepman, and M. P. Connolly. "Comparing the fiscal consequences of controlled and uncontrolled osteoarthritis pain applying a UK public economic perspective". In: *Journal of Health Economics and Outcomes Research* 8.1 (2021), p. 127.

[8] A. G. C. M. Chen, C. Gupte, K. Akhtar, P. Smith, and J. Cobb. "The global economic cost of osteoarthritis: how the UK compares". In: *Arthritis* 2012 (2012).

[9] V. P. Leifer, J. N. Katz, and E. Losina. "The burden of OA-health services and economics". In: *Osteoarthritis and Cartilage* 30.1 (2022), pp. 10–16.

[10] H. Kotlarz, C. L. Gunnarsson, H. Fang, and J. A. Rizzo. "Osteoarthritis and absenteeism costs: evidence from US National Survey Data". In: *Journal of Occupational and Environmental Medicine* (2010), pp. 263–268.

[11] L. S. Simon. "Osteoarthritis: a review". In: *Clinical Cornerstone* 2.2 (1999), pp. 26–37.

[12] P. Maudens, O. Jordan, and E. Allémann. "Recent advances in intra-articular drug delivery systems for osteoarthritis therapy". In: *Drug Discovery Today* 23.10 (2018), pp. 1761–1775.

[13] D. Blalock, A. Miller, M. Tilley, and J. Wang. "Joint instability and osteoarthritis". In: *Clinical Medicine Insights: Arthritis and Musculoskeletal Disorders* 8 (2015), CMAMD–S22147.

[14] J. P. Gong, Y. Katsuyama, T. Kurokawa, and Y. Osada. "Double-network hydrogels with extremely high mechanical strength". In: *Advanced Materials* 15.14 (2003), pp. 1155–1158.

[15] J. W. Alford and B. J. Cole. “Cartilage restoration, part 1: basic science, historical perspective, patient evaluation, and treatment options”. In: *The American Journal of Sports Medicine* 33.2 (2005), pp. 295–306.

[16] Sophia Fox, A. A. J. Bedi, and S. A. Rodeo. “The basic science of articular cartilage: structure, composition, and function”. In: *Sports Health* 1.6 (2009), pp. 461–468.

[17] G. W. Greene, X. Banquy, D. W. Lee, D. D. Lowrey, J. Yu, and J. N. Israelachvili. “Adaptive mechanically controlled lubrication mechanism found in articular joints”. In: *Proceedings of the National Academy of Sciences* 108.13 (2011), pp. 5255–5259.

[18] F. Berenbaum. “Osteoarthritis as an inflammatory disease (osteoarthritis is not osteoarthrosis!)” In: *Osteoarthritis and Cartilage* 21.1 (2013), pp. 16–21.

[19] D. I. Chen, J. Shen, W. Zhao, T. Wang, L. Han, J. L. Hamilton, and H. J. Im. “Osteoarthritis: toward a comprehensive understanding of pathological mechanism”. In: *Bone Research* 5.1 (2017), pp. 1–13.

[20] D. T. Felson. “Osteoarthritis of the knee”. In: *New England Journal of Medicine* 354.8 (2006), pp. 841–848.

[21] M. B. Goldring and S. R. Goldring. “Osteoarthritis”. In: *Journal of Cellular Physiology* 213.3 (2007), pp. 626–634.

[22] S. Krasnokutsky, J. Samuels, and S. B. Abramson. “Osteoarthritis in 2007.” In: *Bulletin of the NYU Hospital for Joint Diseases* 65.3 (2007), pp. 222–228.

[23] R. F. Loeser. “Aging and osteoarthritis: the role of chondrocyte senescence and aging changes in the cartilage matrix”. In: *Osteoarthritis and Cartilage* 17.8 (2009), pp. 971–979.

[24] R. F. Loeser, S. R. Goldring, C. R. Scanzello, and M. B. Goldring. “Osteoarthritis: a disease of the joint as an organ”. In: *Arthritis and Rheumatism* 64.6 (2012), p. 1697.

[25] L. E. Guenther, B. W. Pyle, T. R. Turgeon, E. R. Bohm, U. P. Wyss, T. A. Schmidt, and J. Brandt. “Biochemical analyses of human osteoarthritic and periprosthetic synovial fluid”. In: *Proceedings of the Institution of Mechanical Engineers, Part H: Journal of Engineering in Medicine* 228.2 (2014), pp. 127–139.

[26] M. A. Karsdal, M. Michaelis, C. Ladel, A. S. Siebuhr, A. R. Bihlet, J. R. Andersen, H. Guehring, C. Christiansen, A. C. Bay-Jensen, and V. B. Kraus. “Disease-modifying treatments for osteoarthritis (DMOADs) of the knee and hip: lessons learned from failures and opportunities for the future”. In: *Osteoarthritis and Cartilage* 24.12 (2016), pp. 2013–2021.

[27] M. C. Hochberg, A. Guermazi, H. Guehring, A. Aydemir, S. Wax, P. Fleuranceau-Morel, A. R. Bihlet, I. Byrjalsen, J. R. Andersen, and F. Eckstein. “Effect of intra-articular sprifermin vs placebo on femorotibial joint cartilage thickness in patients with osteoarthritis: the FORWARD randomized clinical trial”. In: *Jama* 322.14 (2019), pp. 1360–1370.

[28] N. Y. Adly, H. Hassani, A. Q. Tran, M. Balski, A. Yakushenko, A. Offenhäusser, D. Mayer, and B. Wolfrum. “Observation of chemically protected polydimethylsiloxane: towards crack-free PDMS”. In: *Soft Matter* 13.37 (2017), pp. 6297–6303.

[29] J. L. Hollander, E. M. Brown, R. A. Jessar, and C. Y. Brown. “Hydrocortisone and cortisone injected into arthritic joints: comparative effects of and use of hydrocortisone as a local antiarthritic agent”. In: *Journal of the American Medical Association* 147.17 (1951), pp. 1629–1635.

[30] C. Nguyen and F. Rannou. “The safety of intra-articular injections for the treatment of knee osteoarthritis: a critical narrative review”. In: *Expert Opinion on Drug Safety* 16.8 (2017), pp. 897–902.

[31] J. Cheng and S. Abdi. “Complications of joint, tendon, and muscle injections”. In: *Techniques in Regional Anesthesia and Pain Management* 11.3 (2007), pp. 141–147.

[32] J. K. Patra, G. Das, L. F. Fraceto, E. V. R. Campos, M. D. P. Rodriguez-Torres, L. S. Acosta-Torres, L. A. Diaz-Torres, R. Grillo, M. K. Swamy, S. Sharma, Habtemariam S., and Shin H. "Nano based drug delivery systems: recent developments and future prospects". In: *Journal of Nanobiotechnology* 16.1 (2018), pp. 1–33.

[33] S. A. Rizvi and A. M. Saleh. "Applications of nanoparticle systems in drug delivery technology". In: *Saudi Pharmaceutical Journal* 26.1 (2018), pp. 64–70.

[34] S. P. Darminesh, N. A. C. Sidik, G. Najafi, R. Mamat, T. L. Ken, and Y. Asako. "Recent development on biodegradable nanolubricant: A review". In: *International Communications in Heat and Mass Transfer* 86 (2017), pp. 159–165.

[35] V. C. Mow, A. Ratcliffe, and A. R. Poole. "Cartilage and diarthrodial joints as paradigms for hierarchical materials and structures". In: *Biomaterials* 13.2 (1992), pp. 67–97.

[36] J. R. Ralphs and M. Benjamin. "The joint capsule: structure, composition, ageing and disease." In: *Journal of Anatomy* 184.Pt 3 (1994), p. 503.

[37] D. Elewaut. *Kelley's Textbook of Rheumatology.* Ed. by Edward D. H. J. and Shaun R. Seventh edition. Elsevier Saunders, 2005. ISBN: 0721601413.

[38] J. DeLee, D. Drez, and M. D. Miller. *DeLee & Drez's orthopaedic sports medicine : principles and practice.* Ed. by J. DeLee, D. Drez, and M. D. Miller. Saunders, 2003. ISBN: 0721688454.

[39] S. Alexander, D. F. Southgate, A. M. Bull, and A. L. Wallace. "The role of negative intraarticular pressure and the long head of biceps tendon on passive stability of the glenohumeral joint". In: *Journal of Shoulder and Elbow Surgery* 22.1 (2013), pp. 94–101.

[40] P. Ziai, E. Benca, G. von Skrbensky, A. Graf, F. Wenzel, E. Basad, R. Windhager, and T. Buchhorn. "The role of the peroneal tendons in passive stabilisation of the

ankle joint: an in vitro study". In: *Knee Surgery, Sports Traumatology, Arthroscopy* 21.6 (2013), pp. 1404–1408.

[41] URL: https://www.healthline.com/health/ligament-vs-tendon#function (visited on 08/22/2022).

[42] E. Rath and J. C. Richmond. "The menisci: basic science and advances in treatment". In: *British Journal of Sports Medicine* 34.4 (2000), pp. 252–257.

[43] J. A. Buckwalter and H. J. Mankin. "Articular cartilage: part I". In: *The Journal of Bone and Joint Surgery* 79.4 (1997), p. 600.

[44] M. G. M. Antons J. Marascio, J. Nohava, R. Martin, L. A. Applegate, P. E. Bourban, and D. P. Pioletti. "Zone-dependent mechanical properties of human articular cartilage obtained by indentation measurements". In: *Journal of Materials Science: Materials in Medicine* 29.5 (2018), pp. 1–8.

[45] R. A. Stockwell. "The interrelationship of cell density and cartilage thickness in mammalian articular cartilage." In: *Journal of Anatomy* 109.Pt 3 (1971), p. 411.

[46] D. J. Responte, R. M. Natoli, and K. A. Athanasiou. "Collagens of articular cartilage: structure, function, and importance in tissue engineering". In: *Critical Reviews ^{TM} in Biomedical Engineering* 35.5 (2007).

[47] M. C. Killen and C. P. Charalambous. "Advances in cartilage restoration techniques". In: *Advances in Medical and Surgical Engineering*. Ed. by W. Ahmed, D. A. Phoenix, M. J. Jackson, and C. P. Charalambous. Elsevier, 2020, pp. 71–83. ISBN: 9780128197127.

[48] H. A. R. O. L. D. Lipshitz, R. Etheredge 3rd, and M. J. Glimcher. "Changes in the hexosamine content and swelling ratio of articular cartilage as functions of depth from the surface." In: *The Journal of bone and joint surgery. American volume* 58.8 (1976), pp. 1149–1153.

[49] L. A. Setton, W. Zhu, and V. C. Mow. “The biphasic poroviscoelastic behavior of articular cartilage: role of the surface zone in governing the compressive behavior”. In: *Journal of Biomechanics* 26.4-5 (1993), pp. 581–592.

[50] M. Mostakhdemin, A. Nand, and M. Ramezani. “Articular and artificial cartilage, characteristics, properties and testing approaches—a review”. In: *Polymers* 13.12 (2021), p. 2000.

[51] A. M. Bhosale and J. B. Richardson. “Articular cartilage: structure, injuries and review of management”. In: *British Medical Bulletin* 87.1 (2008), pp. 77–95.

[52] C. P. Charalambous. “Articular cartilage. Part II: Degeneration and osteoarthrosis, repair, regeneration, and transplantation”. In: *Classic Papers in Orthopaedics.* Ed. by P. A. Banaszkiewicz and D. F. Kader. Springer, 2014, pp. 389–391. ISBN: 9781447154518.

[53] H. Forster and J. Fisher. “The influence of loading time and lubricant on the friction of articular cartilage”. In: *Proceedings of the Institution of Mechanical Engineers, Part H: Journal of Engineering in Medicine* 210.2 (1996), pp. 109–119.

[54] M. Ramachandran. *Basic orthopaedic sciences.* Ed. by M. Ramachandran. CRC Press, 2018. ISBN: 9781444113501.

[55] H. Mahmood, D. Eckold, I. Stead, D. E. Shepherd, D. M. Espino, and K. D. Dearn. “A method for the assessment of the coefficient of friction of articular cartilage and a replacement biomaterial”. In: *Journal of the Mechanical Behavior of Biomedical Materials* 103 (2020), p. 103580.

[56] A. A. Mieloch, M. Richter, T. Trzeciak, M. Giersig, and J. D. Rybka. “Osteoarthritis severely decreases the elasticity and hardness of knee joint cartilage: A nanoindentation study”. In: *Journal of Clinical Medicine* 8.11 (2019), p. 1865.

[57] Z. Pawlak, W. Urbaniak, and A. Oloyede. “Natural articular joints: model of lamellar-roller-bearing lubrication and the nature of the cartilage surface”. In: *Biomaterials and Medical Tribology*. Ed. by Z. Pawlak, W. Urbaniak, and A. Oloyede. Woodhead Publishing, 2013, pp. 253–310. ISBN: 9780857090171.

[58] Z. Pawlak, W. Petelska A. D. Urbaniak, K. Q. Yusuf, and A. Oloyede. “Relationship between wettability and lubrication characteristics of the surfaces of contacting phospholipid-based membranes”. In: *Cell Biochemistry and Biophysics* 65.3 (2013), pp. 335–345.

[59] B. A. Hills and M. K. Monds. “Deficiency of lubricating surfactant lining the articular surfaces of replaced hips and knees”. In: *British Journal of Rheumatology* 37.2 (1998), pp. 143–147.

[60] Z. Pawlak, R. Pai, A. Mrela, M. Kaczmarek, K. Q. Yusuf, and W. Urbaniak. “Natural articular cartilage: A smart biointerface”. In: *Journal of Computational Methods in Sciences and Engineering* 19.2 (2019), pp. 479–489.

[61] WHO Scientific Group on the Burden of Musculoskeletal Conditions at the Start of the New Millennium et al. *The burden of musculoskeletal conditions at the start of the new millennium*. Ed. by WHO Scientific Group on the Burden of Musculoskeletal Conditions at the Start of the New Millennium et al. 2003. ISBN: 9241209194.

[62] J. A. Buckwalter and J. A. Martin. “Osteoarthritis”. In: *Advanced Drug Delivery Reviews* 58.2 (2006), pp. 150–167.

[63] C. M. Fergusson. “The aetiology of osteoarthritis.” In: *Postgraduate Medical Journal* 63.740 (1987), p. 439.

[64] D. McGonagle, A. L. Tan, J. Carey, and M. Benjamin. “The anatomical basis for a novel classification of osteoarthritis and allied disorders”. In: *Journal of Anatomy* 216.3 (2010), pp. 279–291.

[65] I. Meulenbelt, M. Kloppenburg, H. M. Kroon, J. J. Houwing-Duistermaat, P. Garnero, M. P. Hellio-Le Graverand, J. DeGroot, and P. E. Slagboom. “Clusters of biochemical markers are associated with radiographic subtypes of osteoarthritis (OA) in subject with familial OA at multiple sites. The GARP study”. In: *Osteoarthritis and Cartilage* 15.4 (2007), pp. 379–385.

[66] URL: https://www.britannica.com/technology/scanning-electron-microscope#/media/1/526571/110970 (visited on 08/22/2022).

[67] K. P. H. Pritzker, S. Gay, S. A. Jimenez, K. Ostergaard, J. P. Pelletier, P. A. Revell, D. Salter, and W. B. van den Berg. “Osteoarthritis cartilage histopathology: grading and staging”. In: *Osteoarthritis and Cartilage* 14.1 (2006), pp. 13–29.

[68] R. U. Kleemann, D. Krocker, A. Cedraro, J. Tuischer, and G. N. Duda. “Altered cartilage mechanics and histology in knee osteoarthritis: relation to clinical assessment (ICRS Grade)”. In: *Osteoarthritis and Cartilage* 13.11 (2005), pp. 958–963.

[69] N. Ajdari, C. Tempelaere, M. I. Masouleh, R. Abel, D. Delfosse, R. Emery, D. Dini, and U. Hansen. “Hemiarthroplasties: the choice of prosthetic material causes different levels of damage in the articular cartilage”. In: *Journal of Shoulder and Elbow Surgery* 29.5 (2020), pp. 1019–1029.

[70] S. S. Lee, C. T. Duong, S. H. Park, Y. Cho, S. Park, and S. Park. “Frictional response of normal and osteoarthritic articular cartilage in human femoral head”. In: *Proceedings of the Institution of Mechanical Engineers, Part H: Journal of Engineering in Medicine* 227.2 (2013), pp. 129–137.

[71] M. B. Goldring and M. Otero. “Inflammation in osteoarthritis”. In: *Current Opinion in Rheumatology* 23.5 (2011), p. 471.

[72] D. Lajeunesse and P. Reboul. “Subchondral bone in osteoarthritis: a biologic link with articular cartilage leading to abnormal remodeling”. In: *Current Opinion in Rheumatology* 15.5 (2003), pp. 628–633.

[73] S. M. Seed, K. C. Dunican, and A. M. Lynch. “Osteoarthritis: a review of treatment options.” In: *Geriatrics* 64.10 (2009).

[74] J. Sellam and F. Berenbaum. “The role of synovitis in pathophysiology and clinical symptoms of osteoarthritis”. In: *Nature Reviews Rheumatology* 6.11 (2010), pp. 625–635.

[75] C. R. Scanzello, A. Plaas, and M. K. Crow. “Innate immune system activation in osteoarthritis: is osteoarthritis a chronic wound?” In: *Current Opinion in Rheumatology* 20.5 (2008), pp. 565–572.

[76] J. Sokolove and C. M. Lepus. “Role of inflammation in the pathogenesis of osteoarthritis: latest findings and interpretations”. In: *Therapeutic Advances in Musculoskeletal Disease* 5.2 (2013), pp. 77–94.

[77] M. N. Farahat, G. Yanni, R. Poston, and G. S. Panayi. “Cytokine expression in synovial membranes of patients with rheumatoid arthritis and osteoarthritis.” In: *Annals of Rheumatic Diseases* 52.12 (1993), pp. 870–875.

[78] E. G. NNettelbladt and L. K. Sundblad. “Protein patterns in synovial fluid and serum in rheumatoid arthritis and osteoarthritis”. In: *Arthritis & Rheumatism: Official Journal of the American College of Rheumatology* 2.2 (1959), pp. 144–151.

[79] S. P. Messier, R. F. Loeser, G. D. Miller, T. M. Morgan, W. J. Rejeski, M. A. Sevick, W. H. Ettinger Jr, M. Pahor, and J. D. Williamson. “Exercise and dietary weight loss in overweight and obese older adults with knee osteoarthritis: the Arthritis, Diet, and Activity Promotion Trial”. In: *Arthritis & Rheumatism* 50.5 (2004), pp. 1501–1510.

[80] A. Pendleton, N. Arden, M. Dougados, M. Doherty, B. Bannwarth, J. W. J. Bijlsma, F. Cluzeau, C. Cooper, P. A. Dieppe, K. P. Günther, H. J. Hauselmann, G. Herrero-Beaumont, P. M. Kaklamanis, B. Leeb, M Lequesne, S. Lohmander, B. Mazieres, E. Mola, K. Pavelka, U. Serni, B. Swoboda, A. A. Verbruggen, G Weseloh, and I. Zimmermann-Gorska. "EULAR recommendations for the management of knee osteoarthritis: report of a task force of the Standing Committee for International Clinical Studies Including Therapeutic Trials (ESCISIT)". In: *Annals of the Rheumatic Diseases* 59.12 (2000), pp. 936–944.

[81] R. S. Hinman, K. M. Crossley, J. McConnell, and K. L. Bennell. "Efficacy of knee tape in the management of osteoarthritis of the knee: blinded randomised controlled trial". In: *BMJ* 327.7407 (2003), p. 135.

[82] R. Brignardello-Petersen, G. H. Guyatt, R. Buchbinder, R. W. Poolman, S. Schandelmaier, Y. Chang, B. Sadeghirad, N. Evaniew, and P. O. Vandvik. "Knee arthroscopy versus conservative management in patients with degenerative knee disease: a systematic review". In: *BMJ open* 7.5 (2017), e016114.

[83] G. Nazari and J. C. MacDermid. "Appraisal of Clinical Practice Guideline: Arthroscopic surgery for degenerative knee arthritis and meniscal tears: a clinical practice guideline". In: *Journal of Physiotherapy* 66.1 (2020), p. 60.

[84] S. Reichenbach, A. W. Rutjes, E. Nüesch, S. Trelle, and P. Jüni. "Joint lavage for osteoarthritis of the knee". In: *Cochrane Database of Systematic Reviews* 5 (2010).

[85] J. B. Thorlund, C. B. Juhl, E. M. Roos, and L. S. Lohmander. "Arthroscopic surgery for degenerative knee: systematic review and meta-analysis of benefits and harms". In: *BMJ* 350 (2015).

[86] D. J. Hunter and Bierma-Zeinstra S. "Osteoarthritis". In: *Lancet* 393.10182 (2019), pp. 1745–1759.

[87] K. L. Spiller, S. A. Maher, and A. M. Lowman. “Hydrogels for the repair of articular cartilage defects”. In: *Tissue Engineering Part B: Reviews* 17.4 (2011), pp. 281–299.

[88] W. Y. Zhang and A. Li Wan Po. “The effectiveness of topically applied capsaicin. A meta-analysis.” In: *European Journal of Clinical Pharmacology* 46.6 (1994), pp. 517–522.

[89] M. S. Cepeda, F. Camargo, C. Zea, and L. Valencia. “Tramadol for osteoarthritis”. In: *Cochrane Database of Systematic Reviews* 3 (2006).

[90] T. B. Lawson, J. T. Mäkelä, T. Klein, B. D. Snyder, and M. W. Grinstaff. “Nanotechnology and Osteoarthritis. Part 2: Opportunities for advanced devices and therapeutics”. In: *Journal of Orthopaedic Research* 39.3 (2021), pp. 473–484.

[91] C. Larsen, J. Østergaard, S. W. Larsen, H. Jensen, S. Jacobsen, C. Lindegaard, and P. H. Andersen. “Intra-articular depot formulation principles: Role in the management of postoperative pain and arthritic disorders”. In: *Journal of Pharmaceutical Sciences* 97.11 (2008), pp. 4622–4654.

[92] S. Brown, S. Kumar, and B. Sharma. “Intra-articular targeting of nanomaterials for the treatment of osteoarthritis”. In: *Acta Biomaterialia* 93 (2019), pp. 239–257.

[93] E. Horisawa, K. Kubota, I. Tuboi, K. Sato, H. Yamamoto, H. Takeuchi, and Y. Kawashima. “Size-dependency of DL-lactide/glycolide copolymer particulates for intra-articular delivery system on phagocytosis in rat synovium”. In: *Pharmaceutical Research* 19.2 (2002), pp. 132–139.

[94] T. K. Mwangi, I. M. Berke, E. H. Nieves, R. D. Bell, S. B. Adams, and L. A. Setton. “Intra-articular clearance of labeled dextrans from naive and arthritic rat knee joints”. In: *Journal of Controlled Release* 283 (2018), pp. 76–83.

[95] C. Sacchetti, R. Liu-Bryan, A. Magrini, N. Rosato, N. Bottini, and M. Bottini. “Polyethylene-glycol-modified single-walled carbon nanotubes for intra-articular delivery to chondrocytes”. In: *ACS Nano* 8.12 (2014), pp. 12280–12291.

[96] J. Pradal, P. Maudens, C. Gabay, C. A. Seemayer, O. Jordan, and E. Allémann. “Effect of particle size on the biodistribution of nano-and microparticles following intra-articular injection in mice”. In: *International Journal of Pharmaceutics* 498.1-2 (2016), pp. 119–129.

[97] M. L. Kang, J. E. Kim, and G. I. Im. “Thermoresponsive nanospheres with independent dual drug release profiles for the treatment of osteoarthritis”. In: *Acta Biomaterialia* 39 (2016), pp. 65–78.

[98] A. G. Bajpayee, M. Scheu, A. J. Grodzinsky, and R. M. Porter. “Electrostatic interactions enable rapid penetration, enhanced uptake and retention of intra-articular injected avidin in rat knee joints”. In: *Journal of Orthopaedic Research* 32.8 (2014), pp. 1044–1051.

[99] M. Morgen, D. Tung, B. Boras, W. Miller, A. M. Malfait, and M. Tortorella. “Nanoparticles for improved local retention after intra-articular injection into the knee joint”. In: *Pharmaceutical Research* 30.1 (2013), pp. 257–268.

[100] N. Nakano, C. Gohal, A. Duong, O. R. Ayeni, and V. Khanduja. “Outcomes of cartilage repair techniques for chondral injury in the hip—a systematic review”. In: *International Orthopaedics* 42.10 (2018), pp. 2309–2322.

[101] C. Camacho-Hübner, O. Nilsson, and L. Saevendahl. *Cartilage and bone development and its disorders.* Ed. by C. Camacho-Hübner, O. Nilsson, and L. Saevendahl. Karger Medical and Scientific Publishers, 2011. ISBN: 9783805597920.

[102] R. Tuli, W. J. Li, and R. S. Tuan. “Current state of cartilage tissue engineering”. In: *Arthritis Research & Therapy* 5.5 (2003), pp. 1–4.

[103] Y. Ikada. “Challenges in tissue engineering”. In: *Journal of the Royal Society Interface* 3.10 (2006), pp. 589–601.

[104] C. Chung and J. A. Burdick. “Engineering cartilage tissue”. In: *Advanced Drug Delivery Reviews* 60.2 (2008), pp. 243–262.

[105] S. J. Bryant and K. S. Anseth. “Controlling the spatial distribution of ECM components in degradable PEG hydrogels for tissue engineering cartilage”. In: *Journal of Biomedical Materials Research Part A: An Official Journal of The Society for Biomaterials, The Japanese Society for Biomaterials, and The Australian Society for Biomaterials and the Korean Society for Biomaterials* 64.1 (2003), pp. 70–79.

[106] N. Kubota, N. Tatsumoto, T. Sano, and K. Toya. “A simple preparation of half N-acetylated chitosan highly soluble in water and aqueous organic solvents”. In: *Carbohydrate Research* 324.4 (2000), pp. 268–274.

[107] H. Sashiwa, H. Yajima, and S.I. Aiba. “Synthesis of a chitosan- dendrimer hybrid and its biodegradation”. In: *Biomacromolecules* 4.5 (2003), pp. 1244–1249.

[108] M. Brittberg, E. Sjögren-Jansson, A. Lindahl, and L. Peterson. “Influence of fibrin sealant (Tisseel®) on osteochondral defect repair in the rabbit knee”. In: *Biomaterials* 18.3 (1997), pp. 235–242.

[109] S. Trattnig, K. Ohel, V. Mlynarik, V. Juras, S. Zbyn, and A. Korner. “Morphological and compositional monitoring of a new cell-free cartilage repair hydrogel technology–GelrinC by MR using semi-quantitative MOCART scoring and quantitative T2 index and new zonal T2 index calculation”. In: *Osteoarthritis and Cartilage* 23.12 (2015), pp. 2224–2232.

[110] D. L. Nettles, T. P. Vail, M. T. Morgan, M. W. Grinstaff, and L. A. Setton. “Photocrosslinkable hyaluronan as a scaffold for articular cartilage repair”. In: *Annals of Biomedical Engineering* 32.3 (2004), pp. 391–397.

[111] W. S. Toh, E. H. Lee, X. M. Guo, J. K. Chan, C. H. Yeow, A. B. Choo, and T. Cao. "Cartilage repair using hyaluronan hydrogel-encapsulated human embryonic stem cell-derived chondrogenic cells". In: *Biomaterials* 31.27 (2010), pp. 6968–6980.

[112] R. M. Jeuken, A. K. Roth, R. J. Peters, C. C. Van Donkelaar, J. C. Thies, L. W. Van Rhijn, and P. J. Emans. "Polymers in cartilage defect repair of the knee: current status and future prospects". In: *Polymers* 8.6 (2016), p. 219.

[113] P. Gentile, V. Chiono, I. Carmagnola, and P. V. Hatton. "An overview of poly (lactic-co-glycolic) acid (PLGA)-based biomaterials for bone tissue engineering". In: *International Journal of Molecular Sciences* 15.3 (2014), pp. 3640–3659.

[114] P. X. Ma. "Scaffolds for tissue fabrication". In: *Materials Today* 7.5 (2004), pp. 30–40.

[115] R. Ma, D. Xiong, F. Miao, J. Zhang, and Y. Peng. "Novel PVP/PVA hydrogels for articular cartilage replacement". In: *Materials Science and Engineering: C* 29.6 (2009), pp. 1979–1983.

[116] W. S. Toh and X. J. Loh. "Advances in hydrogel delivery systems for tissue regeneration". In: *Materials Science and Engineering: C* 45 (2014), pp. 690–697.

[117] A. Thangprasert, C. Tansakul, N. Thuaksubun, and J. Meesane. "Mimicked hybrid hydrogel based on gelatin/PVA for tissue engineering in subchondral bone interface for osteoarthritis surgery". In: *Materials & Design* 183 (2019), p. 108113.

[118] W. Xia, W. Liu, L. Cui, Y. Liu, W. Zhong, D. Liu, J. Wu, K. Chua, and Y. Cao. "Tissue engineering of cartilage with the use of chitosan-gelatin complex scaffolds". In: *Journal of Biomedical Materials Research Part B* 71.2 (2004), pp. 373–380.

[119] V. F. Sechriest, Y. J. Miao, C. Niyibizi, A. Westerhausen–Larson, H. W. Matthew, C. H. Evans, F. H. Fu, and J. K. Suh. "GAG-augmented polysaccharide hydrogel: A novel biocompatible and biodegradable material to support chondrogenesis". In:

Journal of Biomedical Materials Research: An Official Journal of The Society for Biomaterials and The Japanese Society for Biomaterials 49.4 (2000), pp. 534–541.

[120] I. Y. Kim, S. J. Seo, H. S. Moon, M. K.g Yoo, I. Y. Park, B. C. Kim, and C. S. Cho. “Chitosan and its derivatives for tissue engineering applications”. In: *Biotechnology Advances* 26.1 (2008), pp. 1–21.

[121] A. M. Haaparanta, E. Järvinen, I. F. Cengiz, V. Ellä, H. T. Kokkonen, I. Kiviranta, and M. Kellomäki. “Preparation and characterization of collagen/PLA, chitosan/PLA, and collagen/chitosan/PLA hybrid scaffolds for cartilage tissue engineering”. In: *Journal of Materials Science: Materials in Medicine* 25.4 (2014), pp. 1129–1136.

[122] S. Pina, J. M. Oliveira, and R. L. Reis. “Natural-based nanocomposites for bone tissue engineering and regenerative medicine: A review”. In: *Advanced Materials* 27.7 (2015), pp. 1143–1169.

[123] M. Janitermi, S. G. A. Jorsarai, and E. Fattahi. “Chondrogenic Differentiation of Mesenchymal Stem Cells from Rat Bone Marrow on the Elastic Modulus of Electrospun Silk Fibroin Scaffolds”. In: *Regenerative Engineering and Translational Medicine* 8.1 (2022), pp. 125–133.

[124] J. A. Burdick and G. D. Prestwich. “Hyaluronic acid hydrogels for biomedical applications”. In: *Advanced Materials* 23.12 (2011), H41–H56.

[125] L. K. Shopperly, J. Spinnen, J. P. Krüger, M. Endres, M. Sittinger, T. Lam, L. Kloke, and T. Dehne. “Blends of gelatin and hyaluronic acid stratified by stereolithographic bioprinting approximate cartilaginous matrix gradients”. In: *Journal of Biomedical Materials Research Part B: Applied Biomaterials* (2022).

[126] J. G. Alauzun, S. Young, R. d'Souza, L. Liu, M. A. Brook, and H. D. Sheardown. "Biocompatible, hyaluronic acid modified silicone elastomers". In: *Biomaterials* 31.13 (2010), pp. 3471–3478.

[127] J. M. Anderson, N. P. Ziats, A. Azeez, M. R. Brunstedt, S. Stack, and T. L. Bonfield. "Protein adsorption and macrophage activation on polydimethylsiloxane and silicone rubber". In: *Journal of Biomaterials Science, Polymer Edition* 7.2 (1996), pp. 159–169.

[128] M. Ö. Öztürk. "Preparation and characterization of cartilage mimicked structures". MA thesis. Biyo-Medikal Mühendislik Enstitüsü, 2014.

[129] W. Tan, R. Krishnaraj, and T. A. Desai. "Evaluation of nanostructured composite collagen–chitosan matrices for tissue engineering". In: *Tissue Engineering* 7.2 (2001), pp. 203–210.

[130] D. H. Rosenzweig, E. Carelli, T. Steffen, P. Jarzem, and L. Haglund. "3D-printed ABS and PLA scaffolds for cartilage and nucleus pulposus tissue regeneration". In: *International Journal of Molecular Sciences* 16.7 (2015), pp. 15118–15135.

[131] X. Zhou, G. Zhou, R. Junka, N. Chang, A. Anwar, H. Wang, and X. Yu. "Fabrication of polylactic acid (PLA)-based porous scaffold through the combination of traditional bio-fabrication and 3D printing technology for bone regeneration". In: *Colloids and Surfaces B: Biointerfaces* 197 (2021), p. 111420.

[132] Y. Liu, K. Tian, J. Hao, T. Yang, X. Geng, and W. Zhang. "Biomimetic poly (glycerol sebacate)/polycaprolactone blend scaffolds for cartilage tissue engineering". In: *Journal of Materials Science: Materials in Medicine* 30.5 (2019), pp. 1–11.

[133] D. Bakhshayesh, A. Rahmani, N. Asadi, A. Alihemmati, H. Tayefi Nasrabadi, A. Montaseri, S. Davaran, S. Saghati, A. Akbarzadeh, and A. Abedelahi. "An overview of advanced biocompatible and biomimetic materials for creation of replacement struc-

tures in the musculoskeletal systems: focusing on cartilage tissue engineering". In: *Journal of Biological Engineering* 13.1 (2019), pp. 1–21.

[134] X. Gao, J. Song, P. Ji, X. Zhang, X. Li, X. Xu, M. Wang, S. Zhang, Y. Deng, F. Deng, and S. Wei. "Polydopamine-templated hydroxyapatite reinforced polycaprolactone composite nanofibers with enhanced cytocompatibility and osteogenesis for bone tissue engineering". In: *ACS Applied Materials & Interfaces* 8.5 (2016), pp. 3499–3515.

[135] T. H. Courtney. *Mechanical behavior of materials.* Ed. by T. H. Courtney. McGraw-Hill, 1990. ISBN: 0070132658.

[136] S. Gupta, F. Carrillo, C. Li, L. Pruitt, and C. Puttlitz. "Adhesive forces significantly affect elastic modulus determination of soft polymeric materials in nanoindentation". In: *Materials Letters* 61.2 (2007), pp. 448–451.

[137] Z. Wang, A. A. Volinsky, and N. D. Gallant. "Crosslinking effect on polydimethylsiloxane elastic modulus measured by custom-built compression instrument". In: *Journal of Applied Polymer Science* 131.22 (2014).

[138] I. D. Johnston, D. K. McCluskey, C. K. L. Tan, and M. C. Tracey. "Mechanical characterization of bulk Sylgard 184 for microfluidics and microengineering". In: *Journal of Micromechanics and Microengineering* 24.3 (2014), p. 035017.

[139] M. Liu, J. Sun, and Q. Chen. "Influences of heating temperature on mechanical properties of polydimethylsiloxane". In: *Sensors and Actuators A: Physical* 151.1 (2009), pp. 42–45.

[140] W. M. Kolling. "Handbook of pharmaceutical excipients". In: *American Journal of Pharmaceutical Education* 68.1-5 (2004), BF1.

[141] A. Kumar and S. S. Han. "PVA-based hydrogels for tissue engineering: A review". In: *International Journal of Polymeric Materials and Polymeric Biomaterials* 66.4 (2017), pp. 159–182.

[142] Y. Liu, L. M. Geever, J. E. Kennedy, C. L. Higginbotham, P. A. Cahill, and G. B. McGuinness. “Thermal behavior and mechanical properties of physically crosslinked PVA/Gelatin hydrogels”. In: *Journal of the Mechanical Behavior of Biomedical Materials* 3.2 (2010), pp. 203–209.

[143] C. C. DeMerlis and D. R. Schoneker. “Review of the oral toxicity of polyvinyl alcohol (PVA)”. In: *Food and chemical Toxicology* 41.3 (2003), pp. 319–326.

[144] T. Trantidou, Y. Elani, E. Parsons, and O. Ces. “Hydrophilic surface modification of PDMS for droplet microfluidics using a simple, quick, and robust method via PVA deposition”. In: *Microsystems & Nanoengineering* 3.1 (2017), pp. 1–9.

[145] T. Zhou, J. Yang, D. Zhu, J. Zheng, S. Handschuh-Wang, X. Zhou, J. Zhang, Y. Liu, Z. Liu, C. He, and X. Zhou. “Hydrophilic Sponges for Leaf-Inspired Continuous Pumping of Liquids”. In: *Advanced Science* 4.6 (2017), p. 1700028.

[146] V. Karageorgiou and D. Kaplan. “Porosity of 3D biomaterial scaffolds and osteogenesis”. In: *Biomaterials* 26.27 (2005), pp. 5474–5491.

[147] Z. Pan, P. Duan, X. Liu, H. Wang, L. Cao, Y. He, J. Dong, and J. Ding. “Effect of porosities of bilayered porous scaffolds on spontaneous osteochondral repair in cartilage tissue engineering”. In: *Regenerative Biomaterials* 2.1 (2015), pp. 9–19.

[148] T. B. F. Woodfield, J. Malda, J. De Wijn, F. Peters, J. Riesle, and C. A. van Blitterswijk. “Design of porous scaffolds for cartilage tissue engineering using a three-dimensional fiber-deposition technique”. In: *Biomaterials* 25.18 (2004), pp. 4149–4161.

[149] Y. Wang, H. J. Kim, G. Vunjak-Novakovic, and D. L. Kaplan. “Stem cell-based tissue engineering with silk biomaterials”. In: *Biomaterials* 27.36 (2006), pp. 6064–6082.

[150] R. Nazarov, H. J. Jin, and D. L. Kaplan. “Porous 3-D scaffolds from regenerated silk fibroin”. In: *Biomacromolecules* 5.3 (2004), pp. 718–726.

[151] G. Chen and N. Kawazoe. “Porous scaffolds for regeneration of cartilage, bone and osteochondral tissue”. In: *Osteochondral Tissue Engineering* (2018), pp. 171–191.

[152] V. C. Mow, M. H. Holmes, and W. M. Lai. “Fluid transport and mechanical properties of articular cartilage: a review”. In: *Journal of Biomechanics* 17.5 (1984), pp. 377–394.

[153] G. Han, C. Hess, M. Eriten, and C. R. Henak. “Uncoupled poroelastic and intrinsic viscoelastic dissipation in cartilage”. In: *Journal of the Mechanical Behavior of Biomedical Materials* 84 (2018), pp. 28–34.

[154] D. Zhu, S. Handschuh-Wang, and X. Zhou. “Recent progress in fabrication and application of polydimethylsiloxane sponges”. In: *Journal of Materials Chemistry A* 5.32 (2017), pp. 16467–16497.

[155] S. Liang, Y. Li, J. Yang, J. Zhang, C. He, Y. Liu, and X. Zhou. “3D Stretchable, Compressible, and Highly Conductive Metal-Coated Polydimethylsiloxane Sponges”. In: *Advanced Materials Technologies* 1.7 (2016), p. 1600117.

[156] S. Duan, K. Yang, Z. Wang, M. Chen, L. Zhang, H. Zhang, and C. Li. “Fabrication of highly stretchable conductors based on 3D printed porous poly (dimethylsiloxane) and conductive carbon nanotubes/graphene network”. In: *ACS applied materials & interfaces* 8.3 (2016), pp. 2187–2192.

[157] J.W. Han, B. Kim, J. Li, and M. Meyyappan. “Han, J. W. and Kim, B. and Li, J. and Meyyappan, M.” In: *Applied Physics Letters* 102.5 (2013), p. 051903.

[158] S. J. Choi, T. H. Kwon, H. Im, D. I. Moon, D. J. Baek, M. L. Seol, J. P. Duarte, and Y. K. Choi. “A polydimethylsiloxane (PDMS) sponge for the selective absorption of oil from water”. In: *ACS Applied Materials & Interfaces* 3.12 (2011), pp. 4552–4556.

[159] P. Thurgood, S. Baratchi, C. Szydzik, A. Mitchell, and K. Khoshmanesh. “Porous PDMS structures for the storage and release of aqueous solutions into fluidic environments”. In: *Lab on a Chip* 17.14 (2017), pp. 2517–2527.

[160] J. González-Rivera, R. Iglio, G. Barillaro, C. Duce, and M. R. Tinè. “Structural and thermoanalytical characterization of 3D porous PDMS foam materials: the effect of impurities derived from a sugar templating process”. In: *Polymers* 10.6 (2018), p. 616.

[161] H. Montazerian, M. G. A. Mohamed, M. M. Montazeri, S. Kheiri, A. S. Milani, K. Kim, and M. Hoorfar. “Permeability and mechanical properties of gradient porous PDMS scaffolds fabricated by 3D-printed sacrificial templates designed with minimal surfaces”. In: *Acta Biomaterialia* 96 (2019), pp. 149–160.

[162] Q. Li, T. Duan, J. Shao, and H. Yu. “Fabrication method for structured porous polydimethylsiloxane (PDMS)”. In: *Journal of Materials Science* 53.16 (2018), pp. 11873–11882.

[163] D. Zhang, W. L. Burkes, C. A. Schoener, and M. A. Grunlan. “Porous inorganic–organic shape memory polymers”. In: *Polymer* 53.14 (2012), pp. 2935–2941.

[164] A. Prasad, M. R. Sankar, and V. Katiyar. “State of art on solvent casting particulate leaching method for orthopedic scaffoldsfabrication”. In: *Materials Today: Proceedings* 4.2 (2017), pp. 898–907.

[165] D. Sin, X. Miao, G. Liu, F. Wei, G. Chadwick, C. Yan, and T. Friis. “Polyurethane (PU) scaffolds prepared by solvent casting/particulate leaching (SCPL) combined with centrifugation”. In: *Materials Science and Engineering: C* 30.1 (2010), pp. 78–85.

[166] E. Ayhan, H. Kesmezacar, and I. Akgun. “Intraarticular injections (corticosteroid, hyaluronic acid, platelet rich plasma) for the knee osteoarthritis”. In: *World Journal of Orthopedics* 5.3 (2014), p. 351.

[167] S. Mehta, T. He, and A. G. Bajpayee. “Recent advances in targeted drug delivery for treatment of osteoarthritis”. In: *Current Opinion in Rheumatology* 33.1 (2021), p. 94.

[168] V. Sanna, N. Pala, and M. Sechi. “Targeted therapy using nanotechnology: focus on cancer”. In: *International Journal of Nanomedicine* 9 (2014), p. 467.

[169] Zhiyue Zhang and Guihua Huang. “Micro- and nano-carrier mediated intra-articular drug delivery systems for the treatment of osteoarthritis”. In: *Journal of Nanotechnology* 2012 (2012), p. 748909.

[170] B. Kapoor, S. K. Singh, M. Gulati, R. Gupta, and Y. Vaidya. “Application of liposomes in treatment of rheumatoid arthritis: quo vadis”. In: *The Scientific World Journal* 2014 (2014), p. 978351.

[171] J. B. Lin, S. Poh, and A. Panitch. “Controlled release of anti-inflammatory peptides from reducible thermosensitive nanoparticles suppresses cartilage inflammation”. In: *Nanomedicine: Nanotechnology, Biology and Medicine* 12.7 (2016), pp. 2095–2100.

[172] A. S. Vanniasinghe, V. Bender, and N. Manolios. “The potential of liposomal drug delivery for the treatment of inflammatory arthritis”. In: 39.3 (2009), pp. 182–196.

[173] G. W. Lu and P. Gao. “Emulsions and microemulsions for topical and transdermal drug delivery”. In: *Handbook of non-invasive drug delivery systems*. Ed. by Vitthal S. Kulkarni. William Andrew Publishing, 2010, pp. 59–94. ISBN: 9780815520252.

[174] T. Saeedi, H. F. Alotaibi, and P. Prokopovich. “Polymer colloids as drug delivery systems for the treatment of arthritis”. In: *Advances in Colloid and Interface Science* 285 (2020), p. 102273.

[175] L. Gan, J. Wang, M. Jiang, H. Bartlett, D. Ouyang, F. Eperjesi, J. Liu, and Y. Gan. “Recent advances in topical ophthalmic drug delivery with lipid-based nanocarriers”. In: *Drug Discovery Today* 18.5-6 (2013), pp. 290–297.

[176] V. K. Rai, N. Mishra, K. S. Yadav, and N. P. Yadav. “Nanoemulsion as pharmaceutical carrier for dermal and transdermal drug delivery: Formulation development, stability

issues, basic considerations and applications". In: *Journal of Controlled Release* 270 (2018), pp. 203–225.

[177] A. G. Bajpayee and A. J. Grodzinsky. "Cartilage-targeting drug delivery: can electrostatic interactions help?" In: *Nature Reviews Rheumatology* 13.3 (2017), pp. 183–193.

[178] S. Perni and P. Prokopovich. "Optimisation and feature selection of poly-beta-amino-ester as a drug delivery system for cartilage". In: *Journal of Materials Chemistry B* 8.23 (2020), pp. 5096–5108.

[179] L. A. Fransson. "Mammalian glycosaminoglycans". In: *Molecular Biology* 3 (1985), pp. 337–415.

[180] J. G. Prieto, M. M. Pulido, J. Zapico, A. J. Molina, M. Gimeno, P. Coronel, and A. I. Alvarez. "Comparative study of hyaluronic derivatives: rheological behaviour, mechanical and chemical degradation". In: *International Journal of Biological Macromolecules* 35.1-2 (2005), pp. 63–69.

[181] M. Abate, P. Pelotti, D. De Amicis, A. Di Iorio, S. Galletti, and V. Salini. "Viscosupplementation with hyaluronic acid in hip osteoarthritis (a review)". In: *Upsala Journal of Medical Sciences* 113.3 (2008), pp. 261–278.

[182] T. Kikuchi, H. Yamada, and K. Fujikawa. "Effects of high molecular weight hyaluronan on the distribution and movement of proteoglycan around chondrocytes cultured in alginate beads". In: *Osteoarthritis and Cartilage* 9.4 (2001), pp. 351–356.

[183] V. B. Vad, D. Sakalkale, T. P. Sculco, and T. L. Wickiewicz. "Role of hylan GF 20 in treatment of osteoarthritis of the hip joint". In: *Archives of physical medicine and rehabilitation* 84.8 (2003), pp. 1224–1226.

[184] Health Quality Ontario. “Intra-Articular Viscosupplementation With Hylan GF 20 To Treat Osteoarthritis of the Knee: An Evidence-Based Analysis”. In: *Ontario Health Technology Assessment Series* 5.10 (2005), p. 1.

[185] E. A. Balazs and J. L. Denlinger. “Viscosupplementation: a new concept in the treatment of osteoarthritis.” In: *The Journal of Rheumatology. Supplement* 39 (1993), pp. 3–9.

[186] H. Bagga, D. Burkhardt, P. Sambrook, and L. March. “Longterm effects of intraarticular hyaluronan on synovial fluid in osteoarthritis of the knee.” In: *The Journal of Rheumatology* 33.5 (2006), pp. 946–950.

[187] P. Ghosh and D. Guidolin. “Potential mechanism of action of intra-articular hyaluronan therapy in osteoarthritis: are the effects molecular weight dependent?” In: 32.1 (2002), pp. 10–37.

[188] S. Aihara, N. Murakami, R. Ishii, K. Kariya, Y. Azuma, K. Hamada, J. Umemoto, and S. Maeda. “Effects of sodium hyaluronate on the nociceptive response of rats with experimentally induced arthritis”. In: *Nihon Yakurigaku zasshi. Folia Pharmacologica Japonica* 100.4 (1992), pp. 359–365.

[189] J. V. Forrester and E. A. Balazs. “Inhibition of phagocytosis by high molecular weight hyaluronate.” In: *Immunology* 40.3 (1980), p. 435.

[190] H. Goto, T. Onodera, H. Hirano, and T. Shimamura. “Hyaluronic acid suppresses the reduction of $\alpha2$ (VI) collagen gene expression caused by interleukin-1β in cultured rabbit articular chondrocytes”. In: *The Tohoku Journal of Experimental Medicine* 187.1 (1999), pp. 1–13.

[191] T. Iannitti, D. Lodi, and B. Palmieri. “Intra-articular injections for the treatment of osteoarthritis”. In: *Drugs in R & D* 11.1 (2011), pp. 13–27.

[192] G. Cooper, J. Herrera, J. Kirkbride, and Z. Perlman. *Regenerative Medicine for Spine and Joint Pain*. Ed. by G. Cooper, J. Herrera, J. Kirkbride, and Z. Perlman. Springer, 2020. ISBN: 9783030427702.

[193] K. Lee, Y. Hwang, S. Cheong, Y. Choi, L. Kwon, J. Lee, and Soo H. Kim. “Understanding the role of nanoparticles in nano-oil lubrication”. In: *Tribology Letters* 35.2 (2009), pp. 127–131.

[194] V. N. Bakunin, A. Y. Suslov, G. N. Kuzmina, O. P. Parenago, and A. V. Topchiev. “Synthesis and application of inorganic nanoparticles as lubricant components–a review”. In: *Journal of Nanoparticle Research* 6.2 (2004), pp. 273–284.

[195] N. Canter. “Special Report: Trends in extreme pressure additives”. In: *Tribology and Lubrication Technology* 63.9 (2007), p. 10.

[196] H. H. Masjuki and M. A. Maleque. “Investigation of the anti-wear characteristics of palm oil methyl ester using a four-ball tribometer test”. In: *Wear* 206.1-2 (1997), pp. 179–186.

[197] M. V. Thottackkad, R. K. Perikinalil, and P. N. Kumarapillai. “Experimental evaluation on the tribological properties of coconut oil by the addition of CuO nanoparticles”. In: *International Journal of Precision Engineering and Manufacturing* 13.1 (2012), pp. 111–116.

[198] P. Anilkumar, T. B. Lawson, S. Abbina, J. T.and Sabatelle Mäkelä, L. E. R. C.and Takeuchi, B. D. Snyder, M. W. Grinstaff, and J. N. Kizhakkedathu. “Mega macromolecules as single molecule lubricants for hard and soft surfaces”. In: *Nature Communications* 11.1 (2020), pp. 1–9.

[199] T. B. Lawson, A. T. Joenathan, B. D. Snyder, and M. W. Grinstaff. “A theranostic nanolubricant”. In: *Orthop Res Soc Annual Conference, Phoenix*. Vol. 41, pp. 1–7.

[200] B. Zareh-Desari and B. Davoodi. “Assessing the lubrication performance of vegetable oil-based nano-lubricants for environmentally conscious metal forming processes”. In: *Journal of Cleaner Production* 135 (2016), pp. 1198–1209.

[201] N. A. C. Sidik, I. M. Adamu, and M. M. Jamil. “Preparation methods and thermal performance of hybrid nanofluids”. In: *Journal of Advanced Research in Materials Science* 56.1 (2019), pp. 1–10.

[202] M. Gulzar, H. H. Masjuki, M. Varman, M. A. Kalam, R. A. Mufti, N. W. M. Zulkifli, R. Yunus, and R. Zahid. “Improving the AW/EP ability of chemically modified palm oil by adding CuO and MoS2 nanoparticles”. In: *Tribology International* 88 (2015), pp. 271–279.

[203] Y. Zhang, C. Li, D. Jia, D. Zhang, and X. Zhang. “Experimental evaluation of the lubrication performance of MoS2/CNT nanofluid for minimal quantity lubrication in Ni-based alloy grinding”. In: *International Journal of Machine Tools and Manufacture* 99 (2015), pp. 19–33.

[204] M. Kopycinska-Müller, R. H. Geiss, and D. C. Hurley. “Contact mechanics and tip shape in AFM-based nanomechanical measurements”. In: *Ultramicroscopy* 106.6 (2006), pp. 466–474.

[205] V. L. Popov, M. Heß, and E. Willert. *Handbook of Contact Mechanics: Exact Solutions of Axisymmetric Contact Problems*. Ed. by V. L. Popov, M. Heß, and E. Willert. Springer Berlin Heidelberg, 2019. ISBN: 9783662587096.

[206] X. Zhu. “Tutorial on hertz contact stress”. In: *Opti*. Vol. 521. 2012, pp. 1–8.

[207] URL: https://en.wikipedia.org/wiki/Contact_mechanics (visited on 08/22/2022).

[208] D. Eberli. *Tissue Engineering*. Ed. by D. Eberli. BoD–Books on Demand, 2010. ISBN: 9789533070797.

[209] O. C. Chia, I. S. Suhaimin, S. A. Kassim, S. A. Zubir, and T. K. Abdullah. "Effect of modified solvent casting/particulate leaching (SCPL) technique on the properties of bioactive glass reinforced polyurethane scaffold for biomedical applications". In: *Journal of Physical Science* 30 (2019), pp. 115–126.

[210] D. W. Hutmacher. "Scaffolds in tissue engineering bone and cartilage". In: *Biomaterials* 21.24 (2000), pp. 2529–2543.

[211] K. Whang, C. H. Thomas, K. E. Healy, and G. Nuber. "A novel method to fabricate bioabsorbable scaffolds". In: *Polymer* 36.4 (1995), pp. 837–842.

[212] A. Sola, J. Bertacchini, D. D'Avella, L. Anselmi, T. Maraldi, S. Marmiroli, and M. Messori. "Development of solvent-casting particulate leaching (SCPL) polymer scaffolds as improved three-dimensional supports to mimic the bone marrow niche". In: *Materials Science and Engineering: C* 96 (2019), pp. 153–165.

[213] G. Binnig, C. F. Quate, and C. Gerber. "Atomic force microscope". In: *Physical Review Letters* 56.9 (1986), pp. 930–933.

[214] S. Sinha Ray. "Techniques for characterizing the structure and properties of polymer nanocomposites". In: *Environmentally Friendly Polymer Nanocomposites.* 2013, pp. 74–88. ISBN: 9780857097774.

[215] P. I. Oden, A. Majumdar, B. Bhushan, A. Padmanabhan, and J. J. Graham. "AFM imaging, roughness analysis and contact mechanics of magnetic tape and head surfaces". In: *Journal of Tribology* 114.4 (1992), pp. 666–674.

[216] R. Garcıa and R. Perez. "Dynamic atomic force microscopy methods". In: *Surface Science Reports* 47.6-8 (2002), pp. 197–301.

[217] E. R. N. S. T. Meyer. "Atomic force microscopy". In: *Progress in Surface Science* 41.1 (1992), pp. 3–49.

[218] S. Akamine, R. C. Barrett, and C. F. Quate. “Improved atomic force microscope images using microcantilevers with sharp tips”. In: *Applied Physics Letters* 57.3 (1990), pp. 316–318.

[219] T. R. Albrecht, S. Akamine, T. E. Carver, and C. F. Quate. “Microfabrication of cantilever styli for the atomic force microscope”. In: *Journal of Vacuum Science & Technology A: Vacuum, Surfaces, and Films* 8.4 (1990), pp. 3386–3396.

[220] Y. Seo and W. Jhe. “Atomic force microscopy and spectroscopy”. In: *Reports on Progress in Physics* 71.1 (2007), p. 016101.

[221] S. K. Arumugasamy, G. Chellasamy, S. Govindaraju, and K. Yun. “Recent developments in using atomic force microscopy in microbiology research: An update”. In: *Recent Developments in Applied Microbiology and Biochemistry* (2021), pp. 317–323.

[222] M. C. Piontek and W. H. Roos. “Atomic force microscopy: an introduction”. In: *Single Molecule Analysis*. Springer, 2018, pp. 243–258.

[223] Y. Wang and J. Wang. “Friction determination by atomic force microscopy in Field of biochemical science”. In: *Micromachines* 9.7 (2018), p. 313.

[224] J. Desrochers, M. W. Amrein, and J. R. Matyas. “Viscoelasticity of the articular cartilage surface in early osteoarthritis”. In: *Osteoarthritis and Cartilage* 20.5 (2012), pp. 413–421.

[225] A. Mohammed and A. Abdullah. “Scanning electron microscopy (SEM): A review”. In: *Proceedings of the 2018 International Conference on Hydraulics and Pneumatics—HERVEX, Băile Govora, Romania*. 2018, pp. 7–9.

[226] S. K. Sharma, D. S. Verma, L. U. Khan, S. Kumar, and S. B. Khan. *Handbook of materials characterization*. Ed. by S. B. Khan. Springer, 2018. ISBN: 3319929550.

[227] U. Bonse and F. Busch. “X-ray computed microtomography (μCT) using synchrotron radiation (SR)”. In: *Progress in Biophysics and Molecular Biology* 65.1-2 (1996), pp. 133–169.

[228] K. Uesugi, Y. Suzuki, N. Yagi, A. Tsuchiyama, and T. Nakano. “Development of high spatial resolution X-ray CT system at BL47XU in SPring-8”. In: *Nuclear Instruments and Methods in Physics Research Section A: Accelerators, Spectrometers, Detectors and Associated Equipment* 467 (2001), pp. 853–856.

[229] E. N. Landis and D. T. Keane. “X-ray microtomography”. In: *Materials characterization* 61.12 (2010), pp. 1305–1316.

[230] J. Y. Chen, D. J. Bottjer, G. Li, M. G. Hadfield, F. Gao, A. R. Cameron, C. Y. Zhang, D. C. Xian, P. Tafforeau, X. Liao, and Z. J. Yin. “Complex embryos displaying bilaterian characters from Precambrian Doushantuo phosphate deposits, Weng’an, Guizhou, China”. In: *Proceedings of the National Academy of Sciences* 106.45 (2009), pp. 19056–19060.

[231] F. Fusseis, K. Regenauer-Lieb, J. Liu, R. M. Hough, and F. De Carlo. “Creep cavitation can establish a dynamic granular fluid pump in ductile shear zones”. In: *Nature* 459.7249 (2009), pp. 974–977.

[232] H. Toda, S. Yamamoto, M. Kobayashi, K. Uesugi, and H. Zhang. “Direct measurement procedure for three-dimensional local crack driving force using synchrotron X-ray microtomography”. In: *Acta Materialia* 56.20 (2008), pp. 6027–6039.

[233] A. Tsuchiyama et al. “Three-dimensional structure of Hayabusa samples: origin and evolution of Itokawa regolith”. In: *Science* 333.6046 (2011), pp. 1125–1128.

[234] R. Mizutani and Y. Suzuki. “X-ray microtomography in biology”. In: *Micron* 43.2-3 (2012), pp. 104–115.

[235] E. Maire, J. Y. Buffiere, L. Salvo, J. J. Blandin, W. Ludwig, and J. M. Letang. “On the Application of X-ray Microtomography in the Field of Materials Science”. In: *Advanced Engineering Materials* 3.8 (2001), pp. 539–546.

[236] C. Berthomieu and R. Hienerwadel. “Fourier transform infrared (FTIR) spectroscopy”. In: *Photosynthesis Research* 101.2 (2009), pp. 157–170.

[237] D. Titus, E. J. J. Samuel, and S. M Roopan. “Nanoparticle characterization techniques”. In: *Green synthesis, characterization and applications of nanoparticles*. Elsevier, 2019, pp. 303–319.

[238] B. Arkles. “Hydrophobicity, Hydrophilicity and Silanes”. In: *Kirk-Othmer Encyclopedia of Chemical Technology* 22 (2006), p. 114.

[239] L. Han, A. J. Grodzinsky, and C. Ortiz. “Nanomechanics of the cartilage extracellular matrix”. In: *Annual review of materials research* 41 (2011), p. 133.

[240] N. H. Varady and A. J. Grodzinsky. “Osteoarthritis year in review 2015: mechanics”. In: *Osteoarthritis and Cartilage* 24.1 (2016), pp. 27–35.

[241] W. Lin and J. Klein. “Recent progress in cartilage lubrication”. In: *Advanced Materials* 33.18 (2021), p. 2005513.

[242] S. Jahn, J. Seror, and J. Klein. “Lubrication of articular cartilage”. In: *Annual Review of Biomedical Engineering* 18 (2016), pp. 235–258.

[243] P. Mainil-Varlet, T. Aigner, M. Brittberg, P. Bullough, A. Hollander, E. Hunziker, R. Kandel, S. Nehrer, K. Pritzker, S. Roberts, and E. Stauffer. “Histological assessment of cartilage repair: a report by the Histology Endpoint Committee of the International Cartilage Repair Society (ICRS)”. In: *JBJS* 85.suppl_2 (2003), pp. 45–57.

[244] R. E. Outerbridge. “The etiology of chondromalacia patellae”. In: *The Journal of bone and joint surgery. British volume* 43.4 (1961), pp. 752–757.

[245] L. A. Setton, D. M. Elliott, and V. C. Mow. “Altered mechanics of cartilage with osteoarthritis: human osteoarthritis and an experimental model of joint degeneration”. In: *Osteoarthritis and Cartilage* 7.1 (1999), pp. 2–14.

[246] E. B. Hunziker, M. Michel, and D. Studer. “Ultrastructure of adult human articular cartilage matrix after cryotechnical processing”. In: *Microscopy Research and Technique* 37.4 (1997), pp. 271–284.

[247] S. Ghosh, J. Bowen, K. Jiang, D. M. Espino, and D. E. Shepherd. “Investigation of techniques for the measurement of articular cartilage surface roughness”. In: *Micron* 44 (2013), pp. 179–184.

[248] B. M. Rothschild. “Porosity: a curiosity without diagnostic significance”. In: *American Journal of Physical Anthropology* 104.4 (1997), pp. 529–533.

[249] M. Parkes, D. Dini, C. Myant, and P. Cann. “Tribology-optimised silk protein hydrogels for articular cartilage repair”. In: *Tribology International* 89 (2015), pp. 9–18.

[250] S. Nehrer, H. A. Breinan, A. Ramappa, S. Shortkroff, G. Young, T. Minas, C. B. Sledge, I. V. Yannas, and M. Spector. “Canine chondrocytes seeded in type I and type II collagen implants investigated in vitro”. In: *Journal of Biomedical Materials Research* 38.2 (1997), pp. 95–104.

[251] D. L. Nettles, T. P. Vail, M. T. Morgan, M. W. Grinstaff, and L. A. Setton. “Photocrosslinkable hyaluronan as a scaffold for articular cartilage repair”. In: *Annals of Biomedical Engineering* 32.3 (2004), pp. 391–397.

[252] R. M. Jeuken, A. K. Roth, Rjrw Peters, C. C. Van Donkelaar, J. C. Thies, L. W. Van Rhijn, and P. J. Emans. “Polymers in cartilage defect repair of the knee: current status and future prospects”. In: *Polymers* 8.6 (2016), p. 219.

[253] N. S. Hwang, S. Varghese, H. Li, and J Elisseeff. “Regulation of osteogenic and chondrogenic differentiation of mesenchymal stem cells in PEG-ECM hydrogels”. In: *Cell and tissue research* 344.3 (2011), pp. 499–509.

[254] R. Izquierdo, N. Garcia-Giralt, M. T. Rodriguez, E. Cáceres, S. J. Garcı a, J. L. Gómez Ribelles, M. Monleón, J. C. Monllau, and J. Suay. “Biodegradable PCL scaffolds with an interconnected spherical pore network for tissue engineering”. In: *Journal of Biomedical Materials Research Part A* 85.1 (2008), pp. 25–35.

[255] N. Y. Adly, H. Hassani, A. Q. Tran, M. Balski, A. Yakushenko, A. Offenhäusser, D. Mayer, and B. Wolfrum. “Observation of chemically protected polydimethylsiloxane: towards crack-free PDMS”. In: *Soft Matter* 13.37 (2017), pp. 6297–6303.

[256] M. Kalulu, W. Zhang, X.-K. Xia, O. Oderinde, and Y. Jiang. “Hydrophilic surface modification of polydimetylsiloxane-co-2-hydroxyethylmethacrylate (PDMS-HEMA) by Silwet L-77 (heptamethyltrisiloxane) surface treatment”. In: *Polymers for Advanced Technologies* 29.10 (2018), pp. 2601–2611.

[257] E. Pedraza, A. C. Brady, C. A. Fraker, and C. L. Stabler. “Synthesis of macroporous poly (dimethylsiloxane) scaffolds for tissue engineering applications”. In: *Journal of Biomaterials Science, Polymer Edition* 24.9 (2013), pp. 1041–1056.

[258] T. Khosla, J. Cremaldi, J. S. Erickson, and N. S. Pesika. “Load-induced hydrodynamic lubrication of porous films”. In: *ACS Applied Materials & Interfaces* 7.32 (2015), pp. 17587–17591.

[259] F. De Paoli. “Measuring polydimethylsiloxane (PDMS) mechanical properties using flat punch nanoindentation focusing on obtaining full contact”. PhD thesis. 2015.

[260] S. Gupta, F. Carrillo, C. Li, L. Pruitt, and C. Puttlitz. “Adhesive forces significantly affect elastic modulus determination of soft polymeric materials in nanoindentation”. In: *Materials Letters* 61.2 (2007), pp. 448–451.

[261] T. K. Kim, J. K. Kim, and O. C. Jeong. “Measurement of nonlinear mechanical properties of PDMS elastomer”. In: *Microelectronic Engineering* 88.8 (2011), pp. 1982–1985.

[262] Z. Wang, A. A. Volinsky, and N. D. Gallant. “Crosslinking effect on polydimethylsiloxane elastic modulus measured by custom-built compression instrument”. In: *Journal of Applied Polymer Science* 131.22 (2014).

[263] J. Richmond, D. Hunter, J. Irrgang, M. H. Jones, B. Levy, R. Marx, L. Snyder-Mackler, W. C. Watters III, R. H. Haralson III, C. M. Turkelson, J. L. Wies, K. M. Boyer, S. Anderson, J. Andre, P. Sluka, and R. McGowan. “Treatment of osteoarthritis of the knee (nonarthroplasty)”. In: *The Journal of the American Academy of Orthopaedic Surgeons* 17.9 (2009), p. 591.

[264] M. M. Nava, L. Draghi, C. Giordano, and R. Pietrabissa. “The effect of scaffold pore size in cartilage tissue engineering”. In: *Journal of Applied Biomaterials & Functional Materials* 14.3 (2016), e223–e229.

[265] Z. Pan, P. Duan, X. Liu, H. Wang, L. Cao, Y. He, J. Dong, and J. Ding. “Effect of porosities of bilayered porous scaffolds on spontaneous osteochondral repair in cartilage tissue engineering”. In: *Regenerative Biomaterials* 2.1 (2015), pp. 9–19.

[266] L. Yu, C. M. Li, Q. Zhou, and J. H. Luong. “Poly (vinyl alcohol) functionalized poly (dimethylsiloxane) solid surface for immunoassay”. In: *Bioconjugate Chemistry* 18.2 (2007), pp. 281–284.

[267] D. Bodas and C. Khan-Malek. “Formation of more stable hydrophilic surfaces of PDMS by plasma and chemical treatments”. In: *Microelectronic Engineering* 83.4-9 (2006), pp. 1277–1279.

[268] K. Efimenko, W. E. Wallace, and J. Genzer. "Surface modification of Sylgard-184 poly (dimethyl siloxane) networks by ultraviolet and ultraviolet/ozone treatment". In: *Journal of Colloid and Interface Science* 254.2 (2002), pp. 306–315.

[269] J. Zhou, N. H. Voelcker, and A. V. Ellis. "Simple surface modification of poly (dimethylsiloxane) for DNA hybridization". In: *Biomicrofluidics* 4.4 (2010), p. 046504.

[270] H. Hillborg, J. F. Ankner, U. W. Gedde, G. D. Smith, H. K. Yasuda, and K. Wikström. "Crosslinked polydimethylsiloxane exposed to oxygen plasma studied by neutron reflectometry and other surface specific techniques". In: *Polymer* 41.18 (2000), pp. 6851–6863.

[271] S. H. Tan, N. T. Nguyen, Y. C. Chua, and T. G. Kang. "Oxygen plasma treatment for reducing hydrophobicity of a sealed polydimethylsiloxane microchannel". In: *Biomicrofluidics* 4.3 (2010), p. 032204.

[272] M. J. Owen and P. J. Smith. "Plasma treatment of polydimethylsiloxane". In: *Journal of Adhesion Science and Technology* 8.10 (1994), pp. 1063–1075.

[273] A. Tóth, I. Bertóti, M. Blazsó, G. Bánhegyi, A. Bognar, and P. Szaplonczay. "Oxidative damage and recovery of silicone rubber surfaces. I. X-ray photoelectron spectroscopic study". In: *Journal of Applied Polymer Science* 52.9 (1994), pp. 1293–1307.

[274] D. Xiao, H. Zhang, and M. Wirth. "Chemical modification of the surface of poly (dimethylsiloxane) by atom-transfer radical polymerization of acrylamide". In: *Langmuir* 18.25 (2002), pp. 9971–9976.

[275] L. Yu, Z. Shi, L. Gao, and C. Li. "Mitigated reactive oxygen species generation leads to an improvement of cell proliferation on poly [glycidyl methacrylate-co-poly (ethylene glycol) methacrylate] functionalized polydimethylsiloxane surfaces". In: *Journal of Biomedical Materials Research Part A* 103.9 (2015), pp. 2987–2997.

[276] B. Zuo, L. Bai, Z. Li, H. Xu, Y. Li, and X. Wang. “A Nanoconfinement Effect Imposed by the Limited End-to-End Distance of the Grafted Chains on a Molecular Aggregation of Polymer Brushes with Crystalline Side Groups”. In: *Macromolecules* 51.22 (2018), pp. 9192–9202.

[277] H. Abral, A. Atmajaya, M. Mahardika, F. Hafizulhaq, D. Handayani, S. M. Sapuan, and R. A. Ilyas. “Effect of ultrasonication duration of polyvinyl alcohol (PVA) gel on characterizations of PVA film”. In: *Journal of Materials Research and Technology* 9.2 (2020), pp. 2477–2486.

[278] M. I. Baker, S. P. Walsh, Z. Schwartz, and B. D. Boyan. “A review of polyvinyl alcohol and its uses in cartilage and orthopedic applications”. In: *Journal of Biomedical Materials Research Part B: Applied Biomaterials* 100.5 (2012), pp. 1451–1457.

[279] P. S. Premkumar. “Preparation and electrical studies on pure and oxygen plasma treated polyvinyl alcohol films”. In: *Journal of Materials Research and Technology* 8.2 (2019), pp. 2232–2237.

[280] W. A. W. A. Rahman, Lee Tin Sin, A. R. Rahmat, and A. A. Samad. “Thermal behaviour and interactions of cassava starch filled with glycerol plasticized polyvinyl alcohol blends”. In: *Carbohydrate Polymers* 81.4 (2010), pp. 805–810.

[281] R. Jayasekara, I. Harding, I. Bowater, G. B. Y. Christie, and G. T. Lonergan. “Preparation, surface modification and characterisation of solution cast starch PVA blended films”. In: *Polymer Testing* 23.1 (2004), pp. 17–27.

[282] J. A. Stammen, S. Williams, D. N. Ku, and R. E. Guldberg. “Mechanical properties of a novel PVA hydrogel in shear and unconfined compression”. In: *Biomaterials* 22.8 (2001), pp. 799–806.

[283] A. G. Mikos, A. J. Thorsen, L. A. Czerwonka, Y. Bao, R. Langer, D. N. Winslow, and J. P. Vacanti. “Preparation and characterization of poly (L-lactic acid) foams”. In: *Polymer* 35.5 (1994), pp. 1068–1077.

[284] X. Zhao, L. Li, B. Li, J. Zhang, and A. Wang. “Durable superhydrophobic/superoleophilic PDMS sponges and their applications in selective oil absorption and in plugging oil leakages”. In: *Journal of Materials Chemistry A* 2.43 (2014), pp. 18281–18287.

[285] C. J. Liao, C. F. Chen, J. H. Chen, S. F. Chiang, Y. J. Lin, and K. Y. Chang. “Fabrication of porous biodegradable polymer scaffolds using a solvent merging/particulate leaching method”. In: *Journal of Biomedical Materials Research* 59.4 (2002), pp. 676–681.

[286] B. Stevens, Y. Yang, A. Mohandas, B. Stucker, and K. T. Nguyen. “A review of materials, fabrication methods, and strategies used to enhance bone regeneration in engineered bone tissues”. In: *Journal of Biomedical Materials Research Part B: Applied Biomaterials* 85.2 (2008), pp. 573–582.

[287] C. T. McKee, J. A. Last, P. Russell, and C. J. Murphy. “Indentation versus tensile measurements of Young’s modulus for soft biological tissues”. In: *Tissue Engineering Part B: Reviews* 17.3 (2011), pp. 155–164.

[288] M. J. Rosenbluth, W. A. Lam, and D. A. Fletcher. “Force microscopy of nonadherent cells: a comparison of leukemia cell deformability”. In: *Biophysical Journal* 90.8 (2006), pp. 2994–3003.

[289] D. Burgess, N. Li, N. Rosik, P. J. Fryer, I. McRobbie, H. Zhang, and Z. J. Zhang. “Surface-Grafted Poly (ionic liquid) that Lubricates in Both Non-polar and Polar Solvents”. In: *ACS Macro Letters* 10.7 (2021), pp. 907–913.

[290] T. S. Karande, J. L. Ong, and C. M. Agrawal. “Diffusion in musculoskeletal tissue engineering scaffolds: design issues related to porosity, permeability, architecture, and nutrient mixing”. In: *Annals of Biomedical Engineering* 32.12 (2004), pp. 1728–1743.

[291] F. Carrillo, S. Gupta, M. Balooch, S. J. Marshall, G. W. Marshall, L. Pruitt, and C. M. Puttlitz. “Erratum:“Nanoindentation of polydimethylsiloxane elastomers: Effect of crosslinking, work of adhesion, and fluid environment on elastic modulus”[J. Mater. Res. 20, 2820 (2005)]”. In: *Journal of Materials Research* 21.2 (2006), pp. 535–537.

[292] K. Khanafer, A. Duprey, M. Schlicht, and R. Berguer. “Effects of strain rate, mixing ratio, and stress–strain definition on the mechanical behavior of the polydimethylsiloxane (PDMS) material as related to its biological applications”. In: *Biomedical Microdevices* 11.2 (2009), pp. 503–508.

[293] L. A. Hidalgo-Bastida, J. J. A. Barry, N. M. Everitt, F. R. A. J. Rose, L. D. Buttery, I. P. Hall, W. C. Claycomb, and K. M. Shakesheff. “Cell adhesion and mechanical properties of a flexible scaffold for cardiac tissue engineering”. In: *Acta Biomaterialia* 3.4 (2007), pp. 457–462.

[294] E. Kroner, R. Maboudian, and E. Arzt. “Adhesion characteristics of PDMS surfaces during repeated pull-off force measurements”. In: *Advanced Engineering Materials* 12.5 (2010), pp. 398–404.

[295] Y. Yu, D. Sanchez, and N. Lu. “Work of adhesion/separation between soft elastomers of different mixing ratios”. In: *Journal of Materials Research* 30.18 (2015), pp. 2702–2712.

[296] K. N. G. Fuller and D. Tabor. “The effect of surface roughness on the adhesion of elastic solids”. In: *Proceedings of the Royal Society of London. Series A, Mathematical and Physical Sciences* 345.1642 (1975), pp. 327–342.

[297] K. Meine, K. Kloss, T. Schneider, and D. Spaltmann. “The influence of surface roughness on the adhesion force”. In: *Surface and Interface Analysis* 36.8 (2004), pp. 694–697.

[298] R. Wilson, D. Dini, and B. Van Wachem. “The influence of surface roughness and adhesion on particle rolling”. In: *Powder Technology* 312 (2017), pp. 321–333.

[299] S. A. Chizhik, K. Wierzcholski, A. V. Trushko, M. A. Zhytkova, and A. Miszczak. “Properties of cartilage on micro-and nanolevel”. In: *Advances in Tribology* 2010 (2010), pp. 1–8.

[300] J. S. Jurvelin, M. D. Buschmann, and E. B. Hunziker. “Optical and mechanical determination of Poisson’s ratio of adult bovine humeral articular cartilage”. In: *Journal of biomechanics* 30.3 (1997), pp. 235–241.

[301] C. J. Little, N. K. Bawolin, and X. Chen. “Mechanical properties of natural cartilage and tissue-engineered constructs”. In: *Tissue Engineering Part B: Reviews* 17.4 (2011), pp. 213–227.

[302] A. R. Poole, M. Kobayashi, T. Yasuda, S. Laverty, F. Mwale, T. Kojima, T. Sakai, C. Wahl, S. El-Maadawy, G. Webb, E. Tchetina, and W. Wu. “Type II collagen degradation and its regulation in articular cartilage in osteoarthritis”. In: *Annals of the Rheumatic Diseases* 61.suppl 2 (2002), pp. ii78–ii81.

[303] K. L. Johnson. *Contact mechanics.* Ed. by K. L Johnson. Cambridge University Press, 1985. ISBN: 0521255767.

[304] V. L. Popov. *Contact mechanics and friction.* Ed. by V. L. Popov. 2010.

[305] G. A. Ateshian and H Wang. “A theoretical solution for the frictionless rolling contact of cylindrical biphasic articular cartilage layers”. In: *Journal of Biomechanics* 28.11 (1995), pp. 1341–1355.

[306] M. R. Bonilla, P. Lopez-Sanchez, M. J. Gidley, and J. R. Stokes. “Micromechanical model of biphasic biomaterials with internal adhesion: Application to nanocellulose hydrogel composites”. In: *Acta Biomaterialia* 29 (2016), pp. 149–160.

[307] B. Cohen, W. M. Lai, and V. C. Mow. “A transversely isotropic biphasic model for unconfined compression of growth plate and chondroepiphysis”. In: *Journal of Biomechanical Engineering* 120.4 (1998), pp. 491–496.

[308] A. C. Moore and D. L. Burris. “An analytical model to predict interstitial lubrication of cartilage in migrating contact areas”. In: *Journal of Biomechanics* 47.1 (2014), pp. 148–153.

[309] J. Delavoipière, Y. Tran, E. Verneuil, B. Heurtefeu, C. Y. Hui, and A. Chateauminois. “Friction of poroelastic contacts with thin hydrogel films”. In: *Langmuir* 34.33 (2018), pp. 9617–9626.

[310] H. Montazerian, M. G. A. Mohamed, M. M. Montazeri, S. Kheiri, A. S. Milani, K. Kim, and M. Hoorfar. “Permeability and mechanical properties of gradient porous PDMS scaffolds fabricated by 3D-printed sacrificial templates designed with minimal surfaces”. In: *Acta Biomaterialia* 96 (2019), pp. 149–160.

[311] N. Bowden, S. Brittain, A. G. Evans, J. W. Hutchinson, and G. M. Whitesides. “Spontaneous formation of ordered structures in thin films of metals supported on an elastomeric polymer”. In: *Nature* 393.6681 (1998), pp. 146–149.

[312] W. T. Huck, N. Bowden, P. Onck, T. Pardoen, J. W. Hutchinson, and G. M. Whitesides. “Ordering of spontaneously formed buckles on planar surfaces”. In: *Langmuir* 16.7 (2000), pp. 3497–3501.

[313] X. Yu, B. K. Mahajan, W. Shou, and H. Pan. “Materials, mechanics, and patterning techniques for elastomer-based stretchable conductors”. In: *Micromachines* 8.1 (2016), p. 7.

[314] G. Gioia and M. Ortiz. “Delamination of compressed thin films”. In: vol. 33. 8. New York, NY: Academic Press, 1948-, 1997, pp. 119–192.

[315] N. Jain, V. K. Singh, and S. Chauhan. “A review on mechanical and water absorption properties of polyvinyl alcohol based composites/films”. In: *Journal of the Mechanical Behavior of Materials* 26.5-6 (2017), pp. 213–222.

[316] URL: https://www.bestech.com.au/wp-content/uploads/Thermal-Coefficients-of-Expansion.pdf (visited on 08/22/2022).

[317] J. C. McDonald and G. M. Whitesides. “Poly (dimethylsiloxane) as a material for fabricating microfluidic devices”. In: *Accounts of Chemical Research* 35.7 (2002), pp. 491–499.

[318] F. Chen, D. Kang, and J. H. Park. “New measurement method of Poisson’s ratio of PVA hydrogels using an optical flow analysis for a digital imaging system”. In: *Measurement Science and Technology* 24.5 (2013), p. 055602.

[319] M. Ohring. *Materials Science of Thin Films*. Ed. by M. Ohring. Elsevier Science, 2001. ISBN: 9780080491783.

[320] H. G. Allen. *Analysis and design of structural sandwich panels: the commonwealth and international library: structures and solid body mechanics division*. Ed. by H. G. Allen. Elsevier, 2013. ISBN: 1483159043.

[321] I. Korbag and S. Mohamed Saleh. “Studies on the formation of intermolecular interactions and structural characterization of polyvinyl alcohol/lignin film”. In: *International Journal of Environmental Studies* 73.2 (2016), pp. 226–235.

[322] A. A. Oladipo, M. Gazi, and S. Saber-Samandari. “Adsorption of anthraquinone dye onto eco-friendly semi-IPN biocomposite hydrogel: equilibrium isotherms, kinetic studies and optimization”. In: *Journal of the Taiwan Institute of Chemical Engineers* 45.2 (2014), pp. 653–664.

[323] Q. Shi, N. Vitchuli, L. Ji, J. Nowak, M. McCord, M. Bourham, and X. Zhang. “A facile approach to fabricate porous nylon 6 nanofibers using silica nanotemplate”. In: *Journal of Applied Polymer Science* 120.1 (2011), pp. 425–433.

[324] A. B. D. Cassie and S. Baxter. “Wettability of porous surfaces”. In: *Transactions of the Faraday Society* 40 (1944), pp. 546–551.

[325] T. T. Chau, W. J. Bruckard, P. T. L. Koh, and A. V. Nguyen. “A review of factors that affect contact angle and implications for flotation practice”. In: *Advances in Colloid and Interface Science* 150.2 (2009), pp. 106–115.

[326] R. N. Wenzel. “Resistance of solid surfaces to wetting by water”. In: *Industrial & Engineering Chemistry* 28.8 (1936), pp. 988–994.

[327] J. H. Jia, H. D. Zhou, S. Q. Gao, and J. M. Chen. “A comparative investigation of the friction and wear behavior of polyimide composites under dry sliding and water-lubricated condition”. In: *Materials Science and Engineering: A* 356.1-2 (2003), pp. 48–53.

[328] H. Meng, G. X. Sui, G. Y. Xie, and R. Yang. “Friction and wear behavior of carbon nanotubes reinforced polyamide 6 composites under dry sliding and water lubricated condition”. In: *Composites Science and Technology* 69.5 (2009), pp. 606–611.

[329] S. Amini, S. Abbaszadeh, and M. Lotfi. “Measuring wear-resistance of AISI 1.7225 steel under various heat treatments: Hydraulic spool valve”. In: *Measurement* 98 (2017), pp. 179–185.

[330] I. J. Ford. “Roughness effect on friction for multi-asperity contact between surfaces”. In: *Journal of Physics D: Applied Physics* 26.12 (1993), p. 2219.

[331] V. N. Koinkar and B. Bhushan. “Effect of scan size and surface roughness on microscale friction measurements”. In: *Journal of Applied Physics* 81.6 (1997), pp. 2472–2479.

[332] F. Svahn, Å. Kassman-Rudolphi, and E. Wallén. “The influence of surface roughness on friction and wear of machine element coatings”. In: *Wear* 254.11 (2003), pp. 1092–1098.

[333] J. Carr, X. Milhet, P. Gadaud, S. A. Boyer, G. E. Thompson, and P. Lee. “Quantitative characterization of porosity and determination of elastic modulus for sintered micro-silver joints”. In: *The Journal of Materials Processing Technology* 225 (2015), pp. 19–23.

[334] G. Lu, G. Q. Lu, and Z. M. Xiao. “Mechanical properties of porous materials”. In: *Journal of Porous Materials* 6.4 (1999), pp. 359–368.

[335] N. Ramakrishnan and V. S. Arunachalam. “Effective elastic moduli of porous solids”. In: *Journal of materials science* 25.9 (1990), pp. 3930–3937.

[336] X. Xu, C. Koomson, M. Doddamani, R. K. Behera, and N. Gupta. “Extracting elastic modulus at different strain rates and temperatures from dynamic mechanical analysis data: A study on nanocomposites”. In: *Composites Part B: Engineering* 159 (2019), pp. 346–354.

[337] U. Hansen, R. Zioupos P.and Simpson, J. D. Currey, and D. Hynd. “The effect of strain rate on the mechanical properties of human cortical bone”. In: *Journal of Biomechanical Engineering* 130.1 (2008).

[338] H. J. Niu, Q. Wang, Y. X. Wang, D. Y. Li, Y. B. Fan, and W. F. Chen. “Ultrasonic reflection coefficient and surface roughness index of OA articular cartilage: relation to pathological assessment”. In: *BMC Musculoskeletal Disorders* 13.1 (2012), pp. 1–7.

[339] Y. Xi, H. J. Kaper, C. H. Choi, and P. K. Sharma. “Tribological properties of microporous polydimethylsiloxane (PDMS) surfaces under physiological conditions”. In: *Journal of Colloid and Interface Science* 561 (2020), pp. 220–230.

[340] C. P. Neu, A. H. Reddi, K. Komvopoulos, T. M. Schmid, and P. E Di Cesare. “Increased friction coefficient and superficial zone protein expression in patients with advanced osteoarthritis”. In: *Arthritis & Rheumatism* 62.9 (2010), pp. 2680–2687.

[341] D. Wu, P. Isaksson, S. J. Ferguson, and C. Persson. “Young’s modulus of trabecular bone at the tissue level: A review”. In: *Acta Biomaterialia* 78 (2018), pp. 1–12.

[342] Y. Xiao, E. A. Friis, S. H. Gehrke, and M. S. Detamore. “Mechanical testing of hydrogels in cartilage tissue engineering: beyond the compressive modulus”. In: *Tissue Engineering Part B: Reviews* 19.5 (2013), pp. 403–412.

[343] A. E. Peters, R. Akhtar, E. J. Comerford, and K. T. Bates. “The effect of ageing and osteoarthritis on the mechanical properties of cartilage and bone in the human knee joint”. In: *Scientific Reports* 8.1 (2018), pp. 1–13.

[344] O. N. Musskaya, A. I. Kulak, V. K. Krut’ko, S. A. Ulasevich, L. A. Lesnikovich, and L. F. Suchodub. “Composite Films Based on Hydroxyapatite and Polyvinyl Alcohol”. In: *Journal of Nano- and Electronic Physics* 7.1 (2015).

[345] H. T. Nia, L. Han, Y. Li, C. Ortiz, and A. Grodzinsky. “Poroelasticity of cartilage at the nanoscale”. In: *Biophysical Journal* 101.9 (2011), pp. 2304–2313.

[346] B. A. Hills. “Oligolamellar lubrication of joints by surface active phospholipid.” In: *The Journal of Rheumatology* 16.1 (1989), pp. 82–91.

[347] T. A. Schmidt, N. S. Gastelum, Q. T. Nguyen, B. L. Schumacher, and R. L. Sah. “Boundary lubrication of articular cartilage: role of synovial fluid constituents”. In: *Arthritis & Rheumatism* 56.3 (2007), pp. 882–891.

[348] X. Li, B. Dai, J. Guo, L. Zheng, Q. Guo, J. Peng, J. Xu, and L. Qin. “Nanoparticle–Cartilage Interaction: Pathology-Based Intra-articular Drug Delivery for Osteoarthritis Therapy”. In: *Nano-micro Letters* 13.1 (2021), pp. 1–48.

[349] G. Liu, M. Cai, F. Zhou, and W. Liu. “Charged polymer brushes-grafted hollow silica nanoparticles as a novel promising material for simultaneous joint lubrication and treatment”. In: *The Journal of Physical Chemistry B* 118.18 (2014), pp. 4920–4931.

[350] S. Sivan, Schroeder A., G. Verberne, Verberne G., Y. Merkher, Merkher Y., D. Diminsky, Diminsky D., A. Priev, Priev A., A. Maroudas, Maroudas A., G. Halperin, Halperin G., D. Nitzan, Nitzan D., I. Etsion, Etsion I., Y. Barenholz, and Y. Barenholz. “Liposomes act as effective biolubricants for friction reduction in human synovial joints”. In: *Langmuir* 26.2 (2010), pp. 1107–1116.

[351] L. Wan, Y. Wang, X. Tan, Y. Sun, J. Luo, and H. Zhang. “Biodegradable lubricating mesoporous silica nanoparticles for osteoarthritis therapy”. In: *Friction* 10.1 (2022), pp. 68–79.

[352] D. Kim and L. A. Archer. “Nanoscale organic- inorganic hybrid lubricants”. In: *Langmuir* 27.6 (2011), pp. 3083–3094.

[353] D. X. Peng, Y. Kang, R. M. Hwang, S. S. Shyr, and Y. P. Chang. “Tribological properties of diamond and SiO2 nanoparticles added in paraffin”. In: *Tribology International* 42.6 (2009), pp. 911–917.

[354] M. Gulzar, H. H. Masjuki, M. A. Kalam, M. Varman, N. W. M. Zulkifli, R. A. Mufti, and R. Zahid. “Tribological performance of nanoparticles as lubricating oil additives”. In: *Journal of Nanoparticle Research* 18.8 (2016), pp. 1–25.

[355] Bassem Kheireddin. “Tribological properties of nanoparticle-based lubrication systems”. PhD thesis. 2013.

[356] Q. Sunqing, D. Junxiu, and C. Guoxu. “Tribological properties of CeF3 nanoparticles as additives in lubricating oils”. In: *Wear* 230.1 (1999), pp. 35–38.

[357] X. Song, S. Zheng, J. Zhang, W. Li, Q. Chen, and B. Cao. “Synthesis of monodispersed ZnAl2O4 nanoparticles and their tribology properties as lubricant additives”. In: *Materials Research Bulletin* 47.12 (2012), pp. 4305–4310.

[358] V. Cortes and J. A. Ortega. “Evaluating the rheological and tribological behaviors of coconut oil modified with nanoparticles as lubricant additives”. In: *Lubricants* 7.9 (2019), p. 76.

[359] M. Akbulut. “Nanoparticle-based lubrication systems”. In: *Journal of Powder Metallurgy & Mining* 1.1 (2012), pp. 1–3.

[360] H. Ghaednia and R. L. Jackson. “The effect of nanoparticles on the real area of contact, friction, and wear”. In: *Journal of Tribology* 135.4 (2013), p. 041603.

[361] W. Zhao, H. Wang, H. Wang, Y. Han, Z. Zheng, X. Liu, B. Feng, and H. Zhang. “Light-responsive dual-functional biodegradable mesoporous silica nanoparticles with drug delivery and lubrication enhancement for the treatment of osteoarthritis”. In: *Nanoscale* 13.13 (2021), pp. 6394–6399.

[362] L. Wan, X. Tan, T. Sun, Y. Sun, J. Luo, and H. Zhang. “Lubrication and drug release behaviors of mesoporous silica nanoparticles grafted with sulfobetaine-based zwitterionic polymer”. In: *Materials Science and Engineering: C* 112 (2020), p. 110886.

[363] A. K. Sharma, A. K. Tiwari, and A. R. Dixit. “Rheological behaviour of nanofluids: A review”. In: *Renewable and Sustainable Energy Reviews* 53 (2016), pp. 779–791.

[364] J. M. Balbus, A. D. Maynard, V. L. Colvin, V. Castranova, G. P. Daston, R. A. Denison, K. L. Dreher, P. L. Goering, A. M. Goldberg, K. M. Kulinowski, N. A. Monteiro-Riviere, G. Oberdörster, G. S. Omenn, K. E. Pinkerton, Ramos K. S., Rest K. M., Sass J. B., Silbergeld E. K, and Wong B. A. “Meeting report: hazard assessment for nanoparticles—report from an interdisciplinary workshop”. In: *Environmental Health Perspectives* 115.11 (2007), pp. 1654–1659.

[365] M. Czaun, A. Goeppert, R. B. May, D. Peltier, H. Zhang, G. S. Prakash, and G. A. Olah. “Organoamines-grafted on nano-sized silica for carbon dioxide capture”. In: *Journal of CO2 Utilization* 1 (2013), pp. 1–7.

[366] S. Haruehansapong, T. Pulngern, and S. Chucheepsakul. “Effect of the particle size of nanosilica on the compressive strength and the optimum replacement content of cement mortar containing nano-SiO2”. In: *Construction and Building Materials* 50 (2014), pp. 471–477.

[367] M. M. Karabela and I. D. Sideridou. “Synthesis and study of properties of dental resin composites with different nanosilica particles size”. In: *Dental Materials* 27.8 (2011), pp. 825–835.

[368] L. F. Hakim, J. L. Portman, M. D. Casper, and A. W. Weimer. “Aggregation behavior of nanoparticles in fluidized beds”. In: *Powder Technology* 160.3 (2005), pp. 149–160.

[369] W. Zhang. “Nanoparticle aggregation: principles and modeling”. In: *Nanomaterial* (2014), pp. 19–43.

[370] S. H. Behrens, D. I. Christl, R. Emmerzael, P. Schurtenberger, and M. Borkovec. “Charging and aggregation properties of carboxyl latex particles: Experiments versus DLVO theory”. In: *Langmuir* 16.6 (2000), pp. 2566–2575.

[371] K. L. Chen and M. Elimelech. “Aggregation and deposition kinetics of fullerene (C60) nanoparticles”. In: *Langmuir* 22.26 (2006), pp. 10994–11001.

[372] S. Shahnazar, S. Bagheri, and S. B. Abd Hamid. “Enhancing lubricant properties by nanoparticle additives”. In: *International Journal of Hydrogen Energy* 41.4 (2016), pp. 3153–3170.

[373] B. A. Kheireddin, W. Lu, I. C. Chen, and M. Akbulut. “Inorganic nanoparticle-based ionic liquid lubricants”. In: *Wear* 303.1-2 (2013), pp. 185–190.

[374] S. M. Hsu. "Nano-lubrication: concept and design". In: *Tribology International* 37.7 (2004), pp. 537–545.

[375] URL: https://www.imetra.com/borosilicate-glass-material-properties/ (visited on 08/22/2022).

[376] A. Rudy, C. Kuliasha, J. Uruena, J. Rex, K. D. Schulze, D. Stewart, T. Angelini, W. G. Sawyer, and S. S. Perry. "Lubricous hydrogel surface coatings on polydimethylsiloxane (PDMS)". In: *Tribology Letters* 65.1 (2017), pp. 1–11.

[377] K. Tanaka. "Kinetic friction and dynamic elastic contact behaviour of polymers". In: *Wear* 100.1-3 (1984), pp. 243–262.

[378] J. W. Kim, B. S. Joo, and H. Jang. "The effect of contact area on velocity weakening of the friction coefficient and friction instability: a case study on brake friction materials". In: *Tribology International* 135 (2019), pp. 38–45.

[379] M. A. Chowdhury, M. K. Khalil, D. M. Nuruzzaman, and M. L. Rahaman. "The effect of sliding speed and normal load on friction and wear property of aluminum". In: *International Journal of Mechanical & Mechatronics Engineering* 11.1 (2011), pp. 45–49.

[380] B.J. Hamrock, B.J. Schmid, and B.O. Jacobson. *Fundamentals of fluid film lubrication*. Ed. by B.J. Hamrock, B.J. Schmid, and B.O. Jacobson. CRC Press, 2004. ISBN: 9780203021187.

[381] Y. J. J. Jason, H. G. How, Y. H. Teoh, and H. G. Chuah. "A study on the tribological performance of nanolubricants". In: *Processes* 8.11 (2020), p. 1372.

[382] R. M. Power, S. H. Simpson, J. P. Reid, and A. J. Hudson. "The transition from liquid to solid-like behaviour in ultrahigh viscosity aerosol particles". In: *Chemical Science* 4.6 (2013), pp. 2597–2604.

[383] Y. Zheng, Y. Yan, W. Zhao, H. Wang, Y. Sun, J. Han, and H. Zhang. “Self-Assembled Nanospheres with Enhanced Interfacial Lubrication for the Treatment of Osteoarthritis”. In: *ACS Applied Materials & Interfaces* 14.19 (2022), pp. 21773–21786.

[384] R. E. Rudge, K. Theunissen, J. R. Stokes, E. Scholten, and J. A. Dijksman. “Tribology of hard particles lubricating soft surfaces”. In: *Physical Review Materials* 5.5 (2021), p. 055604.

[385] Y. Hichri, V. Cerezo, and M. T. Do. “Modeling of the surface coverage and application to the calculation of friction on surfaces contaminated by particles”. In: *Wear* 426 (2019), pp. 1082–1093.

[386] W. Lavelle, E. D. Lavelle, and L. Lavelle. “Intra-articular injections”. In: *Anesthesiology Clinics* 25.4 (2007), pp. 853–862.

[387] D. J. Hunter, M. Nevitt, E. Losina, and V. Kraus. “Biomarkers for osteoarthritis: current position and steps towards further validation”. In: *Best Practice & Research Clinical Rheumatology* 28.1 (2014), pp. 61–71.

[388] S. A. Johnston. “Osteoarthritis: joint anatomy, physiology, and pathobiology”. In: *Veterinary Clinics of North America: Small Animal Practice* 27.4 (1997), pp. 699–723.

[389] H. F. Zhang, C. G. Wang, H. Li, Y. T. Huang, and Z. J. Li. “Intra-articular platelet-rich plasma versus hyaluronic acid in the treatment of knee osteoarthritis: a meta-analysis”. In: *Drug Design, Development and Therapy* 12 (2018), p. 445.

[390] H. Huang, Z. Lou, S. Zheng, J. Wu, Q. Yao, R. Chen, L. Kou, and D. Chen. “Intra-articular drug delivery systems for osteoarthritis therapy: Shifting from sustained release to enhancing penetration into cartilage”. In: *Drug Delivery* 29.1 (2022), pp. 767–791.

[391] S. Xue, X. Zhou, W. Sang, C. Wang, H. Lu, Y. Xu, Y. Zhong, L. Zhu, C. He, and J. Ma. "Cartilage-targeting peptide-modified dual-drug delivery nanoplatform with NIR laser response for osteoarthritis therapy". In: *Bioactive Materials* 6.8 (2021), pp. 2372–2389.

[392] A. G. Bajpayee and A. J. Grodzinsky. "Cartilage-targeting drug delivery: can electrostatic interactions help?" In: *Nature Reviews Rheumatology* 13.3 (2017), pp. 183–193.

[393] V. Natarajan, N. Krithica, B. Madhan, and P. K. Sehgal. "Formulation and evaluation of quercetin polycaprolactone microspheres for the treatment of rheumatoid arthritis". In: *Journal of Pharmaceutical Sciences* 100.1 (2011), pp. 195–205.

[394] N. Kamaly, Z. Xiao, P. M. Valencia, A. F. Radovic-Moreno, and O. C. Farokhzad. "Targeted polymeric therapeutic nanoparticles: design, development and clinical translation". In: *Chemical Society Reviews* 41.7 (2012), pp. 2971–3010.

[395] G. Liu, Y. Feng, N. Zhao, Z. Chen, J. Shi, and F. Zhou. "Polymer-based lubricating materials for functional hydration lubrication". In: *Chemical Engineering Journal* 429 (2022), p. 132324.

[396] M. Rahimi, G. Charmi, K. Matyjaszewski, X. Banquy, and J. Pietrasik. "Recent developments in natural and synthetic polymeric drug delivery systems used for the treatment of osteoarthritis". In: *Acta Biomaterialia* 123 (2021), pp. 31–50.

[397] E. M. Ahmed. "Hydrogel: Preparation, characterization, and applications: A review". In: *Journal of Advanced Research* 6.2 (2015), pp. 105–121.

[398] M. L. Oyen. "Mechanical characterisation of hydrogel materials". In: *International Materials Reviews* 59.1 (2014), pp. 44–59.

[399] G. Soni and K. S. Yadav. “Nanogels as potential nanomedicine carrier for treatment of cancer: A mini review of the state of the art”. In: *Saudi Pharmaceutical Journal* 24.2 (2016), pp. 133–139.

[400] D. M. Eckmann, R. J. Composto, A. Tsourkas, and V. R. Muzykantov. “Nanogel carrier design for targeted drug delivery”. In: *Journal of Materials Chemistry B* 2.46 (2014), pp. 8085–8097.

[401] J. Zhu and R. E. Marchant. “Design properties of hydrogel tissue-engineering scaffolds”. In: *Expert Review of Medical Devices* 8.5 (2011), pp. 607–626.

[402] E. Mauri, S. M. Giannitelli, M. Trombetta, and A. Rainer. “Synthesis of nanogels: Current trends and future outlook”. In: *Gels* 7.2 (2021), p. 36.

[403] Y. Zhang, D. Liu, H. Zhang, and H. A. Santos. “Microfluidic mixing and devices for preparing nanoparticulate drug delivery systems”. In: *Microfluidics for Pharmaceutical Applications*. Elsevier, 2019, pp. 155–177.

[404] F. C. Linn and L. Sokoloff. “Movement and composition of interstitial fluid of cartilage”. In: *Arthritis & Rheumatism: Official Journal of the American College of Rheumatology* 8.4 (1965), pp. 481–494.

[405] A. Maroudas. “Physicochemical properties of articlar cartilage”. In: *Adlt Articular Cartilage* (1979).

[406] J. A. Martin and J. A. Buckwalter. “Telomere erosion and senescence in human articular cartilage chondrocytes”. In: *The Journals of Gerontology Series A: Biological Sciences and Medical Sciences* 56.4 (2001), B172–B179.

[407] B. Pouran, A. Raoof, D. M. de Winter, V. Arbabi, R. L. A. W. Bleys, F. J. Beekman, A. A. Zadpoor, J. Malda, and H. Weinans. “Topographic features of nano-pores within the osteochondral interface and their effects on transport properties–a 3D imaging and modeling study”. In: *Journal of Biomechanics* 123 (2021), p. 110504.

[408] M. D. Grynpas, B. Alpert, I. Katz, I. Lieberman, and K. P. H. Pritzker. “Subchondral bone in osteoarthritis”. In: *Calcified tissue international* 49.1 (1991), pp. 20–26.

[409] B. Li, D. Marshall, M. Roe, and R. M. ASPDEN. “The electron microscope appearance of the subchondral bone plate in the human femoral head in osteoarthritis and osteoporosis”. In: *The Journal of Anatomy* 195.1 (1999), pp. 101–110.

[410] A. J. Palmer, E. G. Brown Cp Fau - McNally, A. J. McNally Eg Fau - Price, I. Price Aj Fau - Tracey, P. Tracey I Fau - Jezzard, A. J. Jezzard P Fau - Carr, S. Carr Aj Fau - Glyn-Jones, and S. Glyn-Jones. “Non-invasive imaging of cartilage in early osteoarthritis”. In: *The Bone & Joint Journal* 95.6 (2013), pp. 738–746.

[411] C. Y. Wen, C. B. Wu, B. Tang, T. Wang, C. H. Yan, W. W. Lu, H. Pan, Y. Hu, and K. Y. Chiu. “Collagen fibril stiffening in osteoarthritic cartilage of human beings revealed by atomic force microscopy”. In: *Osteoarthritis and Cartilage* 20.8 (2012), pp. 916–922.

[412] L. C. Hughes, C. W. Archer, and I. Ap Gwynn. “The ultrastructure of mouse articular cartilage: collagen orientation and implications for tissue functionality. A polarised light and scanning electron microscope study and review”. In: *European Cells and Materials* 9.68 (2005), e84.

[413] E. Limiti, P. Mozetic, S. M. Giannitelli, F. Pinelli, X. Han, D. Del Rio, F. Abbruzzese, F. Basoli, L Rosanó, S. Scialla, M. Trombetta, G. Gigli, Zhang Z. J., and E. Mauri. “Hyaluronic Acid–Polyethyleneimine Nanogels for Controlled Drug Delivery in Cancer Treatment”. In: *ACS Applied Nano Materials* 5.4 (2022), pp. 5544–5557.

[414] R. Crockett, S. Roos, P. Rossbach, C. Dora, W. Born, and H. Troxler. “Imaging of the surface of human and bovine articular cartilage with ESEM and AFM”. In: *Tribology Letters* 19.4 (2005), pp. 311–317.

[415] L. Ng, A. J. Grodzinsky, P. Patwari, J. Sandy, A. Plaas, and C. Ortiz. “Individual cartilage aggrecan macromolecules and their constituent glycosaminoglycans visualized via atomic force microscopy”. In: *Journal of Structural Biology* 143.3 (2003), pp. 242–257.

[416] B. Han, H. T. Nia, C. Wang, P. Chandrasekaran, Q. Li, D. R. Chery, H. Li, A. J. Grodzinsky, and L. Han. “AFM-nanomechanical test: an interdisciplinary tool that links the understanding of cartilage and meniscus biomechanics, osteoarthritis degeneration, and tissue engineering”. In: *ACS Biomaterials Science & Engineering* 3.9 (2017), pp. 2033–2049.

[417] D. Majda, A. Bhattarai, J. Riikonen, B. D. Napruszewska, M. Zimowska, A. Michalik-Zym, J. Töyräs, and V. P. Lehto. “New approach for determining cartilage pore size distribution: NaCl-thermoporometry”. In: *Microporous and Mesoporous Materials* 241 (2017), pp. 238–245.

[418] S. L. Graindorge and G. W. Stachowiak. “Changes occurring in the surface morphology of articular cartilage during wear”. In: *Wear* 241.2 (2000), pp. 143–150.

[419] R. F. Loeser. “Molecular mechanisms of cartilage destruction: mechanics, inflammatory mediators, and aging collide”. In: *Arthritis and Rheumatism* 54.5 (2006), p. 1357.

[420] J. Desrochers, M. W. Amrein, and J. R. Matyas. “Microscale surface friction of articular cartilage in early osteoarthritis”. In: *Journal of the Mechanical Behavior of Biomedical Materials* 25 (2013), pp. 11–22.

[421] R. Kumar, D. M. Pierce, V. Isaksen, C. D. L. Davies, J. O. Drogset, and M. B. Lilledahl. “Comparison of compressive stress-relaxation behavior in osteoarthritic (ICRS graded) human articular cartilage”. In: *International Journal of Molecular Sciences* 19.2 (2018), p. 413.

[422] F. P. Bowden and D. Tabor. *The friction and lubrication of solids.* Vol. 1. Oxford university press, 2001.

[423] D. Maksuta, S. Dalvi, A. Gujrati, L. Pastewka, T. D. B. Jacobs, and A. Dhinojwala. “Dependence of adhesive friction on surface roughness and elastic modulus”. In: *Soft Matter* 18.31 (2022), pp. 5843–5849.

[424] P. Manninen, H. Riihimäki, M. Heliövaara, and P. Mäkelä. “Overweight, gender and knee osteoarthritis.” In: *International Journal of Obesity and Related Metabolic Disorders: Journal of the International Association for the Study of Obesity* 20.6 (1996), pp. 595–597.

[425] D. Prieto-Alhambra, A. Judge, M. K. Javaid, C. Cooper, A. Diez-Perez, and N. K. Arden. “Incidence and risk factors for clinically diagnosed knee, hip and hand osteoarthritis: influences of age, gender and osteoarthritis affecting other joints”. In: *Annals of the Rheumatic Diseases* 73.9 (2014), pp. 1659–1664.

[426] V. K. Srikanth, J. L. Fryer, G. Zhai, T. M. Winzenberg, D. Hosmer, and G. Jones. “A meta-analysis of sex differences prevalence, incidence and severity of osteoarthritis”. In: *Osteoarthritis and Cartilage* 13.9 (2005), pp. 769–781.

[427] E. Mauri, P. Veglianese, S. Papa, A. Mariani, M. De Paola, R. Rigamonti, G. M. F. Chincarini, I. Vismara, S. Rimondo, A. Sacchetti, and F. Rossi. “Double conjugated nanogels for selective intracellular drug delivery”. In: *RSC Advances* 7.48 (2017), pp. 30345–30356.

[428] S. M. Giannitelli, E. Limiti, P. Mozetic, F. Pinelli, X. Han, F. Abbruzzese, F. Basoli, D. Del Rio, S. Scialla, F. Rossi, M. Trombetta, L. Rosanó, G. Gigli, Z. J. Zhang, E. Mauri, and A. Rainer. “Droplet-based microfluidic synthesis of nanogels for controlled drug delivery: tailoring nanomaterial properties via pneumatically actuated flow-focusing junction”. In: *Nanoscale* (2022).

[429] B. B. Seo, Y. j. Kwon, J. Kim, K. H. Hong, S. E. Kim, H. R. Song, Y. M. Kim, and S. C. Song. “Injectable polymeric nanoparticle hydrogel system for long-term anti-inflammatory effect to treat osteoarthritis”. In: *Bioactive Materials* 7 (2022), pp. 14–25.

[430] S. Mori, M. Naito, and S. Moriyama. “Highly viscous sodium hyaluronate and joint lubrication”. In: *International Orthopaedics* 26.2 (2002), pp. 116–121.

[431] J. M. Coles, J. J. Blum, G. D. Jay, E. M. Darling, F. Guilak, and S. Zauscher. “In situ friction measurement on murine cartilage by atomic force microscopy”. In: *Journal of Biomechanics* 41.3 (2008), pp. 541–548.

[432] S. Park, K. D. Costa, and G. A. Ateshian. “Microscale frictional response of bovine articular cartilage from atomic force microscopy”. In: *Journal of Biomechanics* 37.11 (2004), pp. 1679–1687.

[433] S. Boutaleb, F. Zaïri, A. Mesbah, M. Nait-Abdelaziz, J. M. Gloaguen, T. Boukharouba, and J. M. Lefebvre. “Micromechanics-based modelling of stiffness and yield stress for silica/polymer nanocomposites”. In: *International Journal of Solids and Structures* 46.7-8 (2009), pp. 1716–1726.

[434] J. Lee, Z. Wang, J. Zhang, J. Yan, T. Deng, Y. Zhao, K. Matyjaszewski, and M. R. Bockstaller. “Molecular parameters governing the elastic properties of brush particle films”. In: *Macromolecules* 53.4 (2020), pp. 1502–1513.

[435] A. Scotti, M. F. Schulte, C. G. Lopez, J. J. Crassous, S. Bochenek, and W. Richtering. “How Softness Matters in Soft Nanogels and Nanogel Assemblies”. In: *Chemical Reviews* (2022).

[436] F. Scheffold, P. Díaz-Leyva, M. Reufer, N. B. Braham, I. Lynch, and J. L. Harden. “Brushlike interactions between thermoresponsive microgel particles”. In: *Physical Review Letters* 104.12 (2010), p. 128304.

[437] S. M. Hashmi and E. R. Dufresne. "Mechanical properties of individual microgel particles through the deswelling transition". In: *Soft Matter* 5.19 (2009), pp. 3682–3688.

[438] O. Tagit, N. Tomczak, and G. J. Vancso. "Probing the Morphology and Nanoscale Mechanics of Single Poly (N-isopropylacrylamide) Microgels Across the Lower-Critical-Solution Temperature by Atomic Force Microscopy". In: *Small* 4.1 (2008), pp. 119–126.

[439] H. Mao, Z. Qiu, Z. Shen, and W. Huang. "Hydrophobic associated polymer based silica nanoparticles composite with core–shell structure as a filtrate reducer for drilling fluid at utra-high temperature". In: *Journal of Petroleum Science and Engineering* 129 (2015), pp. 1–14.

[440] Z. Zangiabadi and M. J. Hadianfard. "The role of hollow silica nanospheres and rigid silica nanoparticles on acoustic wave absorption of flexible polyurethane foam nanocomposites". In: *Journal of Cellular Plastics* 56.4 (2020), pp. 395–410.

[441] L. Ding, E. Heying, N. Nicholson, N. J. Stroud, G. A. Homandberg, J. A. Buckwalter, D. Guo, and J. A. Martin. "Mechanical impact induces cartilage degradation via mitogen activated protein kinases". In: *Osteoarthritis and Cartilage* 18.11 (2010), pp. 1509–1517.

[442] W. Goodwin, D. McCabe, E. Sauter, E. Reese, M. Walter, J. A. Buckwalter, and J. A. Martin. "Rotenone prevents impact-induced chondrocyte death". In: *Journal of Orthopaedic Research* 28.8 (2010), pp. 1057–1063.

[443] D. Hayashi, F. W. Roemer, A. Katur, D. T. Felson, S. O. Yang, F. Alomran, and A. Guermazi. "Imaging of synovitis in osteoarthritis: current status and outlook". In: 41.2 (2011), pp. 116–130.

[444] W. A. Hodge, R. S. Fijan, K. L. Carlson, R. G. Burgess, W. H. Harris, and R. W. Mann. “Contact pressures in the human hip joint measured in vivo.” In: *Proceedings of the National Academy of Sciences* 83.9 (1986), pp. 2879–2883.

[445] M. Kalin, I. Velkavrh, and J. Vižintin. “The Stribeck curve and lubrication design for non-fully wetted surfaces”. In: *Wear* 267.5-8 (2009), pp. 1232–1240.

[446] T. Kawai and S. Akira. “The role of pattern-recognition receptors in innate immunity: update on Toll-like receptors”. In: *Nature Immunology* 11.5 (2010), pp. 373–384.

[447] W. Li, J. Liu, and D. Zhao. “Mesoporous materials for energy conversion and storage devices”. In: *Nature Reviews Materials* 1.6 (2016), pp. 1–17.

[448] K. Meyer. “Chemical structure of hyaluronic acid”. In: *Federation Proceedings* 17.4 (1958), pp. 1075–7.

[449] U. Požgan, D. Caglič, B. Rozman, H. Nagase, V. Turk, and B. Turk. “Expression and activity profiling of selected cysteine cathepsins and matrix metalloproteinases in synovial fluids from patients with rheumatoid arthritis and osteoarthritis”. In: *Biological Chemistry* 391.5 (2010), pp. 571–579.

[450] S. W. Suh, J. Y. Shin, J. Kim, J. Kim, C. H. Beak, D. I. Kim, H. Kim, S. S. Jeon, and I. W. Choo. “Effect of different particles on cell proliferation in polymer scaffolds using a solvent-casting and particulate leaching technique”. In: *ASAIO Journal* 48.5 (2002), pp. 460–464.

[451] B. Wang, P. Prinsen, H. Wang, Z. Bai, H. Wang, R. Luque, and J. Xuan. “Macroporous materials: microfluidic fabrication, functionalization and applications”. In: *Chemical Society Reviews* 46.3 (2017), pp. 855–914.

[452] E. Yilgör and I. Yilgör. “Silicone containing copolymers: Synthesis, properties and applications”. In: *Progress in Polymer Science* 39.6 (2014), pp. 1165–1195.

[453] J. P. Gleghorn, S. B. Doty, R. F. Warren, T. M. Wright, S. A. Maher, and L. J. Bonassar. “Analysis of frictional behavior and changes in morphology resulting from cartilage articulation with porous polyurethane foams”. In: *Journal of Orthopaedic Research* 28.10 (2010), pp. 1292–1299.

[454] S. Graindorge, W. Ferrandez, E. Ingham, Z. Jin, P. Twigg, and J. Fisher. “The role of the surface amorphous layer of articular cartilage in joint lubrication”. In: *Proceedings of the Institution of Mechanical Engineers, Part H: Journal of Engineering in Medicine* 220.5 (2006), pp. 597–607.

[455] J. D. Kaufman, G. J. Miller, E. F. Morgan, and C. M. Klapperich. “Time-dependent mechanical characterization of poly (2-hydroxyethyl methacrylate) hydrogels using nanoindentation and unconfined compression”. In: *Journal of Materials Research* 23.5 (2008), pp. 1472–1481.

[456] J. M. Kemppainen and S. J. Hollister. “Tailoring the mechanical properties of 3D-designed poly (glycerol sebacate) scaffolds for cartilage applications”. In: *Journal of Biomedical Materials Research Part A* 94.1 (2010), pp. 9–18.

[457] P. Kumar, M. Oka, J. Toguchida, M. Kobayashi, E. Uchida, T. Nakamura, and K. Tanaka. “Role of uppermost superficial surface layer of articular cartilage in the lubrication mechanism of joints”. In: *The Journal of Anatomy* 199.3 (2001), pp. 241–250.

[458] N. S. Landínez-Parra, D. A. Garzón-Alvarado, and J. C. Vanegas-Acosta. “Mechanical behavior of articular cartilage”. In: IntechOpen, 2012, pp. 197–216.

[459] P. Liu, H. Lai, X. Luo, Q. Xia, D. Zhang, Z. Cheng, Y. Liu, and L. Jiang. “Superlyophilic shape memory porous sponge for smart liquid permeation”. In: *ACS Nano* 14.10 (2020), pp. 14047–14056.

[460] V. C. Mow and X. E. Guo. “Mechano-electrochemical properties of articular cartilage: their inhomogeneities and anisotropies”. In: *Annual Review of Biomedical Engineering* 4.1 (2002), pp. 175–209.

[461] C. A. Poole, M. H. Flint, and B. W. Beaumont. “Morphological and functional interrelationships of articular cartilage matrices.” In: *Journal of Anatomy* 138.Pt 1 (1984), p. 113.

[462] S. L. Vega, M. Y. Kwon, and J. A. Burdick. “Recent advances in hydrogels for cartilage tissue engineering”. In: *European cells & materials* 33 (2017), p. 59.

[463] S. Asgary, M. J. Eghbal, M. Parirokh, and J. Ghoddusi. “Effect of two storage solutions on surface topography of two root-end fillings”. In: *Australian Endodontic Journal* 35.3 (2009), pp. 147–152.

[464] M. Ashtarayeh, T. Streubel, K. Püschel, and S. Mohammadi. “Effect of autolysis, fixation, and storage in PBS on relaxation rates and macro-molecular tissue volume across fiber pathways of the human brain”. In: *Proceedings of the International Society for Magnetic Resonance in Medicine*. Vol. 26. 2018, p. 2066.

[465] S. R. Brannan and D. A. Jerrard. “Synovial fluid analysis”. In: *The Journal of Emergency Medicine* 30.3 (2006), pp. 331–339.

[466] F. Eckstein, F. Cicuttini, J. P. Raynauld, J. C. Waterton, and C. Peterfy. “Magnetic resonance imaging (MRI) of articular cartilage in knee osteoarthritis (OA): morphological assessment”. In: *Osteoarthritis and Cartilage* 14 (2006), pp. 46–75.

[467] S. Koo, G. E. Gold, and T. P. Andriacchi. “Considerations in measuring cartilage thickness using MRI: factors influencing reproducibility and accuracy”. In: *Osteoarthritis and Cartilage* 13.9 (2005), pp. 782–789.

[468] D. Terčič and B. Božič. “The basis of the synovial fluid analysis”. In: *Clinical Chemistry and Laboratory Medicine* 39.12 (2001), pp. 1221–1226.

[469] P. J. Wu, M. I. Masouleh, D. Dini, C. Paterson, P. Török, D. R. Overby, and I. V. Kabakova. “Detection of proteoglycan loss from articular cartilage using Brillouin microscopy, with applications to osteoarthritis”. In: *Biomedical Optics Express* 10.5 (2019), pp. 2457–2466.

[470] L. R. Gale, R. Coller, D. J. Hargreaves, B. A. Hills, and R. Crawford. “The role of SAPL as a boundary lubricant in prosthetic joints”. In: *Tribology International* 40.4 (2007), pp. 601–606.

[471] A. Szeri, E. Zaretsky, I. Etsion, M. Bryant, S. Jacobson, S. Hogmark, R. Glovnea, M. Khonsari, E. Booser, X. Xue, A. Polycarpou, and G. Nikas. *Recent Developments in Wear Prevention, Friction and Lubrication*. Ed. by George K. N. Research Signpost, 2010. ISBN: 9788130803777.

[472] URL: https://www.tribonet.org/wiki/stribeck-curve/%5C#Measuring_Stribeck_Curve (visited on 08/22/2022).

[473] B. Baroli. “Hydrogels for tissue engineering and delivery of tissue-inducing substances”. In: *Journal of Pharmaceutical Sciences* 96.9 (2007), pp. 2197–2223.

[474] URL: https://yorkshirekneeclinic.com/possible-new-treatments-for-osteoarthritis/ (visited on 08/22/2022).

[475] M. N. V. R. Kumar. “Nano and microparticles as controlled drug delivery devices”. In: *Journal of Pharmaceutical Sciences* 3.2 (2000), pp. 234–258.